Mapping Porous Solid Catalysts with Fluorescent Molecules and Nanoparticles

Erik Maris

Mapping Porous Solid Catalysts with Fluorescent Molecules and Nanoparticles

Mapping Porous Solid Catalysts with Fluorescent Molecules and Nanoparticles

Het in kaart brengen van poreuze, vaste katalysatoren met fluorescente moleculen en nanodeeltjes

(met een samenvatting in het Nederlands)

Proefschrift

ter verkrijging van de graad van doctor aan de
Universiteit Utrecht
op gezag van de
rector magnificus, prof. dr. H.R.B.M. Kummeling,
ingevolge het besluit van het college voor promoties
in het openbaar te verdedigen op

woensdag 7 juni 2023 des middags te 12.15 uur

door

Jacob Jan Erik Maris

geboren op 10 mei 1994
te Gouda

Promotor:
Prof. dr. ir. B.M. Weckhuysen

Copromotoren:
Dr. F. Meirer
Dr. F.T. Rabouw

Beoordelingscommissie:
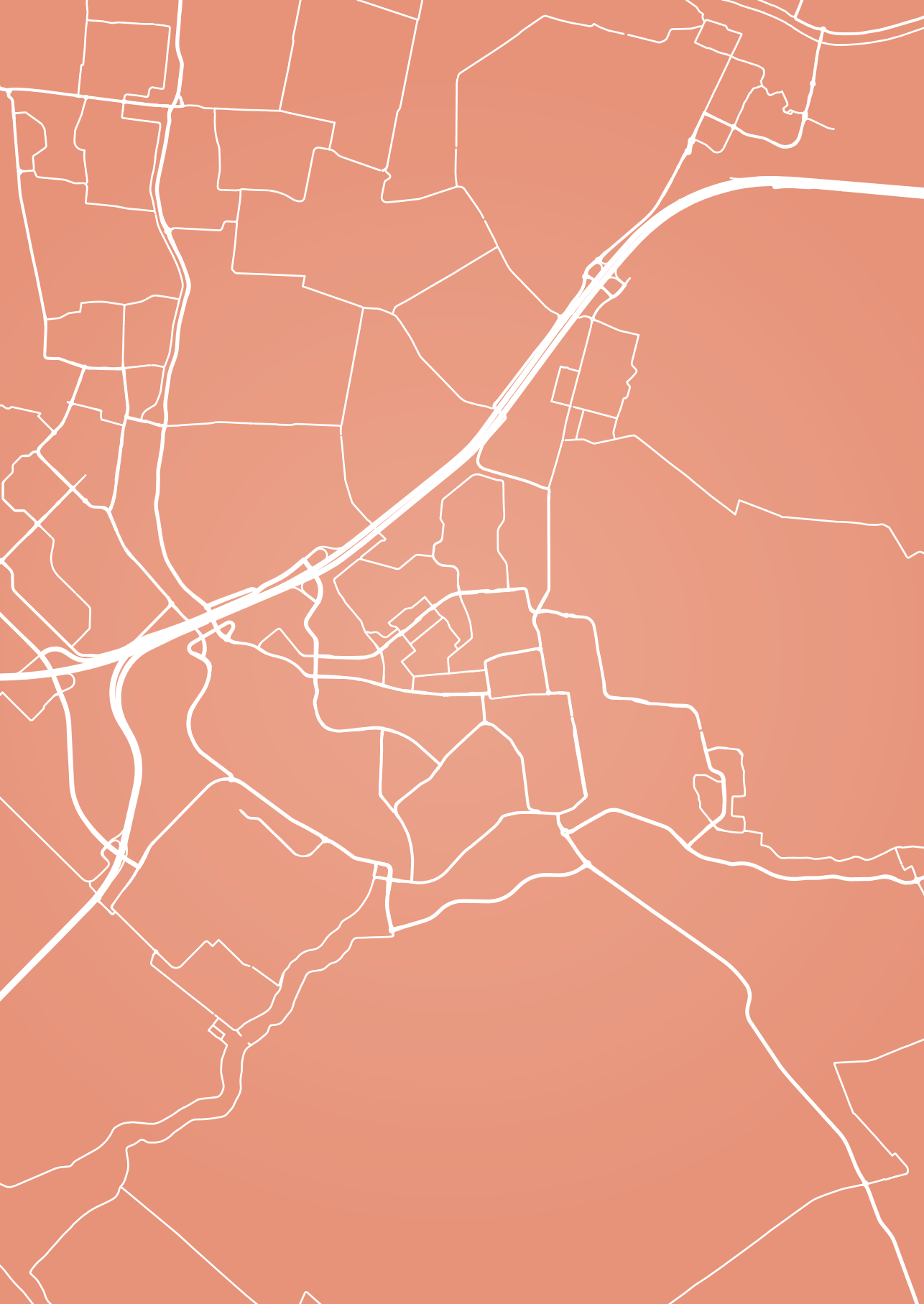Prof. dr. A. van Blaaderen
Prof. dr. P. Chen
Prof. dr. A. Meijerink
Prof. dr. ir. M.B.J. Roeffaers
Prof. dr. E.T.C. Vogt

Table of contents

Chapter 1

Introduction

1.1 • The challenge

We are confronted with societal challenges on an unprecedented scale. Over the past decade, climate change has become evident: rising global temperatures result in more extreme weather conditions, ocean warming and acidification, and rising sea levels. Its implications are severe and the existential danger that lies in the climate change cannot be overstated. One of the main driving forces behind climate change is the emission of greenhouse gasses by human activities. These gasses trap heat in the atmosphere as a result of the greenhouse effect, causing global temperatures to rise. The burning of fossil fuels as energy source results in the release of enormous amounts of carbon dioxide (CO_2) into the atmosphere. Despite initiatives to remove this gas from the carbon cycle via CO_2 capture and storage (better known as CCS) technologies, more is added than removed and carbon dioxide accumulates.[1] Each year the greenhouse effect is amplified and more profound solutions are required. Unfortunately, there is no silver bullet to reducing our greenhouse gas emissions.

Catalysis plays an important role in the reduction of fossil fuel consumption and greenhouse gas emissions by making existing chemical production processes more efficient, cleaner, and circular. Much can be gained as 29% of greenhouse gas emissions in 2016 originated from an industrial source (Figure 1.1), and about 85–90% of the products of the chemical industry are made involving a catalytic transformation.[2,3] The development of better catalyst materials results in lower energy consumption and waste production. Furthermore, the transition to circular production processes reduces CO_2 release from incineration of the spent products and lowers the need for virgin chemical building blocks, which are often derived from fossil fuels. The evolution to a circular economy requires many new catalyst materials to be developed. Both on the short and long term, catalysis seems to play an important role in combatting climate change.

1.2 • What is a catalyst?

Catalysis is the acceleration of a chemical reaction by addition of a substance, which in principle is recovered unchanged after the reaction. This substance we call a catalyst. A well-known example is the catalyst material in car exhausts that converts harmful compounds, such as carbon monoxide, nitric oxide, and nitrogen
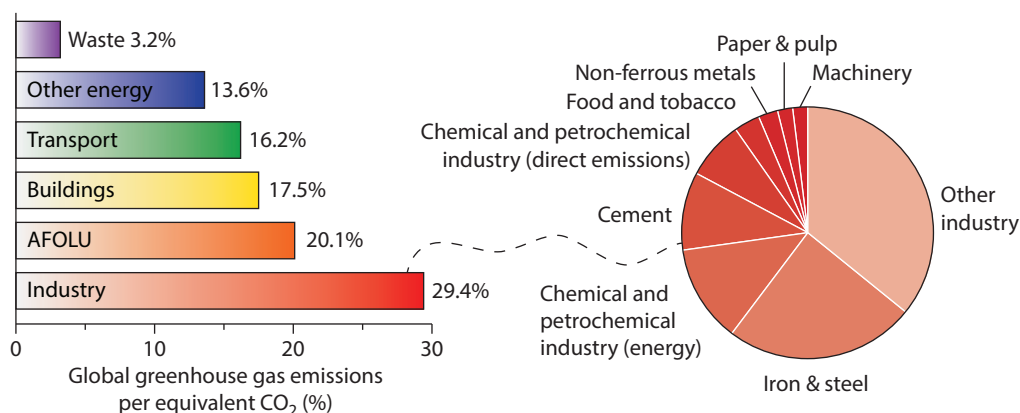
Figure 1.1 • Total greenhouse gas emissions in equivalent carbon dioxide (CO_2) from (economic) sectors in 2016 (**left**). The sector *agriculture, forestry, and other land uses* is denoted by AFOLU. Indirect emissions from electricity and heat production have been included in the emissions per sector. The *industry* emissions have been categorized in subsectors, as shown in the circle diagram (**right**). *Other industry* includes mining and quarrying, construction, textiles, wood products, and transport equipment such as car manufacturing. Data from Ritchie and Roser.[2]
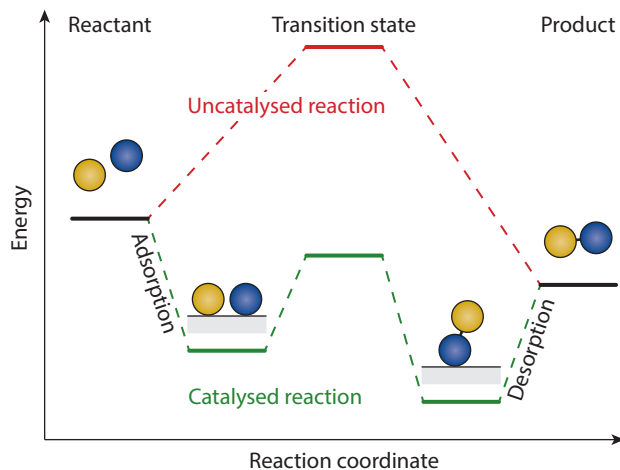
Figure 1.2 • Schematic representation of the energy as a function of the reaction progress for a catalysed and uncatalysed reaction. The catalyst reduces the energy barrier by stabilisation of the transition state.

dioxide, into less harmful substances, such as molecular nitrogen and CO_2. Also life would not have been possible without enzymes, which are the biocatalysts in organisms. A catalyst stabilises the transition state in a chemical reaction by making and breaking of chemical bonds, thereby reducing the energy barrier that must be overcome to complete the chemical reaction. This is depicted in Figure 1.2. The catalyst allows the chemical reaction to proceed faster or at milder conditions. It does not change the energy of the reactants and products as this would be a violation of the first law of thermodynamics. The catalytic process is much like taking a series of tunnels through the mountain range instead of a windy road over the summits. The tunnels allow the destination to be reached more efficiently without changing the destination itself. Ideally, the catalyst is used rather than consumed in the catalytic process because the catalyst returns to the same state as before the chemical reaction.[4] However, in practice the catalyst deactivates over time and must be replaced occasionally.

In heterogeneous catalysis, the catalyst and reactants are in a different phase of matter. The catalyst is often a solid, while the reactants are in the gas or liquid phase. Facile separation of the catalyst from the reaction products as well as high stability under the harsh conditions applied in a chemical reactor have helped hetero-geneous catalysts to become the workhorse of the chemical industry. Heterogeneous catalysis is a process that involves many different length scales as is visualised in Figure 1.3. Catalysed reactions usually take place on the surface of a material, called the active site, which is often a metal. To use the metal in an economical way, nanometre-sized metal particles are used to optimise the surface area per gram of material. Moreover, other effects that may be beneficial for catalysis start to play a role at these length scales. The arrangement of the metal surface atoms is highly dependent on the dimensions of the nanoparticle, altering its local surface geometry and electronic properties. Highly active surfaces are usually formed in the size range of 1–10 nm, but the optimal nanoparticle size is dependent on the chemical reaction.[3,5] The metal nanoparticles are placed on a porous support material to stabilise the nanoparticles, while keeping them accessible to the reactants. The result is often a complex material with heterogeneous composition and function. Heterogeneous catalysts come in a variety of shapes and sizes: from micrometre-sized catalyst powders to centimetre-sized catalyst bodies. The choice is strongly dependent on the type of reactor and reaction.

Active sites are not exclusive to metal nanoparticles, and zeolites are another important class of catalytically active materials. Zeolites
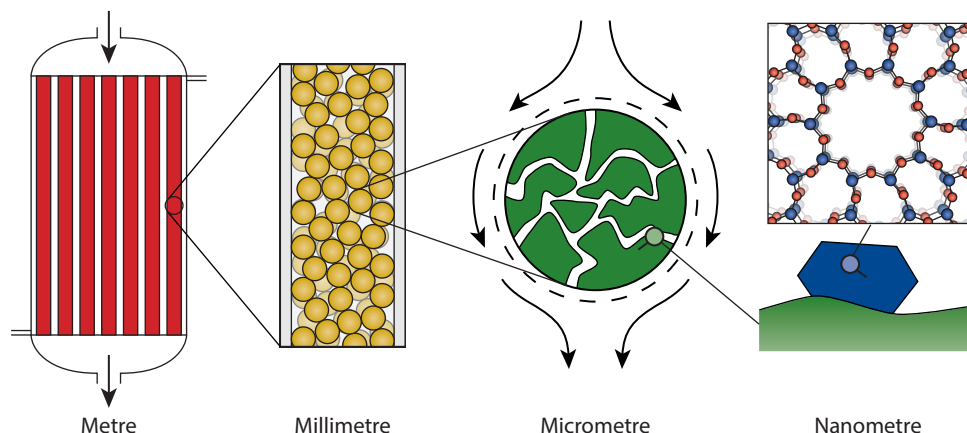
Figure 1.3 • Schematical depiction of the length scales involved in catalysis. A reactor (metre) is filled with a packing of porous catalyst particles (millimetre). Each particle has a porous network (micrometre) with active sites (nanometre). Here, we show zeolite active sites, but these active sites can also be metal nanoparticles or even other materials.

are crystalline aluminosilicates with well-defined pore sizes. Their pore diameter is usually smaller than a nanometre, which is in the size range of many industrially relevant molecules. Zeolites are built up from tetrahedra with silicon or aluminium atoms that are bridged by oxygen atoms, which is depicted in Figure 1.4. The tetrahedra assemble into larger structures, such as four-rings, six-rings, double four-rings, and double six-rings, which are called the secondary building units (SBUs) of a zeolite material. A zeolite crystal structure—or framework—can be typically constructed from a single type of SBU, but in some rare cases, combinations of SBUs are required to fully describe the framework. Incorporation of the aluminium tetrahedra into the zeolite structure leads to a charge disbalance. Because the aluminium atoms (Al^{3+}) have a lower positive charge than the silicon atoms (Si^{4+}), their charge in the zeolite framework must be compensated with a positively charged ion. When this framework ion is a proton (H^+), the material gains Brønsted acidity, making the zeolite a solid acid. It is these positively charged ions that give the zeolite its catalytic power.[3,6,7]

The crystal structure of a zeolite results in pores with a well-defined size and shape. An advantage of the well-defined pore structure is that the zeolite solely allows molecules of a certain size range to enter in its pores, imposing restrictions on the reactants, transition state, and products. This so-called size selectivity is beneficial for catalysis because it limits the formation of (undesired) side products and makes the overall chemical process more controlled. Many different zeolites have been discovered and their framework structures are denoted by a three-letter code. In Figure 1.4, three different frameworks are shown—SOD (sodalite), LTA (Linde type A), and FAU (faujasite)—which share a structural motif called the sodalite cage.[6–8] The pore opening of the framework is dependent on the ordering of the sodalite cage. As a result, zeolite A (LTA framework) and zeolite Y (FAU framework) have been successfully commercialised in different applications. Zeolite A is widely applied as water softener in detergents. It effectively removes calcium ions (Ca^{2+}) from water by exchanging them with the framework ion, which is often sodium (Na^+).[9] Contrarily, zeolite Y is an important catalyst for the petrochemical industry and is traditionally used to crack large molecules into smaller, useful products.[10]

The movement of molecules through a zeolite is rather slow; therefore, the zeolite crystal size is kept small to minimise the distance molecules must travel through the material. The zeolites are embedded in a support material for stability, analogous to supported metal nanoparticles. They are mixed with other active materials and a binder, such as silica (SiO_2), alumina (Al_2O_3), and/or clay. The resulting catalyst particle is a mixture of different active components, resulting in a complex heterogeneous functionality and pore network. An example of such a catalyst particle is the fluid catalytic cracking particle, also known as an FCC particle, which contains zeolite Y as the active zeolite component.[10,11] The catalyst material plays a major role in oil refining, but it was recently shown that the particles also have potential for the chemical recycling of plastic waste.[12] The particles have a diameter around 0.1 millimetre and are comparable in size and appearance to fine sand. Another example of such a catalyst particle is millimetre-sized shaped catalyst bodies. The advantage of using shaped catalyst bodies is that they can be easily loaded in an industrial reactor. They play an enormous role in numerous chemical processes, mainly involving the chemical transformation of hydrocarbons.[13,14] Any improvements based on the fundamental understanding of zeolite-based catalysts would have a large impact on CO_2 emissions simply because of the enormous scale at which they are applied.

1.3 • Transport of molecules through a catalyst particle

Transport of reactant and product molecules through the porous catalyst particle is often the limiting factor in their application.[15,16] Therefore, optimisation of the pore network is an important aspect in the quest for more effi-
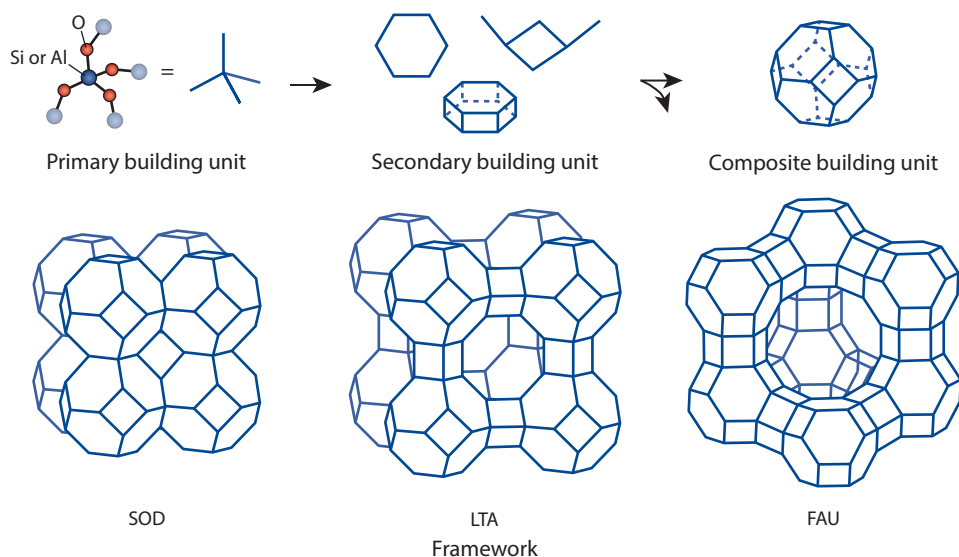
Figure 1.4 • Zeolites are built up from the primary building unit, which assemble into larger structures called secondary building units (SBUs). The primary building unit is a silicon (Si) or aluminium (Al) tetrahedron, which shares four oxygen (O) atoms with neighbouring tetrahedra. The SBU are structures consisting of up to sixteen tetrahedra, and three example structures are shown. They are derived assuming that the entire framework is made up of one type of SBU only, although exceptions to this rule exist. Some zeolite framework structures share a composite building unit, which is a structural motif that is used to find similarities between different frameworks. Three frameworks with the sodalite composite building unit are shown. Their pore size increases from left to right.

+ Fast transport
− Few active sites

+ Many active sites
− Slow transport

+ Many active sites
+ Fast transport

Figure 1.5 • A hierarchical pore structure has both large pores to facilitate rapid molecular transport to the active sites and a large internal surface area to expose the active sites to the pores.

cient catalysts as well as catalysts for new, more sustainable chemical reactions. The transport of molecules to the catalyst's active sites can be loosely compared to commuters traveling through a metropole to their workplace. The highways serve the major in- and outflux of commuter traffic, whereas smaller streets allow commuters to travel into the neighbourhoods. A balance between int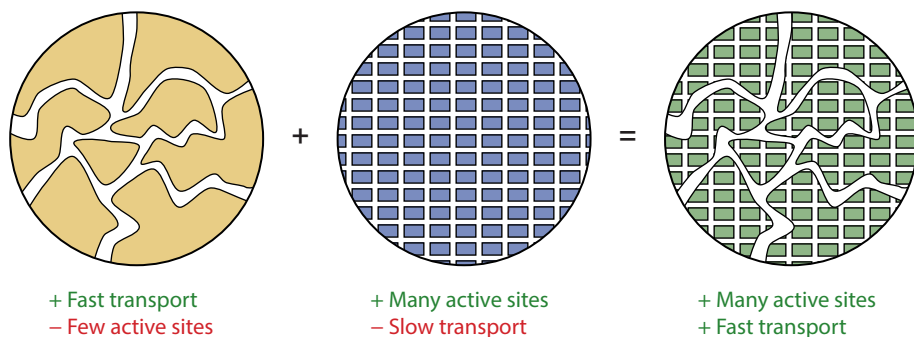erconnected streets and highways is crucial to make sure that the travel time to a workplace is minimal. In a catalyst particle, we would like to achieve the same. Instead of a metropole with roads and working spaces, we have a particle with pores and active sites. In a catalyst with long travel times caused by small pores, the reactants are fully converted into products before they reach the centre of the catalyst particle, leaving it unused. Slow transport could even result in more undesired products due to sequential reaction mechanisms, which in turn can clog up the pores and deactivate the catalyst. Contrarily, large pores facilitate fast transport and short travel times, but the density of active sites that can be placed on the support surface is low. A successful approach is to utilise a so-called hierarchical pore structure comprising a wide range of pore sizes with macro- (> 50 nm), meso- (2–50 nm) and micropores (< 2 nm), which is depicted in Figure 1.5. Exactly like in a metropole, a good balance between the differently sized, interconnected pores is of paramount importance for an efficient catalyst—and is a major factor to be optimised.[17]

1.4 • Fluorescence microscopy as an analytical tool to study catalyst heterogeneity

Heterogeneous catalysts are heterogeneous in almost every aspect.[18] Because of the preparation method, the catalysts' pore space is heterogeneous within and between single particles. Moreover, frequent interactions between molecules and catalyst pores strongly affect mass transport behaviour giving rise to complex heterogeneous motion.[15,16] Heterogeneity is not limited to the pore space and molecular mass transport: zeolite aggregate domains with seemingly identical structural features have been shown to exhibit significantly different catalytic reactivity.[19] To understand the catalyst, one has to understand its heterogeneity. Traditionally, the pore space and mass transport are characterised in bulk *ensemble*, and only average values are obtained. The downside of the ensemble approach is that heterogeneities in the measured property are averaged out (Figure 1.6). To optimise the catalysts' performance, we need to understand the type and number of heterogeneities in the catalyst, and this study demands a different approach.

Fluorescence microscopy can be considered as a Swiss army knife for the characterisation of pore space and mass transport therein. The fluorescence of molecules and nanoparticles can be mapped with sub-micrometre resolution and high sensitivity using fluorescence micros-
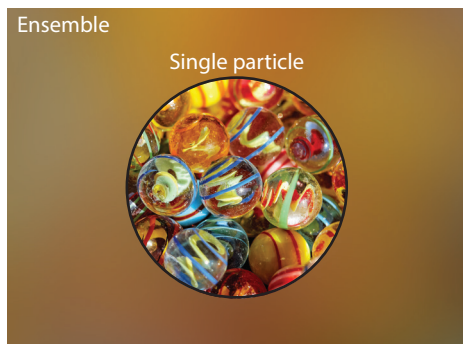
Figure 1.6 • The sample must be investigated at the single-particle level to uncover heterogeneities among and within the individual particles, here depicted as marbles.

copy techniques. This allows us to detect heterogeneities in both space and time. We use the fluorescence emission of the reporters as a sensor for the local pore environment. Changes in the colour or brightness of the fluorescence allow us to specifically map properties of the pores. Alternatively, we follow the motion of single probes or their ensemble movement to study the interaction between the pore space and fluorescent reporter. Either this reveals directly how mass transport is affected by the local pore space, or indirectly by characterisation of the pore space via probe–pore interactions. Altogether, imaging of fluorescent reporters allows for the study of the pore space and mass transport at the level of individual catalyst particles and/or molecules. The aim of this PhD thesis is: 1) to expand the toolbox of fluorescent probes and fluorescence-based microscopy methods for the study of heterogeneity in pore space and mass transport and 2) their application in industrially relevant zeolite materials and other porous catalysts. The significance of the findings is not limited to the study of porous catalysts but extends to the technological application of porous solids in general, e.g., for sorption, separation, and sensing processes.[15]

1.5 • Outline of this PhD thesis

In this PhD thesis, we use fluorescent probes to trace mass transport through porous solid catalysts and to characterise the catalysts' pore space. By increasing the complexity—starting from a model pore and going all the way up to an industrially relevant zeolite particle—we are building a picture of the different relationships between mass transport and pore space in porous solid catalysts. The PhD thesis is organised as follows:

Chapter 2 provides the theoretical and practical background required to understand the work described in this PhD thesis. A perspective is given on mass transport in zeolites and single-molecule tracking experiments in solid porous catalysts. The fundamentals of molecular fluorescence are discussed followed by an introduction of the two fluorescence microscopy techniques used in the thesis.

Chapter 3 discusses the *DiffusionLab* software and workflow used to quantify mass transport from single-molecule trajectories. In this method, the trajectories are first classified into populations with similar characteristics to which the motion analysis is tailored in a second step. This approach is particularly powerful for trajectory datasets with short trajectories and heterogeneous underlying motion behaviour—often found in porous solids. We demonstrate the DiffusionLab method via the analysis of a simulated dataset with motion behaviours experimentally observed in porous catalyst materials.

In **Chapter 4**, we present a nanofluidic device designed for the characterisation of fluorescent probes in confinement. The device consists of a two-dimensional model pore with a height of 50 nm, mimicking a catalyst macropore. We investigate the trap behaviour of single quantum-dot emitters at the pore wall and their

diffusion through the pore. The quantum-dot trapping can be tuned via the solution pH, likely because of a change in the electrostatic repulsion between the probe and pore wall. Furthermore, we find that—in the reported conditions—the diffusion coefficient is not substantially affected by the short, transient trap events. Building on this knowledge, we define conditions that allow mapping of the accessible pore space of a one-dimensional pore network as well as a real-life polymerisation catalyst particle.

Chapter 5 gives the results of a single-molecule tracking study of fluorescent oligomers in industrially important ZSM-5 zeolites. We quantify the oligomers' motion behaviours and mobility in the sinusoidal and straight channels of zeolite ZSM-5 using the methodology outlined in Chapter 3. Both factors are strongly affected by the geometry of the zeolite channels resulting in diffusion anisotropy. We extend the study to hierarchical zeolites, which have additional secondary meso- and macropore networks in the material. We find that the addition of these networks primarily enhances molecular diffusion through the si-nusoidal zeolite channels, alleviating diffusion limitations of microporous zeolites.

Chapter 6 investigates a fluorescent reporter molecule that is sufficiently small to fit in the zeolite micropores. We find that the resorufin molecule changes its fluorescence behaviour when confined in the micropores of zeolite-β. Aggregation-induced quenching as well as fluorescence loss pathways are suppressed within the zeolite, boosting fluorescence in confinement. Several factors affect the measured resorufin fluorescence emission inside the zeolite. Notably, its fluorescence emission is pH sensitive showing resorufin's potential to be applied as pH sensor in the zeolite's micropores. We demonstrate the application of resorufin by direct visualisation of anisotropic diffusion through zeolite-β's straight channels and the diffusion barrier imposed by the boundaries between the zeolite subunits.

In **Chapter 7**, a short summary of the main results of this PhD thesis is given. We also provide an outlook on possible future research directions and related applications.

1
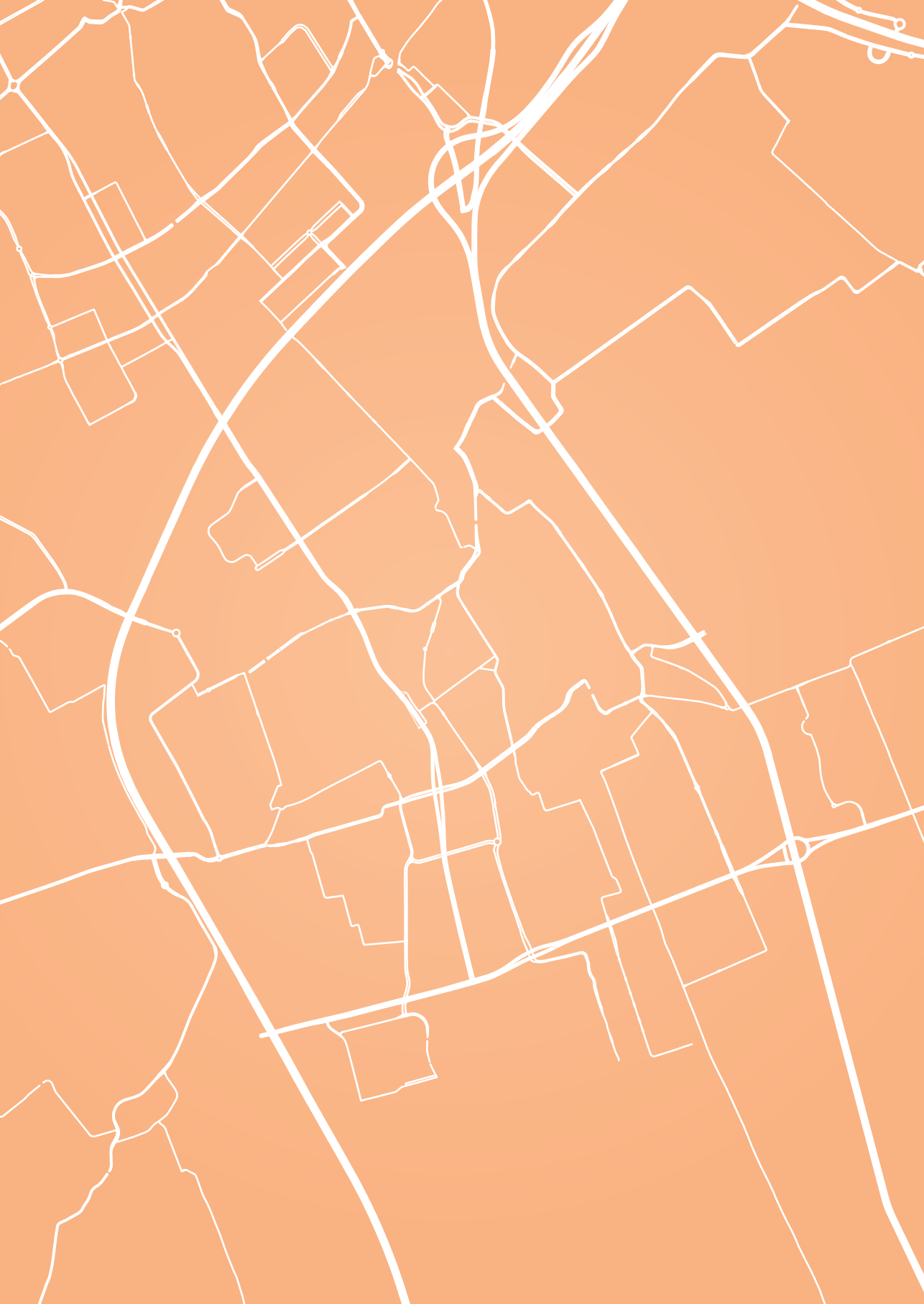
Chapter **2**

Thesis background on diffusion in porous solids and fluorescence microscopy

This chapter is based on the following scientific publications:

- Maris, J. J. E., Fu, D., Meirer, F. & Weckhuysen, B. M. *Adsorption* **27**, 423–452 (2021).
- Fu, D.,[+] Maris, J. J. E.,[+] Stanciakova, K., Nikolopoulos, N., Van der Heijden, O., Mandemaker, L. D. B., Siemons, M. E., Salas Pastene, D., Kapitein, L. C., Rabouw, F. T., Meirer, F. & Weckhuysen, B. M. *Angew. Chem. Int. Ed.* **64**, e202114388 (2022).
- Maris, J. J. E., Rabouw, F. T., Weckhuysen, B. M., & Meirer, F. *Sci. Rep.* **12**, 9595 (2022).
- Maris, J. J. E.,[+] Parker, L. A.,[+] Stanciakova, K., Nikolopoulos, N., Berendsen, K. M. H., Van Blaaderen, A., Meirer, F., Rabouw, F. T., & Weckhuysen, B. M. *Submitted.*

[+] Both authors contributed equally to this work.

Abstract • Diffusion and fluorescence play a key role in this PhD thesis, and the required theoretical and practical background is introduced in this chapter. We discuss the concepts and historical context of molecular diffusion in porous solids, including catalyst particles. Microscopy techniques have a prominent role in the measurement of diffusion barriers and the heterogeneous motion of individual molecules as they move through a porous solid. The physical origin of fluorescence is introduced, which provides the required background to understand the advantages and caveats of using fluorescent reporters in porous solids. We predominantly use two fluorescence microscopy techniques throughout the work to image the fluorescent reporter molecules and nanoparticles, that is, confocal laser scanning microscopy and single-molecule localisation microscopy. We explain their working principle and motivate their application for the characterisation of porous solids. Finally, we illustrate how single-molecule localisation microscopy can be used to track individual molecules and to determine their diffusion coefficients.

2.1 • Measuring diffusion in porous solids

2.1.1 • Macroscopic versus microscopic measurement

Molecules—in fact all matter—tend to move around in such a way that their concentration is homogenised throughout space, ensuring maximum randomness or entropy. It is the thermal motion of molecules that causes spontaneous mixing. This phenomenon can be easily demonstrated by the deposition of a droplet of ink into a glass of water without stirring. After a few hours, the ink will have spread out over a distance of a few millimetres, while the solution will be homogeneously coloured after a few days. This process is called diffusion and occurs at temperatures above absolute zero. It is also the driving force behind the transport of reactant and product molecules during catalysis.

The quantification of diffusion started halfway the nineteenth century with the work of two pioneers: Thomas Graham and Adolf Fick.[15,20,21] Two decades earlier, Graham's initial study of diffusion in gasses led to Graham's law of diffusion, which states that the rate of spontaneous diffusion of one gas into another is inversely proportional to the square root of the density of that gas.[22] Later, Graham extended his study to the diffusion of salt in water and noted that diffusion in liquids is many orders of magnitude slower than in gasses.[23] Fick regretted that this investigation did not lead to the development of a fundamental law for diffusion and set out to formulate one.[24] He recognised that

Graham's results could be described by a law in the same general form as Fourier's praised law of heat conduction, resulting in an equation which is generally known as Fick's first law

$$J = -D\frac{\partial c}{\partial x} \tag{2.1}$$

where the flux of matter J in the x-direction is proportional to the gradient of the concentration c. He introduced a proportionality constant, which is the formal definition of the diffusion coefficient D. Using the equations of conservation of matter, analogous to Fourier's treatment of heat conduction, Fick derived his second law

$$\frac{\partial c}{\partial t} = D\frac{\partial^2 c}{\partial x^2} \tag{2.2}$$

with time t, assuming a parallel-sided duct with a constant diffusivity. Depending on the boundary conditions, different solutions exist, and we will only discuss one relevant for the treatment of Brownian motion.

The mathematical formulation of the random walk bridged the macroscopic Fick's laws to the microscopic world of atoms, molecules, and granules.[15,20,21] Robert Brown had already reported, years before the seminal work by Graham and Fick, that grains inside pollen suspended in water undergo a random movement.[25] Nowadays we know that this movement is caused by random collisions of the surrounding solvent molecules and pollen grains, and we refer to this phenomenon as Brownian

motion—also known as a random walk. To understand its link with the macroscopic quantity of diffusion, let us go back to Equation 2.2. If we consider the boundary conditions where at the beginning of the experiment ($t = 0$) all particles are at one position in space ($x = 0$), the solution of Equation 2.2 can be expressed as a

$$P(x,t) = \frac{e^{-x^2/4Dt}}{\sqrt{4\pi Dt}} \quad (2.3)$$

which is the probability of finding a Brownian particle after a certain time t displaced over a distance x. Using Equation 2.3, we find that the mean squared displacement is

$$\langle x^2(t) \rangle \equiv \int_{\infty}^{-\infty} x^2 P(x,t)\mathrm{d}x = 2Dt, \quad (2.4)$$

which scales linearly with observation time t. This relation was presented by Albert Einstein in 1905, fifty years after the publication of Fick's laws, and is generally referred to as Einstein's diffusion equation.[26] An excellent way to capture the motion of a single moving particle is to record its location as a function of time, yielding a so-called trajectory. A few years after Einstein's seminal work, Jean Baptiste Perrin studied the movement of single granular and colloidal particles by recording their trajectory, and by doing so, was the first to experimentally verify Einstein's work on Brownian motion.[27,28] Altogether, Einstein's diffusion equation (Equation 2.4) connects the macroscopically observable diffusion coefficient described by Fick's first law (Equation 2.1) to the mean squared displacement of individual particles, which can be directly obtained from a microscopic single-particle trajectory.

Transport and self-diffusion. Two fundamentally different types of collective diffusion exist: transport diffusion and self-diffusion.[15,29] Transport diffusion is the spontaneous mixing in the presence of a concentration (or chemical potential) gradient (Figure 2.1a), while self-diffusion occurs under equilibrium conditions, i.e., without such a gradient. The latter can be followed via the displacement of individual molecules or particles, as was demonstrated in the experiments of Brown and Perrin (Figure 2.1b), or by following the concentration gradient of a small fraction of labelled molecules, for instance using isotopically labelled tracers (Figure 2.1c). The coefficient of self-diffusion has an additional self-exchange diffusivity component, which accounts for the resistance of counter-diffusing molecules. In the limit of a negligible self-exchange component, e.g., due to a large resistance of the porous host's pore network, the transport diffusion D_T and self-diffusion D_self coefficients are related by

$$D_\mathrm{T} = D_\mathrm{self} \frac{\partial \ln p}{\partial \ln c} \quad (2.5)$$

with p the gas pressure and c the equilibrium concentration of the diffusing molecules. The
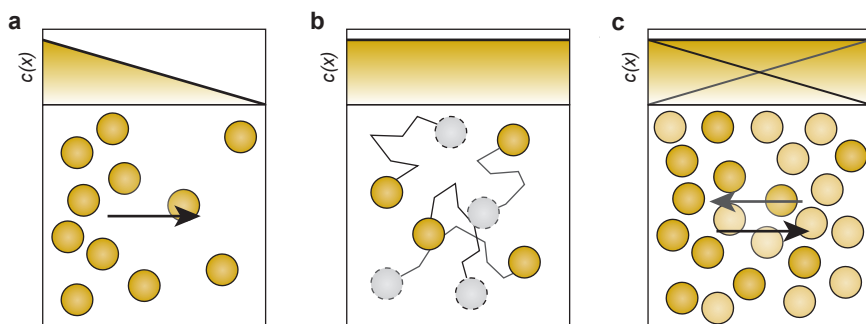

Figure 2.1 • Microscopic representation of diffusion measurements and the concentration profile $c(x)$: (**a**) transport diffusion via the concentration gradient; (**b**) self-diffusion via displacements; and (**c**) self-diffusion through the concentration gradient of a tracer subpopulation. Adapted from Kärger et al.[29]

$\partial \ln p / \partial \ln c$ component is a thermodynamic factor that accounts for attraction and repulsion between the molecules.[29,30] At low molecular concentration, the molecular interactions are negligible and transport- and self-diffusion have identical values. This has been shown experimentally for solute diffusion in dilute conditions[15,31] and in a microporous catalyst at the low concentration limit, when encounters between diffusing molecules are rare.[15,32]

2.1.2 • Diffusion barriers in porous solids

Diffusion in porous solids, such as heterogeneous catalysts, is dominated by the interaction between guest molecules and the porous host. As a result, it is much more complex than free diffusion in the liquid or gas phase and gives rise to interesting new phenomena. Diffusion in porous solids is traditionally measured with uptake or release experiments. The number of molecules in the solid is measured as a function of molecule concentration in the surrounding atmosphere, i.e., by a stepwise change in pressure. The diffusion coefficient is derived from the molecular uptake or release by comparison with a predictive kinetic model for the internal fluxes. The model is based on the assumption that the diffusion is only limited by the pore network of the porous host.[15,30] A different light was shed on this assumption with the development of pulsed-field-gradient nuclear magnetic resonance (PFG NMR) spectroscopy, which introduced the possibility to measure diffusion displacements of molecules over micrometre length scales.

In zeolites, a great disparity between the measured diffusion coefficients from uptake experiments and PFG NMR was found. The diffusion barrier of the pore network itself was frequently found to be one of many resistances present.[33,34] Others were discovered, including diffusion barriers in the intracrystalline space[35] and on the external surface.[36] The measured diffusion coefficients in zeolites with PFG NMR were corroborated by quasi-elastic neutron scattering, which measures diffusion displacements over nanometre length scales, and molecular dynamics simulations.[30] Whereas uptake experiments measured the *macroscop-ic* diffusion including diffusion barriers, the *microscopic* (predominantly) intracrystalline diffusion was measured with PFG NMR. Diffusion barriers turned out to have a large impact on molecular diffusion in porous solids, which is evident from the orders of magnitude difference in values for the diffusion coefficient found in micro- and macroscopic diffusion measurements.

Microimaging for the study of diffusion barriers. The application of microimaging techniques, particularly interference microscopy and infrared microspectroscopy, have been essential in the study of diffusion barriers.[30,37] Average diffusion coefficients were obtained with uptake and PFG NMR techniques, but spatial heterogeneity could not be inferred. To better understand the functioning of porous materials and the origin of the diffusion barriers, a microscopic understanding of the local pore geometry and functionality correlated with molecular motion was required. This has driven the search for microscopic techniques that are able to measure local variations in mass transport within a single porous particle. Using microimaging techniques, transient concentration profiles of guest molecules can be measured with micrometre resolution, and these methods allow for the direct measurement of diffusion barriers.

The investigation of surface barriers with microimaging has given much insight in heterogeneity at the single-zeolite-crystallite level. Two extreme cases of surface resistance have been identified. Access to the pores is either restricted inhomogeneously, leaving only a few areas of the surface area permeable, or homogeneously, e.g., due to a poor interconnectivity between the intracrystalline pore network and outer surface.[37,38] The surface permeation was found to vary more than an order of magnitude between different zeolite crystals from the same batch—underlining the heterogeneity of porous catalysts particles.[39] Interestingly, the surface permeabilities of different faces of the same crystal were found to be basically identical.[37] It is likely that the faces of the same crystal experience roughly the same synthesis, treatment, and storage conditions, while this is

not the same for different crystals of the same batch. However, the intracrystalline diffusivity was found to be identical for crystals of the same batch and does not appear to be as sensitive to external factors.

2.1.3 • Diffusion heterogeneities in porous solids

Frequent interactions between guest molecules and porous solid hosts strongly affect diffusion and adsorption behaviour giving rise to complex heterogeneous motion.[15,16,40,41] Investigations at the single-molecule level can reveal these heterogeneities and thus provide deeper insight into such guest–host interactions and their effect on mass transport.[15,18,42–47] Single-molecule localisation microscopy is a direct way to visualise and quantify molecular motion and heterogeneities therein. Locations of single molecules can be extracted with nanometre precision from time-lapse videos recorded with super-resolution fluorescence microscopy. Diffusion is then quantified from the displacements of a molecule within a trajectory.[48,49] This allows for spatial and temporal mapping of the heterogeneities without a priori knowledge of the diffusion process. It was shown that the diffusion coefficients obtained from single-molecule trajectories, that is the time-average, and the ensemble value measured with PFG NMR are in perfect agreement as predicted by the ergodicity theorem.[50,51] This demonstrates the consistency between the two conceptually different approaches in equilibrium conditions and validates the interpretation of diffusion coefficients obtained from single-molecule trajectories. Alternatively, single-molecule localisation microscopy can be employed to record single reaction events using fluorogenic molecules, which directly maps the reactivity and provides indirect information about mass transport to the active reaction sites.[52–54]

Single-molecule tracking experiments in mesoporous silica have laid the foundation for our understanding of single-molecule diffusion in porous solids. It makes an excellent model system to study diffusion due to the high degree of control over both pore size and chemical environment inside the pores. The first observations of single-molecule trajectories in mesoporous silica revealed strong heterogeneities in molecular motion.[55–58] Inter- and intra-trajectory heterogeneities were observed in both non-ordered glassy and ordered templated mesoporous silicas with pore sizes of respectively 3 and 22 nm. In the non-ordered glassy sample, trajectory segments were observed in which the molecule appeared to be trapped for some time (Figure 2.2a). The authors speculated that this could either be an adsorption event by temporary bonding to the silica surface or confinement, e.g., in a narrow pore, leading to strongly hindered motion.[56] The term *adsorption* is used in this thesis, although trapping as a result of confinement often cannot be excluded. In the ordered mesoporous silica, no temporary trapping was observed, but the motion could not be described by a single diffusion coefficient (Figure 2.2b,d).[55] These different diffusion regimes were not spatially separated within a single trajectory and indicated variations in the microenvironment of the reporter molecule.[55,59] A final remarkable observation was that the probe diffusion appeared to follow a specific direction instead of moving randomly as would be expected for normal (Brownian) diffusion (Figure 2.2c).[55] The pore geometry and local obstructions could confine the probe into a pore domain. Transient trapping of the fluorescent probe, multiple diffusion regimes, and apparent confinement to the pore geometries turned out to be key observations and have led to two decades of single-molecule studies of motion heterogeneity in mesoporous silica.[44,47,60]

Building on the single-molecule tracking work in mesoporous silica, the step to poorly defined, industrially relevant, porous catalysts was made in 2017. Hendriks and Meirer et al. studied single-molecule diffusion of a perylene diimide (PDI)-based fluorescent probe in fluid catalytic cracking (FCC) particles, an important industrial catalyst described in Chapter 1 (Figure 2.3a,b).[61] Even though the large PDI-based molecule could not probe the microporous zeolite domains, single-molecule diffusion in a single FCC particle revealed a large range of diffusion coefficients spanning at least

three orders of magnitude. Much like mesoporous silica, heterogeneity in motion patterns was observed including transient trapping of the molecular probes. The trajectories were segmented into *mobile*, *immobile* and *hybrid* categories to quantify the diffusion coefficient and trap behaviour of the diffusing molecules (Figure 2.3c–g). We build upon this methodology in Chapters 3 & 5. The mobile and hybrid trajectories were spatially homogeneously distributed, and the pore network could not be resolved directly from the trajectories mainly due to the limited trajectory lengths obtained (Figure 2.3h). The spread in diffusion coefficients (Figure 2.3i) was attributed to the large pore size distribution; however, the heterogeneous material composition could also have contributed via intermittent physisorption events. The next frontier is to derive local material properties and/or pore sizes from the shape of the single-molecule trajectories. This requires an understanding of the physical origin of transient trap events, which is discussed in Chapter 4 and 5.

2.2 • Molecular fluorescence for diffusion measurements

2.2.1 • Transitions between electronic states

Microscopy techniques play a large role in the measurement of diffusion in porous solids. Microimaging has been important for the measurement of diffusion barriers, whereas single-molecule localisation microscopy has been crucial in the measurement of diffusion heterogeneities. In this section, we provide a theoretical and practical background of the two fluorescence microscopy techniques used in this PhD thesis. First, we introduce the fundamentals of fluorescence and provide a qualitative description of the effect of molecular aggregation on the fluorescence emission. Then, fluorescence microscopy and the optical resolution are introduced. Building on this, we discuss confocal laser scanning microscopy, which is followed by the explanation of single-molecule localisation microscopy in the context of diffusion measurements at the single-molecule level.
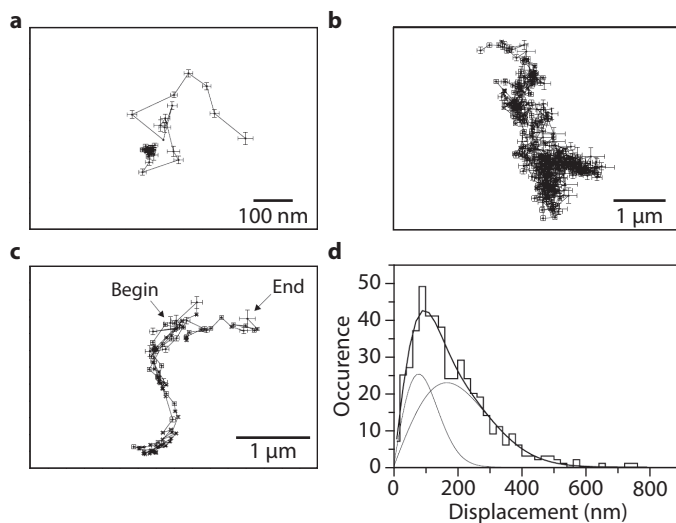
Figure 2.2 • Examples of heterogeneous diffusion behaviour in mesoporous silica as observed in early days of single-molecule tracking in porous solids: (**a**) single-molecule trajectories displaying trapping of the molecule; (**b**) anomalous diffusion; and (**c**) diffusion along the pore direction. (**d**) Step-length histogram and fit (thick solid line) of the trajectory displayed in panel **b**. The full step-length distribution can only be explained by the contribution of two different diffusion coefficients (thin solid lines) indicating at least two different underlying diffusion regimes. Adapted from Hellriegel et al.[55]

Figure 2.3 • Single-molecule trajectory classification and motion analysis of perylene diimide-containing fluorescent molecules in a single fluid catalytic cracking (FCC) catalyst particle. (**a**) Schematic of the imaging plane at the middle cross section in the FCC particle. (**b**) Schematic representation of the hierarchical pore structure of an FCC particle, where light grey represents the matrix and the darker grey squares the embedded zeolite crystallites. (**c**) Color-coded map of each recorded trajectory within the FCC particle, showing (**d**) immobile (red), (**e**) hybrid (green) and (**f**) mobile trajectories (blue)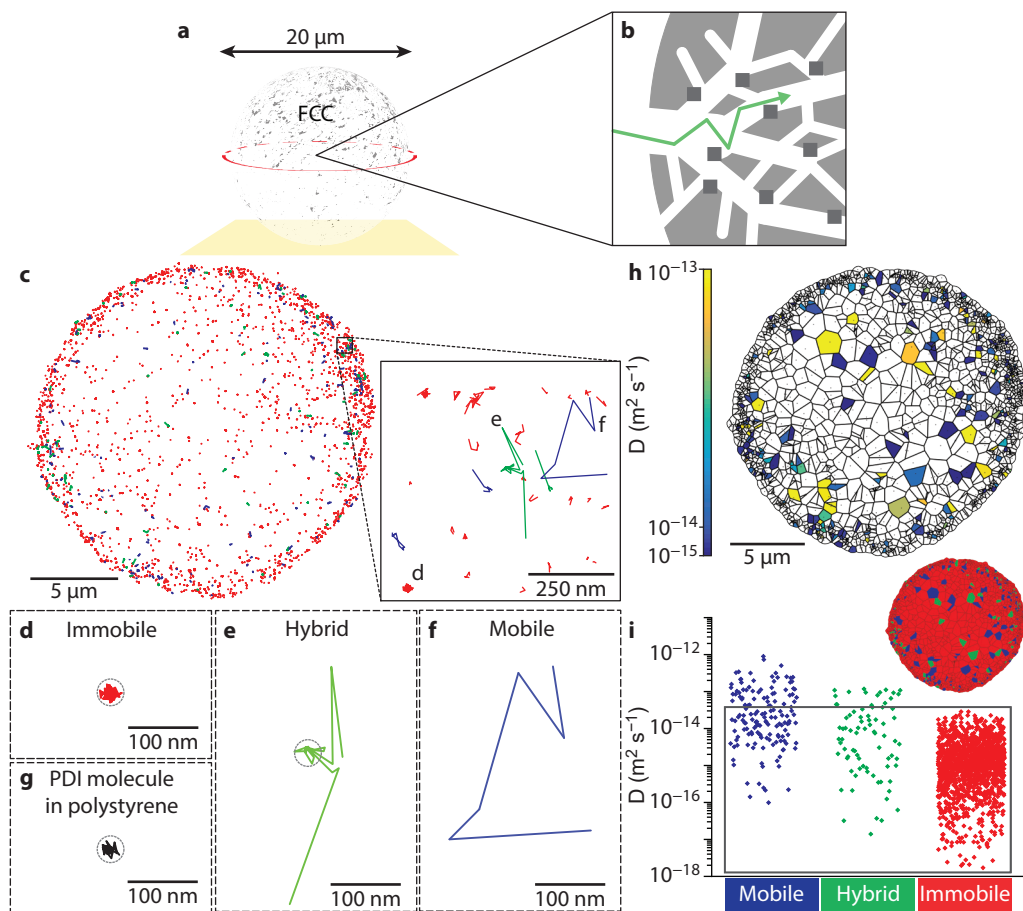. (**g**) Trajectory of the probe molecule immobilised in a polystyrene thin film, which has a similar radius as the immobile trajectory in panel **d** indicating a correct classification. (**h**) Voronoi diagram showing a spatial map of single trajectory diffusion coefficients. The centre of mass of the trajectories are indicated by a dot, which is surrounded by an area that is closer to that trajectory than to any other. The colour of each area indicates the diffusion coefficient, with areas around immobile trajectories being white. (**i**) The diffusion coefficients of all trajectories; the grey box indicates the values which fall within the localisation inaccuracy. The inset Voronoi diagram shows the spatial distribution of each trajectory type. Adapted from Hendriks and Meirer et al.[61] under the CC BY-NC-ND 4.0 license.

Photoluminescence is the emission of light by a luminescent material following absorption of light. The electronic structure of a lumi-nescent material is described by a set of allowed states, called orbitals. Upon absorption of a single light quantum, that is a photon, an
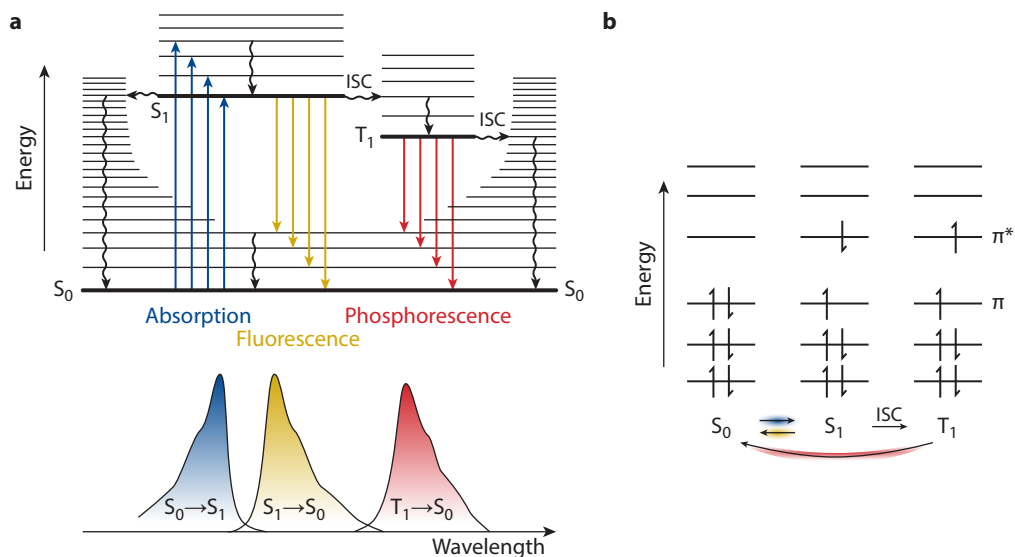
Figure 2.4 • (**a**) Jablonski diagram showing the relation between absorption, fluorescence, and phosphorescence. The electron configurations S_0, S_1, and T_1 are shown, where S_0 is the ground state and S_1 and T_1 are excited states. The thick lines indicate vibrational ground states of electronic states, whereas the thin lines are vibrationally excited states. Radiative and non-radiative transitions are indicated by solid straight and wiggly arrows, respectively. Horizontal wiggly arrows mark a transition to a different electron configuration, which is called intersystem crossing (ISC) when it involves a flip of the electron spin. Examples of absorption, fluorescence and phosphorescence spectra are shown below. (**b**) Molecular-orbital diagram of a hypothetical photoluminescent molecule. Some transitions between the electronic states are indicated with coloured arrows to show the relation to transitions in the Jablonski diagram in panel **a**.

electron is lifted into a higher-energy orbital. The electronic transition induced by the absorption of a photon is generally the change of the lowest-energy state (*ground state*) to a higher-energy state (*excited state*). The photon is only absorbed when its energy matches the energy difference between the ground and excited state, as dictated by the conservation of energy. When an electron is promoted to an excited state, it decays back to the ground state after a certain amount of time. The characteristic time spent in the excited state is called the excited-state lifetime.[62,63]

The transition between electronic states in a luminescent molecule is usually depicted in a Jablonski diagram, see Figure 2.4a. The energy of the material is determined by the configuration of the electrons and molecular vibrations. A set of horizontal solid lines indicates an al-lowed configuration of electrons (e.g., S_0, S_1, T_1), where the closely spaced solid lines mark the allowed molecular vibrations at a specific electron configuration. The vibrational ground state is represented with a thick solid line. For the S_0, S_1, T_1 configurations, the electron distribution over the molecular orbitals is shown in Figure 2.4b. When one of the two *paired* electrons in the π molecular orbital is promoted to the π* orbital, the electrons keep their antiparallel spins as absorption of light cannot flip the spin. However, once the molecule is in the excited state (e.g., S_1 configuration), the spin of the electron can flip spontaneously because it is unpaired. This process is called intersystem crossing, which reduces the energy of the system (Hund's rule) as the former electron pair now has parallel spins (T_1 configuration).[62,63]

There are multiple ways the molecule can lose its excited-state energy and decay back to the ground state, which are in competition with each other (see Figure 2.4a). First, the molecule can lose its energy by emission of a fluorescence photon, which happens on the order of nanoseconds. However, because the system typically decays even more rapidly back to a lower vibrational energy level before emission of a fluorescence photon, the emission is red-shifted with respect to the wavelength of light absorption. The difference in (vibrational) energy is dissipated as heat. Second, when an electron spontaneously flips its spin via intersystem crossing, the molecule can decay back to the ground state by emission of a phosphorescence photon, which requires the electron spin to flip back (Figure 2.4b). A transition involving the flip of an electron spin is *forbidden* but can occur via the relativistic effect *spin–orbit coupling*. Since phosphorescence is forbidden, the excited-state lifetime is on the order of microseconds to seconds and is much longer than when a fluorescence photon is emitted. The phosphorescence emission is more red-shifted than fluorescence emission, because of the lower energy of the T_1 than the S_1 electronic state. Finally, the material can lose energy without emission of a photon, which is called non-radiative decay, and the energy is dissipated as heat.[62,63]

Excited-state dynamics. The excited-state lifetime provides information about electronic transitions that occur in or involving an excited fluorophore. These transitions can be dependent on the local environment, and lifetime measurements are often the key to understanding fluorescence behaviour. The kinetics of the transition from the excited state to the ground state is described by a mono-exponential decay[62,63]

$$[S_1](t) = [S_1]_0 e^{-k_{tot}t} \qquad (2.6)$$

with $[S_1](t)$ the population of the excited state at decay time t, $[S_1]_0$ the population of the excited state at $t = 0$, and k_{tot} the total decay rate. The excited-state lifetime τ is simply given by

$$\tau = \frac{1}{k_{tot}} \qquad (2.7)$$

and has typical values on the order of nanoseconds for fluorescent molecules. k_{tot} is the sum of the rate of all decay processes, including radiative and non-radiative decay processes. The photoluminescence quantum yield (QY) is the average number of photons emitted per absorbed photon and can be written as

$$QY = \frac{k_{rad}}{k_{tot}} = \frac{k_{rad}}{k_{rad} + k_{non-rad}}, \qquad (2.8)$$

where k_{rad} and $k_{non-rad}$ are constants associated with the sum of all radiative and non-radiative decay processes, respectively.[62,63] k_{tot} is increased when additional non-radiative decay pathways have become possible, which decreases τ and the QY.

The excited-state lifetime is measured with a time-correlated spectrophotometer (Figure 2.5a). The sample is excited with a pulsed laser and the time between the laser pulse and detected photons is recorded, which is called the delay time (Figure 2.5b). The fluorescence intensity decay curve is constructed as a histogram of the measured delay times. The decay curve is mono-exponential for a single fluorescent species following Equation 2.6, which can be recognised as a straight line when plotted on a logarithmic y-axis (Figure 2.5c).[62,63]

The optical and electronic components of a time-correlated spectrophotometer have a timing imprecision, which results in a broadening of the decay curve. When the lifetime is short, the broadening of the decay curve results in an overestimation of the lifetime, and in such cases, it is necessary to take the timing imprecision of the setup into account. The instrument response function (IRF) describes such timing imprecision. The measured decay curve is a convolution of the IRF with the true decay curve.[64] The IRF can be included in the fitting procedure to account for the broadening by the IRF via a method called *iterative reconvolution*. In every step of the fitting routine, the model of the fluorescent decay is convoluted
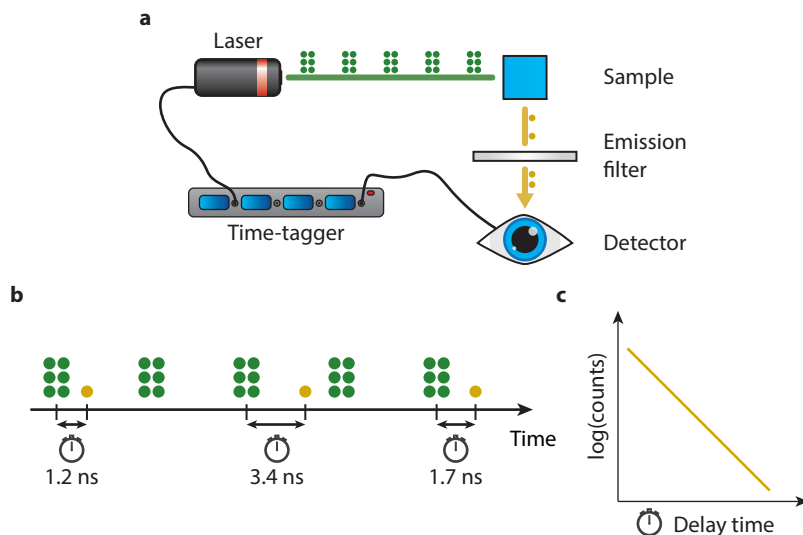
Figure 2.5 • (a) Schematic representation of a time-correlated spectrophotometer. A pulsed laser illuminates the sample and the sample's photoluminescence is detected. A time-tagger device records the time when a laser pulse is fired, and emitted photons are detected. **(b)** During an experiment, the time between a laser pulse and a detected photon is recorded, which is called the delay time, until the statistical distribution of the delay times is captured. **(c)** A histogram of the delay times is called a decay curve, which can be fit with a model to obtain the excited-state lifetime. A single fluorescent molecule generally has a mono-exponential distribution of delay times, which is a straight line when plotted on a logarithmic y-axis.

with the measured IRF, before computing the loss function.[62,64] As a rule of thumb, one can assume that under favourable conditions, most importantly sufficient counts in the histogram, lifetimes down to 1/10 of the IRF full width at half maximum can still be recovered via iterative reconvolution.[64]

Molecular aggregation. Molecular aggregation can drastically alter the light-absorption and fluorescence-emission characteristics resulting in spectral shifts and band splitting. Aggregation of fluorescent reporter molecules in zeolite micropores can have significant consequences for their probing behaviour (see Chapter 6). Exciton theory is a quantum-mechanical formulation that can be used to interpret the spectral changes as a result of aggregation.[65–68] It predicts the splitting of excited states of the monomers when aggregated, as is schematically depicted in Figure 2.6. The energy gaps (i.e., absorption and emission wavelengths) and the transition probabilities depend on the relative orientation of the monomer units constituting the dimer aggregates (as well as the polarisation of the emitted photons). A set of dimers with parallel transition dipole moments can be oriented side-to-side and head-to-tail, which are called H- and J-dimers, respectively. Exciton theory predicts a blue shift of the absorption spectrum for H-dimers and -aggregates since the transition from the ground state to the first excited state is forbidden, while the transition to the second excited state is allowed. Fluorescence quenching occurs (i.e., a decrease in QY) as a result of rapid non-radiative decay from the second to first excited state followed by non-radiative decay to the ground state. Contrarily, J-dimers and -aggregates have a red-shifted absorption spectrum and they do fluoresce because the transition from the ground state to the first excited state is allowed, while the transition to the second excited state is forbidden (see Figure 2.6). Exciton theory predicts an enhancement of the QY for J-dimers and aggregates, which has
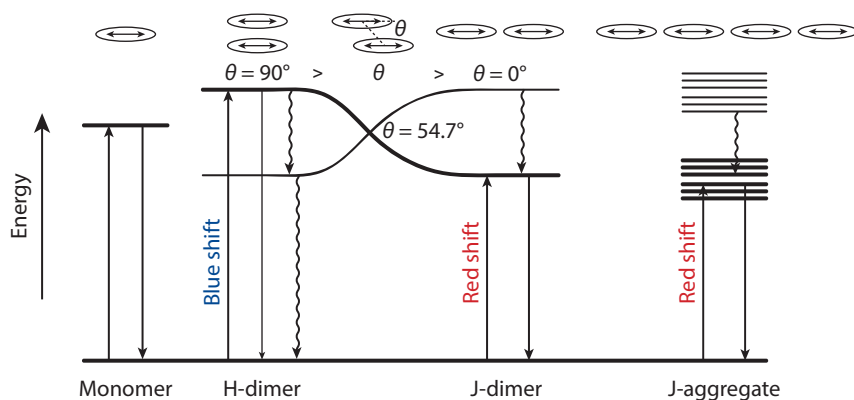
Figure 2.6 • Electronic energy-level diagram for a monomer, H-dimer, J-dimer, and J-aggregate with the orientation of the transition dipole moment of the monomer units shown above the energy levels. Vibrational energy levels are not shown here. The electronic transitions are indicated with straight lines and wiggly lines. Straight lines indicate light absorption *up* and fluorescence emission *down*, whereas wiggly lines mark non-radiative decay processes. The colour shift of the allowed absorption transition with respect to the monomer is indicated. The angle between the transition dipole moments θ is 90° for a perfect H-dimer and 0° for a perfect J-dimer. No net effect of the splitting of the excited states is present at $\theta = 54.7°$. The energy-level scheme of the H-aggregate is analogous to the J-aggregate and is not shown. Adapted from Martínez-Martínez et al. and Wang et al.[68,71]

been observed for instance in (surfactant-aided) supramolecular assemblies in solution.[69,70] The molecules often do not aggregate perfectly side-to-side or head-to-tail, and the aggregates can adopt structures with intermediate geometries. These geometries can result in either a blue/red shift, or a splitting of the absorption band into a blue and red-shifted fraction when the transition dipole moments are not perfectly parallel.[68]

2.2.2 • Fluorescence microscopy

Fluorescence microscopy is an optical microscopy technique that images fluorescence emission of luminescent materials, such as fluorescent molecules and nanoparticles. Illumination of the sample excites the material, and its fluorescence is projected onto a detector (Figure 2.7a). The sample is usually excited with a laser at, or close to, the absorption maximum of the material. Fluorescence emission of other species than the material of interest is removed with emission filters. A range of different fluorescence microscopy techniques have emerged, which aim at imaging with a

high spatial resolution. The resolution in optical microscopy is fundamentally limited by the diffraction limit. Diffraction is well demonstrated by a *single-slit experiment*, in which a coherent light source is imaged onto a plane via a circular aperture. The interference of light then generates the well-known pattern consisting of a bright centre surrounded by alternating dark and bright concentric rings, which is better known as the Airy disk. In an optical microscope, the objective lens has a finite angle under which it can collect light from the sample (Figure 2.7a). It therefore effectively acts as an aperture that gives rise to the same Airy-disk diffraction pattern. The pattern is now denoted as the point spread function (PSF) as it describes the microscope's response to a point emitter. The full width at half maximum of the PSF is often used as a short-hand resolution limit for conventional light microscopy, and results in a maximum resolution of ~250 nm.[49,72] The diffraction limit is often not the only factor that governs the resolution of a fluorescence microscope. Out-of-focus photoluminescence or scattering results in a blurry background signal, which reduces the signal-

to-noise ratio and thus the resolving power of the microscope.

2.2.3 • Confocal laser scanning microscopy

Confocal laser scanning microscopy (CLSM) is a fluorescence microscopy technique that uses a set of apertures (*pinholes*) to remove out-of-focus light before it reaches the detector. This increases the resolving power of the microscope, which is particularly beneficial for imaging strongly scattering media, such as porous solids. The major impact of the pinholes is in generating *z*-resolution while also improving the resolution in the *xy*-plane, which facilitates three-dimensional imaging. The lateral resolution of a good CLSM system is limited by the optical diffraction limit; however, the axial resolution is at least 3–4 times worse than the resolution in the lateral dimension. The working principle of a CLSM is depicted in Figure 2.7b. First, the laser light is focussed onto the sample to excite in a diffraction-limited spot. The fluorescence is collected, and a pinhole is placed in a conjugated plane to the diffraction-limited excitation spot, which filters out nearly all light outside this location. The filtered light is then measured using a point de-

tector or a small number of pixels on a camera. An image is built up pixel-by-pixel by raster scanning over the sample, and consequently CLSM has a long acquisition time compared to non-scanning techniques.[73]

CLSM is an interesting addition to the toolbox of microimaging techniques, since it allows the mapping of concentration profiles in three spatial dimensions. This overcomes an important limitation of interference microscopy and infrared microspectroscopy techniques, where the average guest concentration is obtained over the depth of the sample, thus only providing a two-dimensional concentration profile over time. We explore CLSM in Chapter 6 for the direct measurement of transport diffusion and diffusion barriers in zeolites.

2.2.4 • Single-molecule localisation microscopy

Super-resolution fluorescence microscopy is a hypernym for techniques that bypass the diffraction limit.[49] One super-resolution microscopy technique is single-molecule localisation microscopy (SMLM), which allows the localisation of individual fluorophores with a
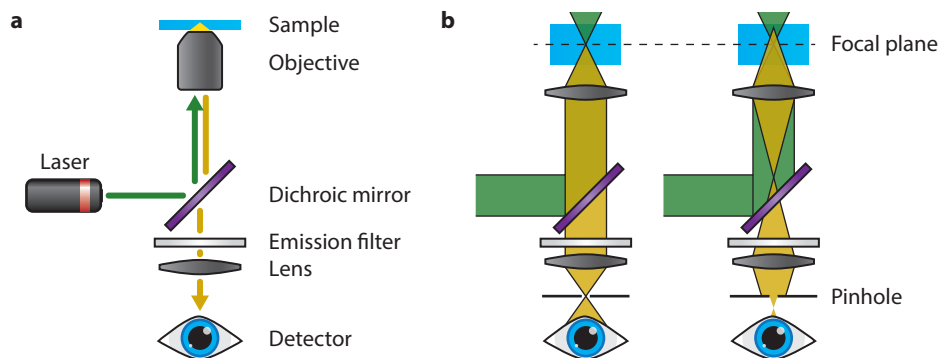
Figure 2.7 • (a) A typical fluorescence microscope set-up consists of a laser excitation source, a dichroic mirror, an objective lens, and a detector. The dichroic mirror reflects the excitation light (green) via the objective onto the sample, but lets the light emitted by the sample (yellow) pass to the detector. A parallel beam can be used to illuminate the sample over the field of view (i.e., wide-field microscopy) or a focused spot can be scanned over the sample (i.e., confocal microscopy). The fluorescence emission of the excited fluorophores is recorded by the detector creating a micrograph. **(b)** Demonstration of out-of-focus light removal by a pinhole in a confocal laser scanning microscope. The fluorescence emission only passes through the pinhole efficiently when the light originates from the excitation spot in the focal plane.
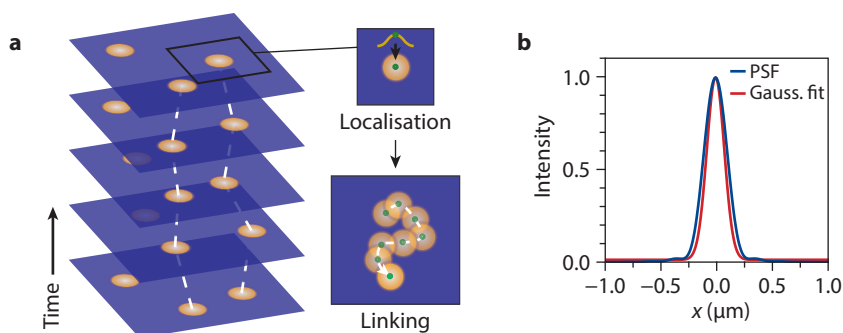
Figure 2.8 • (**a**) Schematic representation of single-molecule localisation and tracking. When tracking individual emitters, the centre of the diffraction-limited spots in the time-lapse movie are fitted, and the individual localisations are grouped together in a trajectory. Adapted from Manzo and Garcia-Parajo.[48] (**b**) Simulated point spread function (PSF) in one dimension of emission with a wavelength of 600 nm. The fitted Gaussian function describes the PSF well.

spatial resolution on the order of tens of nanometres. As the location of the fluorescent molecule is at the centre of the PSF, the position of a single fluorescent molecule can be determined—with a precision much higher than the diffraction limit—by fitting the PSF's centre position. Since the fluorophores are generally small, the PSF is virtually the same for light emitted anywhere from the fluorophore's volume and they can be regarded as point sources. Eric Betzig recognised that a prerequisite for sub-diffraction localisation is sparsity in the molecules' diffraction-limited spots,[74] that is, overlapping PSF's need to be avoided. Then, by selective excitation of subpopulations of fluorophores, a super-resolution image with a high fluorophore density can be reconstructed. Two years later, a new piece of the puzzle was added: pioneering in the field of single-molecule spectroscopy, William E. Moerner reported a specific mutant of the green fluorescent protein with strong intermittent fluorescence, so-called blinking, before going to a stable dark state. The blinking behaviour could be recovered with a burst of UV-light,[75] giving exactly the fluorophore properties and control over emission Betzig was looking for. Using Moerner's discovery, Betzig in collaboration with the biologist Jennifer Lippincott-Schwartz, demonstrated super-resolution imaging of labelled intracellular proteins using SMLM.[76]

After this first demonstration, SMLM quickly became a standard imaging tool in the fields of biology and chemistry, and it should not come as a surprise that a share of the 2014 Nobel prize for chemistry was awarded to Eric Betzig and William E. Moerner for their pioneering work in the field.

Single-molecule tracking. Single-molecule tracking is the analysis of SMLM time-lapse videos to obtain the travelled path of fluorescent emitters. We will focus here on the application of tracking for single-molecule diffusion studies. The first step is the localisation of the emitters by fitting a known function to their PSF (Figure 2.8a). To understand this process, we will have a closer look at the PSF. The PSF is a function that describes how a point source at position r in the sample makes an image at position r' on the camera. The PSF stretches over all positions r' on the camera but is virtually zero apart from a small region. If the pixel size is sufficiently small, a mathematical description of the PSF can be fit to the camera image r' and the position of the point emitter r is retrieved with nanometre precision. A Gaussian function with a full width at half maximum on the order of the emission wavelength is often used to describe the PSF (Figure 2.8b).[77,78] More accurate descriptions of the PSF increase the localisation precision.[79] If the fluorophore
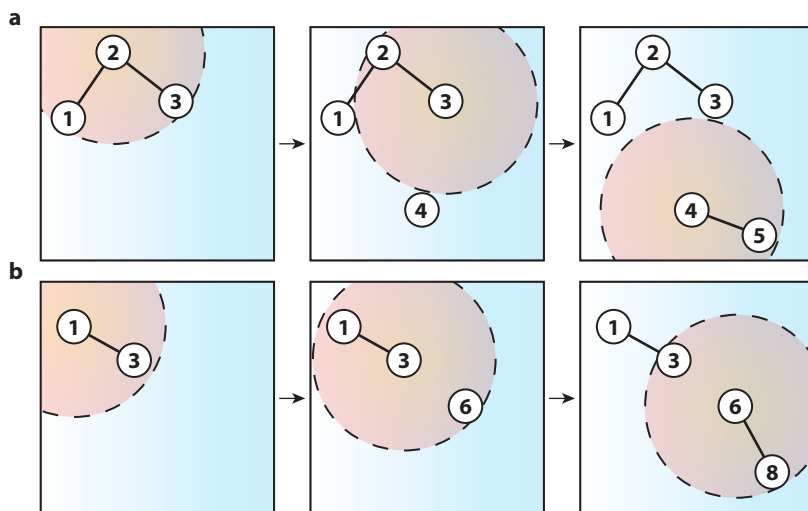
Figure 2.9 • (**a,b**) Schematic representation of the linking algorithm via two examples. The circles mark the localisation, where the number indicates the frame number in which the localisation was recorded. The solid lines are the links between localisations made by the tracking algorithm, and the dashed circle represents the pixel jump radius. The first example shown in panel **a** demonstrates the grouping process for a molecule that does not blink, and we only have to consider the pixel jump. When the pixel jump is shorter than the displacement between two subsequent localisations, such as between localisation two and three, it is recognised by the algorithm. However, if the displacement is larger than the pixel jump, which happens between localisation three and four, the displacement is not recognised. The trajectory is then falsely cut, and we obtain two measured trajectories. In the second example shown in panel **b**, the molecule blinks and we also must consider the blinking gap. Depending on its value, the algorithm still recognises a displacement even though the molecule is off for one or more frames. The blinking gap is the maximum number of dark frames allowed, and its value is one in this example. Thus, a pair of localisations with displacement shorter than the pixel jump will be recognised, if the number of dark frames between the localisations does not exceed one. For instance, between localisations one and three, the molecule blinks for one frame and the displacement is recognised. However, between localisation three and six, the molecule is dark for two frames, which is longer than the blinking gap of one. The trajectory is falsely cut even though the displacement is smaller than the pixel jump, and we obtain two measured trajectories.

density in a single micrograph is sufficiently low that the non-zero regions of the PSFs do not overlap, the location of each fluorophore can be determined rapidly with available algorithms.[77,78]

In the next step, single-molecule localisations are identified that likely originate from the same molecule based on their vicinity in space and time. These localisations are grouped into what we call a trajectory, which is depicted in Figure 2.8a. Most algorithms that generate trajectories minimise a cost function, which depends on, e.g., the displacement between consecutive coordinates, to find a likely set of trajectories from the localisation coordinates.[48,77,78,80,81] In the grouping process, two input values are important: the *pixel jump* and the *blinking gap*. The pixel jump specifies the maximum spatial separation between two consecutive localisations in a trajectory, which is depicted in Figure 2.9a. Similarly, the blinking gap accounts for the possibility that the fluorescence of a single molecule *blinks*, i.e., sometimes turns off for a few tens of ms.[82] The blinking gap is the maximum number of

dark frames by which we allow a trajectory to be interrupted, which is shown in Figure 2.9b. Finding the optimal set of cut-off values is challenging, and even the most optimal set can limit the range of diffusion coefficients that can be reliably extracted from the experiments. If the pixel jump value is too small, the algorithm does not recognise that two consecutive localisations originate from the same molecule when they are further spaced apart than the pixel jump (Figure 2.9a). The trajectory is falsely cut, and motion analysis will measure a reduced average diffusion coefficient. Instead, if the pixel jump is too large, we will connect localisations of different molecules that are in each other's vicinity, which will increase the measured average diffusion coefficient in the analysis. In practise, both pixel jump and blinking gap are optimised manually such that the probability of either scenario is minimised.

Diffusion coefficient estimation from single-molecule trajectories. Mean squared displacement (MSD) analysis is one of the most common tools to quantify the motion of an emitter described by a trajectory because of its visual interpretability.[83,84] The shape of the MSD curve as a function of delay time is dependent on the motion behaviour of the diffusing particle. While normal diffusion is characterised by a linear relation between the MSD and the delay time t_n, confined motion results in an MSD that reaches a plateau for long delay times, and directed motion can be identified by a parabolic MSD curve. Anomalous diffusion can in some cases be mistaken for normal diffusion in the MSD analysis, and careful interpretation is required in systems where anomalous diffusion is expected.[48,85] The MSD is computed from a time series of positions x_0, x_1, …, x_N for a single trajectory as

$$\mathrm{MSD}(t_n) = \frac{1}{N-n+1} \sum_{i=0}^{N-n} |x_{i+n} - x_i|^2 \quad (2.9)$$

with the delay time $t_n = n\Delta t$ for $n = 1, 2, …, N$ and the time between frames Δt.[83,84,86,87] We will refer to this MSD as the time-averaged MSD to distinguish it from the time–ensemble-averaged MSD, which will be discussed in Chapter 3.2.1. The term MSD will be used

when this distinction is not required. In practice, the MSD curve will be affected by noise on the coordinates x_i determined experimentally. Specifically, photon-counting noise introduces a localisation error, and motion within the exposure time of a microscopy frame leads to motion blur. For free two-dimensional normal diffusion including localisation error and motion blur, the measured $\mathrm{MSD}(t_n)$ is described by,[83,86]

$$\mathrm{MSD}(t_n) = 4Dt_n + 4\left(\sigma^2 - 2RD\Delta t\right)$$
$$\text{for} \quad n \geq 1 \quad (2.10)$$

with D the diffusion coefficient, σ the localisation error, and R the motion blur coefficient. The first term in Equation 2.10 describes how the MSD increases as a function of delay time due to normal diffusion, while the second term adds a constant factor accounting the localisation error and motion blur, which are both errors introduced by the experimental measurement. R can take values in the interval [0, 1/4] and is dependent on the detection scheme. In the case of no motion blur, $R = 0$, while $R = 1/6$ if the exposure time of the camera equals the time between frames. Ideally one would fit (a set of) trajectories that can be described by a single diffusion coefficient; however, if the individual emitters switch between different diffusive states, the MSD analysis will report only an average diffusion coefficient.

The $\mathrm{MSD}(t_n)$ values are highly correlated and statistically dependent when they originate from the same time series of positions x_0, x_1, …, x_N satisfying Equation 2.10 (Figure 2.10a,b). In other words, because x_i and x_{i+1} as well as x_{i+n} and x_{i+1+n} are in proximity to each other, the squared displacements $|x_{i+n} - x_i|^2$ and $|x_{i+1+n} - x_{i+1}|^2$ used to compute the MSD(t_n) with Equation 2.9 are correlated as well (Figure 2.10c). The fit to the MSD curve yields an accurate estimate of the diffusion coefficient of a single trajectory. However, it is an imprecise estimate of the ensemble "true" diffusion coefficient when based on a single trajectory because of the correlation in the trajectory's displacements. Here, one would expect that by adding more data points to the fit of the MSD,
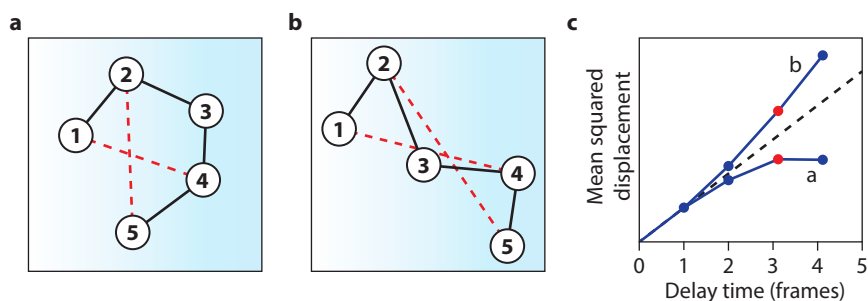
Figure 2.10 • (**a,b**) Schematic representation of two trajectories spanning five frames that could have the same underlying diffusion coefficient. The localisations are indicated by circles with the frame number noted inside. The black lines are guides to eye for visualisation of the trajectories. The longest displacements are statistically dependent and highly correlated due to the shape of the trajectory, e.g., when the trajectory is folded back onto itself (panel **a**) or stretched out (panel **b**). This is illustrated by the similar length of the displacements with a delay time $t_n = 3$ frames (red dashed lines). (**c**) Schematic of the mean squared displacement (MSD) curve of a single trajectory similar to those in panels **a,b**. When the trajectory is folded onto itself (panel **a**), the displacements at longer delay times are all shorter than expected for normal diffusion (black dashed line). Contrarily, for a stretched trajectory (panel **b**), the displacements are longer than expected for normal diffusion. Correlations in the trajectory manifest themselve in correlations in the MSD curve, which results in bias in the fitted parameters.

i.e., at longer delay times, the quality of the fit would improve. However, the correlation between displacements at longer delay times is so strong that—at some point—when more delay times are included in the fit, no more information about the ensemble diffusion coefficient is added and its estimate becomes less precise.[86] This problem is inherent to Equation 2.9 and cannot be solved by recording finite trajectories with more localisations, simply because the displacements of a single trajectory remain correlated at longer delay times. Consequently, the precision of the diffusion coefficient estimate is strongly dependent on the number of delay times that are included in the fit of the MSD curve. The optimal number of delay times to include in the fit can be computed and used in the MSD curve fit.[84,88] However, this is not straightforward when the trajectory has missing positions due to blinking and becomes unfeasible when the emitter switches between diffusive states. Therefore, we fit a constant fraction of the total number of delay times in the MSD with a minimum of three.[84,87–89]

Trajectories with many localisations are required for reliable diffusion coefficient estima-

tion, particularly with MSD analysis.[86] This is often not possible as molecules rapidly diffuse out of focus or photobleach too quickly, which in turn has driven the search for alternative measures. A maximum likelihood estimator (MLE) has been derived for free diffusion[83,84] considering blinking,[90] motion blur, and variable localisation error.[91] However, one of the challenges is that both the MSD and MLE diffusion coefficient estimates are biased for trajectories typically obtained in experiments. The unbiased covariance-based estimator (CVE) was therefore derived as an alternative to MSD and MLE analysis; however, it does not perform well in cases where the displacement per step is short with respect to the localisation error.[86,92] A promising way to increase the precision of diffusion coefficient estimate is to quantify the localisation error and include this in the model for the MLE or CVE.[86,93] When multiple underlying diffusional states are present, the model becomes more complex, and other approaches have been developed for this task, which are often based on Bayesian statistics.[94–97] Considering these recent developments, motion analysis of multistate diffusion seems to come within reach, but there is no

golden standard yet, and the optimal analysis method still has to be determined on a case-by-case basis.

Fluorophores for single-molecule tracking. The optimal fluorophore is a trade-off between many competing factors, and good fluorophore selection is the fundament of any SMLM experiment. In material science, we cannot directly copy the toolkit developed for SMLM in biological systems. There are multiple reasons for this: 1) as biological samples are often water-based, the solvent and the material have a more similar refractive index compared to inorganic systems. In porous solids, the refractive index of the host material is less homogeneous and can be much higher than that of the solvent. In that case, light scattering of the host material, due to the refractive index mismatch with the solvent, results in a high background hindering or even preventing localisation. A careful choice of the solvent, i.e., index matching, minimises this effect. 2) As inorganic materials of interest are often apolar, compatibility with polar fluorophores used in biological media is limited because their fluorescence and solubility is often low in apolar media.[98] 3) The typical conditions of interest are completely different for biological systems and catalyst materials. Rigorously air- and moisture-free conditions and non-ambient temperature and pressure are not common in biological systems, but can be, for example, in heterogeneous catalysis.[99] 4) To probe diffusion in porous materials, the size of the diffusing probe is another important factor closely linked to the research question of the study. Preferably, the probe size is comparable to that of the relevant species, such as the reactant and product in a porous catalyst, but strong light scattering of the host might require very bright fluorophores. Altogether, the selection of the optimal fluorophore is paramount for experimental success.

For optimal diffusion coefficient estimation from single-molecule trajectories, a fluorophore with minimum blinking, limited photobleaching, and a high photon-emission rate is desired as this results in long trajectories.[100] Blinking and photobleaching can be controlled in aqueous systems by buffering the solution with oxygen scavengers or oxidiser–reductor couples.[82,101] Such protocols would be desirable for non-polar solvents as well.[99] Nevertheless, enhanced photostability inside *para*-ter-
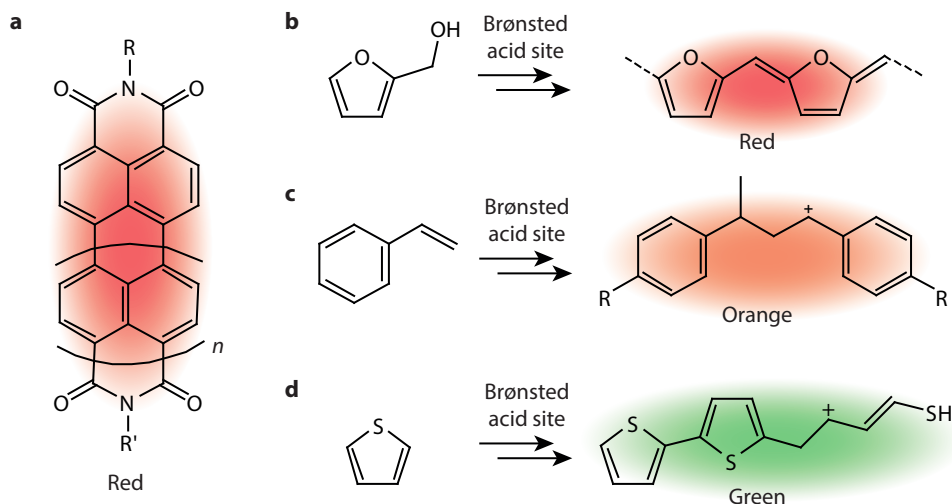
Figure 2.11 • Overview of fluorescent molecules (**a**) to probe diffusion and (**b**–**d**) reactivity in zeolites: rylene fluorophores such as perylene diimide ($n = 1$) and terylene diimide ($n = 2$) in panel **a**; oligomerisation of furfuryl alcohol in panel **b**; dimerisation of styrene derivatives in panel **c**; and thiophene oligomerisation in panel **d**.

phenyl crystals was observed without oxygen scavengers due to shielding from oxidative species directly by the host.[102] For a high photon-emission rate, the fluorophore needs to possess a large absorption cross section and high QY. This is not an intrinsic property of the fluorophore and can be highly dependent on the solvent. Rylene fluorescent molecules, such as PDI and terylene diimide derivatives, are particularly popular for tracking studies[55,59,61,103–106] owing to their high photon emission rate, photostability, and modifiability (Figure 2.11a).[107,108] It is worth mentioning that nanoparticles, in particular quantum dots, have already been proven to be excellent probes to study mass transport in porous solids because of their even higher photon emission rate and excellent photostability.[109,110] However, their larger size in comparison to fluorescent molecules limits the applicability in many micro- and mesoporous systems. Here, nanographenes hold great potential for SMLM as they are the *happy medium* between the small size of molecules and favourable photoemission properties of quantum dots.[111]

Fluorogenic molecules are commonly used to study catalytic events in zeolites at the single-molecule level. Their small size, determined by carbon five- and six-rings, allows these reactants to enter the micropores of zeolites and oligomerise at its active sites (Figure 2.11b–d). In Chapter 5, we use these small fluorogenic molecules to study diffusion through the micropores of a ZSM-5 zeolite. The number of reported reactive fluorophores is limited as their design, synthesis, and purification is not straightforward. In zeolites, the oligomerisation products of furfuryl alcohol, thiophene, and styrene have been successfully reported as fluorescent single-molecule probes by the groups of Roeffaers, Hofkens, and Weckhuysen (Figure 2.11b–d).[19,112,113] Oligomerisation is an acid-catalysed process and happens readily over the Brønsted-acid sites in the zeolite pores. The conversion rate of styrene and thiophene reactants is strongly dependent on their side groups because these groups alter the stability of the carbocation in the fluorescent product and limit transport into the porous catalyst. Systematic studies of these substituent effects have been proven valuable at the single-particle and single-molecule level.[112,114–117] A challenge in the analysis of these single-molecule events is the strong intrinsic blinking due to proton transfer from the acid sites.[52,112,116] To discriminate between the formation of a new oligomer, which is an indication of mass transport of the reactant to the active site, and proton transfer, careful experimental design and analysis are required.

2.3 • Concluding remarks

In summary, microscopic observation of diffusion via the MSD of molecules (or particles) is linked to the macroscopically observable diffusion coefficient via Einstein's diffusion equation. Based on these principles, fundamentally different approaches exist to measure diffusion. In zeolite materials, it was found that microscopically measured diffusion coefficients were in discrepancy with macroscopic measurements. Because of the presence of diffusion barriers, different diffusivities were measured depending on the probed length and time scales. Further investigations at the single-molecule level revealed that the molecular diffusion dynamics in porous solids are inherently heterogeneous. Microscopy techniques have a prominent role in the measurement of diffusion heterogeneities because of their ability to measure diffusion at the single-molecule and single-particle level.

Two fluorescence microscopy techniques that are used in this PhD thesis to measure diffusion in porous solids were discussed. The fluorescence intensity distribution in three dimensions can be imaged with CLSM. This microimaging technique has the potential to measure diffusion and pore space with diffraction-limited resolution. Out-of-focus fluorescence is mostly filtered out, which is useful in highly scattering samples, such as porous solids. Understanding factors that affect the QY, such as molecular aggregation, is important to apply this technique in the study of diffusion. The trajectories of individual molecules can be obtained from the tracking of SMLM time-lapse videos. Careful selection of tracking parameters during the localisation and

linking process is crucial to accurately capture the single-molecule dynamics. MSD analysis is the most common way to analyse single-molecule trajectories, but interpretation must be done with care because of correlations in the MSD curve. Finally, selection of the fluorophore is essential for experimental success, and the choice is dependent on the porous host. However, in zeolites the number of applicable fluorophores is limited because most common fluorescent molecules are too large to fit in the zeolite's micropores.

2.4 • Contributions & acknowledgements

Donglong Fu (Utrecht University) is thanked for fruitful discussions.
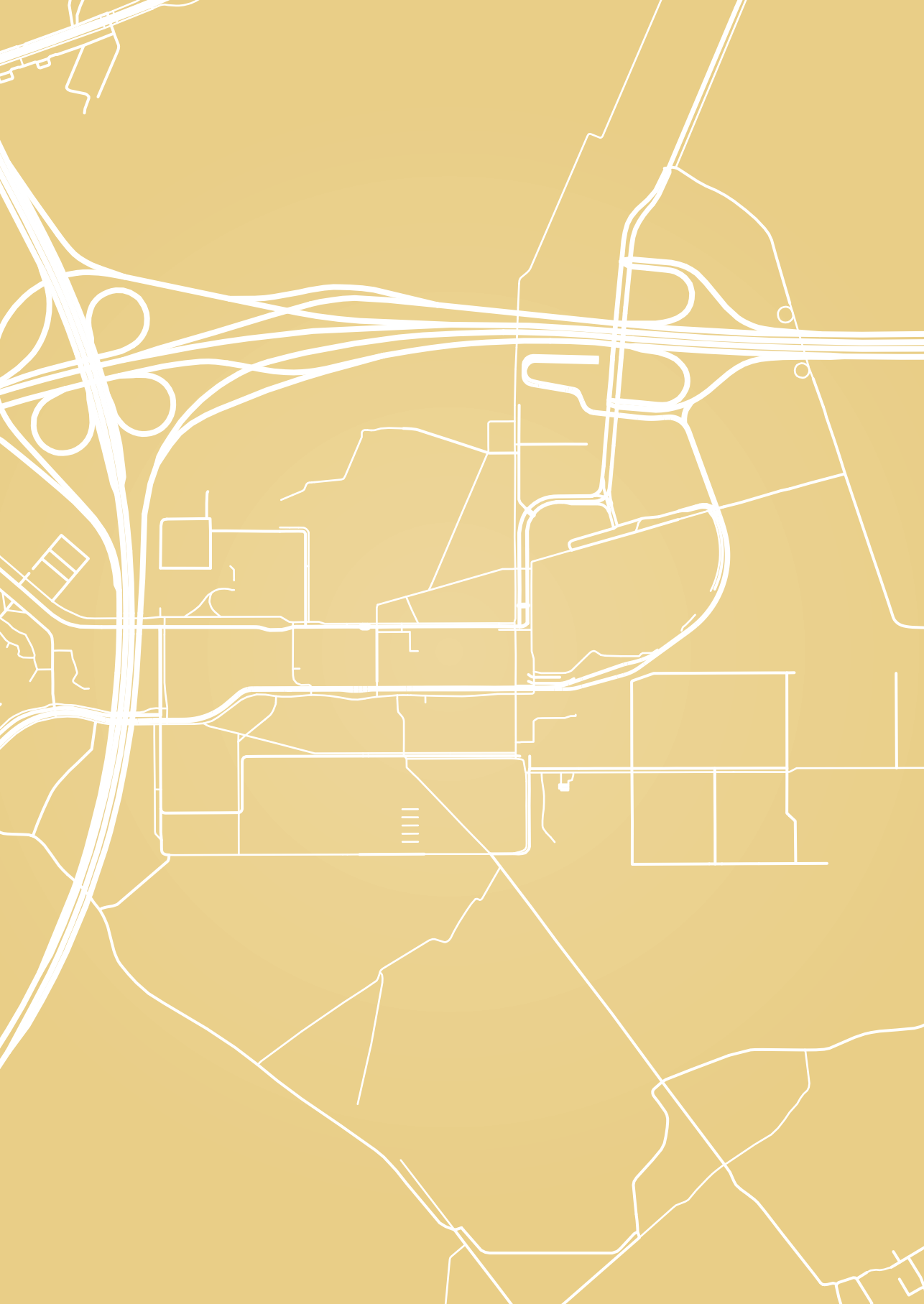
Chapter **3**

Classification-based motion analysis of single-molecule trajectories using DiffusionLab

This chapter is based on the following paper:

- Maris, J. J. E., Rabouw, F. T., Weckhuysen, B. M., & Meirer, F. *Sci. Rep.* **12**, 9595 (2022).

Abstract • Single-particle tracking is a powerful approach to study the motion of individual molecules and particles. It can uncover heterogeneities that are invisible to ensemble techniques, which places it uniquely among techniques to study mass transport. Analysis of the trajectories obtained with single-particle tracking in inorganic porous hosts is often challenging because trajectories are short and/or motion is heterogeneous. In this chapter, we present a software package, coined DiffusionLab, for motion analysis of such challenging datasets. Trajectories are first classified into populations with similar characteristics to which the motion analysis is tailored in a second step. DiffusionLab provides tools to classify trajectories based on the motion behaviour either with machine learning or manually. It also offers quantitative mean squared displacement analysis of the trajectories. The software can compute the diffusion coefficient for an individual trajectory if it is sufficiently long, or the average diffusion coefficient for multiple shorter trajectories. We demonstrate the DiffusionLab approach via the analysis of a simulated dataset with motion behaviours frequently observed in inorganic porous hosts, such as zeolites. The software package with graphical user interface and its documentation are freely available.

3.1 • Introduction

Molecules with the same chemical identity can display different motion behaviour as a result of the complex environment where the diffusion takes place. To understand and model transport phenomena and predict associated properties, quantitative experimental input is crucial. An excellent way to capture heterogeneous motion is to record the location of a single moving object, such as a molecule or nanoparticle, as a function of time, yielding a so-called trajectory. High-throughput trajectory-based analysis has been made possible with the development of algorithms to localise and track particles from time-lapse microscopy videos.[80,118] These methods together with fluorescence microscopy techniques, such as single-molecule localisation microscopy, enable tracking of single fluorescing molecules, quantum dots, and colloids with nanometre resolution.[48,119]

Driven by the notion that ensemble-averaging obscures heterogeneities, and thus hides important features for cellular function, single-particle tracking has had a crucial role in the discovery of cellular organisation and a variety of cellular processes.[48,119] In the field of materials science, different motion behaviours have been observed for fluorescent molecules diffusing through a porous catalyst particle (see also Section 2.1.3).[55,61,106,120,121] Interpretation of a dataset with fluorophores displaying different motion behaviours requires sufficient statistics on the occurrence of the motion behaviours and a quantitative description of each motion behaviour via a diffusion model. This is challenging as the measured trajectories are often short, i.e., ~5–15 frames, as a result of fast diffusion, rapid photobleaching, and blinking of the fluorophores, and individually do not contain sufficient information for a reliable quantification of the motion.

We present in this chapter an open access, freely available software package *DiffusionLab* to perform quantitative analysis of datasets of single-molecule trajectories. DiffusionLab is versatile, is user-friendly, and can be readily used to perform complex tasks without the need for programming experience. Most other software packages focus on the quantification of multiple normal diffusion states directly from the analysis of the displacements, using various methods such as fitting of the cumulative distribution of squared displacements.[96,122–127] In contrast to these software packages, DiffusionLab first simplifies the dataset by classification of the trajectories into smaller populations with similar motion behaviour prior to diffusion quantification. In this way, motion heterogeneity can be visualised and quantified in a robust way that is not only dependent on fitting of a single (multistate) diffusion model to the displacements.[61] Consequently, the DiffusionLab software can handle trajectory datasets containing a mixture of motion types such as normal, confined, and directed diffusion by treating them separately. DiffusionLab

focusses on robustness and ease of use to make the tools for quantitative analysis of complex trajectory datasets broadly available to the scientific community.

The combination of trajectory classification and motion analysis has been proven to be a powerful approach for the analysis of complex datasets with short trajectories, particularly in the field of materials science as evidenced by work from our group using the DiffusionLab software (see Chapter 5 and ref. 61). The potential of feature-based classification has also been reported by Lerner et al. for the classification of confinement in trajectories mixed with normal or directed diffusion.[128] They classified the trajectories based on three features that described properties of individual trajectories, and subsequently quantified confinement within the classified trajectories with mean squared displacement (MSD) analysis using the *msdanalyzer* software.[129] DiffusionLab has a wide range of built-in trajectory features (or *properties*) as well as the option to add custom features by the user to provide descriptors for many different motion behaviours. The classification is done using these features, either by setting thresholds manually or with feature-based machine learning methods on a user-generated training set.

We include MSD curve analysis in DiffusionLab as primary motion estimator because it is accessible, well known across the scientific community, and robust for many different motion behaviours. The caveat of time-average MSD (T-MSD) analysis is that the fitted parameters can be biased when the trajectories are short (Chapter 2.2.4).[48,86] This is particularly a problem for single-molecule trajectories recorded in inorganic porous hosts, which are generally short and have heterogeneous underlying motion behaviour. Bias in the T-MSD curve makes the identification of the motion behaviour ambiguous and introduces bias in the fitted parameters. Unfortunately, these trajectory properties are inherent to the experiment and cannot be changed substantially—even by experiment design. Therefore, we classify the individual trajectories based on similarity and pool them to get their popula-

tion average, which is a well-known concept in processing hyperspectral images.[130] With this approach we reduce noise and bias in the time–ensemble-averaged MSD curve, and as a result we obtain the motion type and fitted parameters of the pooled trajectories with improved performance. Ultimately, it allows the spatial mapping of motion heterogeneity on level of single short trajectories.

The presence of anomalous diffusion is in some cases not clear from MSD analysis and can be confused with normal diffusion.[48,85] Recently, machine learning methods have been developed for the detection and classification of the different diffusion types, which are mostly focussed on the recognition of anomalous diffusion.[131–137] In contrast to the approach employed in DiffusionLab, these models are trained by simulated trajectories with a known set of diffusion models. Further classification by state-of-the-art machine learning models after classification in DiffusionLab could be required to identify the type of anomalous diffusion.[138]

In this chapter, we explain the methodology of DiffusionLab and demonstrate it via the classification of trajectories of a simulated example dataset. This example contains trajectories of fluorophores that show transient adsorption, which is common for fluorophores diffusing in a porous solid host.[55,61,106,120,121] We demonstrate how to perform classification via machine learning, and the motion of the classified populations is analysed and quantified with MSD analysis. Finally, we show how the classification model can be adapted to trajectory datasets with similar motion behaviour, such as transient confinement.

3.2 • Results and discussion

3.2.1 • The workflow and concepts of DiffusionLab

The workflow of the classification-based motion analysis in DiffusionLab is given in Figure 3.1. In the first step, the trajectories are imported from a tracking software of choice. At the time of writing, DiffusionLab supports

the import of trajectories from the software package Localizer[77] and the ImageJ plug-in DoM.[78,139] Moreover, the import of simulated trajectories from COMSOL Multiphysics® is supported to compare experimental and simulated datasets.[140] Step-by-step instructions for how to export the trajectories from the respective software are given in the Diffusion-Lab Documentation Section 2.2. In the second step, a set of descriptors of each trajectory is computed, which are scalars that capture a property of the trajectory. Examples of these properties are the *length* and *tortuosity* of the trajectory. Both two and three-dimensional trajectories are supported; however, not all properties are defined in three dimensions. A description and physical interpretation of the properties is given in the DiffusionLab Documentation Section 3.1.1.

A classification model is constructed to classify the trajectories into populations with similar motion behaviour. The populations are identified by the user and classification is done via a hierarchical classification tree. The hierarchical classification tree is read from top to bottom for each trajectory, weighing one property at each branch, until the trajectory is classified (example in Figure 3.3). Hierarchical classification trees have the advantage that they are easily interpretable and important properties and their thresholds are readily available from the model.[141] This aids rational design of the classification model when constructed manually. For machine learning, the classification tree model has the advantage that it is well interpretable compared to other machine learning models.

In DiffusionLab, hierarchical classification trees can be constructed manually or via supervised machine learning. For manual construction, DiffusionLab has various tools to find important properties for classification and to set the thresholds. The biplot tool shows the properties with a high dispersion that are therefore good candidates to implement in the tree. Histograms and correlation plots can be generated to find thresholds in, e.g., bimodal distributions as is shown in Figure 3.1, step 3a. These thresholds can be optimised by ap-

plying the classification and visually assessing the result. In supervised machine learning, the model maps an input (trajectory properties) to an output (motion behaviour type) based on example input–output pairs. The example pairs are called a *training set*, which are here a set of representative trajectories labelled with their motion behaviour. DiffusionLab offers a tool to manually classify a subset of experimental trajectories to obtain such a training set. This is then used to compute a hierarchical classification tree model. On top of that, MAT-LAB's Classification Learner app can be used to construct a classification model with any classification models available in MATLAB, which includes support vector machines and K-nearest neighbours. In the fourth step, the classification model is used to classify all trajectories in populations.

The motion of the classified populations is analysed in the last step (Figure 3.1, step 5), and this is where the power of the classification-based approach becomes truly visible. With DiffusionLab, the user can quantify both the motion of individual trajectories and the ensemble behaviour of each population. Analysis of the individual trajectories reveals the heterogeneity in molecular motion at the single-molecule level. However, in datasets with short trajectories, the statistical relevance of a single trajectory is limited. Because the trajectories have been classified into populations with similar motion behaviour, we can overcome this by analysing the ensemble-averaged behaviour and diffusion parameters. T-MSD analysis is known to suffer from imprecision in the estimated (ensemble) diffusion parameters due to correlation in the displacements (see Section 2.2.4).[48,86] Since the detected motion behaviour is dependent on the relation between the MSD and the delay time, this correlation makes it particularly challenging to determine the diffusion model that best characterises the motion of the emitters.[48] The time–ensemble-averaged MSD (TE-MSD) averages the T-MSD over a subset of trajectories, thereby averaging over any correlations within the trajectories
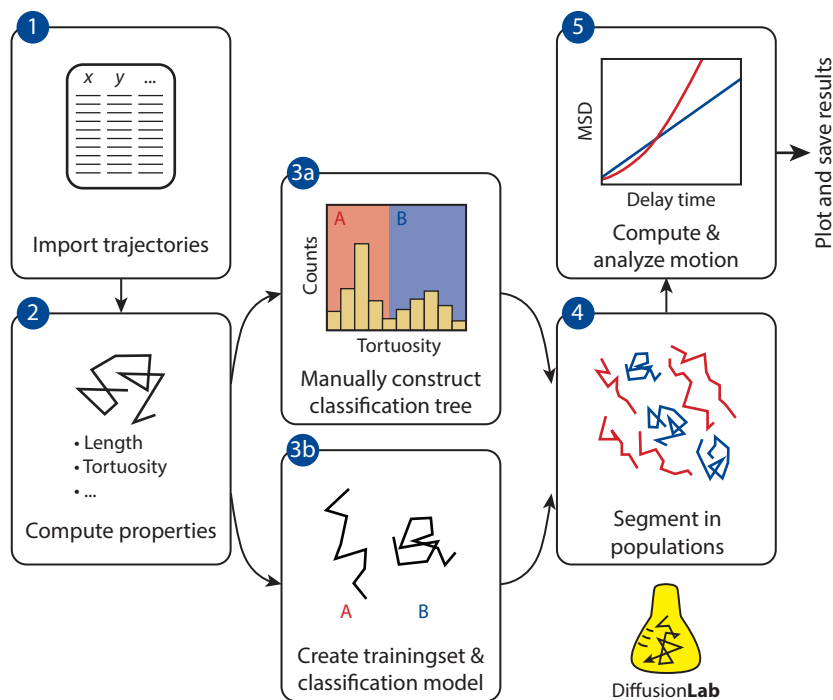
Figure 3.1 • Workflow of population-based motion analysis in DiffusionLab: (**1**) the trajectories are imported; (**2**) a set of descriptors (properties) of each trajectory is computed; (**3**) a classification model is constructed, this can be done manually either as a hierarchical classification tree (**3a**) or via supervised machine learning (**3b**); (**4**) the classification model is used to classify all trajectories in populations with similar motion behaviour; and (**5**) the mean squared displacement (MSD) of the populations is analysed separately. Finally, the properties and motion analysis results can be plotted, saved and/or exported.

$$\text{TE-MSD}(t_n) =$$

$$\frac{1}{J_n} \sum_{j, N_j \geq n} \frac{1}{N_j - n + 1} \sum_{i=0}^{N_j - n} \left| \boldsymbol{x}_{j,i+n} - \boldsymbol{x}_{j,i} \right|^2 \quad (3.1)$$

with the time series of positions $\boldsymbol{x}_{j,0}$, $\boldsymbol{x}_{j,1}$, …, $\boldsymbol{x}_{j,Nj}$ for trajectory j. The index i sums and averages over all segments in trajectory j spanning over a delay time of t_n. For each t_n, we include an ensemble of J_n trajectories with $N_j \geq n$. This means that the trajectories should have at least one segment spanning t_n. The correlations in the TE-MSD at longer delay times are strongly reduced with respect to the T-MSD, which results in an interpretable relation between the MSD and the delay time over a longer time domain, facilitating the determination of the motion behaviour type.[48] Moreover, the dif-

fusion coefficient can be estimated with high precision from the TE-MSD, which allows direct comparison within and between different experiments. We use the T-MSD for the analysis of individual trajectories, while TE-MSD is used to analyse a population of trajectories. Altogether, using these two complementary approaches we obtain both insight in the motion heterogeneity at the single-molecule level as well as the mean diffusion parameters.

3.2.2 • A simulated example of trajectory classification and motion analysis

We demonstrate the workflow of Diffusion-Lab on a dataset of simulated trajectories (see Methods). The trajectories were simulated from random walkers in three dimensions that

could switch between an immobile ($D_1 = 0$ m^2 s^{-1}) and mobile state ($D_2 = 1.0 \times 10^{-12}$ m^2 s^{-1}), mimicking transient adsorption often observed in porous solids (see also Chapter 5).[55,61,106,121] We imported the dataset into Diffusion-Lab and found 10600 individual trajectories (Figure 3.1, step 1). Before computing the properties in step 2, we removed trajectories with fewer than five localisations.[128] In this way, we reject trajectories and unconnected localisations whose properties, such as a *minimum bounding circle radius*, are not or ill-defined. Moreover, the localisation and tracking algorithm sometimes finds localisations due to fluctuations in the camera noise. Since these erroneous localisations are random, the probability that they form a trajectory becomes smaller for longer trajectories. Thus, we can eliminate most of these from the analysis by removing trajectories with fewer than five localisations. Finally, for a trajectory of five localisations, the minimum number of points in the MSD curve is four, which we consider the minimum for MSD analysis. Removing the trajectories with less than five localisations reduced the number of trajectories to 2433. Diffusion-Lab then computed and stored the trajectory properties, as explained in the DiffusionLab Documentation Section 3.1.1.

Next, the hierarchical classification tree was created (Figure 3.1, step 3), and we first identified the motion behaviours present in the dataset. Although the movement of all emitters was simulated using two underlying diffusion coefficients, we observed three qualitatively different types of trajectories, in agreement with the results of Hendriks et al.[61] (Figure 3.2). For some trajectories, the coordinates are separated from each other by no more than the localisation error. These do likely not reflect actual movement, but the apparent motion is due to

the localisation error. We call these trajectories *immobile*. Other trajectories show continuous movement without interruptions, which we label *mobile* trajectories. A third group of *hybrid* trajectories has both mobile and immobile periods.

We manually classified a hundred trajectories, assigning each to one of the three motion behaviours, and used this as a training set for machine learning. A training set of just a hundred trajectories is typically considered to be very small for machine learning; nevertheless, we show that this can be sufficient to construct a classification tree with reasonable accuracy. The classification tree has a resubstitution loss of 2%, which means that two of the hundred trajectories in our training set were incorrectly classified by the tree. With a small training set as is discussed here, we highly recommend assessing the tree's performance via the resubstitution loss as well as by visual inspection of the complete dataset after classification.

The classification performance of the classification tree model and other supervised machine learning models is shown in Table 3.1. The classification tree model performed well compared to the other tested models. The accuracy computed with validation was slightly lower than the accuracy without validation. This is likely because the training set contained 5% fewer trajectories, which is significant for a small training set with only a hundred trajectories and resulted in a poorer performing model. Using the 20-fold cross-validation accuracy metric, the classification tree is even the best performing model. It is important to realise that the accuracy is computed against the user-generated training set that might not perfectly represent the ground truth because of inconsequent classification by the user. An

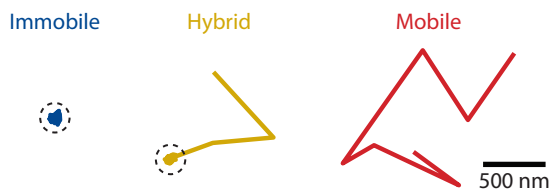**Immobile**   **Hybrid**   **Mobile**

500 nm

Figure 3.2 • Example trajectories of the immobile, hybrid, and mobile population. The dashed circle has a radius of the minimum bounding circle radius in the classification tree and marks the immobile segments in the trajectories.

Table 3.1 • Accuracy of various supervised machine leaning models trained with the same training set. The models performed classification into immobile, hybrid, and mobile populations. The accuracy was computed via the resubstitution loss (no validation) and after 20-fold cross validation. The reported models are: the classification tree in Figure 3.3; Gaussian Naive Bayes and Naive Bayes with a Gaussian Kernel; support-vector machines (SVM) with different kernel functions using an automatic kernel scale mode; K-nearest neighbours (KNN) with a default of 10 neighbours computed following various distance metrics (Euclidean, cosine, and cubic Minkowski). The medium and coarse KNN have respectively 1 and 10 nearest neighbours. The weighed KNN uses a Euclidean distance metric with the squared inverse distance weight. The classification tree was computed directly in DiffusionLab's Classification Trainer App. The other models were computed in MATLAB's Classification Learner App. Export of training sets to and import of classification models from MATLAB's Classification Learner App are supported by DiffusionLab.

Model	Accuracy no validation (%)	Accuracy 20-fold cross validation (%)
Classification tree — Figure 3.3	98	95
Naive Bayes — Gaussian	91	89
Naive Bayes — Kernel	95	91
SVM — Linear	92	87
SVM — Quadratic	97	87
SVM — Cubic	100	87
SVM — Gaussian	98	83
KNN — Medium	84	80
KNN — Coarse	38	38
KNN — Cosine	86	81
KNN — Cubic	87	82
KNN — Weighted	100	84

explanation for the good performance of the classification tree could be that the maximum number of splits is kept low (< 10), which prevents overfitting and makes it less susceptible to imperfections in the training set. The reduction of the number of dimensions by principal component analysis before model fit drastically reduced the classification accuracy for this training set.

The classification tree is shown in Figure 3.3. Interestingly, the same trajectory properties, that is, the *minimum bounding circle radius* (MBCR), the *minimum bounding circle centre minus the centre of mass* (MBCC–CoM), and the *number of points*, were again found to be most important as previously reported in the classification tree of Hendriks et al.[61] The tree

in this work was constructed with machine learning from a training set with mobile, hybrid, and immobile trajectories obtained from an experimental dataset of molecules diffusing in a porous catalyst particle. At every split of our classification tree, the histogram of the respective trajectory property is given in Figure 3.3. A bimodal distribution is clearly visible in the histogram of the MBCR and MBCC–CoM. The machine learning algorithm had found good threshold values to split the bimodal distribution without having access to the complete dataset (shown in Figure 3.3). The stochastic nature of the random walk results in some overlap between the properties of the various motion behaviours, as can been seen in the histogram, and the classification is successful if a vast majority of the
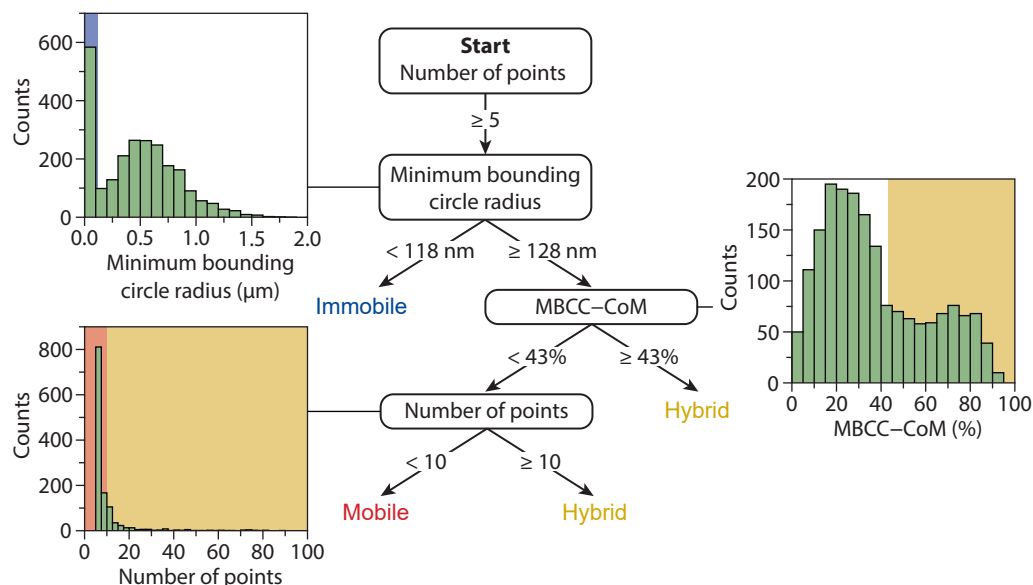
Figure 3.3 • Classification tree obtained with machine learning on a training set of a hundred manually classified trajectories for a simulated dataset with transient adsorption. The classification tree is read from top to bottom for each trajectory, weighing one property at each branch, until the trajectory is classified as either immobile, hybrid, or mobile. At each split, the histogram of the property is given for all trajectories of the branch, with the background colour indicating the threshold value of the split.

trajectories in a population have been correctly classified.

We can rationalise why the MBCR, MBCC–CoM, and number of points are good properties to classify a dataset with transient adsorption. It is no surprise that the MBCR is a good property to classify immobile trajectories. Because the emitter does not move, localisations are scattered around the emitter's true position. We calculate the probability that an immobile trajectory falls entirely within a minimum bounding circle with some threshold radius (see Methods). A threshold value of the MBCR of 118 nm is reasonable compared to the localisation errors of 12 and 28 nm of an in-focus and 400 nm out-of-focus fluorophore.[142,143] The probability that a trajectory with 17 localisations, which is the mean length for the immobile population, fits within the minimum bounding circle is > 99.99% for an in-focus immobile emitter, while it drops to 99.95% for an out-of-focus one. Thus, the value

of the MBCR allows for out-of-focus emitters to be classified as immobile, while keeping it as low as possible to not include many hybrid trajectories.

The MBCC–CoM is a good property to distinguish hybrid trajectories from mobile ones. Because it describes how far the centre of the minimum bounding circle and the centre of mass are apart, its value will be higher when the trajectory has a spatially asymmetric distribution of localisations. This is a characteristic of a trajectory with an immobile segment followed by a mobile segment, in other words: a hybrid trajectory. The number of points is a good indicator for whether the trajectory is either hybrid or mobile. Mobile trajectories are a result of emitters rapidly moving in- and out-of-focus resulting in short trajectories, while the immobile segments in hybrid trajectories make the trajectory longer. Because the MBCR, MBCC–CoM, and number of points are good descriptors for this type of motion
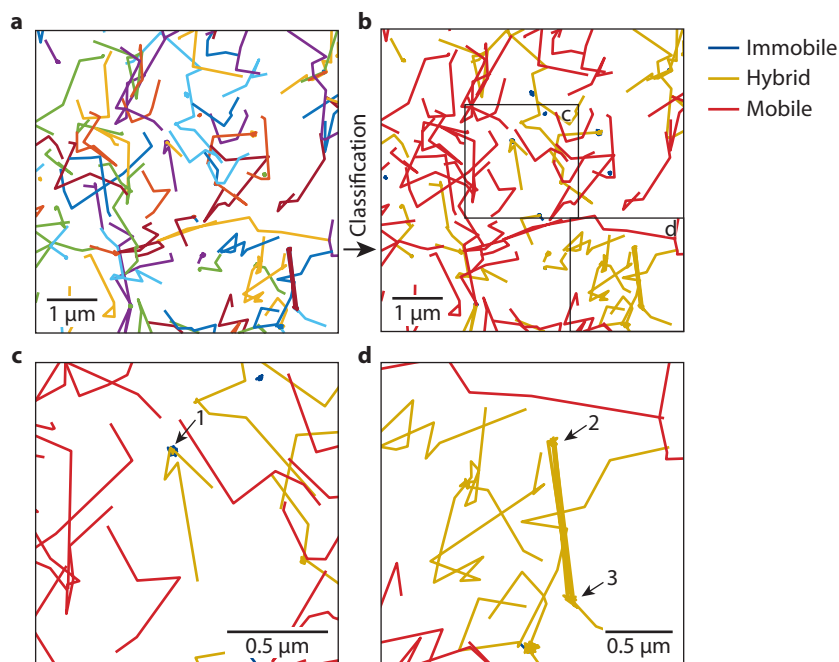
Figure 3.4 • (**a,b**) Individual trajectories (≥5 localisations) prior to (panel **a**) and after classification (panel **b**) into immobile, hybrid, and mobile populations. Classification appeared to be successful in most cases. (**c,d**) Zoom-in of the trajectories in panel **b** displaying the classification of common tracking artefacts. In panel **c**, an immobile trajectory overlaps with the immobile section of two hybrid trajectories (arrow 1). Due to missing localisations as a result of a low signal (or blinking of the fluorophore—not included in the simulation), long trajectories can be split into multiple shorter ones. The classification tree correctly identifies the individual components: a hybrid trajectory, followed by an immobile trajectory and a hybrid trajectory. In panel **d**, a crossover between two immobile fluorophores (arrows 2 & 3) occurs in a single trajectory. These artefacts are classified as hybrid because they are similar to the naturally occurring hybrid trajectories in the dataset, containing both mobile and immobile displacements.

behaviour, we demonstrated that the presented classification tree can be manually adapted to classify a dataset with transient confinement (Section 3.2.4). Next, we used the obtained classification tree to classify all trajectories in the transient adsorption dataset (Figure 3.1, step 4).

A plot of the trajectories prior to and after classification is shown in Figure 3.4a,b. Some of the simulated trajectories contain unphysical *artefacts* or *mistakes* that have been introduced during tracking. In our experience, these artefacts are difficult to avoid completely and easily arise when many fluorophores are immobile or

confined. The trajectories containing artefacts are classified as one of the motion behaviours—immobile, hybrid, and mobile—in a predictable manner (Figure 3.4c,d). If these artefacts would occur frequently, they could have been classified into a separate population in the training set and removed from the analysis.

The motion of the different populations was quantified with MSD analysis of individual trajectories and in ensemble (Figure 3.1, step 5). The diffusion coefficient was measured from a linear least-squares fit of the T-MSD curve including 25% of the shortest delay times and at least three points in the fit. A histogram of

the measured diffusion coefficients of individual trajectories is given in Figure 3.5a,b. Prior to classification, we found a continuous range of diffusion coefficients over six orders of magnitude (Figure 3.5a). The distribution contains all information about the heterogeneity of mobility and motion behaviour, but it is hard to interpret. By pooling the data into motion behaviour classes, we learn how the mobility and motion behaviour are related and how they change per experiment. To understand the origin of this wide range in diffusion coefficients, we considered the same histogram after classification (Figure 3.5b). Remarkably, the immobile trajectories make up for most of the spread, but their diffusion coefficient is close to zero. Localisation noise dominates the measured diffusion coefficients of these immobile emitters, and the spread does not reflect a true distribution of diffusion coefficients. For mobile trajectories, the distribution of the diffusion coefficient of is narrower and centred around $D = D_2 = 10^{-12}$ m^2 s^{-1}, i.e., the true mobility of the mobile diffusion state in the simulation. The hybrid trajectories have a wider range of diffusion coefficients in between those of the immobile and mobile diffusion states because of the varying length of mobile and immobile periods in the trajectories.

The TE-MSD curve provides insight in the mean motion behaviour of the emitters via the shape of the curve and fit of an appropriate diffusion model. We compared the TE-MSD before and after classification (Figure 3.6a,b). The shape of the TE-MSD curve prior to classification in Figure 3.6a resembles confined motion, marked by the plateau at long delay times.[144] However, we do not expect confined motion in this dataset, since the transient adsorption diffusion model does not impose confinement on the emitters. Interestingly, we found the same plateau after classification in the hybrid trajectories' TE-MSD curve, while the mobile and immobile TE-MSD curves were a straight line (Figure 3.6b). To explain the plateau at long delay times, we first considered the TE-MSD curve of the hybrid trajectories. The correlation plot of the diffusion coefficient and the number of localisations of the hybrid trajectories showed that trajectories with few localisations have a high diffusion coefficient and vice versa (Figure 3.6c). The number of localisations in the trajectory is highly dependent on the number of immobile segments because the emitter cannot move out of focus during these immobile periods. At long delay times in the TE-MSD curve, only the trajectories with many localisations (thus a longer time in the immobile state) contribute, which results in a decrease in the slope of the curve. Now that we understand the origin of the plateau at long delay times in the TE-MSD of the hybrid trajectories, we can explain the TE-MSD prior to classification (Figure 3.6b). Here, the curve also flattens to a plateau value—even more rapidly than for the hybrid trajectories—because short mobile trajectories and long immobile trajectories contribute to the TE-MSD curve as well.

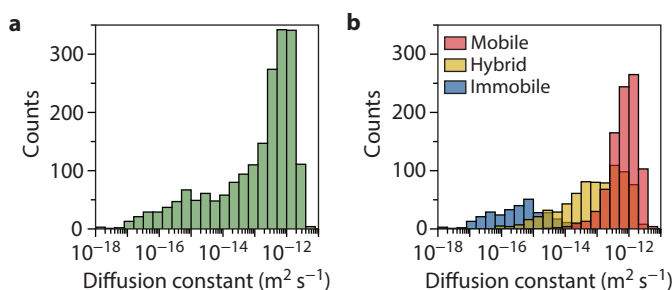**Figure 3.5** • (**a,b**) Histogram of the measured diffusion coefficient as obtained by time-averaged mean squared displacement (T-MSD) analysis per trajectory before (panel **a**) and after classification (panel **b**). A fitted negative slope of T-MSD as function of the delay time can yield unphysical, negative values for the diffusion coefficient. These diffusion coefficients are not displayed in the logarithmic scale.
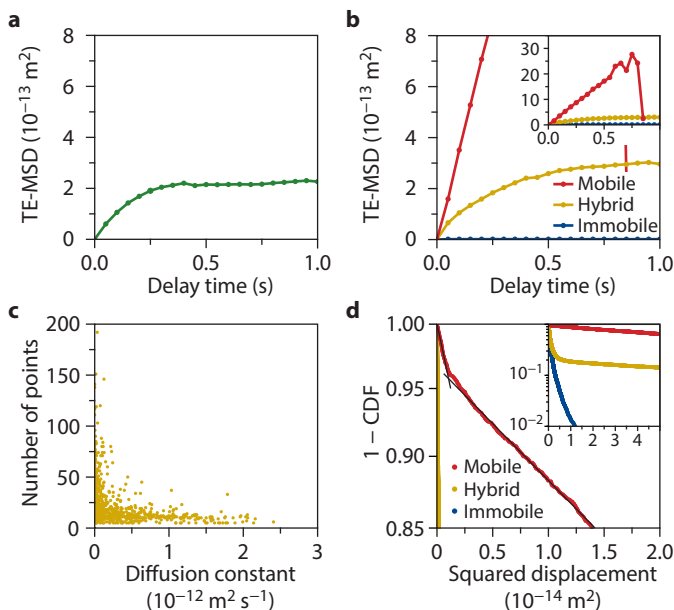
Figure 3.6 • (**a,b**) Zoom of the time–ensemble-averaged mean squared displacement (TE-MSD) before (panel **a**) and after classification (panel **b**). A zoom-out is shown in the inset in panel **b**. (**c**) Correlation plot of the diffusion coefficient and number of points of the hybrid population. Each dot represents a single trajectory. (**d**) One minus the cumulative distribution function (CDF) of squared displacements for a delay time of one frame (50 ms) of all trajectories plotted with a logarithmic *y*-axis. The colours indicate the populations after classification. The solid black lines are a guide to the eye to indicate two regimes in the CDF of the mobile trajectories. A zoom-out is shown in the inset.

In contrast to the hybrid trajectories, the TE-MSD curves of the mobile and immobile trajectories are a straight line. This confirms that the mobile trajectories are due to normal diffusion. The slope of the TE-MSD of the immobile trajectories is zero, i.e., the apparent diffusion coefficient is zero, which is in line with their immobile motion behaviour. The diffusion coefficient of the mobile trajectories was extracted from the TE-MSD curves using the model for normal diffusion. For our dataset, we found $D = 9.23 \pm 0.14 \times 10^{-13}$ m^2 s^{-1}. The value is slightly but significantly lower than the true diffusion coefficient of the mobile state of $D = 1.0 \times 10^{-12}$ m^2 s^{-1} that we had put in our simulations. This is attributed to a small number of immobile steps in the mobile trajectories, which reduces the measured diffusion coefficient of the population.

We can estimate the fraction of immobile steps in the mobile population with the cumulative distribution function (CDF) of squared displacements for a delay time of one frame (Figure 3.6d). Normal diffusion measured in two dimensions should yield,[97,145]

$$1 - \mathrm{CDF}(r^2, t_n) = \exp\left(\frac{-r^2}{\mathrm{MSD}\,(t_n)}\right) \quad (3.2)$$

with r^2 the squared displacement at a delay time t_n. The CDF(r^2, t_n) describes the probability of finding a squared displacement in the population with a length $\leq r^2$ at a fixed delay time. The CDF runs from zero to one. The lefthand side of Equation 3.2 is the CDF but reversed, running from one to zero, which can be plotted directly from the trajectories' squared displacements (see Methods). This representation of the CDF is convenient because the 1 – CDF

curve is described by a mono-exponential decay (see the righthand side of Equation 3.2), given that the MSD is constant (i.e., constant diffusion coefficient and localisation error). The decay produces a straight line in a semi-log plot of $1 - CDF$ against r^2, which can be easily inspected and fitted. Multiple slopes in the $1 - CDF$ curve indicate that multiple populations of emitters with a different diffusion coefficient (or localisation error) are present, each with a different MSD, resulting in a different slope of the curve.

For the mobile trajectories, we found a transition from a steep slope (immobile displacements) to a lower slope (mobile displacements) in the $1 - CDF$ curve (see black guides to the eye in Figure 3.6d). This confirms that ~4% of the displacements in mobile trajectories are immobile, which mainly explains the slight underestimation of the true simulated diffusion coefficient in the TE-MSD analysis. It also shows that the classification is not perfect, and that motion analysis of the ensemble could be further improved by fitting the $1 - CDF$ curve directly. The remainder of the discrepancy between the measured and true diffusion coeffi-

cient originates from imperfect linking of the localisations into trajectories. For the immobile trajectories, we find $D = 0 \pm 4 \times 10^{-18}$ m^2 s^{-1} confirming that the diffusion coefficient of the immobile trajectories is zero—as expected.

3.2.3 • Robustness of classification tree computation with machine learning

We generated different training sets of hundred trajectories from the dataset discussed in the previous section to test the robustness of the classification tree computation. Reproduction of the classification using a different training set yielded a similar tree and classification results. We generally found variations of the same classification tree with the MBCR at the first split and the MBCC–COM at the second split. Moreover, the *number of points* property was frequently found after the MBCC–COM branch. An example is shown in Figure 3.7 and the analysis of all classified trajectories using this classification tree is shown in Figure 3.8a–f, which was plotted on the same axes as in Figure 3.5a,b and Figure 3.6a–d for comparison. The similarity both in classification tree and motion analysis results is striking. The

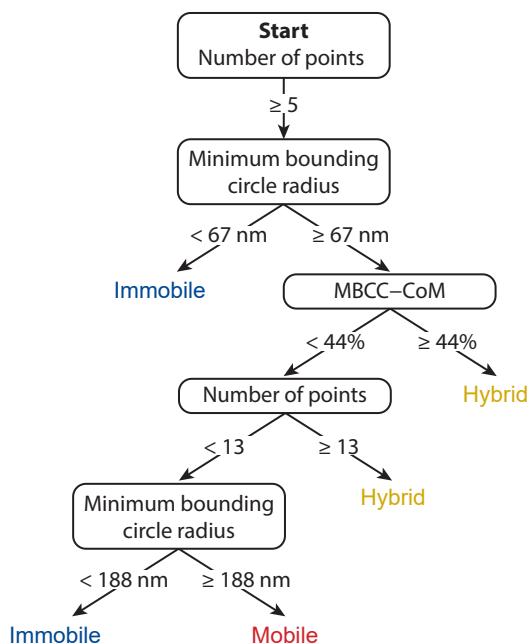**Figure 3.7 •** Classification tree obtained with machine learning on a training set of a hundred manually classified trajectories for a simulated dataset with transient adsorption. The training set comprises a different subset of classified trajectories than shown in Figures 3.3–3.6. A maximum number of five splits was set for this tree, and the full tree (without maximum number of splits) yielded virtually the same results.

classification tree has a resubstitution loss of 6%, which is 4% higher than for the classification tree in the previous section. The MBCR is smaller in the classification tree presented in this section (67 nm vs. 118 nm), which is compensated for by an extra split based on the MBCR to separate the mobile and immobile trajectories. Other splits are similar in both classification trees. As expected, the histogram of trajectory diffusion coefficients after classification (Figure 3.5b and Figure 3.8b), TE-MSD after classification (Figure 3.6b and Figure 3.8d), and 1 − CDF of squared displacements (Figure 3.6d and Figure 3.8f) are almost identical. The classification into mobile motion behaviour is marginally better in the classifi-
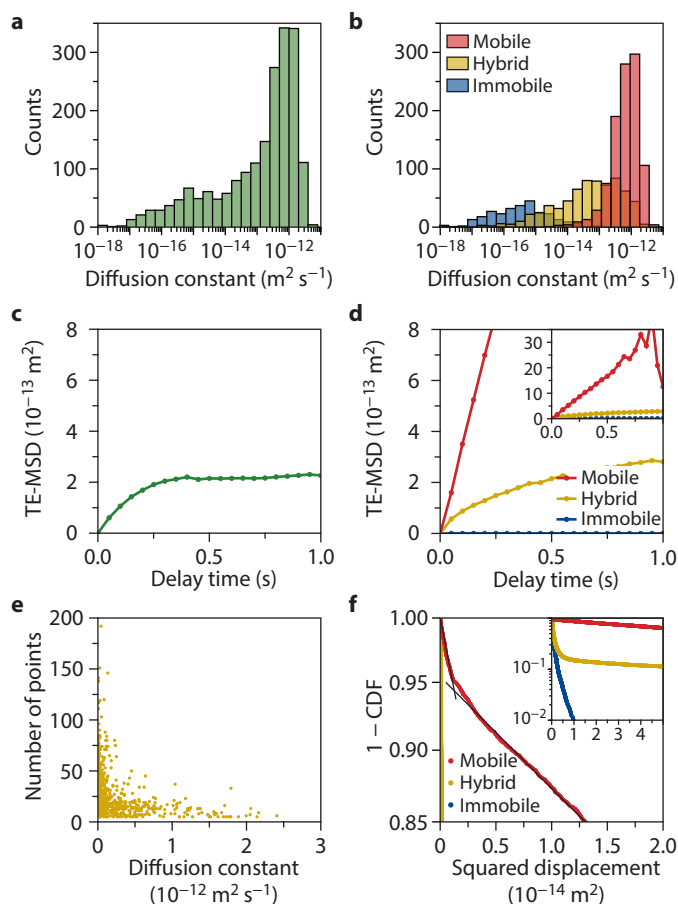
Figure 3.8 • (**a,b**) Histogram of the measured diffusion coefficient as obtained per trajectory time-averaged mean squared displacement analysis before (panel **a**) and after classification using the classification tree in Figure 3.7 (panel **b**). Negative measured diffusion coefficients are not displayed in the logarithmic scale. (**c,d**) Zoom of the time–ensemble-averaged mean squared displacement (TE-MSD) before (panel **c**) and after classification (panel **d**). A zoom-out is shown in the inset. (**e**) Correlation plot of the diffusion coefficient and number of points of the hybrid population. Each dot represents a single trajectory. (**f**) One minus the cumulative distribution function (CDF) of squared displacements for a delay time of one frame (50 ms) of all trajectories plotted with a logarithmic y-axis. The colours indicate the populations after classification. The solid black lines are a guide to the eye to indicate two regimes in the cumulative density probability of the mobile trajectories. A zoom-out is shown in the inset.
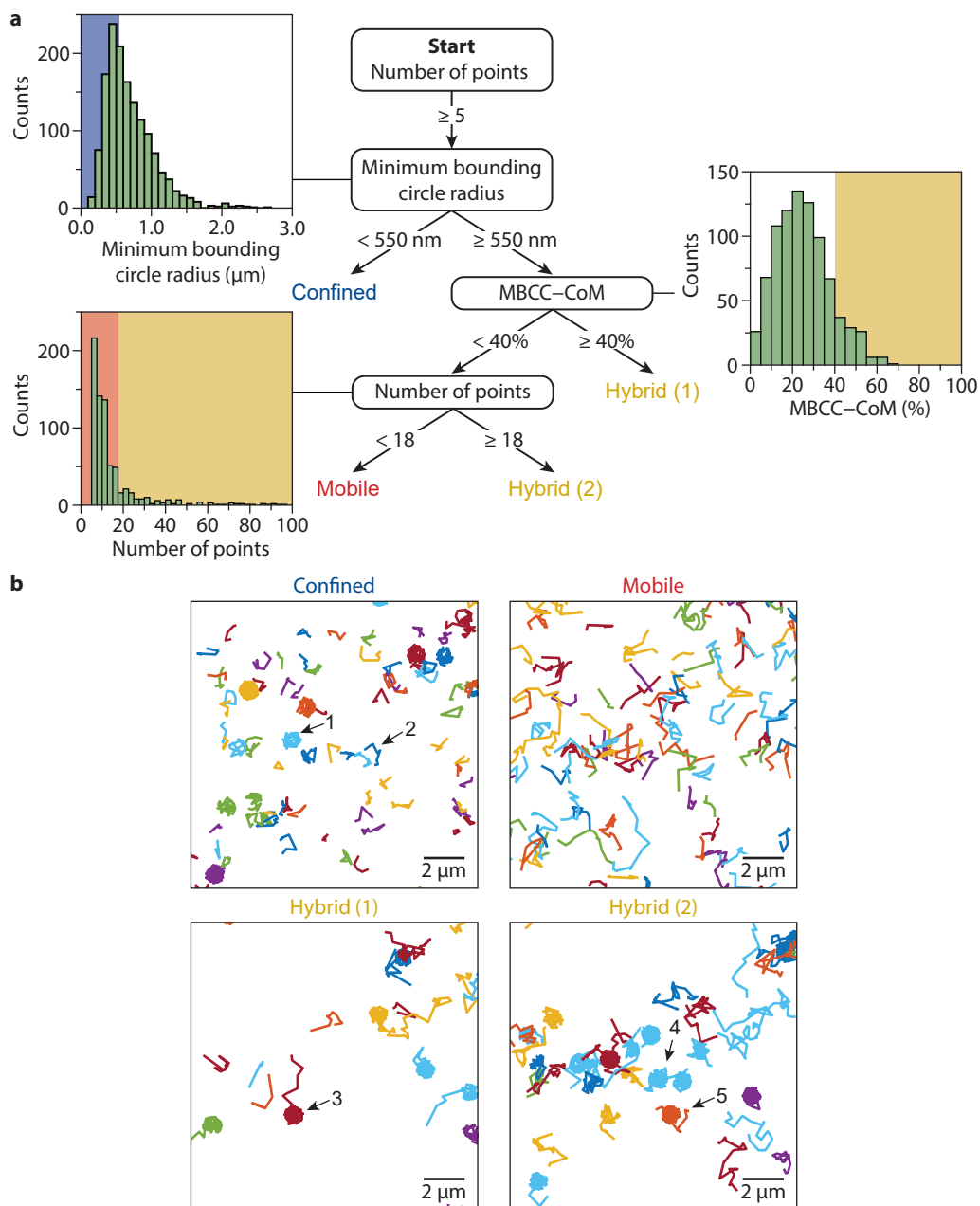
Figure 3.9 • (**a**) Classification tree obtained by manual modification of the thresholds in the classification tree shown in Figure 3.3 for a simulated dataset with transient confinement. The classification tree is read from top to bottom for each trajectory, weighing one property at each branch, until the trajectory is classified as either confined, hybrid or immobile. At each split, the histogram of the property is given for all trajectories of the branch, with the background colour indicating the threshold value of the split. (**b**) Individual trajectories of the same region of interest at each end point branch: confined, hybrid (1), hybrid (2), and mobile. The numbered arrows indicate regions discussed in the text.
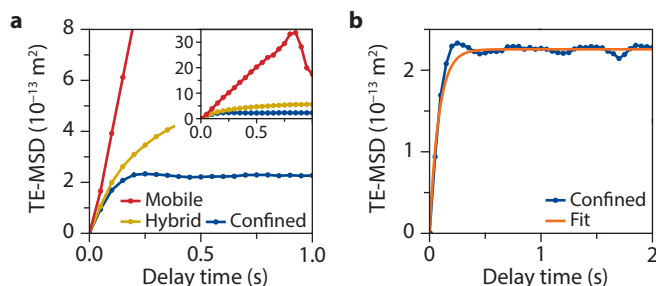
Figure 3.10 • (**a**) Zoom of the time–ensemble-averaged mean squared displacement (TE-MSD) of the transient confinement dataset after classification. A zoom-out is shown in the inset. (**b**) Fit of the confined population in panel **a** with Equation 3.3.

cation tree shown in the previous section. The obtained diffusion coefficient of the TE-MSD fit of the mobile population is slightly lower than for the dataset shown in the main text ($D = 8.98 \pm 0.15 \times 10^{-13}$ m^2 s^{-1} vs. $9.23 \pm 0.14 \times 10^{-13}$ m^2 s^{-1}), which can be explained by the lightly higher fraction of immobile displacements in the $1 - \text{CDF}$ (5–6% vs. 4%). In conclusion, the robustness of the classification tree computation is sufficiently good for applications described in this chapter, even for small training sets of a hundred trajectories.

3.2.4 • Classification of transient confinement with a modified classification tree

In this section, we demonstrate how the reported classification tree (Figure 3.3) can be adapted for classification of trajectories with qualitatively similar motion behaviour. Instead of adsorption with $D_1 = 0$ m^2 s^{-1}, we simulated confinement parallel to the observation plane in a circular disk with a radius of 500 nm using reflective boundary conditions.[146] The trajectories were simulated with the same parameters as in the transient confinement example discussed in Section 3.2.2. The adapted classification tree and the individual trajectories at each classification end point branch is shown in Figure 3.9. We manually changed the value of the MBCR at the first split until all trajectories that appeared fully confined were captured. The optimum value of 550 nm just includes the mode of the MBCR histogram (Figure 3.9a). This indicates that trajectories which explore an area corresponding to the confinement domain are most abundant (Figure 3.9b, arrow 1). Several short trajectories are also included in the *confined* population; however, their classification

is ambiguous as they only explore a limited area (Figure 3.9b, arrow 2). The user could decide to group these trajectories with the mobile trajectories. This can be done by adding an additional split at the confined branch, segmenting based on the number of points. At the split of the MBCC–CoM, the distribution in the histogram was not bimodal as in the classification tree for transient adsorption (Figure 3.3b). Nevertheless, we found that approximately the same threshold as used in Figure 3.3b filters out hybrid trajectories with a mobile segment connected to confined segment (Figure 3.9a and Figure 3.9b, arrow 3). In the next split, we increased the threshold of the number of points to 18 (Figure 3.9a), which makes a good distinction between mobile trajectories and hybrid trajectories with multiple domains of confinement or two mobile segments connected with an immobile one (Figure 3.9b, arrows 4 & 5). The performance of the classification tree is assessed via the motion analysis of the classified populations.

We show the motion characteristics of the classified populations via the TE-MSD in Figure 3.10a. The diffusion coefficient of the mobile trajectories was found to be $D = 1.099 \pm 0.016 \times 10^{-12}$ m^2 s^{-1}, which is approximately 10% larger than simulated value of 1×10^{-12} m^2 s^{-1}. The origin of the overestimation of the diffusion coefficient is a result of the relatively large MBCR of 550 nm. As discussed in the previous paragraph, the classification of the trajectories that fall within the MBCR is ambiguous. Short trajectories with short displacements could have been selectively filtered out at this split, resulting in an overestimation of the diffusion coefficient. Indeed, the addition of an extra

split removing mobile trajectories from the confined population as described before, using a *number of points < 7*, resulted in a more accurate estimation of the diffusion coefficient of the mobile trajectories, i.e., $D = 1.011 \pm 0.006 \times 10^{-12}$ m^2 s^{-1}. This demonstrates that the adaptation of a classification tree to a qualitatively similar dataset in some cases requires the addition or removal of splits.

We fitted the TE-MSD of the confined population with a model describing confinement on a circular disk (Figure 3.10b). The MSD can be described by

$$\text{MSD}(t_n) \ = \ R^2 \left(1 - \exp\left(-\frac{t_n}{\tau} \right) \right) \qquad (3.3)$$

with t_n the delay time, R the radius of the circular disk, and τ the characteristic equilibration time after which the effect of the confinement boundaries become evident and the MSD fully flattens.[48,87,144,147] We obtained $R = 475 \pm 28$ nm and correctly retrieved the simulated confinement radius of 500 nm.[147]

3.2.5 • DiffusionLab in experimental works

We have demonstrated how the DiffusionLab software can be used to analyse a set of trajectories originating from complex heterogeneous motion. The software is a powerful tool for a wide range of materials scientists studying the motion of molecules and nanoparticles in porous materials, including but not limited to zeolite-based materials.[61] Adsorption and confinement play a big role in such porous materials, and classification prior to motion analysis can greatly increase interpretability, avoid bias, and allows for more reliable spatial mapping of diffusion heterogeneity. In previous experimental work using the DiffusionLab software, the approach was demonstrated in a study of molecular diffusion through a porous fluid catalytic cracking particle (discussion of this work in Section 2.1.3).[61] The pore space of the catalyst particle is heterogeneous in material composition and porosity, with pore sizes ranging from the sub-nanometre to micrometre domain. The complex structure was reflected in the measured heterogeneous molecular mo-

tion behaviour. By classification in mobile, hybrid, and immobile trajectories, diffusivity of only the mobile trajectories could be compared with the bulk diffusion coefficient of feedstock molecules, which turned out to be similar in magnitude, thereby validating the approach. In other work using DiffusionLab, presented in Chapter 5, we have tracked the motion of single oligomers in the pores of ZSM-5 zeolites. By performing classification and motion analysis, we could not only compare the average diffusion coefficient between experiments, but also explain whether differences were the result of a change in diffusivity during and/or frequency of the mobile periods. This had led to a detailed insight in pore geometry–mass transport relationships on the microscopic scale. These successful examples from materials science highlight potential of the DiffusionLab approach for the field of life sciences. The motion behaviours supported by DiffusionLab have been frequently observed in cellular environments. For instance, directed motion has been reported when vesicles are transported along microtubules by molecular motors, transient adsorption when molecules interact with actin proteins, or confined diffusion when molecules are confined by cell-membrane components.[48,139]

3.3 • Conclusions

The DiffusionLab software package, which is open access and freely available to the scientific community, was developed for the analysis and quantification of motion from single-particle trajectories with 1) heterogeneous motion and/or 2) trajectories with only a few localisations. The trajectories are first classified into populations with similar characteristics to which the motion analysis is tailored in a second step. DiffusionLab provides the tools to classify trajectories based on their motion behaviour either with machine learning or manually. MSD analysis is available to perform quantitative motion analysis of the trajectories. The software can compute the diffusion coefficient for an individual trajectory if it is sufficiently long, or the average diffusion coefficient for multiple shorter trajectories. We demonstrated DiffusionLab's workflow with a set of simulated

trajectories with a transient adsorption model. The dataset showed heterogeneous motion behaviour and contained many trajectories with only a few localisations. Using DiffusionLab, we were able to interpret and quantify the motion in this complex dataset. Moreover, DiffusionLab has been successfully used to analyse experimental single-molecule trajectories recorded in porous materials as reported by our group (see Chapter 5 and ref. 61). Future developments of the software will focus on the extension of the motion analysis methods, including a fit of the 1 − CDF curves, as well as the addition of new properties for trajectories with many localisations.

3.4 • Contributions & acknowledgements

Donglong Fu (Utrecht University, UU) and Rafael Mayorga González (UU) are thanked for fruitful discussions.

3.5 • Methods

3.5.1 • Trajectory simulations

We simulated synthetic trajectories of emitters exhibiting transient adsorption following the procedure outlined in Figure 3.11. Estimation of the localisation error of an out-of-focus emitter is not trivial, particularly when the emitter moves more than roughly one pixel per frame thereby introducing an additional localisation error called motion blur. On top of that, the localisation algorithm fails to recognise the emitter when it is far out-of-focus.[100] To simulate a set of trajectories that closely resembles an experimental dataset, we generated realistic time-lapse movie frames from three-dimensional trajectory coordinates. We converted these time-lapse movies back in two-dimensional trajectories with third-party localisation and tracking software—just like it would be done with experimentally obtained micrographs.

Briefly, a synthetic dataset was generated in three steps: (1) simulation of the coordinates of 3-dimensional $xyzt$ trajectories;[144] (2) generation of synthetic xyt time lapse video frames from 3-dimensional trajectories using a simulated point spread function (PSF)[148,149] and homogeneous background signal; and (3) localisation and tracking of the generated

synthetic time lapse video with conventional fitting routines.[78] To simulate transient adsorption, the coordinates of a random walk with two diffusion states was simulated in step 1. The diffusion coefficient of the first diffusion state was set to zero ($D_1 = 0$) while the other was set to $D_2 = 1.0 \times 10^{-12}$ m^2 s^{-1}. The probability to change diffusion state was 0.02 per frame (0.4 s^{-1}). Every trajectory coordinate in (1) resulted in a PSF (step 2a) placed in the time-lapse video (step 2b). To simulate motion blur, the trajectory coordinates in step 1 were computed with a five times higher time resolution than the synthetic time lapse video in step 2b. This means that we placed five PSFs along the path the emitter has travelled during the frame. Photon-counting noise and camera noise were simulated in steps 3–4 resulting in an imprecision in the localisation in (5), which altogether introduced a localisation error. In step 5, localisation and tracking were done with the DoM plugin v.1.2.0 for ImageJ.[78,139]

Number of localisations per trajectory was not fixed and was based on the time the emitter was in focus. A fixed number of trajectories was simulated in a three-dimensional box with periodic boundary conditions during the full simulation time. A small fraction of the simulated emitters was in the microscope frame, i.e., focal volume, at the same time. Importantly, the emitter was only tracked by the DoM plugin when it was sufficiently in focus. Out-of-focus emitters were too broad or had insufficient counts to be picked up by the tracking algorithm. As a result, in- and out-of-focus movement of the simulated emitters split the three-dimensional trajectories into many shorter two-dimensional ones. Each step is described in more detail below and the simulation parameters are given in Table 3.2.

Three-dimensional trajectories were simulated as a multistate normal random walk (step 1, Figure 3.11). The displacement probability in all directions was given by a normal distribution with a standard deviation of $\sqrt{2D_i t}$, with D_i the diffusion coefficient of state i and t the delay time.[144] The diffusion state during one frame was computed from a discrete-time Markov chain with a specified state transition matrix and random initial state. This kind of model generates a sequence of events (diffusion states), where the probability of each event depends only on the state in the previous one. To simulate transient adsorption, the diffusion coefficient
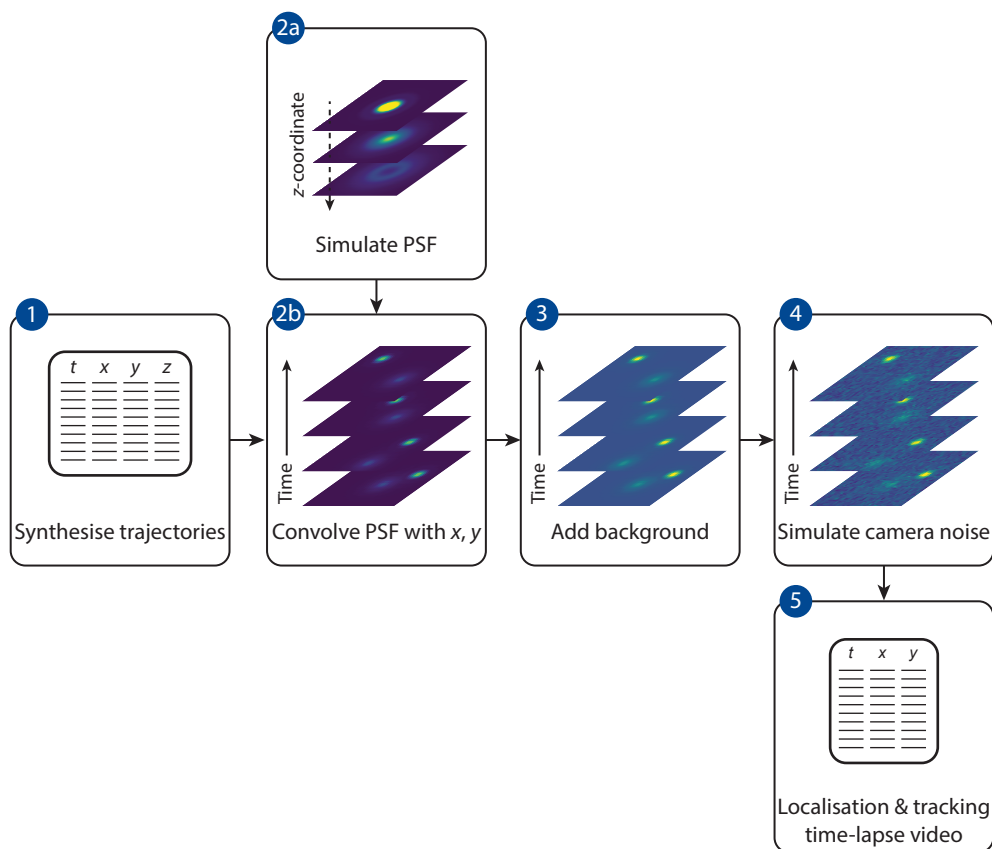
Figure 3.11 • Schematic overview of the simulation of the synthetic dataset: (**1**) raw trajectories are simulated and the *xyzt* coordinates are saved; (**2**) the point spread function (PSF) is simulated at various *z*-coordinates (**2a**), which is convolved with the trajectory coordinates (**2b**) to obtain a time-lapse video of the point emitters; (**3**) a fixed background is added; (**4**) camera noise is simulated over the signal in (**3**); and (**5**) the resulting time-lapse images are localised and tracked to obtain the simulated trajectories.

of the first diffusion state was set to zero ($D_1 = 0$) while the other was set to $D_2 = 1.0 \times 10^{-12}$ m^2 s^{-1}. The probability to change diffusion state was 0.02 per frame. Transient confinement was simulated with reflective boundary conditions in a circular disk with a radius of 500 nm.[146] Periodic boundary conditions were applied with a bounding box equal to the field of view in *x*, *y*, and 8.2 *μ*m in *z*. The concentration of emitters was kept constant at a density of 0.034 *μ*m^{-3} (5.66×10^{-14} M), which was achieved by simulation of a fixed number of trajectories for the full simulation time. The number of localisations during one frame was over-sampled five times to simulate motion blur. The

obtained synthetic trajectories are called the *raw* trajectories.

The raw trajectories were converted into time-lapse videos (step 2, Figure 3.11). The coordinates of the trajectory were translated into images via the PSF, which is the response of an optical system (microscope) to a point emitter. The measured PSF is dependent on the depth of the emitter with respect to the focus, and the recorded PSF changes as a function emitter's depth coordinates. We first simulated an isotropic PSF following vectorial diffraction theory as described by Backer and Moerner (step 2a, Figure 3.11).[149] The centre of the image of the PSF

Table 3.2 • Overview of the parameters used in the simulation of the synthetic transient adsorption dataset.

Parameter	Value
Experiment	
Field of view	$32.8 \times 32.8 \ \mu m^2$
Pixel size	64 nm
Number of pixels	512×512
Number of frames	2000
Frame time	50 ms
Temporal oversampling	5
Bounding box ($x \times y \times z$)	$32.8 \times 32.8 \times 8.2 \ \mu m^3$
Number of emitters	300
Emitter density	$0.034 \ \mu m^{-3}$
Diffusion coefficients $[D_1; D_2]$	$[0; 1 \times 10^{-12}] \ m^2 \ s^{-1}$
Transition matrix	$\begin{pmatrix} 0.98 & 0.02 \\ 0.02 & 0.98 \end{pmatrix}$ frame^{-1}
Background	$100 \ s^{-1} \ pixel^{-1}$
Point spread function	
Number of photons per emitter	$12889 \ s^{-1}$
Sampling x, y	10 nm
Sampling z	10 nm
Convolution resolution	1 nm
Cut-off in z	$1 \ \mu m$
Wavelength	600 nm
Refractive index	1.518
Magnification microscope	91
Numerical aperture	1.40

Table continues on next page.

Camera	
Quantum efficiency	0.9
Readout noise	74.4
Spurious charge	0.0002
Electron magnification gain	300
Baseline	100
Electrons per ADC	45
Localisation and tracking	
Sigma	2.0
Signal-to-noise	3.0
Blinking gap	2 frames
Pixel jump	20 pixels (training set: 15 and 20 pixels)

corresponding to the z-coordinates of the raw trajectory was convolved with the trajectory's x,y-coordinates (step 2b, Figure 3.11). Since we can only convolve the PSF image with whole pixels, we translated the PSF image before convolution to achieve subpixel resolution. The PSF was oversampled in x,y with respect to the pixel size of the time-lapse movie to ensure accurate interpolation during translation of the PSF image. To speed up the calculation, the x,y-coordinates of the trajectory were rounded to the nearest value on a grid with intervals of 0.1 pixel. The normalised intensity of the in-focus PSF image was scaled by the photon flux per emitter. Altogether, this resulted in a dimensionality reduction because the depth information in the time-lapse images is encoded in the shape of the PSF.

A constant auto-fluorescent background was added to the noise-free time-lapse images, which was subjected to an electron-multiplying charge-coupled device (EMCCD) camera noise model as described in Sage et al. (step 3–4, Figure 3.11).[148] We have taken the same model parameters because these values are similar for EMCCD cameras from other manufacturers. Finally, the simulated time-lapse images have been localised and tracked, which we call the

simulated trajectories (step 5, Figure 3.11). We have excluded false positives in the tracking. The DoM results table was exported to .csv and imported in DiffusionLab.

3.5.2 • Data processing, analysis, and modelling

Classification and analysis. The hierarchical classification tree was constructed from a manually classified training set of a hundred trajectories. The training set was used to automatically select the threshold and the trajectory properties, i.e., features. We allowed all trajectory properties available in DiffusionLab to be used by the model, which was the *elongation*, *elongation angle*, *entropy*, *length*, *minimum bounding circle radius*, *minimum bounding circle radius minus centre of mass*, *number of points*, and *tortuosity* (see also DiffusionLab Documentation Section 3.1.1). The maximum number of splits in the tree was limited to five in all examples because a larger tree did not lead to better classification and could cause overfitting.

The classification and analysis of the simulated trajectories was done with version 1.1.0 of the Diffu-

sionLab software package. The MATLAB installer and source code are available online: https://github.com/ErikMaris/DiffusionLab. The latest version of the documentation can be downloaded via https://diffusionlab.readthedocs.io/_/downloads/en/latest/pdf/.

Modelling of the probability of an immobile trajectory to fall within the minimum bounding circle radius. We considered how likely immobile trajectories fall entirely within a minimum bounding circle with some threshold radius. If an immobile emitter is localised over many images, the localisation coordinate in one dimension would be normally distributed around the true position of the emitter. The localisation error σ is defined as the standard deviation of this normal distribution. Thus, assuming that the centre of the minimum bounding circle is equal to the true position of the emitter, we could compute the fraction of localisations that are measured within the threshold radius α

$$\varepsilon(\alpha, \sigma) = \text{erf}\left(\frac{\alpha}{\sigma\sqrt{2}}\right) \qquad (3.4)$$

with erf the error function. Then, the probability that all localisations of a trajectory fall within the minimum bounding circle with threshold radius α is simply

$$\gamma = \varepsilon^k \qquad (3.5)$$

with k the number of localisations in a trajectory. We used $k = 17$ for the computations reported below, which is the mean number of localisations in the immobile population.

First, to compute ε and γ, we need to obtain a value for the localisation error σ. We estimated σ as the best possible localisation uncertainty obtained with a least-squares fit of a two-dimensional Gaussian distribution to the observed point spread function (PSF). This limit was first described by Thomson et al.[150] and later corrected by Mortensen et al.,[142] and is

$$\sigma_g^2 = \frac{\sigma_a^2}{N}\left(\frac{16}{9} + \frac{8\pi\sigma_a^2 b^2}{Na^2}\right) \qquad (3.6)$$

with $\sigma_a^2 = \sigma_{\text{PSF}}^2 + a^2/12$, σ_{PSF} the standard deviation

of the PSF, a^2 the pixel area, N the signal photon count, and b the background photons per pixel. Equation 3.6 was multiplied by a factor two to account for the excess noise introduced by the electron multiplication process in the EMCCD camera. The formula reproduces the localisation error found in computer experiments with a known truth.[142] Please note that we did not consider the contribution of motion blur to the localisation error. To estimate the localisation error of an out-of-focus emitter, we computed σ_{PSF} following Deschout et al. for an emitter with a distance z from the focal plane[143]

$$\sigma_{\text{PSF}}^2(z) = \sigma_{\text{PSF},0}^2\left(1 + \frac{z^2}{\left[(4\pi n/\lambda)\,\sigma_{\text{PSF},0}{}^2\right]^2}\right) \qquad (3.7)$$

with $\sigma_{\text{PSF},0}$ the standard deviation of the PSF at the in-focus plane, n the refractive index of the immersion medium, and λ the emission wavelength. The $\sigma_{\text{PSF},0}$ was extracted from a fit of the true (simulated) PSF at the in-focus plane and was found to be 98.6 nm. The values for a^2, N, b, n, and λ were taken from Table 3.2, with N the number of photons per emitter multiplied by the camera quantum efficiency. When in focus, $z = 0$, Equation 3.7 reduces to $\sigma_{\text{PSF}}^2(0) = \sigma_{\text{PSF},0}^2$ resulting in $\sigma_g = 12.4$ nm, which was substituted for σ in Equation 3.4 and Equation 3.5. For $\alpha = 118$ nm and $z = 0$, we found $\varepsilon > 99.99\%$ and $\gamma > 99.99\%$; and for $\alpha = 118$ nm and $z = \pm400$ nm, $\sigma_g = 28.2$ nm, $\varepsilon > 99.99\%$, and $\gamma = 99.95\%$.

Plotting the 1 − CDF curve. We plotted the lefthand side of Equation 3.2 by calculating the individual squared displacements r^2 at a fixed delay time t_n of all trajectories. Every squared displacement has the same weight in the cumulative distribution function (CDF). Thus, for M squared displacements, every r^2 contributes $1/M$ to the CDF, and the i-th largest squared displacement r^2 has a CDF value of $i \times 1/M$. To implement this, all r^2 were sorted from low to high and given an $1 − \text{CDF}$ value that was equally spaced from one to zero, i.e., with intervals of $1/M$.[97] In this way, the $1 − \text{CDF}$ value of the i-th squared displacement r^2 correctly contributed $1 − i \times 1/M$ to the $1 − \text{CDF}$. The $1 − \text{CDF}$ versus r^2 were plotted in Figure 3.6d and Figure 3.8f.

Chapter **4**

Fluorescent-probe characterisation for pore-space mapping with single-particle tracking

Abstract • Porous solids are often characterised by a complex network of interconnecting pores of various dimensions. Tracking fluorescent probes, either molecules or nanoparticles, as they diffuse through the porous solid can be used to characterise a pore network with tens of nanometre resolution. However, understanding how the motion behaviour of fluorophores changes in confinement is necessary to reliably derive properties of the pore network. In this chapter, we introduce a well-defined lithography-made model pore developed to study this probe behaviour in confinement. We investigate the influence of probe–host interactions on diffusion and trapping of confined single-emitter quantum-dot probes. Using pH-responsiveness of the probes, we are able to largely suppress trapping at the pore wall and in turn define experimental conditions that allow mapping of the accessible pore space of a one-dimensional pore array as well as a real-life polymerisation catalyst particle. Furthermore, we use these conditions to quantify flow in the one-dimensional pores.

4.1 • Introduction

Efficient molecular transport through porous solids improves their performance and lifetime in applications such as heterogeneous catalysis.[151] Therefore, the accessibility and interconnectivity of the pore structure is of paramount importance for the catalytic efficiency. The pore structure of solid catalysts is often a complex network of macropores (> 50 nm diameter), mesopores (2−50 nm diameter), and micropores (< 2 nm diameter) with a heterogeneous composition.[11,14,152,153] A more rational design of the pore space holds great promise for the improvement of catalysts. Thus, high-resolution characterisation of the pore volume is needed to investigate the relation between synthesis parameters and resulting pore networks. However, this approach requires complex sample preparation and/or analytical techniques such as X-ray imaging using synchrotron radiation, making it time-consuming and expensive.[13,151,154,155]

A promising alternative is to use single-molecule (particle) localisation microscopy (SMLM) for the characterisation of porous solids.[52,55,61,106,121,156] These experiments are relatively inexpensive and fast to perform. Fluorescent probes, either molecules or nanoparticles, are tracked with a resolution on the order of 10 nm as they diffuse through the accessible pore network. The travelled paths of the probes, or trajectories, contain information about the pore network accessibility and interconnectivity (Figure 4.1).[55,106] Furthermore, the size and surface properties of the pores might be derived from the duration and frequency of probe–host adsorption events as well as diffusivity of the probes, but this has not yet been experimentally demonstrated.[157–159] Imaging of the dynamic uptake of fluorescent tracers using confocal laser scanning microscopy has proven effective to reconstruct the accessibility of fluorescent probes in millimetre-sized catalysts.[153] However, the resolution of this method is restricted by the diffraction limit (~250 nm), and is—in this respect—strongly outperformed by SMLM.[73]

To reconstruct the pore space of a porous solid, understanding of the relation between the probe's trajectory and local pore environment is required. This is complicated by the observation that diffusion of single-molecule probes in porous materials is heterogeneous and temporary adsorption events characterise the motion behaviour.[44,61,160] The physical origin of the heterogeneous motion is hard to resolve because of the complex catalyst material in which these observations were done. Therefore, a thorough characterisation of the adsorption and diffusion behaviour of the fluorescent probes in well-defined pore structures is essential for a proper interpretation of SMLM experiments in more complex porous solids.

The adsorption behaviour of molecules and nanoparticles cannot be compared directly. Although the same forces—including electrostatic interactions, van der Waals forces, and hydrogen bonds—may act on molecules and nanoparticles, their adsorption behaviour is qualitatively and quantitatively different. The pair interaction energy scales with the size of the molecule or nanoparticle, and with that, its
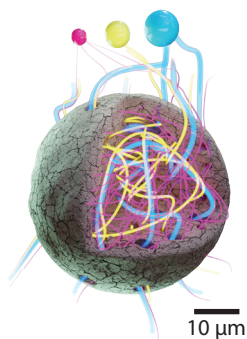
Figure 4.1 • Fluorescent probes can be used to map the pore space of complex porous solids, such as catalyst particles. In this impression, differently sized fluorescent probes (not to scale) are used to map a different fraction of the pore space as smaller probes can access smaller pores.

10 μm

absolute range and strength. Here, the interaction energy of a nanoparticle can be larger than kT, even at separation distances of 100 nm, whereas molecular interactions are generally weaker and shorter ranged in the liquid phase, i.e. < 1 nm.[161] For adsorption of a molecule or nanoparticle to a solid surface, such as a pore wall, the same trends hold. Because of the strong forces, nanoparticles often have a secondary potential energy minimum.[161] Here, a repulsion barrier has to be overcome to reach the overall energy minimum, usually causing irreversible adsorption.

In this chapter, we introduce a well-defined, lithography-made model pore with known geometry and composition designed for the characterisation of fluorophore dynamics. Characterisation of a fluorophore using the model pore enables the design and interpretation of pore-space-mapping experiments. We studied commercially available polyethylene-glycol (PEG)-coated quantum dots (QDs) in the model pore using SMLM. These nanoparticles are promising probes due to their bright fluorescence and small hydrodynamic radius of about 7.5 nm. We investigated the influence of probe–host interactions on diffusion and (temporary) immobilisation of confined single QD probes. Based on the probe characterisation, we defined a set of experimental conditions that allowed mapping of the accessible pore space of a one-dimensional pore array as well as a *real-life* polymerisation catalyst particle. Furthermore, we were able to quantify flow within the one-dimensional pore using the PEG-QD probes.

4.2 • Results and discussion

4.2.1 • Fluorescent-probe characterisation with a model pore

The model pore system is a microfluidic device containing well-defined pores to characterise the motion behaviour of fluorescent probes in confinement. The device was constructed with nanolithography and wet etching from silica wafers. Its layout is shown in Figure 4.2a. The model pores are two-dimensional (2D) slit-shaped patches with a size of 60×175 μm and a depth of 50 nm, imposing confinement only in the depth direction. We call these shallow patches 2D pores, and it is in these domains where we track the motion of the fluorescent probes. The 2D pores are accessible from the side openings via 20-μm-deep supply channels, via which we transfer the solution containing the fluorescent probes to the 2D pores. The depth profile is displayed in Figure 4.2b,c, and shows that the slit depth is 48 nm. A 5.4 nm root-mean-square surface roughness was found with atomic force microscopy over a 500×500 nm^2 region (Figure 4.2d). Prior to each experiment, the chip was loaded with a fluorescent-probe solution and sealed. The probe fluorescence was imaged in the plane perpendicular to the confinement direction using SMLM.

We recorded the trajectories of PEG-coated QDs suspended in a water/glycerol mixture, while diffusing inside the 2D pore. A selection of trajectories within the field of view is shown in Figure 4.3a. The longest trajectories
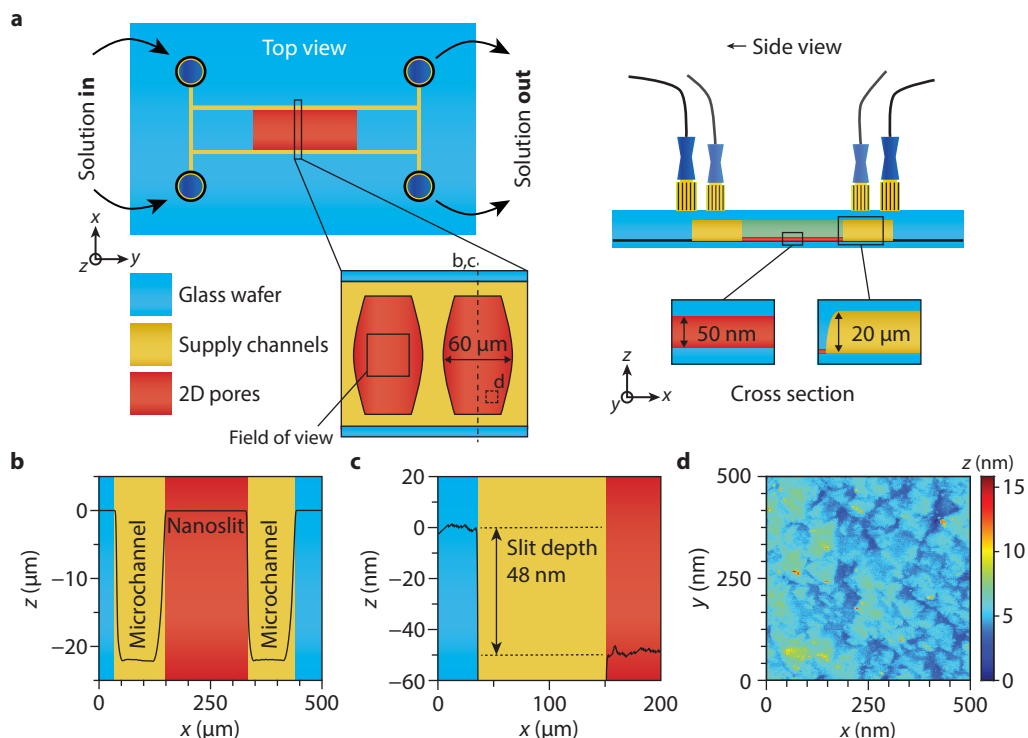
Figure 4.2 • (**a**) Schematic representation of the microfluidic device containing model pores. The top view, side view, and a cross section through a two-dimensional (2D) pore and a supply channel is shown. (**b**) Measured profile with a stylus profilometer displaying the supply channels. The profile is depicted with the dashed line in panel **a**. (**c**) Zoom of panel **b** displaying the height difference in *z* between the lithography-patterned 2D pores and the unexposed part of the wafer, prior to bonding. (**d**) Surface roughness as measured with atomic force microscopy. The mapped area is depicted with the dashed box in panel **a** (not to scale).

of QDs diffusing through the 2D pore contained over a thousand localisations and were tracked over more than 30 s. Because the 800 nm depth-of-focus is larger than the 2D-pore depth of 50 nm, the fluorophores remained in focus throughout the experiments. The absence of background fluorescence from out-of-focus probes resulted in a high signal-to-noise ratio, which facilitated tracking. Therefore, the trajectories contained many localisations compared to trajectories recorded in three dimensions (e.g., Chapter 3), which is pivotal for characterisation of probe diffusion and trapping. In Figure 4.3b, three example trajectories are enlarged, where one trajectory describes a QD that was trapped for a time. The trajectories appear to have some similarities to the

hybrid and *immobile* trajectories described in Chapter 3, although containing many more localisations. We will demonstrate the detailed analysis of the QD trajectories recorded in different pH conditions to characterise the effect of the pH on the trap behaviour and diffusion dynamics. Once we understand the QD's behaviour in confinement, we can design an experiment with the right conditions to explore the pore volume of more complex pore systems.

4.2.2 • Characterisation of probe trapping within a model pore

In this section, we will focus on the characterisation of QD trapping as a function of

different pH conditions. Both probe–pore wall adsorption and increased hydrodynamic drag near the wall can cause QD trapping in the model pore. In this case, adsorption is the trapping of the QD in a potential energy minimum at the silica surface. Because QDs usually have an inorganic core surrounded by organic ligands (Figure 4.4a), their interaction potential contains contributions from both the core and ligands. Here, van der Waals attraction (mainly core) is balanced by electrostatic repulsion (core and ligands) and entropic repulsion (mainly ligands). The net interaction is known to be dependent on external factors, such as the pH and temperature, which could affect the QD's adsorption behaviour.[161] In addition to adsorption, the hydrodynamic drag force increases dramatically when a nanoparticle approaches the pore wall, which can cause the particle to slow down and appear trapped.[162,163] We cannot discriminate between adsorption and hydrodynamic drag effects in our experiment.

For comparison with the 2D model pore, QD trapping was first screened on an unconfined liquid–silica interface as a function of pH (Figure 4.4b). At increasing base concentration—from 0 to 20 mM NaOH—trapping decreased to the point that no trapped QDs were observed, showing that this behaviour can be tuned via the solvent pH. To understand the

trap behaviour, the hydrodynamic radius of the QDs was measured at various pH.

The QD were tracked in a solution of 85/15 glycerol/water (m/m) with 0, 7.5, or 20 mM NaOH to obtain their hydrodynamic radius. This solution has a higher glycerol content than the 50/50 glycerol/water solution employed for tracking experiments in the model pore. The higher viscosity was necessary to slow the particles down within the regime where they could be tracked in free solution. The average diffusion coefficient D was obtained from a fit of the time–ensemble-averaged mean squared displacement curves at each NaOH concentration. Then, the particle's hydrodynamic radius r_h was computed from the Stokes–Einstein equation

$$r_\mathrm{h} = \frac{k_B T}{6\pi\eta D} \tag{4.1}$$

with k_B Boltzmann's constant, T the temperature, and η the viscosity. We used $\eta = 0.11084$ Pa·s for the calculation of the hydrodynamic radius.[164] The computed radii are shown in Figure 4.4c. Adding base to decrease QD trapping led to a reduction in size from circa 14 nm to 7–8 nm. We ascribe this to shrinking of the PEG shell since it has been previously reported in literature that suspended PEG shrinks when the ionic strength of the
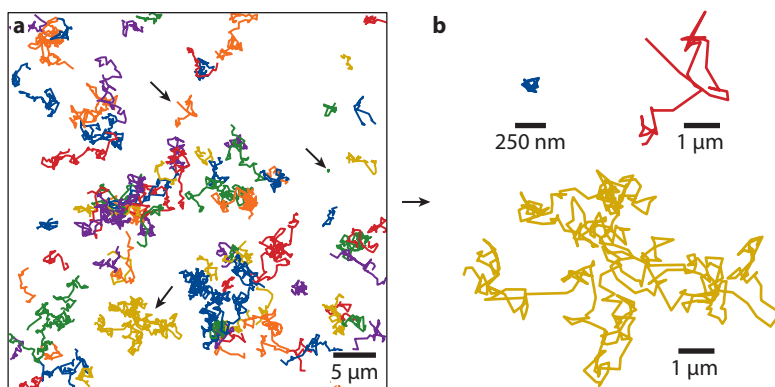

Figure 4.3 • (a) A small selection of quantum-dot trajectories observed within the field of view of the device in Figure 4.2a. The quantum dots were suspended in 50/50 (m/m) glycerol/water with 7.5 mM NaOH. **(b)** Three enlarged trajectories, which are indicated by an arrow in panel **a**.
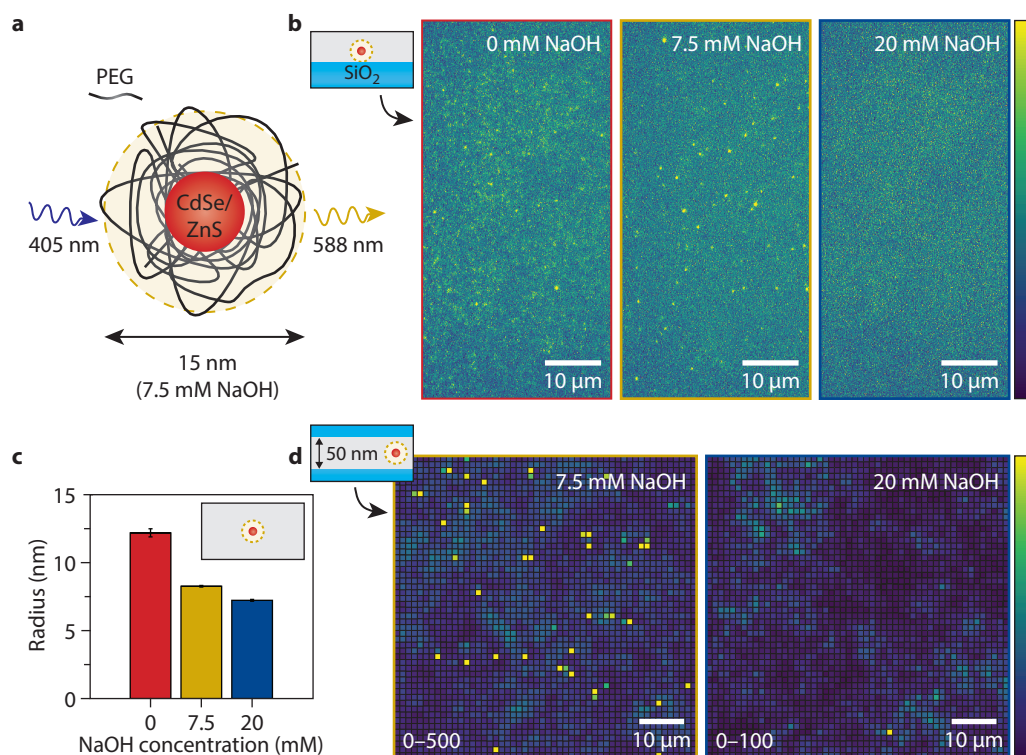
Figure 4.4 • (**a**) Polyethylene-glycol (PEG)-coated CdSe/ZnS core–shell quantum-dots (QDs) were excited with a 405 nm laser, and their fluorescence emission was recorded around 588 nm. (**b**) QD probes trapped on the surface of a silica coverslip as a function of NaOH base concentration. The 7.5 mM NaOH sample had an additional 2.5 mM NaCl to keep the Debye length < 2.5 nm. (**c**) Estimated quantum-dot hydrodynamic radius as a function of base concentration. The radius was estimated from the diffusion coefficient in free solution using Equation 4.1. The salt concentrations match conditions in panel **b**. The error bar is computed from the standard error in the fit of the diffusion coefficient. (**c**) Two-dimensional histogram of the single-particle coordinates in the two-dimensional pore during 4000 frames in 7.5 mM (left) and 20 mM NaOH (right) with 10 × 10 pixels (0.87 × 0.87 µm²) bins. The displayed range is given in frames (35 ms) in the bottom left corner. The particles were suspended in 50/50 (m/m) glycerol/water in panels **b,d** and 85/15 (m/m) glycerol/water in panel **c**.

solution increases.[165] Furthermore, zeta potential measurements on the QDs in water revealed that the nanoparticles were negatively charged with a zeta potential of −23.9 ± 0.6 mV. For increasing pH, we concluded that the hydrodynamic radius of the negatively charged QDs decreased due to contraction of the PEG shell (Figure 4.4a,c),[165,166] likely increasing electrostatic repulsion between the QD and negatively charged silica pore wall.[167] This repulsion prevents the QD from getting close to the silica, keeping it outside the

regime where probe–wall attraction dominates and/or the hydrodynamic drag increases dramatically.

To assess the trap behaviour in confinement, the same solutions as measured at the unconfined liquid–silica interface were loaded in the 2D model pore. Two timeframes were investigated: *short* trap events lasting for 5–100 frames and *long* trap events spanning for hundreds/thousands of frames. We identified long events via a 2D histogram of the localisation
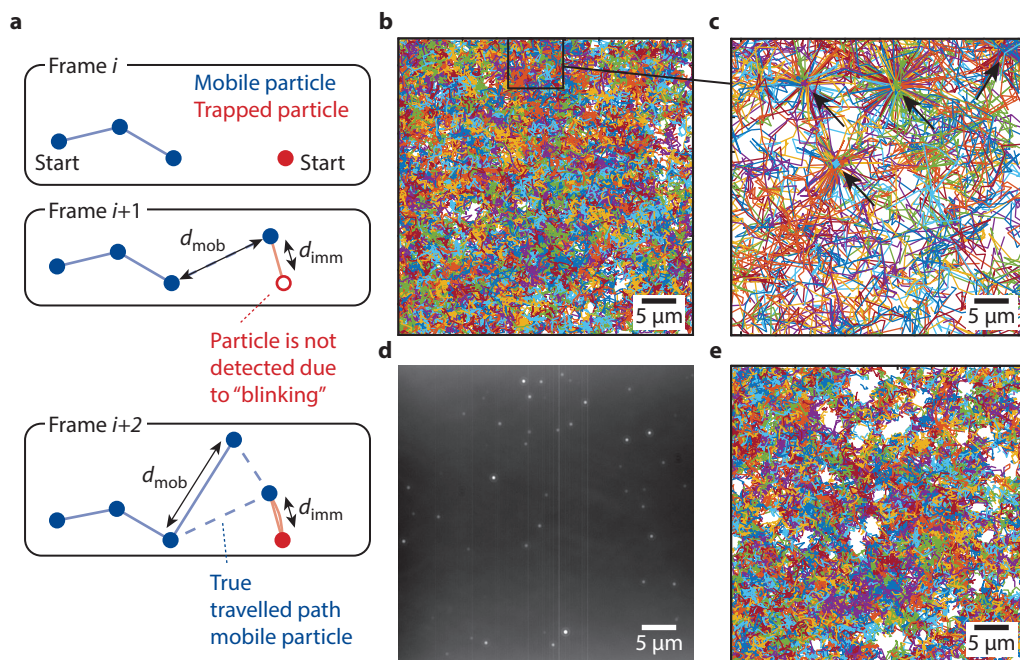
Figure 4.5 • (**a**) Example of an artefact created by the presence of a mobile particle that closely passes by a trapped, non-detected particle. Two nearby trajectories of a mobile (blue) and trapped particle (red) are shown in frame *i*. In the next frame *i*+1, the trapped particle is not detected. The sum $d_{mob}^2 + d_{imm}^2$ (i.e., cost) is minimised when the localisation of the mobile trajectory is added to the trajectory of the trapped particle. No localisation is added to the mobile trajectory. In the frame *i*+2, the trapped particle is detected and the sum $d_{mob}^2 + d_{imm}^2$ is minimised when the mobile localisation is added to the mobile trajectory and the trapped one to the trajectory of the trapped particle. This process can occur several times resulting in a trajectory with star shape (arrows in panel **c**). (**b,c**) Overlay of trajectories obtained during 4000 frames in the two-dimensional model pore at 7.5 mM NaOH. A zoom of panel **b** is shown in panel **c**. The black arrows point to artefacts, which were caused by particles that were trapped for hundreds of frames. (**d**) Average intensity of the fluorescence microscopy video used to track the trajectories in panels **a,b**. Particles that correspond to long trap events can be easily recognised. (**e**) Overlay of trajectories after removal of trajectories close to the trapped particles. Note that the empty regions correspond to the trapped particles visible in panel **d**.

coordinates, which displays the spatial distribution of all recorded localisations during a single movie of 4000 frames (Figure 4.4d). Bins with significantly more counts than their direct neighbours indicate the presence of trapped particles. Visual inspection of the histogram revealed long trap events at 7.5 mM NaOH concentration, while only one was observed at 20 mM NaOH. This followed the same trend as on the unconfined liquid–silica interface, shown in Figure 4.4b.

Unexpectedly, the long trap events resulted in artefacts in the trajectory generation process because trajectories belonging to moving particles were often wrongly linked to trapped ones. If the trapped particle is not detected, e.g., due to blinking, a localisation belonging to a mobile QD can be included in its trajectory. This happens when the localisation belonging to the trapped QD is closer than a localisation belonging to a mobile one (detailed visual explanation in Figure 4.5a). In the datasets presented in this chapter, the QDs travel

many pixels per frame (i.e., pixel jump is 16 pixels), which increases the probability that such an artefact occurs. These artefacts add large displacements to trajectories of trapped QDs and can even swap trajectory segments of a mobile and trapped particle. The artefacts can be recognised in a plot of all trajectories as *star-shaped* trajectories in the vicinity of trapped particles (arrows in Figure 4.5b,c). The centres of the stars are the localisations of the trapped probes, and the spikes are caused by sporadic erroneous linking with nearby passing particles. We removed trajectories close to the positions of long trap events based unless otherwise stated (Figure 4.5d,e). Note that this filtering step leads to undesired blind spots with no reliable trajectory data, which can be seen in Figure 4.5e.

Because long trap events were present in the data, we also expected shorter events to occur that could not be recognised by eye. Therefore, we performed trap analysis to detect short, transient trap events within single trajectories (see Methods).[168–170] This analysis captures both transient adsorption and a slowing down of the QDs as result of large hydrodynamic drag forces near the pore wall. Thus, the short trap events are a measure for how frequently the probe is able to get near the pore wall. The result of the trap analysis is shown in Figure 4.6. Trapping occurred in both pH conditions. We found fewer and shorter trap events at 20 mM than at 7.5 mM NaOH. This followed the trend observed on the unconfined liquid–silica interface in Figure 4.4b. In contrast to our observations in the 2D pore, no trap events were detected at the unconfined interface at 20 mM

NaOH, which demonstrates the limitations of using such surface to characterise QD trapping in confinement. Using another type of nanoparticle probes called carbon dots, we found an even larger discrepancy between the trap behaviour of the probes on an open surface and in confinement (Figure 4.7).[171] These observations highlight the necessity to characterise trapping in confinement, which can be readily done using our model-pore platform. Furthermore, transient trap events are hard to quantify because they often only last a few frames and occur rarely. Their detection was possible because of the many localisations per trajectory that were recorded in the model pore.

4.2.3 • Characterisation of diffusion within a model pore

We investigated the diffusion dynamics of QDs in the 2D model pore, and whether it is affected by the short, transient trapping characterised in the previous section. First, we studied the diffusion type of the PEG-coated QDs in confinement via mean squared displacement (MSD) analysis (see background in Section 2.2.4). The shape of the MSD as a function of the delay time is dependent on the motion type of the probe. A linear relationship is indicative for normal (Brownian) diffusion, whereas complete flattening of the MSD curve indicates confinement within the observation plane.[48,87] A power law relation of the MSD as a function of the delay time is called anomalous diffusion and is often found in cells as a result of molecular crowding.[48] Various models to describe different types of anomalous diffusion exist.[48,85,138] The diffusion coefficient can be

Figure 4.6 • Frequency of short trap events in the two-dimensional pore in the same conditions as reported in Figure 4.4d. The histogram is normalised by the total number of localisations in the dataset and corrected for the number of expected false positives. Here, only trajectories displaying mobility in their initial and final localisations were considered to ensure that solely complete trap events were included in the analysis. Trajectories with long trap events spanning of hundreds of frames were not considered.
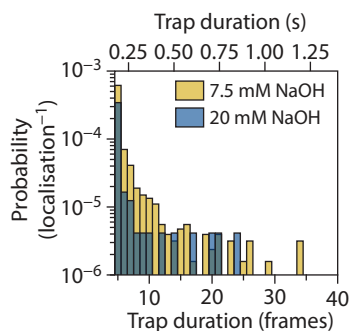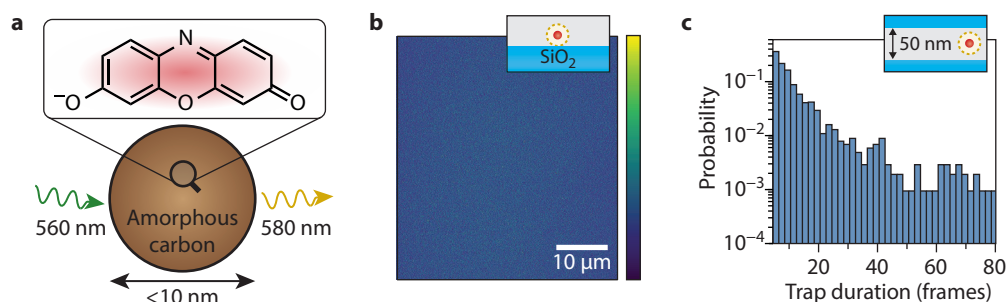
Figure 4.7 • (**a**) Carbon-dot (CD) nanoparticles embedded with the fluorescent resorufin molecule were excited with a 560 nm laser and their fluorescence emission was recorded around 580 nm. The chemical structure of resorufin is shown in the inset. (**b**) CD fluorescent probes imaged at the 50/50 (m/m) glycerol/water (10 mM H_3PO_4) liquid–silica coverslip interface. No trapped particles were observed on the coverslip. (**c**) Histogram of the trap duration (35 ms frame time) of CDs inside the silica two-dimensional pores using the same solution as in panel **b**.

reliably determined with the appropriate diffusion model if the diffusion type is known. In the time–ensemble-averaged MSD (TE-MSD), the MSD is averaged over all trajectories in the dataset (Section 3.2.1). The TE-MSDs are compared in conditions where trapping frequently (7.5 mM NaOH) and rarely (20 mM NaOH) occurs. In both conditions, the TE-MSDs as a function of delay time were found to be linear for trajectories with a similar span, and two example TE-MSDs are shown in Figure 4.8. Here, we defined the span of a trajectory as the number of frames between the first and last localisation of the trajectory. The linear TE-MSDs indicate that the QDs exhibit normal diffusion in the direction parallel to the 2D pore.

We should be careful to distinguish between normal and anomalous diffusion dynamics. The TE-MSD can be linear even though the underlying motion can be best described by an anomalous diffusion model. This is known to occur in situations where there is *weak ergodicity breaking* as a result of time-dependent and space-dependent diffusion. We investigated whether there is time-dependent diffusion by plotting the MSD with a fixed delay time as a function of the starting time in the experiment (Figure 4.9a–d).[48,85] We coin this the ensemble-averaged MSD (E-MSD). If the system ages, e.g., due to pore narrowing by adsorption of organic material or heating by the laser, the E-MSD is expected to change over the experiment duration. A linear fit was performed on the E-MSDs as a function of the experiment time for different delay times. For single videos recorded in the same conditions, we found both positive and negative slopes of the linear fits, and two examples are shown in Figure 4.9a,b. To demonstrate that the average
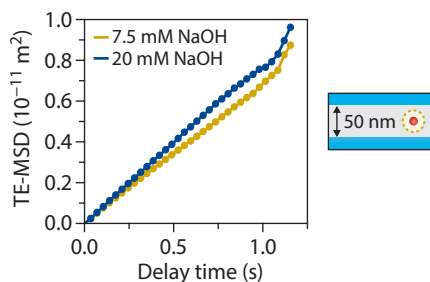
Figure 4.8 • Time–ensemble-averaged mean squared displacement (TE-MSD) curve of trajectories with a span between 25 and 34. Both TE-MSD curves are linear.
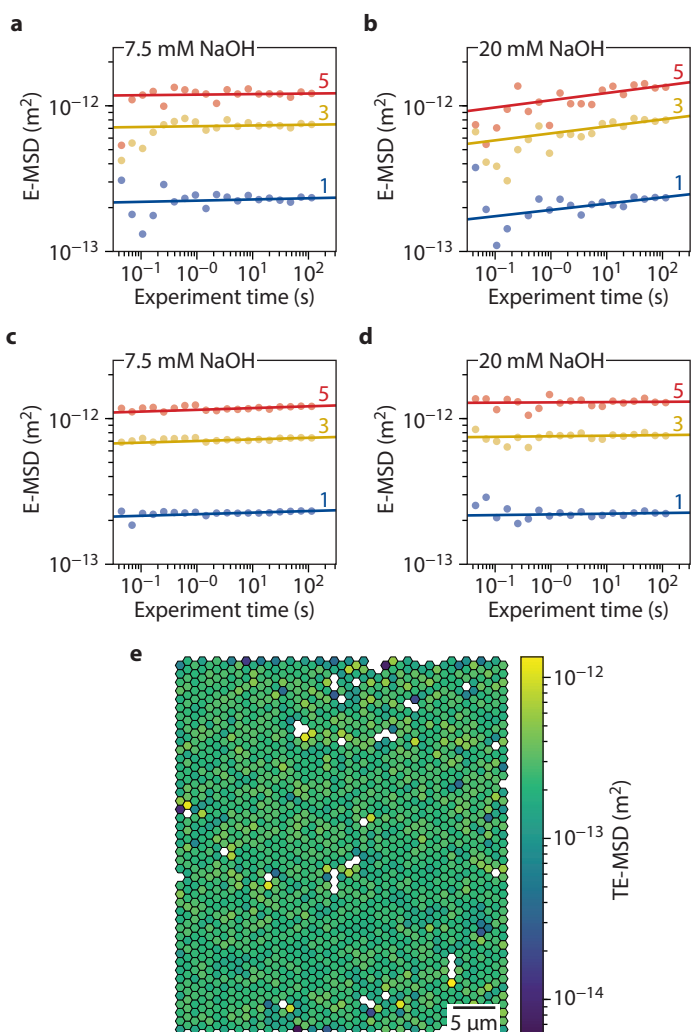
Figure 4.9 • (**a–d**) Time–ensemble-averaged mean squared displacement (TE-MSD) as a function of the experiment time for delay times of one (blue), three (yellow), and five frames (red dots). Both a 7.5 mM NaOH concentration (panels **a,c**) and 20 mM NaOH concentration (panels **b,d**) are shown for one video (panels **a,b**) and averaged over all (ten) videos (panels **c,d**). The slope of the individual TE-MSD with the same delay time as a function of experiment time was obtained with a weighted linear fit in the log–log plot (solid lines). All slopes were close to zero, which indicates no ergodicity breaking. Only trajectories after artefact removal were considered (see Methods). (**e**) Spatial distribution of the average TE-MSD in panel **a** for a delay time of one frame. Each hexagonal bin is 1 μm in size. The centre of mass of each pair of consecutive localisations within a trajectory (i.e., localisation of displacement) was used for the binning. Only bins with ten and more displacements are displayed. Note that the TE-MSD is displayed with a logarithmic colour scaling.

of the fitted slopes goes towards zero, we show the same analysis for all ten videos in Figure 4.9c,d. Despite variations in individual videos, the slopes average to a value close to zero, excluding anomalous diffusion as a result of time-dependent diffusion. Further, we investi-

Figure 4.10 • (**a**) Diffusion coefficients fitted from the time-averaged mean squared displacement of individual trajectories. (**b**) The diffusion coefficient as a function of the trajectory span for quantum-dots probes at 7.5 mM and 20 mM NaOH concentration. The span is defined as the number of frames between the first and last localisation of the trajectory. The bandwidth is ten frames, which means that a span of ten frames constitutes trajectories with a span of 5–14 frames. The diffusion coefficient was obtained from a linear fit of th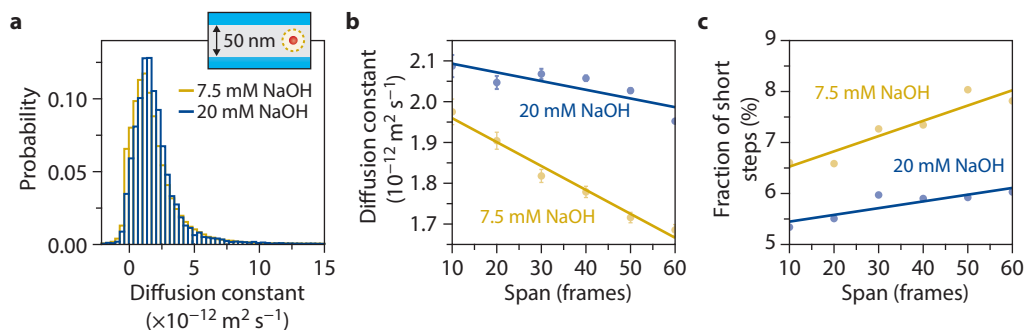e time–ensemble-averaged mean squared displacement as a function of delay time. The error bars indicate the standard error in the fit of the diffusion coefficient, and the solid lines are a linear fit to the plotted data points. (**c**) The average fraction of short displacement steps (< 139 nm) per trajectory as a function of the span of the trajectories in panel **b**. The solid lines are a linear fit to the shown data points.

gated whether there is space-dependent diffusion via the spatial distribution of the TE-MSD at a delay time of one frame (Figure 4.9e). The spatially homogeneous distribution of the TE-MSD does not indicate the occurrence of weak ergodicity breaking on the tens-of-micrometre length scale. We conclude from this distribution and the absence of temporal aging effects that the fluorescent probes do not exhibit anomalous diffusion and can be described by a normal diffusion model.

Using the 2D model pore, we investigated the diffusion coefficient of the PEG-coated QDs in conditions where trapping frequently and rarely occurs, respectively in 7.5 and 20 mM NaOH. The transient trapping events are accounted for in the analysis of the diffusion coefficient, and its value can be considered as describing an effective diffusivity (excluding long trap events). The distribution of the diffusion coefficient of individual trajectories was shifted to slightly lower values in 7.5 mM than in 20 mM NaOH conditions (Figure 4.10a). The same trend was observed at the ensemble via TE-MSD analysis. We found that the diffusion coefficient and the span of a trajectory are correlated in this dataset, which is particularly pronounced in 7.5 mM NaOH conditions (Figure 4.10b). The correlation is likely an artefact of the linking algorithm, where trajectories with short displacement steps have a higher probability to be successfully linked (Figure 4.10c), which is described in detail in Section 2.2.4. Thus, the computed average diffusion coefficient of the full dataset is dependent on the weighing of the trajectories. Here, we first computed the average diffusion coefficient per span, which we weighted by the number of displacements of the trajectories contributing to that span. Using a normal diffusion model, we found a diffusion coefficient parallel to the plane walls of the pore of $1.816 \pm 0.009 \times 10^{-12}$ $m^2\ s^{-1}$ and $1.963 \pm 0.004 \times 10^{-12}\ m^2\ s^{-1}$ in 7.5 mM and 20 mM NaOH, respectively.

The difference in the average diffusion coefficient at the measured pH could be due to the different QD size or trap behaviour. We found that diffusion was $7.5 \pm 0.6\%$ slower in 7.5 mM compared to 20 mM NaOH conditions. Based on the computed drag force in confinement, a slowing down of 5.4% (8.5%) for a QD positioned 0.50 (0.25) pore diameter from the wall is expected.[157] The agreement in the computed and measured diffusivity ratio indicates that
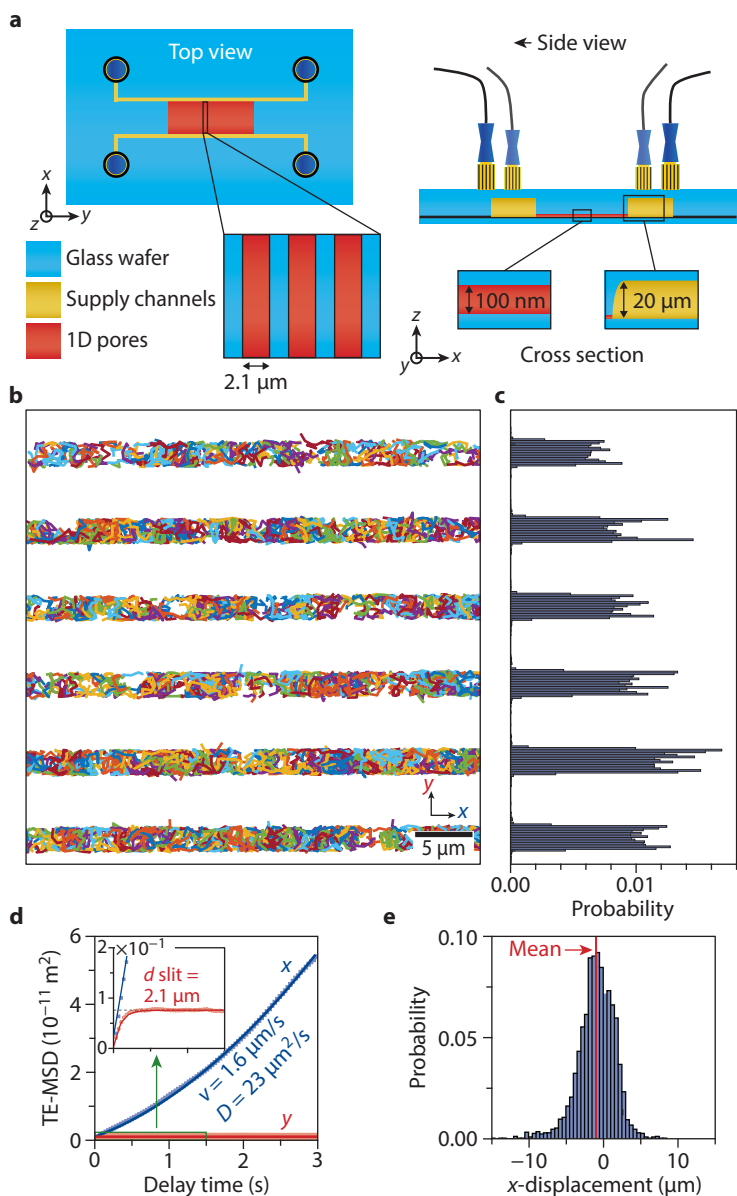
Figure 4.11 • (**a**) Schematic representation of the microfluidic device consisting of lithography-patterned one-dimensional pores. (**b**) Overlay of trajectories obtained over 4000 frames obtained over 140 s within pores in panel **a**. Quantum dots were tracked in 25/75 (m/m) glycerol/water. Trajectories representing QD clusters were removed (see Methods). (**c**) Histogram of *y*-coordinate localisations aligned with panel **b**. (**d**) Time–ensemble-averaged mean squared displacement (TE-MSD) in *x* and *y* as a function of time of the trajectories in panel **b**. The solid lines show the fit of a normal diffusion model accounting for flow in *x* and a confinement diffusion model in *y*. The velocity *v* and diffusion coefficient *D* were obtained from the fit with the normal diffusion model, and the slit diameter *d* was obtained from the confinement diffusion model. (**e**) Histogram of the total displacement in the *x*-direction for all trajectories. The distribution has a tail on the

negative side and a mean value below zero. In a system without flow, a symmetric distribution mean-centred at zero displacement would be expected.

the diffusion behaviour can be mainly explained by the size of the QDs. A large effect of trapping on the measured diffusivity would have been evident from a larger slowing down in 7.5 mM NaOH conditions than purely based on the computed hydrodynamic drag. To better understand the difference diffusivity in the measured conditions, three-dimensional particle coordinates or a simulated distribution of the distance between the QD and pore wall should be available. The drag force of the QDs was estimated using the 2D-pore depth and the hydrodynamic radii of the QDs measured in bulk (Figure 4.4c).[157] Because the QD size in free solution was determined in 85/15 (m/m) glycerol/water, whereas the experiments in the 2D pore were done in 50/50 glycerol/water, we assumed that the QD radius was the same in both solutions. Altogether, our analysis indicates that the diffusivity of the particles is governed by their size.

4.2.4 • Pore-space mapping of complex pore spaces

Based on the diffusion and trapping behaviour of PEG-coated QDs in confinement, we can now design an experiment to map the pore space of a catalyst particle. We found that long trap events resulted in undesired blind spots in the pore-space map. These trap events could be supressed in 20 mM NaOH conditions. Short trapping events rarely occurred in these conditions, allowing rapid exploration of the pore space by the QD probes. Furthermore, it was found that the diffusion coefficient could be estimated using a normal diffusion model. We demonstrate how the QD probes can be applied to map the pore space of a well-defined one-dimensional pore. We further show pore-space mapping of a silica-based polymerisation catalyst particle.

We fabricated a set of one-dimensional (1D) slit-shaped pores similarly to our 2D model pore (Figure 4.11a). The slit was only accessible from two opposing ends and had a depth of

100 nm, creating a 1D pore with dimensions of $0.1 \times 2 \ \mu m^2$. Note that the depth of the 1D pore is 2× larger than the depth of our 2D model pore discussed previously. In the 1D pores, the QD trapping was negligible, which allowed for characterisation of the pore system. An overlay of the trajectories recorded over 140 s (4000 frames) is shown in Figure 4.11b. The individual channels can be readily discerned, and the width of the channels in the overlay matches their width on the lithography mask. Some localisations appear outside the pore, which are random localisations found in the camera noise by the localisation algorithm. A histogram of the occurrence of localisations along the length of the 1D pore is displayed in Figure 4.11c. The abrupt decrease in localisations beyond the slit wall in y indicates that the QDs are closely confined in the pores. The QDs appear to be localised more frequently close to the pore wall in the y-direction, possibly due to increased hydrodynamic drag at these locations resulting in a longer residence time.

In Figure 4.11d, we plotted the TE-MSD in x and y as a function delay time to characterise the confinement. From the plateau of the y-TE-MSD curve, we estimated a 1D-pore diameter of 2.1 μm. The x-TE-MSD curve was parabolic and could be described by a normal diffusion model accounting for flow along the direction of the pores.[87] The presence of flow was confirmed by the mean linear displacement of each trajectory, which showed a preferential movement in x (Figure 4.11e). In these conditions, the negligible transient trapping allowed for quantification of the flow directly from the fit of the x-TE-MSD, which we found to be 1.6 μm s^{-1}. Using QD probes in nearly non-trapping conditions, we were able to map the accessible pore space and quantify flow in a well-defined 1D pore.

Next, we mapped the pore space of a real-life silica-supported polymerisation catalyst. The catalyst particles were dispersed in a dry liquid cell before the QD solution was added, and the
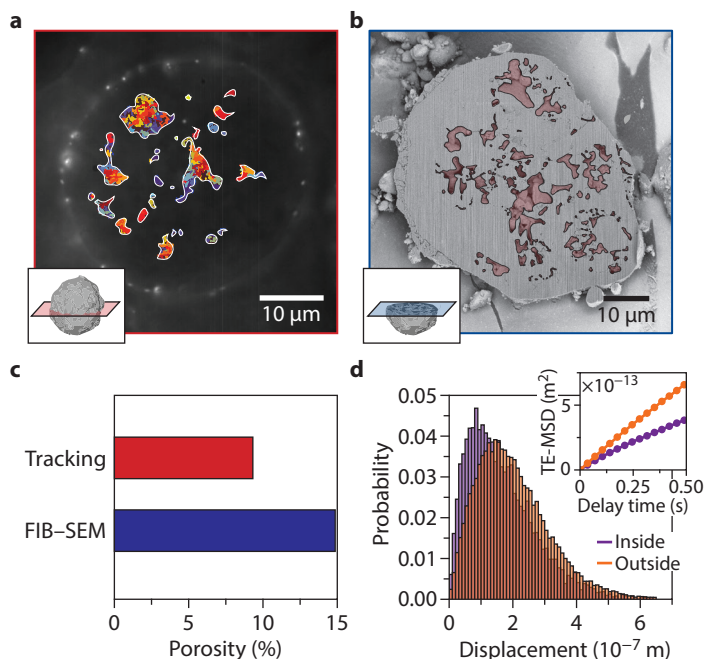
Figure 4.12 • (**a**) Trajectories overlaid with the summed fluorescence intensity obtained within a silica-based polymerisation catalyst support over 70 s. The trajectories indicate the accessible pores. The segmented pore area is marked by the white outlines. Quantum dots were tracked in 85/15 (m/m) glycerol/water. (**b**) Focused ion beam–scanning electron microscopy (FIB–SEM) imaging of a particle of the same batch as in panel **a**. The segmented pore area is marked by the red overlay and black outlines. (**c**) Accessible porosity of the particle in (panel **a**; tracking) and total porosity of the particle in (panel **b**; FIB–SEM) based on the segmented areas. (**d**) Histogram of displacements of trajectories in panel **a** for a delay time of one frame (35 ms). The time–ensemble-averaged mean squared displacement (TE-MSD) is shown in the inset.

cell was sealed. The liquid cell was left to equilibrate for 10 min prior to the measurement. Three-dimensional resolution was achieved automatically as QDs outside the focal volume (depth 800 nm) were not localised due to their diffuse fluorescence signal. Figure 4.12a shows the mapped accessible pore space overlayed on the fluorescence intensity averaged over all frames. All trajectories are in the centre of the particle, suggesting that most of the accessible porosity is in this region. Some pores are smaller than the diffraction limit (~250 nm) and their size would have been overestimated when mapped with confocal laser scanning microscopy. We imaged the cross section of a catalyst particle of the same batch prepared via focused ion beam (FIB) milling using scanning electron microscopy (SEM) (Figure 4.12b).

The morphology of the pores matches qualitatively: there are large pores in the inner particle as well as a denser crust in the outer part. The porosity observed via FIB–SEM is larger (15%) than the one mapped with single-particle tracking (9%; Figure 4.12c). As SMLM only probed the accessible porosity, it is likely that this difference is due to inaccessibility of some pore domains in the particle. Nevertheless, we cannot exclude that there are statistical differences of this magnitude between single catalyst particles of the same batch nor that the tracking time was too short to fully explore the entire pore space of the catalyst.

The diffusion dynamics of the QDs have changed considerably as result of their confinement. This is evident from the histogram

of displacements plotted for the trajectories inside and outside the catalyst particle in Figure 4.12d. Even at the shortest measured delay time, that is, one frame, we found that the displacements are shorter inside the catalyst particle than outside. The limited distance over which a QD can travel before it hits a pore wall as well as the increased viscosity in the pore contribute to the shorter displacements. At longer delay times, the mean travelled distance is even further reduced as a result of confinement and a flattening of the TE-MSD is observed (inset Figure 4.12d).

4.3 • Conclusions

A well-defined 2D model pore to characterise the diffusion and trap behaviour of individual QD probes in confinement was developed. The geometry of the model pore was pivotal for the measurement of long single-QD trajectories, which allowed for detailed probe characterisation. We found that QD trapping could be reduced via the solution pH, likely because of a stronger electrostatic repulsion between the QD and pore wall. Using the 2D model pore, we could even quantify short, transient trap events, and found that these were almost completely suppressed in 20 mM NaOH. No evidence was found that trapping at the pore wall had a large effect on the measured QD diffusivity, and the diffusion coefficient was mainly dependent on the size of the QD. We successfully demonstrated the use of QDs in nearly non-trapping conditions for pore-space mapping of a silica 1D-pore network and polymerisation catalyst particle—all with tens of nanometres resolution. Further research should be focused on the systematic characterisation of the relation between the measured diffusion coefficient in the model pore and the pore size, pore shape, and probe–wall interactions. This could provide insight in the factors that promote mass transport through porous solids and/or used to validate diffusion models for these materials. The application of our model-pore platform is not limited to pure silica systems since the device can be modified for the characterisation of fluorescent probes in a multitude of metal oxide and carbon-based pore environments. Finally, this approach paves the way for the characterisation of fluorescent probes at various temperatures.

4.4 • Contributions & acknowledgements

4.5 • Methods

4.5.1 • Experimental

Chemicals and materials. CdSe/ZnS core–shell quantum dots (QDs) with polyethylene-glycol functionalisation (900246-250UL, Sigma-Aldrich), citric acid (≥ 99.5%, Sigma-Aldrich), ES70X silica (PQ Corporation), glycerol (≥ 99.5%, Sigma-Aldrich), 170 μm and 500 μm thick MEMpax wafers (Schott), phosphoric acid (H_3PO_4, Sigma-Aldrich), resazurin sodium salt (~80%, Sigma-Aldrich), sodium chloride (≥ 99%, Sigma-Aldrich), sodium hydroxide (analysis grade, Merck KGaA), and urea (≥ 99%, Sigma-Aldrich). All chemicals were used as received with no further purification except water, which in all cases was purified through a Milli-Q system to a resistivity of 18.2 MΩ·cm.

Carbon-dot synthesis. Resorufin/resazurin-embedded carbon dot (CD) nanoparticles were prepared with the following procedure. First, 40 mg of urea, 20 mg of citric acid, and 20 mg of resazurin sodium salt were mixed in a 10 mL glass vial. The vial was heated up to 250 °C for 15 min under stirring to pyrolyse and carbonise the mixed precursors. After cooling, 5 mg of the obtained black pow-

der was mixed in 10 mL water. Finally, the solution was dialysed using a 12.4 kDa membrane (D0530, Sigma-Aldrich) against deionised water for 1 week in order to remove unreacted small molecules and resorufin/resazurin.

Nanoparticle characterisation. Fluorescence spectroscopy was performed using a home-built setup equipped with a 405 nm laser and 520 nm long pass filter for excitation. The fluorescence emission was collected under a 90° angle with an Ocean Optics HR4000 spectrophotometer. The zeta potential was measured with a Malvern Zetasizer Nano ZS using a folded capillary zeta cell (DTS1070, Malvern). The average value over a series of five measurements was reported.

Microfluidic device fabrication and characterisation. The one-dimensional (Figure 4.11a) and two-dimensional (Figure 4.2a) pores were patterned in 500 μm thick MEMpax wafers (Schott). To avoid underetching, a 15 nm Cr layer was first sputtered on the wafer with a home-built T'COathy system (MESA+, NanoLab). A positive photo resist (Olin OilR908-17) layer was spin-coated on top and locally exposed with UV light using a lithography mask (EVG®620 NT). After removing the exposed photoresist, the wafer was submerged in a Cr etchant. Then, the glass in the UV-exposed area was etched by submerging the wafer with 1% buffered HF, creating the model pores. The supply channels were patterned in a similar way, but 25% HF was used for their etching. The inlet holes were also lithography-patterned and powerblasted in the wafer. A second, 170 μm MEMpax thick wafer (Schott) was thermally bonded to the first wafer at 625 °C. The thickness of the second wafer is within the range where the microscope objective corrects most optimally for optical aberrations.

The etched wafer was characterised prior to bonding. The depth of the two-dimensional pore was measured with a stylus profilometer (DektakXT, Bruker) and the surface roughness was mapped with atomic force microscopy (Dimension FastScan, Bruker).

Microfluidic device loading. Prior to fluorescence microscopy, the microfluidic device was placed in dedicated chip holder (Figure 4.13a,b) and loaded with a fluorescent probe solution with a syringe pump (kdS scientific) at a flow rate of 10 μL/min. Microfluidic connectors and fittings (IDEX Health & Science) as well as plastic tubing (Avantor Fluid Handling) and fused silica capillaries (Molex) were used to transport the liquid from the syringe into the powder-blasted inlet holes of the microfluidic chip (Figure 4.13c–e). After loading, the system was sealed with caps (IDEX Health & Science) to avoid evaporation during imaging (Figure 4.13c).

Fluorescence microscopy. Single-particle tracking experiments were performed on a home-built fluorescence microscope. This setup consisted of a Nikon Ti-U inverted microscope equipped with an oil-immersion objective (Nikon CFI Plan Apochromat Lambda 100×, NA 1.45). The excitation light source was a 405 nm (PicoQuant D-C-405) or 561 nm diode laser (PicoQuant LDH-D-TA-560B) operated in continuous wave and was focused on the back focal plane of the objective with a 150 mm achromat lens. The 561 nm laser side bands were removed with a clean-up band-pass filter, and the light was led through a linear polariser followed by a lambda ¼ plate to obtain circularly polarised light through the objective. The lasers were used in conjunction with appropriate dichroic and long-pass mirrors as well as a 585/40 nm band-pass filter to remove background from the fluorescence emission signal. The filtered emission signal was collected with an electron-multiplying charge-coupled device (EMCCD) camera (Andor iXon Ultra 888) operated at a gain of 300, exposure time of 30 ms, and frame time of 35 ms.

The QDs were 1000× diluted from the stock (4 μM in H_2O) to reach a 50/50 (m/m) glycerol/water mixture unless otherwise stated. The dialysed carbon-dot aqueous suspension was 100× diluted from the stock to reach a 50/50 (m/m) glycerol/water mixture. To prepare the carbon dots in slightly acidic conditions, 1M H_3PO_4 acid was added to obtain a 10 mM concentration, whereas 1M NaOH was added to the QD suspension to obtain slightly basic conditions of 7.5 mM and 20 mM NaOH. Only in the 7.5 mM NaOH QD suspension, additional NaCl was added to a concentration of 2.5 mM. The ES70X silica catalyst particles were placed in a 25 μL Gene Frame (Thermo Scientific) liquid cell and 20 μL QD solution was added. The liquid cell was left to equilibrate for ten minutes. To make sure that the recorded trajectories were located within the
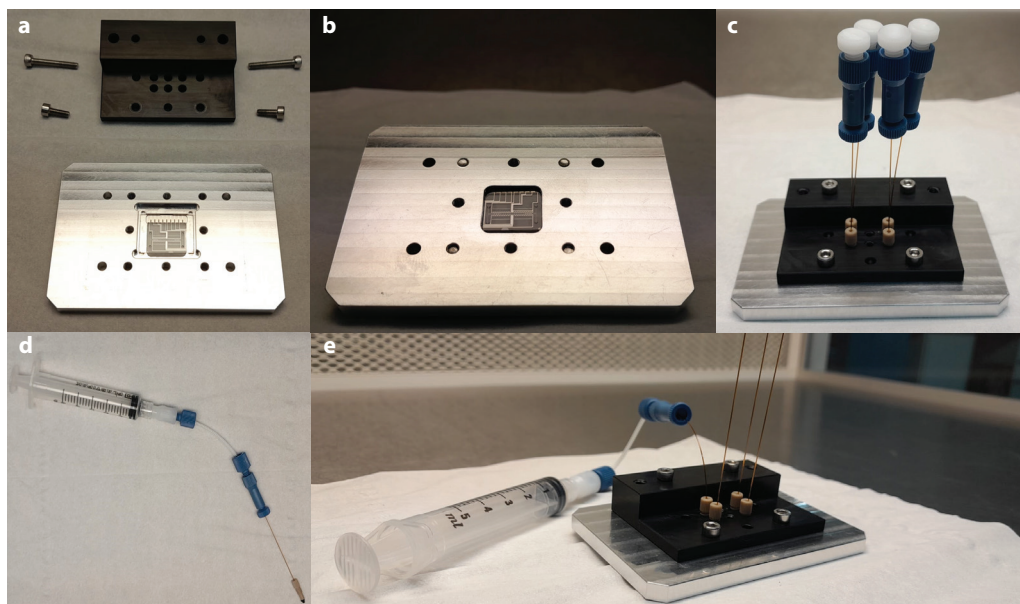
Figure 4.13 • (**a**) Microfluidic device placed in the chip holder before mounting. (**b**) The oil-immersion objective can approach the chip through the shown hole from below. (**c**) Sealed system after fluorescent probe solution loading. (**d**) Microfluidic connections, fitting and tubing used to transport the liquid from the syringe to the chip. (**e**) Syringe connected to chip through microfluidic device.

catalyst pores, we focussed in the centre plane of the catalyst particle.

Focused ion beam–scanning electron microscopy (FIB–SEM). FIB–SEM was done with a FEI Helios NanoLab G3 UC scanning electron microscope, following procedures from the literature.[155] For each experiment, the catalyst sample was dispersed onto double-sided adhesive, conductive carbon tape, which was attached to an aluminium SEM stub. Using a Cressington 208HR sputter coater, a Pt coating of ~6 nm was applied. During the process of FIB cutting, slices were milled horizontally to the SEM stub surface using a 45° angled SEM stub at a suitable stage tilt angle. Cross-sectional SEM images were recorded in backscattered electron mode at 2 kV and 0.1 nA using a through-the-lens detector and an immersion lens.

4.5.2 • Data processing and analysis

Localisation and tracking. The recorded fluorescence microscopy time-lapse movies were analysed with the DoM plugin v.1.2.0 for ImageJ.[78,139] The localisation of fluorescent nanoparticles was done by independent classification of each frame into emissive spots and background. A list of initial emitter positions was determined with a sub-diffraction limited spatial resolution by fitting a two-dimensional Gaussian using the Levenberg–Marquardt least-squares algorithm. The localisation was performed with a standard deviation of 2.6 pixels and signal-to-noise ratio of 2.3. For trajectory analysis, particles were allowed to blink (i.e., it is fluorescing intermittently) for a maximum of one frame (35 ms). A maximum distance between consecutive localisations of 16 pixels (1.39 μm) was used as constraint (one pixel, 87 nm for the carbon dots). The pixel jump was 10 pixels (0.87 μm) for the mapping and 17 pixels (1.47 μm) for the mean squared displacement analysis in the one-dimensional pores. In the polymerisation particle, the localisations were linked with a pixel jump of five pixels (433 nm) and a blinking gap of 50 frames (1.75 s).

1. Set evaluation window

2. Compute the *largest* displacement *R* from first localisation to others in evaluation window

4. If probability Ψ < threshold Ψ_c, mark all localisations in evaluation window as "trapped". Repeat for all windows

Frames

3. Compute probability Ψ from *R*

Figure 4.14 • Schematic representation of the trap analysis in four steps. (**1**) The evaluation window (yellow arrow) is a sliding window starting at the first localisation (grey circles). Only window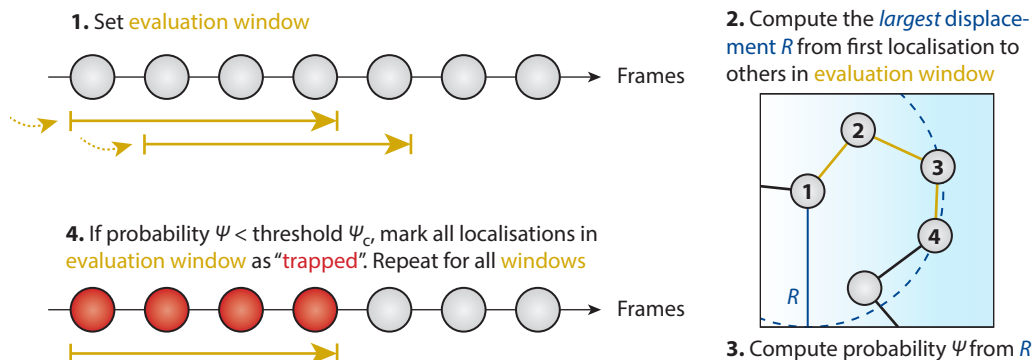s spanning exactly the window length *n* are considered, *n* = 4 in this example. Steps **2–4** are performed for each evaluation window in the trajectory. (**2**) All displacements from the first localisation to all other localisations in the evaluation window are computed and the largest displacement *R* is found. (**3**) The largest displacement *R* is used to compute the probability ψ (Equation 4.2). (**4**) All localisations in the sliding window are marked as trapped if ψ is smaller than the threshold ψ_c. Repeat the procedure for all evaluation windows.

Removal of trajectory artefacts, clusters or long trap events. To remove all trajectories that could have been corrupted by artefacts (see discussion Figure 4.5), we adopted the following procedure. First, the intensity average of the time-lapse recording over all frames was calculated with ImageJ. The coordinates of the long trap events (immobile particles) were determined using ImageJ DoM plugin v.1.2.0 with a standard deviation of 2.0 pixels and signal-to-noise ratio of 30.[78,139] All trajectories containing at least one localisation closer than 433 nm (five pixels) to a localised particle were discarded.

In the one-dimensional model pore, a fraction of the trajectories contained frequent transient trap events and moved considerably slower than the rest of the trajectories. The number of these kind of trajectories increased with a pore depth from 100 to 150 nm. We believe that these trajectories represent QD clusters. These trajectories were filtered out in mean squared displacement analysis by removing all trajectories with a diffusion coefficient $< 1.29 \times 10^{-12}$ m^2 s^{-1}.

In Figure 4.12a,c,d, trajectories with $\geq$ 100 localisations and a minimum bounding circle radius $\leq$ 433 nm were considered as immobile and were excluded from analysis.

Diffusion analysis. Diffusion analysis and plotting were done in MATLAB (The MathWorks) using the DiffusionLab software presented in Chapter 3. Only trajectories with at least five localisations were considered to ensure sufficient displacements per trajectory for mean squared displacement (MSD) analysis and to remove unphysical trajectories originated from incorrect localisations. MSD analysis on individual trajectories was done including the first 10% of the delay times and at least four points. To determine the QD hydrodynamic radius from the diffusion coefficient, only the first four points were used in the fit of the time–ensemble-averaged MSD because the number of trajectories contributing to the MSD was constant within this fit range. The normal, normal with flow (directed), and confinement diffusion models were used as implemented in DiffusionLab.

Trap analysis. We identified transient trapping by evaluation of the probability that an unconstrained diffuser with a known diffusion coefficient would spontaneously stay within a certain spatial domain.[168–170] When this probability is smaller than a certain threshold value, it is unlikely that spontaneous fluctuations make the diffuser appear immobile. Then, the trajectory—or segment thereof—is considered *trapped*. The probability ψ that

a unconstrained diffuser remains in a region $r < R$ for all times $\leq t$ given its diffusion coefficient D was solved by Saxton et al., which is for $Dt/R^2 > 0.1$ the relation[168]

$$\log \psi = 0.2048 - 2.5117 \left(\frac{Dt}{R^2} \right) \qquad (4.2)$$

for a fixed D and circle radius R. The probability ψ decreases for an increased t because the diffuser has more time to explore the space, which reduces the probability that it spontaneously appears trapped. The diffuser is considered trapped if the probability ψ is smaller than a threshold ψ_c. We implemented this approach using a sliding window of n frames with a $t = (n-1)t_{\mathrm{frame}}$ and t_{frame} the frame time. The algorithm is depicted in Figure 4.14. The selection of the threshold ψ_c is discussed below. We reported
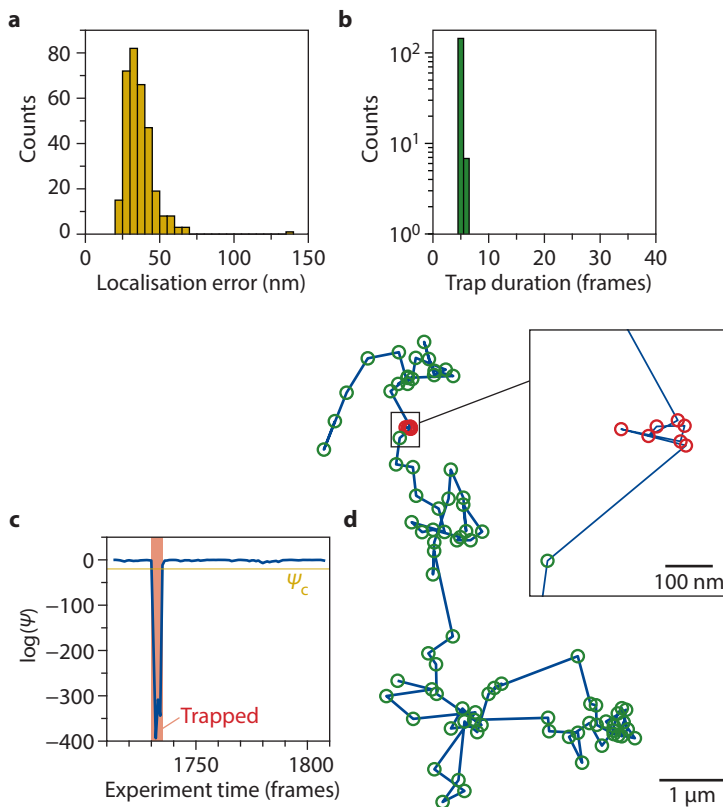
Figure 4.15 • (**a**) Histogram of the experimental localisation error as determined from the standard deviation of the localisations in x and y of individual trajectories representing immobile quantum dots (QDs). All trajectories with 100 or more localisations and a minimum bounding circle radius of maximum 400 nm were considered. The QD trajectories were recorded in slightly basic conditions (7.5 mM NaOH). (**b**) Histogram of the adsorption times of trajectories simulated with two-dimensional normal diffusion with a diffusion coefficient of 2×10^{-12} m^2 s^{-1} and a localisation error of 36 nm. The sliding window time $n = 5$ frames restricted the detection of adsorption times with a duration $n < 5$ frames. (**c,d**) Demonstration of the adsorption analysis on an individual trajectory recorded from QD diffusion in the two-dimensional pore (7.5 mM NaOH). The trajectory is shown with the individual localisations marked either as non-adsorbed (green) or adsorbed (red) in panel **d**. The logarithm of the probability ψ is given as a function of the experiment time for the trajectory in panel **c**. A drop in ψ below the adsorption threshold ψ_c marks the adsorbed time domain, which matches the red localisations in panel **d**.

the trap durations as the number of frames in the segment (i.e., $t + t_{frame}$). The minimum length of a segment with trapping is equal to n frames.

Selection of the threshold for trap analysis. We optimised the threshold ψ_c for our experiment using simulations of unconstrained diffusers (see Trap analysis). The threshold ψ_c is dependent on the diffusion coefficient and the sliding window time, and it must be optimised for every combination thereof. To find a value of ψ_c that did not include a larger amount of false positives, i.e., localisations incorrectly marked as trapped, we lowered ψ_c until a negligible number of false positive were present in simulated trajectories of unconstrained diffusers (following the protocol of Vrljic et al.[170]). For this, we used the quantum-dot (QD) diffusion in the two-dimensional pore as reference experiment to set ψ_c. Faster diffusion in the carbon-dot dataset would allow for a less strict threshold; however, we used the same ψ_c as in the QD dataset for comparability. We simulated two-dimensional Brownian motion with a displacement probability in x and y given by a normal distribution with a standard deviation of $\sqrt{2Dt}$, with D the diffusion coefficient and t the delay time.[144] We assumed that the error in the localisations is normally distributed with a standard deviation of σ. We used simulation parameters that matched the experiment, that is $D = 2 \times 10^{-12}$ m^2 s^{-1} and $\sigma = 36$ nm, and simulated 1000 trajectories, each with 1000 localisations. The localisation error used in the simulation was estimated from the experimental trajectories of fully trapped particles (Figure 4.15a). The mean of the distribution of the localisation error was taken for the simulation. We found that a sliding window of $n < 5$ frames required extremely low ψ_c, which resulted in poor performance; therefore, we used $n = 5$ throughout the

analysis. To use a short sliding window, we accepted a small number of false positives and found $\psi_c = 2 \times 10^{-9}$ (i.e., $Dt/R^2 = 8.05$ and $R = 187$ nm) being a good trade-off between a low number of false positives and sufficiently high sensitivity to trapping.

The short sliding window provided the highest time resolution possible, which maximises the probability to find trap events in conditions with little QD trapping (as expected in 20 mM NaOH conditions). A histogram of the trap duration in the simulation is shown in Figure 4.15b. The sliding window of 5 frames restricted the detection of trapping times shorter than five frames and we cannot detect trap events shorter than this time. The measured trap events are false positives as no QD trapping was included in these simulations. We demonstrate the trap analysis for an experimentally obtained trajectory with short, transient trapping in Figure 4.15c,d. Overall, the number of false positives in simulations is at least an order of magnitude lower than the total number of measured trap events in experiment. This indicates that in both 7.5 mM and 20 mM NaOH conditions, a significant number of trap events is recorded.

Segmentation of the pore space. The accessible pore space was estimated by segmentation of the projection of all trajectories within a single time-lapse recording. The area where probes were localised as well as the total particle area were both segmented manually using ImageJ. The accessible porosity was then estimated by dividing the number of pixels containing trajectories within the particle by the number of pixels that were assigned to the particle. A similar procedure to segment the visible pores was performed to estimate the porosity of the particle cut by FIB–SEM.

4

Chapter **5**

Unravelling channel structure–diffusivity relationships in zeolite ZSM-5 at the single-molecule level

Abstract • The development of improved zeolite materials for applications in catalysis and separation requires understanding of mass transport therein. In this chapter, we track the diffusion of single molecules in the straight and sinusoidal channels of industrially relevant ZSM-5 zeolites. For this, we use a combination of single-molecule localisation microscopy and uniformly oriented zeolite thin films. We observe heterogeneous motion behaviours in zeolite channels with the same geometry. Quantification of the diffusion heterogeneities in the sinusoidal and straight channels shows that the geometry of zeolite channels dictates the mobility and motion behaviour of the guest molecules, which results in diffusion anisotropy. We further study single-molecule diffusion in hierarchical zeolites. The addition of secondary pore networks primarily enhances the diffusivity through the sinusoidal zeolite channels, which alleviates diffusion limitations in microporous zeolites.

5.1 • Introduction

ZSM-5 (Zeolite Socony Mobil–5) was invented by Argauer and Landolt at Mobil Oil Corporation in the 1970s.[172] Historically, the zeolite has been used as additive in fluid catalytic cracking (FCC) particles to boost the yield of olefin products during the FCC process. The impact of its introduction to FCC catalyst formulation was substantial as it directly led to a large increase in the gasoline yield in the 1970s and 1980s.[10,11] Furthermore, ZSM-5 was discovered as catalyst for the methanol-to-hydrocarbons (MTH) process in the late 1970s.[173] MTH is a group of chemical conversion processes that convert methanol into olefins and/or gasoline products. As methanol can be obtained from various carbon sources, such as natural gas, biomass, coal, and even carbon dioxide, it bypasses the need for oil to make high-demand chemical building blocks and products. The MTH process has been successfully applied on an industrial scale. Despite its commercialisation, the challenge remains to steer the reaction towards the desired products.[174,175]

ZSM-5 zeolite has the MFI framework and belongs to the family of zeolites with a pentasil composite building unit (Figure 5.1a). The material contains interconnected sinusoidal (*a*-direction) and straight (*b*-direction) zeolite channels with distinct geometries and slightly different sizes (Figure 5.1b). The two-dimensional pore network comprises straight channels with 5.6-×-5.3-Å-large rings, which are intersected by 5.1-×-5.5-Å-large sinusoidal channels every ~8 Å.[7,8] The pore channels are build up from rings of ten tetrahedra, making it a medium pore-size zeolite.[6–8] The pore or channel structure of zeolites strongly affects the overall performance by imposing diffusion limitations on the guest molecules.[15,176–178] The working lifetime of zeolites in catalysis has been dramatically improved by introducing secondary pore networks to overcome the intrinsic diffusion limit of the zeolite channels. These pore networks consist of meso- and macropores ($\geq$ 2 nm diameter) while leaving the *primary* micropores (< 2 nm diameter) intact.[11,177,179–181]

The selectivity of zeolite-based catalysts (and membranes) is highly dependent on the molecular diffusivity through their channels. Measures to boost catalyst selectivity in zeolites usually come at the price of a lower catalyst utilisation as these properties are generally two sides of the same coin.[182] A clear example is the selectivity towards *para*-xylene in xylene separation processes and toluene methylation reactions using ZSM-5 zeolites. The selectivity can be enhanced in some degree by maximising the diffusion resistance of xylene in the ZSM-5 pores, which favours the diffusion of the *para* isomer over other isomers because of its smallest molecular size. However, this comes at the expense of catalyst utilisation due to slower mass transport through the zeolite.[182–186] Similarly, larger ZSM-5 crystals exhibited a higher selectivity towards *para*-xylene as a result of the longer diffusion length through the zeolite pores.[183] An alternative approach is the selective opening of the sinusoidal channels on the zeolite's outer surface, which resulted in an excellent *para*-xylene selectivity in toluene methylation reactions.[184] The smaller, zigzag-shaped sinusoidal pores impose a larger diffusion resistance on the xy-
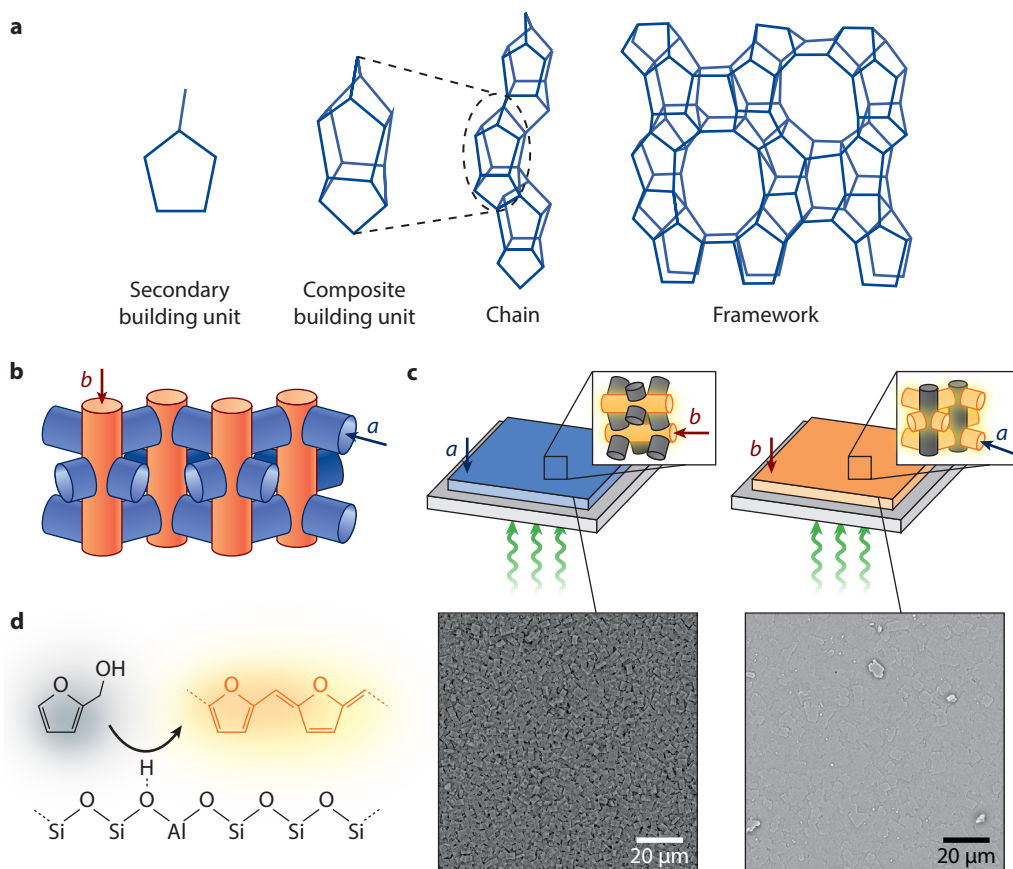
Figure 5.1 • (**a**) Structural organisation of the MFI zeolite framework type. The edges are the silica or alumina tetrahedra, which are bridged by oxygen atoms. The framework is built up from the 5-1 secondary building unit. A pentasil composite building unit assembles into a chain, which can be recognised in the framework structure. (**b**) Micropore topology of the MFI zeolite framework. Arrows indicate the sinusoidal and straight zeolite channels aligned in the crystallographic *a*-direction and *b*-direction, respectively. (**c**) Schematic for probing the diffusivity of molecules within single-oriented zeolite channels using single-molecule localisation microscopy. Only in-plane fluorophores (orange channels) can be efficiently excited by the circularly polarised laser light, and therefore diffusivities within the straight and sinusoidal zeolite channels were obtained selectively using *a*-oriented and *b*-oriented zeolite ZSM-5 films. A scanning electron microscopy image of either ZSM-5 film is shown below. (**d**) Formation of fluorescent products (red) from the acid-catalysed oligomerisation of furfuryl alcohol (black) on a Brønsted-acid site.

lene molecules than the straight pores, which is beneficial for *para*-xylene selectivity. The introduction of a secondary pore network to improve catalyst utilisation would counteract the discussed selectivity effects by reducing the diffusion length and/or negate selective accessibility of one channel type. These examples highlight the necessity to understand channel structure–diffusivity relationships for the rational improvement of zeolite design as these relations are strongly related to the zeolites' selectivity, utilisation, and even lifetime.[187]

Great efforts have been dedicated in the past decades to the quantification of molecular mobility in zeolites,[15,188] using a number of techniques, such as uptake measurements,[189] pulsed-field-gradient nuclear magnetic resonance (PFG NMR) spectroscopy,[178,190–193] quasi-elastic neutron scattering[194–196], microimaging,[30,37,197] and molecular simulations (see also Section 2.1.2).[198–200] It was found that the zeolite channel geometry often dictates the diffusivity. For instance, up to an order of magnitude differences in diffusion coefficients were observed for the straight and sinusoidal zeolite channels of zeolite ZSM-5.[189,191,192] However, a mechanistic understanding of this relationship remains elusive.

To better understand channel structure–diffusivity relationships, it is of utmost importance to capture diffusion and the heterogeneities therein at the single-molecule level. The study of single-molecule catalytic turnovers revealed intracrystalline heterogeneities in the reactivity of large zeolite ZSM-5 crystals.[52] Moreover, diffusion in porous solids is heterogeneous, and adsorption of the diffusing molecules and nanoparticles occurs frequently, as we have observed at the single-nanoparticle level in Chapter 4.[55,61,106,120,121] This underlines that the microporous domain in zeolites is intrinsically heterogeneous, owing to their framework defects, heterogeneous distribution of adsorption sites, and channel connectivity.[201,202] In this chapter, we gain a deeper mechanistic understanding of channel structure–diffusivity relationships in zeolite ZSM-5 by measuring the heterogeneous diffusion dynamics of single molecules.

5.2 • Results and discussion

5.2.1 • Single-molecule tracking and classification

We quantified diffusion heterogeneity in microporous and hierarchical zeolite ZSM-5 at the single-molecule level. The molecular motion was captured selectively in the direction of the straight or sinusoidal pores. As shown in Figure 5.1c, this was made possible by combining the recently developed, uniformly oriented zeolite thin films[203] with single-molecule localisation microscopy (SMLM). Fluorescent oligomer molecules were generated in-situ from furfuryl alcohol (FFA) over the Brønsted-acid sites in the zeolite thin films (Figure 5.1d).[204] This approach allowed us to track diffusion of single molecules selectively within the straight and sinusoidal zeolite channels over the a- and b-oriented zeolite thin films, respectively. The reason for this is twofold. First, the maximum absorption and fluorescent emission of molecules is obtained when the electric field of the excitation light is parallel to the dipole moment of the entrapped guest molecules, which for FFA oligomers is along the host channels.[205] Therefore, with plane-polarised laser light, only the molecules within the channels parallel to the observation plane were efficiently excited and tracked. Second, we only measured displacements in the observation plane, which is in the direction of the pore type of interest.

The FFA oligomerisation reaction products can have various lengths. Depending on the size of the conjugated π-system in the oligomer, the light absorption and fluorescence emission colour changes. Only oligomers that are efficiently excited by the laser and emit fluorescence are imaged, which allows them to be tracked. To identify these FFA oligomers, we compared the measured ultraviolet–visible (UV–Vis) absorption spectrum with the calculated UV-Vis absorption bands of oligomers with various lengths (Figure 5.2a). The protonated and neutral oligomer structures used for the calculation are shown in Figure 5.2b. Because no absorption at wavelengths longer than 620 nm was observed, the largest and dominant stable species formed during the FFA oligomerisation was the tetramer oligomer. It is also the tetramer that is the most efficiently excited oligomer since it has an absorption maximum close to the laser excitation wavelength of 560 nm. Note that we assumed in our calculations that the size of the conjugated π-system is equal to the size of the oligomer (see Figure 5.2b). As no red-shifted absorption bands corresponding to larger FFA oligomers were observed, it is not likely that the tetramer conjugated π-system is part of a larger oligomer molecule.[206]

Thus, the diffusion of tetramer FFA oligomers is measured selectively in the tracking experiments described in this chapter.

We localised and tracked the SMLM time-lapse videos to reconstruct the trajectories of the tetramer FFA oligomers. A linear fit of the time-average mean squared displacement (T-MSD) curves of each trajectory in a representative oriented ZSM-5 thin film resulted in a continuous range of diffusion coefficients spanning several orders of magnitude (Figure 5.3a). This shows that guest molecules diffusing through macroscopically uniform zeolite channels have a heterogeneous motion behaviour. These results again highlight the importance of tracking diffusion in zeolites at the single-molecule level.

Further inspection of the individual trajectories revealed three types of trajectories with distinct motion behaviour in the zeolite ZSM-5 thin films (Figure 5.3b). These types are quali-tatively similar to the types observed in Chapter 3: *immobile* molecules remained at or near a single location, while *mobile* ones moved almost constantly with large, up to 200 nm, steps between consecutive frames. Only occasionally these molecules have short moments of impeded diffusion due to their interaction with the surroundings. The third group of molecules displayed *hybrid* behaviour and alternated between mobile and immobile periods with long segments of immobility. The different motion behaviour is clearly reflected in the slope of the T-MSD curve, which is directly proportional to the diffusion coefficient (Figure 5.3c).

The observed two-dimensional diffusion (Figure 5.3b) could be a result of the fluorophores travelling through two or more different zeolite crystal domains oriented in the plane of the film. This is unlikely to occur frequently as the crystal domains are on the order of ~3 μm, therefore the diffusion coefficient would not be severely affected. Moreover, it might be
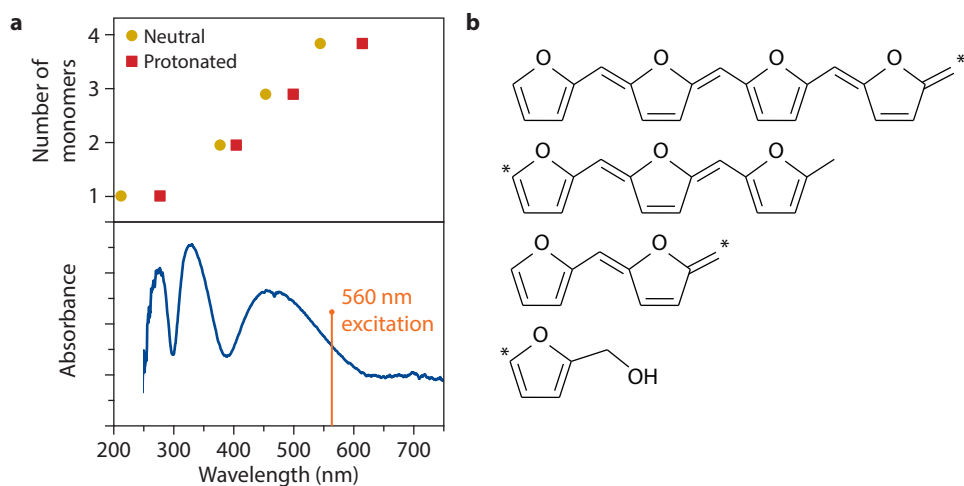
Figure 5.2 • (**a**) Time-dependent density functional theory calculated ultraviolet–visible (UV–Vis) absorption maxima for oligomers trapped in zeolite channels (top) compared with the experimental absorption spectrum of the furfuryl alcohol (FFA) oligomerisation reaction products in a representative ZSM-5 zeolite thin film (bottom). Only computed values for the cis isomer are shown because this isomer had the lowest relative enthalpy in the zeolite channels. The experimental UV–Vis absorption spectrum was measured with UV–Vis diffuse-reflectance spectroscopy. The excitation wavelength used during the single-molecule localisation microscopy experiment is indicated in the spectrum. (**b**) Chemical structure of the FFA monomer and cis oligomers that were used in the computation of the UV–Vis absorption maxima. Both neutral and cationic species were considered. The protonation site is indicated by an asterisk.
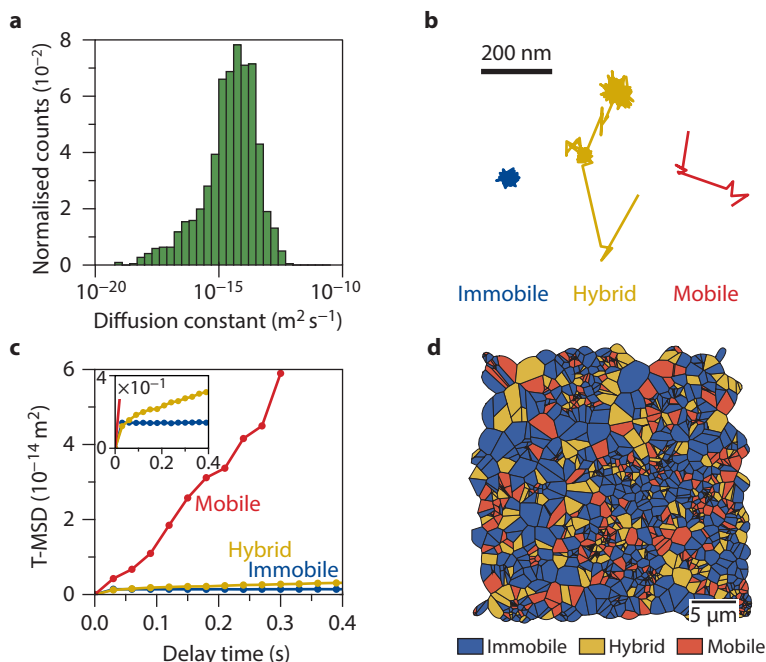
Figure 5.3 • (**a**) Histogram of the diffusion coefficients for all trajectories in the *a*-oriented ZSM-5 thin films plotted on a logarithmic *x*-axis. Fits resulted in a(n) (unphysical) negative diffusion coefficient are not shown. (**b**) Three representative trajectories with immobile, hybrid, and mobile motion behaviours. (**c**) The corresponding time-average mean squared displacement (T-MSD) curves of the trajectories in panel **b**. (**d**) Spatial map of the distribution of trajectories with different motion behaviours. The area assigned to a trajectory is the Voronoi polygon derived from the centres of mass of the individual trajectories.

possible that one molecule transfers from one channel type to the other. Given the length of the molecule, we conjecture that it is unlikely that the molecules frequently change channel type. If they do, they will rapidly leave the zeolite film due to the thinness of the zeolite film (~800 nm), and will not contribute to the measured molecular motion. Furthermore, confinement of molecules within nanometre-sized zeolite domains has been observed in molecular dynamics simulations, and this motion behaviour was coined *extensive local motion*.[207] Because of the spatial resolution of the trajectories, we cannot discriminate between extensive local motion and molecules that are fully adsorbed to the zeolite. Both motion behaviours are subcategories of the term *immobile* used in this work.

Each trajectory was classified as either mobile, hybrid, or immobile based on the trajectory properties following the previously developed approach in Chapter 3. The spatial distribution (Figure 5.3d) of the classified trajectories shows that the diffusion heterogeneity occurs randomly over the sample.

5.2.2 • Is the estimated diffusion coefficient biased?

Before we can compare the diffusivities between the various zeolite ZSM-5 films, we investigated whether the measured diffusion coefficient is limited (i.e., biased) by the tracking process. Depending on the pixel jump value, our tracking algorithm may tend to underestimate the diffusion coefficient of the fastest molecules in the sample (see also Section

2.2.4). These molecules would show large displacements, which the tracking algorithm fails to recognise. When this happens frequently, the probability decreases that all localisations of a single molecule are grouped in the same trajectory leading to an underestimation of the measured diffusion coefficient. This probability is an important parameter, which we coin the *trajectory recognition success probability*, and its derivation can be found in the methods section of this chapter. A probability close to one means that the algorithm can group the localisations correctly, while a probability close to zero shows that it often misses displacements and is not able to group all localisations of a molecule in the same trajectory. We want the algorithm to recognise the full trajectory, so a probability close to one is desired to ensure a correct measurement of the diffusion coefficient.

We found that the trajectory recognition success probability P strongly depends on the diffusion coefficient D and the span of the trajectory. Here, the span of a trajectory is the number of frames between the first and last localisation of the trajectory following the definition introduced in Chapter 4. A probability map of P can be plotted if we assume a constant localisation error, pixel jump, and frame time, which is given in Figure 5.4. Trajectories with a shorter span have a higher probability to be successfully recognised by the algorithm. Furthermore, a close-to-zero recognition probability was found for fast molecules ($D = 10^{-11}$–10^{-12} m^2 s^{-1}), near-perfect detection for slow molecules ($D = 10^{-14}$–10^{-13} m^2 s^{-1}), and a

transition region between $D = 10^{-12}$–10^{-13} m^2 s^{-1}. The transition region is important because it shows the fastest molecules that can be recognised by the tracking algorithm.

To quantitatively compare the experimentally obtained diffusion coefficients, the diffusion coefficient of the fastest molecules should not be underestimated. If this is true, we call the pixel jump *good*—otherwise it is *too short*. We investigated whether the pixel jump is good by comparison of the experimental trajectories with the trajectory recognition success probability map. Every trajectory is a point on the probability map, and from the distribution of trajectories it should be indicative whether the pixel jump is good or too short. The problem is that we do not know the true diffusion coefficient and trajectory span of a measured trajectory. Therefore, we learned how the trajectory behaves near the transition region by looking at simulated trajectories with a known diffusion coefficient and trajectory span.

First, we studied how the distribution of trajectories on the probability map looks like if the pixel jump is good. To this end, we simulated trajectories with a diffusion coefficient and statistical distribution of localisation gaps representative for the experiments, and we call these the *true* trajectories. Two-dimensional Brownian motion was assumed, and the simulation details are given in the methods section. The simulated trajectories were first converted into localisations. These localisations were linked back to new trajectories, which we call the *measured* trajectories. The linking was done

Figure 5.4 • Map of the trajectory recognition success probability as a function of the diffusion coefficient and trajectory span. The recognition probability is low for fast molecules ($D = 10^{-11}$–10^{-12} m^2 s^{-1}), near unity for slow molecules ($D = 10^{-14}$–10^{-13} m^2 s^{-1}), and intermediate for a transition region between $D = 10^{-12}$–10^{-13} m^2 s^{-1}. The localisation error was fixed at 10 nm, pixel jump at 384 nm (six pixels), and the frame time at 30 ms.

with the same pixel jump and blinking gap as was used in the experiment. We simulated true trajectories with a span of 40 frames and diffusion coefficient of 10^{-13} m^2 s^{-1} and overlaid this with the probability map of P (Figure 5.5a). According to our model, the simulation parameters resulted in trajectories with $P \approx 0.9$. We found that most measured trajectories spanned 40 frames, like the true trajectories, which confirms that the pixel jump is good. A few measured trajectories were shorter than the true trajectories because of the ~0.1 probability that a true trajectory is not successfully recognised at $P \approx 0.9$.

Now that we know how the distribution of trajectories looks if the pixel jump is good, we considered simulated trajectories for which the pixel jump is too short. We simulated trajectories with a diffusion coefficient slightly higher (5×10^{-13} m^2 s^{-1}) and far higher than the transition region (10^{-12} m^2 s^{-1}) and overlaid the resulting measured trajectories with their probability map (Figure 5.5b,c). The pixel jump was too short according to our model since the simulated parameters would result in $P < 0.1$ for both simulations. Because the longest

displacements were not included in the measured trajectories, we expect that these trajectories would become shorter and have a lower diffusion coefficient than the true trajectories. We indeed found this trend in our simulation results. Overall, this led to many trajectories in the blue-coloured region of the probability maps (with $P < 0.2$), opposed to the simulation with a good pixel jump where we didn't find any trajectories in this region. We will use this characteristic to estimate whether the experimentally measured trajectories are linked by a pixel jump that is too short.

We compared the experimentally obtained trajectories with their probability map of P (Figure 5.6a–d) and did not find strong indications that the pixel jump was too short. Indeed, all trajectories are in or below the transition region with a $P > 0.2$. When we considered a smaller pixel jump value of 2 pixels, we found clear signatures that this affects our estimates of diffusion coefficients (Figure 5.6e–g). Here, a significant portion of the trajectories were in the $P < 0.2$ domain, which indicates that the pixel jump is indeed too short. Altogether, this analysis demonstrates a proper selection of the
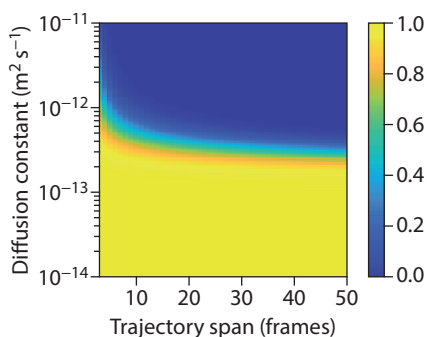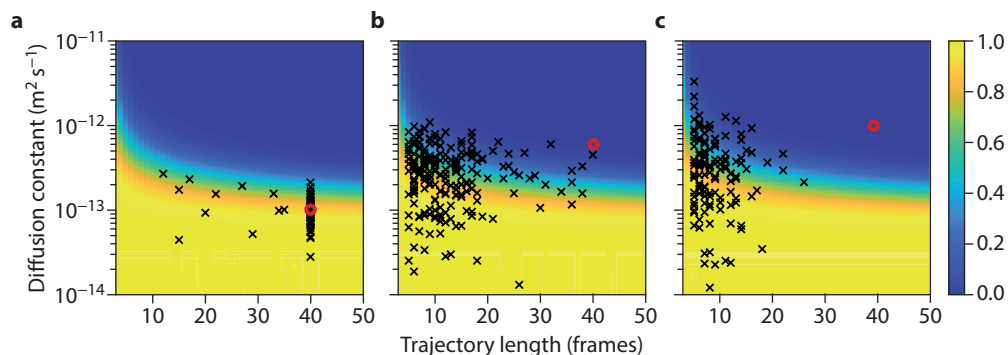

Figure 5.5 • (**a–c**) Maps of the trajectory recognition success probability as a function of the diffusion coefficient and the trajectory span are given for each set of simulated trajectories. The localisation error was fixed at 10 nm, the pixel size at 64 nm, and the frame time at 30 ms. Overlaid black crosses are the *measured* simulated two-dimensional trajectories originating from a hundred *true* simulated trajectories with a diffusion coefficient of 10^{-13} (panel **a**), 5×10^{-13} (panel **b**), and 10^{-12} m^2 s^{-1} (panel **c**). The true trajectories were simulated spanning 40 frames and with a statistical distribution of localisation gaps of the mobile trajectories in the *a*-oriented parent zeolite film. Linking into measured trajectories was performed with a pixel jump of at 384 nm (six pixels) and a blinking gap of 90 ms (three frames). The diffusion coefficient of the measured trajectories was obtained with time-averaged mean squared displacement analysis, fitting the first 25% or at least three points. The red dots mark the input parameters of the true trajectories.
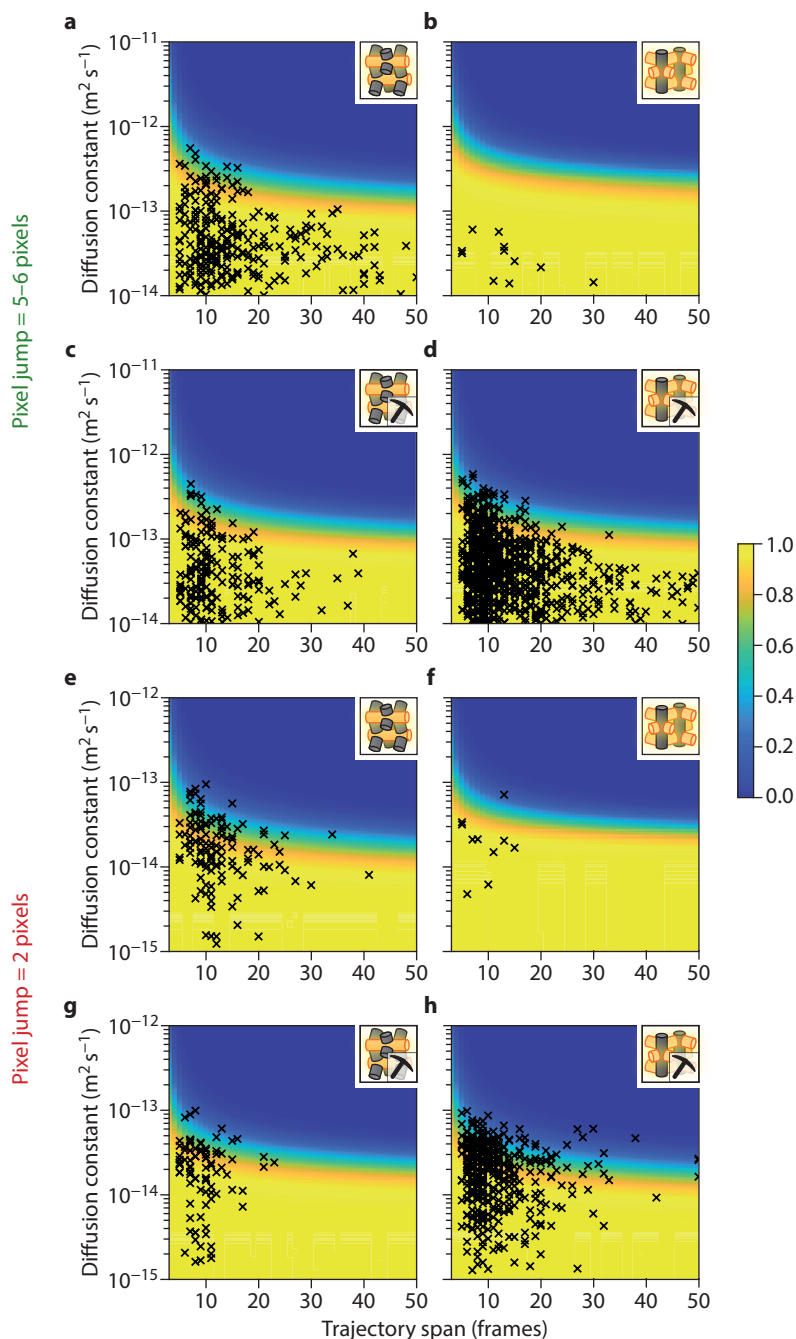
Figure 5.6 • (**a–h**) Maps of the trajectory recognition success probability as a function of the diffusion coefficient and the trajectory span. The localisation error was fixed at 10 nm and the frame time at 30 ms. Overlaid black crosses are the experimental mobile trajectories linked with a pixel jump of six (panels **a,b**), five (panels **c,d**) and two pixels (panels **e–h**). The mobile trajectories were obtained from *(continued on the next page)*

parent *a*-oriented (panels **a,e**) and *b*-oriented (panels **b,f**) as well as hierarchical *a*-oriented (panels **c,g**) and *b*-oriented zeolite ZSM-5 films (panels **d,h**). The statistical distribution of localisation gaps of the corresponding trajectories is used in the model. Black crosses represent individual trajectories, where the diffusion coefficient was obtained with time-averaged mean squared displacement analysis, fitting the first 25% or at least three points. Note that the value of the *y*-axis in panels **e–h** is an order of magnitude lower than in panels **a–d**.

---

pixel jump that does not introduce bias in the estimated diffusion coefficient.

5.2.3 • Channel geometry–diffusion relationships

We investigated the impact of channel geometry on the diffusion heterogeneity to unravel the microscopic origin of diffusion anisotropy in zeolites. A summary of the motion analysis results after classification in the populations mobile, hybrid, and immobile can be found in Appendix 5.6.1. T-MSD analysis of individual trajectories (Figure 5.7a,b) revealed a continuous range of diffusion coefficients spanning several orders of magnitude for both channel types. We quantified the diffusion coefficient from a fit of the time–ensemble-averaged mean squared displacement (TE-MSD) curves, which average over the entire population. The TE-MSD curves of the different populations in straight and sinusoidal zeolite channels are shown in Figure 5.7c,d. A large difference in the slope of these curves of the mobile trajectories is evident, while the immobile and hybrid trajectories' TE-MSD curves all have a similar slope. The calculated diffusion coefficients confirm that the mean diffusion coefficient of the mobile molecules is higher in the straight zeolite channels ($2.64 \pm 0.24 \times 10^{-14}$ m^2 s^{-1}) than in the sinusoidal zeolite channels ($1.38 \pm 0.11 \times 10^{-14}$ m^2 s^{-1}). The mean diffusion coefficient of the hybrid population is much lower than that of the mobile population because the hybrid population contains long immobile segments, while the diffusion coefficient of the immobile population approaches zero. The channel geometry also impacts the occurrence of each trajectory type (Figure 5.7e). We observed a two times larger fraction of mobile trajectories in the straight zeolite channels (22%) than in the sinusoidal analogue (11%). Meanwhile, we found fewer immobile trajectories in the straight

zeolite channels than in sinusoidal zeolite channels.

The effective diffusion coefficient (Figure 5.7f), calculated by considering the fraction and mobility of all types of trajectories, shows that the molecules move on average ten times faster in the straight zeolite channels ($3.10 \pm 0.21 \times 10^{-15}$ m^2 s^{-1}) than those in the sinusoidal zeolite channels ($0.27 \pm 0.10 \times 10^{-15}$ m^2 s^{-1}). The reported diffusion anisotropy is consistent with the results obtained by PFG NMR,[190–193] validating the developed method in this work. However, PFG NMR was not able to uncover the origin of diffusion anisotropy due to the ensemble nature of the technique. Our results demonstrated that the distinct channel geometries of the sinusoidal and straight channels of zeolite ZSM-5 favour both the fraction of mobile molecules as well as their mobility in the straight channels, resulting in diffusion anisotropy.

Further, we investigated the impact of the secondary pore networks on diffusivities within single-oriented zeolite channels over hierarchical zeolite thin films (Figure 5.8a). The secondary pore networks were introduced by NH$_4$F etching, which does not affect the acidity of the zeolites by equally removing silicon and aluminium.[201] Similar to the parent zeolite channels, we observed a large span of diffusion coefficients for each population in the hierarchical zeolite channels from individual MSD analysis. However, the diffusion anisotropy was significantly altered in both channel types, which have similar diffusion coefficients for the mobile population ($\sim 2.5 \times 10^{-14}$ m^2 s^{-1}, Figure 5.8b,c). As shown in Figure 5.8d, a higher fraction of mobile and hybrid trajectories as well as a lower fraction of immobile trajectories was present within the sinusoidal zeolite channels compared to the straight channels. These factors together resulted in a more than 1.5 times
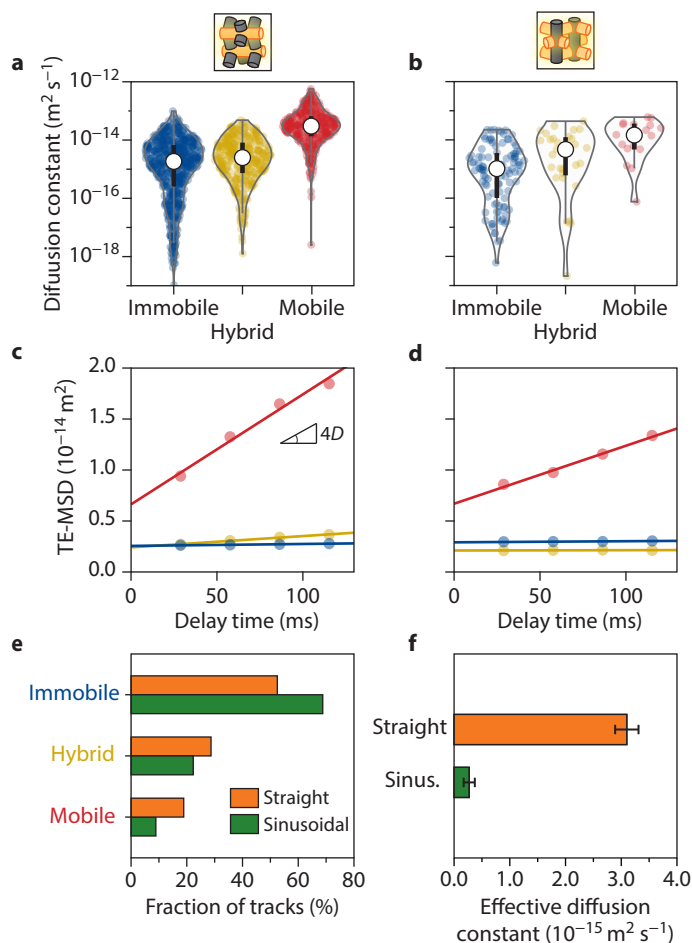
Figure 5.7 • (**a,b**) Violin plot of diffusion coefficients obtained via time-average mean squared displacement analysis of each individual trajectory in the straight (panel **a**) and sinusoidal zeolite channels (panel **b**). The white dot and the bold black line indicate the median and first to third quartile of the distribution, respectively. (**c,d**) The time–ensemble-averaged mean squared displacement (TE-MSD) curves of the mobile, hybrid, and immobile trajectories within the straight (panel **c**) and sinusoidal zeolite channels (panel **d**). The circles and lines represent the experimental data and the linear fit of the TE-MSD curve, respectively. (**e**) The fraction of each type of trajectory within the straight (orange) and sinusoidal (green) zeolite channels. (**f**) The effective diffusion coefficients of the straight (orange) and sinusoidal (green) zeolite channels. The error bars indicate the standard error.

faster effective molecular diffusion within the sinusoidal zeolite channels ($3.51 \pm 0.20 \times 10^{-15}$ m^2 s^{-1}) than in their straight counterpart ($2.20 \pm 0.24 \times 10^{-15}$ m^2 s^{-1}, Figure 5.8e).

We quantified the change of diffusion heterogeneity in each channel orientation by com-

paring the parent and hierarchical zeolites. Surprisingly, the effective diffusion coefficient of the molecules in the sinusoidal zeolite channels increased an order of magnitude with respect to the parent zeolite, while we observed a slight decrease in the straight channels (Figure 5.8e). The increase in effective diffusivity in

the sinusoidal zeolite channels is explained by a factor of two increase in both the diffusivity and fraction of the mobile molecules (Figure 5.8d). Interestingly, we did not find an apparent change in diffusivity (2.64 ± 0.24 to $2.51 \pm 0.13 \times 10^{-14}$ m² s⁻¹) for the mobile molecules in the straight zeolite channels (Figure 5.8b). The fraction of immobile molecules increased at the expense of hybrid and mobile fractions (Figure 5.8d), which explains the observed overall slight decrease in effective diffusivity.

The straight and the sinusoidal pores are affected differently by the etching procedure. Mass transport in the direction of the straight pores was not enhanced by the etching. Previous work showed that diffusivity in hierarchical zeolites was unaffected by steaming due to a lack of connectivity of the introduced mesopores.[181,208] Moreover, it has been demonstrat-

ed that the mesopores introduced using NH_4F etching are interconnected and aligned in zeolite ZSM-5.[201] We suspect that the introduced secondary channels along the straight zeolite channels are disconnected. Therefore, the diffusivity in this direction would be limited by the diffusion resistance of the micropores.

In contrast to the sinusoidal channels, a decline in the fraction of mobile trajectories was found in the straight channels in favour of the fraction of immobile trajectories (Figure 5.8d). This suggests that some channels along the straight zeolite channels are blocked by the formation of extra-framework silicon and aluminium—resulting in adsorption sites. Preferential adsorption of extra-framework aluminium in the straight channels and at intersections was predicted by density functional theory computations,[209] but it was never experimen-
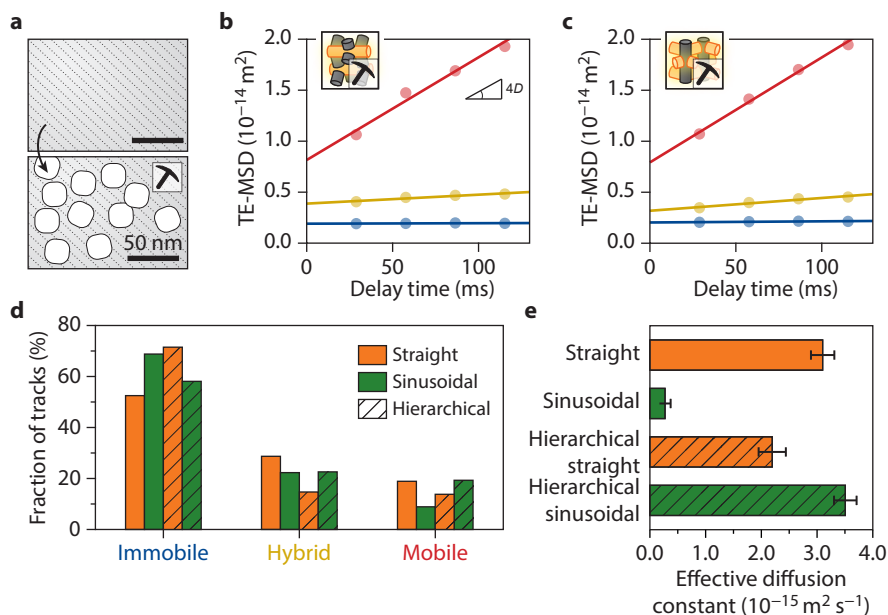
Figure 5.8 • (**a**) Schematic representation of the introduction of secondary pore networks into zeolites. (**b,c**) The corresponding time–ensemble-averaged mean squared displacement (TE-MSD) curves of the straight (panel **b**) and sinusoidal zeolite channels (panel **c**) after classification into mobile, hybrid, and immobile trajectories. The circles represent the experimental data, and the straight line is the fit of the TE-MSD curve. (**d**) The fraction of each type of trajectory within the straight (orange) and sinusoidal (green) zeolite channels with secondary porosity (hatched bars) in comparison with the parent zeolite. (**e**) The effective diffusion coefficients for the straight (orange) and sinusoidal (green) zeolite channels for the parent and hierarchical zeolite (hatched bars). The error bars indicate the standard error.

tally observed due to the limitations of current characterisation techniques. Taken together, these results demonstrate that the addition of secondary pore networks primarily enhances the diffusivity of sinusoidal zeolite channels, and thus alleviating the diffusion limitations of microporous zeolites.

5.3 • Conclusions

Channel structure–diffusivity relationships in zeolites could be unravelled by capturing the diffusion heterogeneities at the single-molecule level over single-oriented channels of zeolite ZSM-5. Our results demonstrated that the distinct channel geometries dictate the mobility and motion behaviour of the molecules, which resulted in diffusion anisotropy. Further investigation of the diffusion heterogeneity in hierarchical zeolites provides direct insights on the working principle of the secondary pore networks on the enhancement of diffusivity. We showed that the introduced secondary channels greatly promote the diffusivity in the sinusoidal zeolite channels and slightly suppress the diffusivity in the straight analogue. Such knowledge is directly applicable to materials engineering using controlled channel structures thereby maximising and/or suppressing the diffusion of reactant, product molecules as well as metal active sites.[210] For example, when the zeolite is embedded in a porous support, selective exposure of one channel type to the reactant stream could promote diffusion in and out the zeolite. Based on our results, the straight channels should be preferentially exposed for pristine ZSM-5 and the sinusoidal channels for the hierarchical zeolite. Altogether, the developed approach can be applied more broadly in a diagnostic manner to study the chemistry of porous materials at the level of single-oriented channels.

5.4 • Contributions & acknowledgements

5.5 • Methods

5.5.1 • Experimental

Chemicals and materials. Aluminum sulfate hexadecahydrate ($Al_2(SO_4)_3 \cdot 18H_2O$, 98%, Sigma-Aldrich), ammonium fluoride (NH_4F), ammonium nitrate (NH_4NO_3, > 99%, Acros Organics), anhydrous potassium carbonate, bis(hexamethylene)triamine, branched polyethylenimine (PEI, M_w ≈ 25000, M_n ≈ 10000, Sigma-Aldrich), 2-butanone, diethyl ether, 1,4-dioxane (99.8%, Sigma-Aldrich), ethanol (anhydrous, absolute, Biosolve), ethyl acetate, furfuryl alcohol (98%, Sigma-Aldrich), hydrogen peroxide (H_2O_2, 35 wt% aqueous solution), 1-iodopropane, polyethylenimine (PEI), potassium hydroxide (KOH, pellets, 85%, Alfa Aesar), sodium silicate solution ($Na_2O(SiO_2)_x \cdot xH_2O$, ~10.6% Na_2O, ~26.5% SiO_2, Sigma-Aldrich), sulfuric acid (95%, Fischer Scientific), tetraethyl orthosilicate (TEOS, 98%, Sigma Aldrich), tetrapropylammonium hydroxide (TPAOH, 1M aq., Alfa Aesar), and quartz plates (LSP Quartz B.V., 20 mm in diameter). All chemicals were used as received with no further purification except water, which in all cases was purified through a Milli-Q system to a resistivity of 18.2 MΩ·cm.

Preparation of *a*-oriented and *b*-oriented zeolite ZSM-5 films on quartz plates. The preparation of the *a*-oriented and *b*-oriented zeolite ZSM-5 films (thickness approximately 800 nm, Si/Al = 125) followed the same protocol reported by our group using the secondary growth method.[187] Silicalite-1 seed crystals for a-oriented and b-oriented films

Table 5.1 • Overview of the optimal concentration of furfuryl alcohol in 1,4-dioxane for the single-molecule localisation microscopy measurements.

Zeolite films	Concentrations of furfuryl alcohol in 1,4-dioxane (mmol/L)	
	a-oriented	*b*-oriented
Parent	0.001	0.02
Hierarchical	0.01	0.05

were synthesised first. For manual assembly of the seed crystals on the substrate, the quartz plates were pre-coated with PEI or pre-treated with H_2O_2, respectively for the *a*-oriented and *b*-oriented zeolite ZSM-5 films. Then ~30 mg of *a*-oriented or *b*-oriented silicalite-1 crystals were sprinkled on the surface of a quartz plate followed by pressing and rubbing using a finger with soft latex gloves. Subsequently, the loosely attached top layers were removed by gently wiping using glass wool for ~30 s. The *a*-oriented monolayers were calcined at 823 K overnight to remove the organic layers before secondary growth. The *b*-oriented monolayers were calcined for 2 h at 423 K to enhance the strength of the attachment. After the synthesis, the films were first treated with 0.2 M NH_4F solution for 2 h—without stirring—to remove the outermost amorphous silica layers that can block the channels of the membranes. Then the films were calcined at 823 K overnight with a ramp rate of 1.5 K/min under an airflow to remove the ethanol.

Ion exchange. The proton form sample was obtained by three times repeating the ion exchange of the calcined Na-type sample with a 1 M NH_4NO_3 solution at 333 K overnight followed by calcination at 823 K for 6 h with a ramp rate of 1.5 K/min.

Etching of the oriented zeolite ZSM-5 films. The films with hierarchical pores were prepared using the fluoride-etching method.[201] Typically, the as-synthesised zeolite films were put into a 40 wt% NH_4F aqueous solution and react at 333 K for 20 min under mechanical stirring. The etched products were thoroughly washed with distilled water after the fluoride treatment.

Physicochemical characterisation of the oriented zeolite ZSM-5 films. The images of the zeolite monolayers and films were examined using a scanning electron microscope (SEM) from XL-30 (Philips) operating at an accelerating voltage of 5 kV. Before measurement, the surface of the materials was coated with a Pt layer of ~5 nm to avoid charging effects. X-ray diffraction (XRD) was used to confirm the orientation of the as-synthesised zeolite monolayers and films. The XRD patterns were collected using a Bruker D2 Phaser (2nd Gen) instrument using a cobalt radiation source, Co Kα = 1.789 Å. UV/Vis diffuse-reflectance spectroscopy (DRS) was applied to determine the absorption property of the zeolite ZSM-5 films after the oligomerisation of furfuryl alcohol (FFA). The UV/Vis DRS spectra were collected using an AvaSpec 2048L spectrometer connected to a high-temperature UV/Vis optical fibre probe, which was used to collect spectra in reflection mode. Focused ion beam–SEM images were recorded on a FEI Helios NanoLab G3 UC instrument. A protective layer of Pt was deposited on top of the region of interest before milling trenches on either side. Slices were milled perpendicular to the surface before SEM images were recorded (5 kV, 50 pA). Atomic force microscopy micrographs were recorded using a Bruker Multimode 8 with a *n*-type silicon tips with a hard diamond-like coating and aluminium background (having a resonance frequency of 160 kHz and a force constant of 5 N/m). The data was post-processed in the Gwyddion software.

Fluorescence microscopy. Single-molecule localisation microscopy experiments were performed using a custom-made fluorescence microscope setup. An inverted epi-fluorescence wide-field fluorescence microscope (Nikon Eclipse-TI) with a 100× oil immersion objective (NA = 1.49) was used. A diode-pumped solid-state laser (Cobolt Jive-100, 560 nm) provided 54 mW to the sample. Fluorescence microscopy images were recorded as movies using an electron-multiplying charge-coupled device (EMCCD) camera (Andor iXon 897), after passing

through a bandpass filter (Chroma, ZET560/10x), dichroic mirror (Chroma, ZT560rdc), long-pass filter (Chroma, ET575lp), quarter wave plate (Newport, 10RP44-1) and a 2.5× camera lens. Time-lapse videos were recorded with a resulting field of view of 32×32 μm^2 with 64×64 nm^2 per pixel (512 × 512 pixels) and a frame time of 30 ms. The reaction was performed in a 25 μL Gene Frame (Thermo Scientific) liquid cell. The cell consisted of a Gene Frame, which forms a sealed liquid microscopy cell after adhesion to a coverslip and plastic cover on each side. The oligomerisation of FFA was performed on activated zeolite ZSM-5 films loaded on the top of the coverslip in the liquid cell. The zeolite materials were exposed to FFA, previously diluted in 1,4-dioxane, to achieve the desired catalytic activity. The optimal concentration (Table 5.1) of FFA for high-resolution imaging was determined in a series of concentration-dependent measurements. The sample was equilibrated for at least two hours and exposed to maximum laser power for 5 min (10.9 mW through objective) for fluorescence photobleaching before the measurement.

5.5.2 • Data processing, analysis, and modelling

Localisation and tracking. Single-molecule tracking was performed with the DoM plugin v.1.1.6 for ImageJ.[78,139] A blinking gap of three (parent zeolite) and two frames (hierarchical zeolite) and a pixel jump of six (parent zeolite) and five pixels (hierar-

chical zeolite) was used. Only trajectories with at least five localisations were considered.

Trajectory analysis. Trajectory classification, analysis and plotting were done using the methodology and DiffusionLab software described in Chapter 3. We manually built a decision tree based on the previously reported decision tree by Hendriks et al.[61] (Figure 5.9). Motion analysis of individual trajectories was performed with time-averaged mean squared displacement (T-MSD) analysis (Equation 2.9) or a set of trajectories, i.e., a population, with the time–ensemble-averaged MSD (TE-MSD) analysis (Equation 3.1). The diffusion coefficient and localisation error were obtained from a linear fit of the MSD curve ignoring motion blur, i.e., $R = 0$ (Equation 2.10). T-MSD analysis on individual trajectories was done including the first 25% of the delay times and at least three points. Only the first four points were used in the fit of the TE-MSD because the number of trajectories contributing to the TE-MSD was constant in this fit range.

Effective diffusion coefficient. Comparison with the previously reported ensemble diffusion coefficients, e.g., obtained with pulsed-field-gradient nuclear magnetic resonance (PFG-NMR), requires the computation of an effective diffusion coefficient.[16] This is the weighted mean of the diffusion coefficient of each population following[16,211]

Figure 5.9 • The decision tree used for the classification of trajectories. Trajectories were grouped into immobile, hybrid, and mobile categories. Elongation is the covariance first eigen value of the localisations rescaled from 0.5–1 to 0–1. The entropy is a statistical measurement of randomness (Shannon's entropy) applied to the distribution of the points within the enclosing square that is defined by the smallest enclosing circle.

$$D_{\text{eff}} = f_{\text{mobile}}D_{\text{mobile}} + f_{\text{hybrid}}D_{\text{hybrid}} \qquad (5.1)$$

with f_X and D_X the fraction of guest molecules and the diffusion coefficient of population X, respectively. As the diffusion coefficient of the immobile population is zero by definition, this population is left out of the equation. We estimated the weight f as the average fraction of molecules per frame per motion behaviour, i.e., the average localisation density of a population. We computed the molecules per frame, where we included all frames between the first and last localisation—even when localisations are missing. We used the standard error of the mean to compute the error in f_X and the uncertainties were propagated following the well-known formulas.[212]

Density functional theory calculations. The static and dynamic absorption maxima for the neutral and protonated oligomers were calculated using density functional theory (DFT) simulations. The ground state structures of a series of neutral and charged FFA oligomers were obtained using the density functional theory method as implemented in version 6.1 of CP2K software.[213] The gas-phase geometries were optimised using GAPW method[214] with CAM-B3LYP functional[215,216] and 6-311++G** basis set. Plane-wave cut-off value of 600 Ry was used. The structures of selected oligomers derived from the literature.[113,206] For each of the oligomers, several possible conformers were generated and their stability both in a vacuum and within the zeolite (vide infra) was tested at CAM-B3LYP and BLYP-D3 level of theory, respectively. We found that in a vacuum the trans oligomers were the most stable, whereas cis oligomers were preferred in the zeolite. Therefore, for all subsequent calculations we used cis oligomers.

Vertical electronic excitation energies were determined by using time-dependent DFT as implemented in ADF package[217–220] at the CAM-B3LYP/TZV2P[221] level of theory, which has proven to be accurate for modelling of absorption bands of five-membered heterocyclic compounds.[222] The ability of CAM-B3LYP functional to correctly reproduce exited states of FFA and its derivates was further confirmed by comparing experimentally measured absorption maximum of FFA in water. The experimental value 217 nm[223] is close to

time-dependent DFT computations (220 nm) providing that a polarisable continuum model for water is used. Therefore, we concluded that CAM-B3LYP functional can be used to resolve main spectral features of ultraviolet–visible (UV–Vis) absorption of the FFA oligomerisation reaction products.

To account for a flexibility of the UV–Vis-active compounds and confinement arising from the zeolite network, we followed the same procedure as Hemelsoet et al.[224] Different conformations of both neutral and charged oligomers entrapped in zeolite pores were generated by ab-initio molecular dynamics (MD) simulations. As model system of the environment for both the neutral and protonated oligomers, silicalite-1 and H-ZSM-5 with a Si/Al ratio of 95 were used, respectively. The Al atom was introduced in the zeolite network by replacing one Si atom located at a T12 position. Density functional theory calculations were performed within the CP2K software and GPW method[225] by using a DZVP MOLOPT basis set, GTH pseudopotentials, and BLYP functional[226,227] with the -D3 dispersion correction scheme of Grimme.[228] MD simulations were performed in the canonical (NVT) ensemble at a temperature 298 K with a time step of 0.5 fs. A Nosé-Hoover thermostat of length three was used to control the temperature. Prior each MD simulation, the unit cell of entrapped oligomers was optimised and then kept fixed during the MD run. The system was initially allowed to equilibrate for 1 ps, which was followed by a 5 ps production run. The time-averaged spectra were obtained by taking 50 different snapshots (every 200 steps), on which separate time-dependent DFT calculations were performed. During the time-dependent DFT simulations, the zeolite structure was not considered due to enormous computational cost this would require. Finally, the averaged spectrum from all snapshots was computed.

Modelling of the effect of the pixel jump on the measured diffusion coefficient. We modelled the *trajectory recognition success probability, P,* to estimate whether we can reliably measure the diffusion coefficient of the fastest molecules in the sample. A detailed description of the problem is given in Section 2.2.4. We did not consider the false grouping of different molecules into a trajectory because we manually selected values of the pixel jump and the blinking gap at which this should not occur.
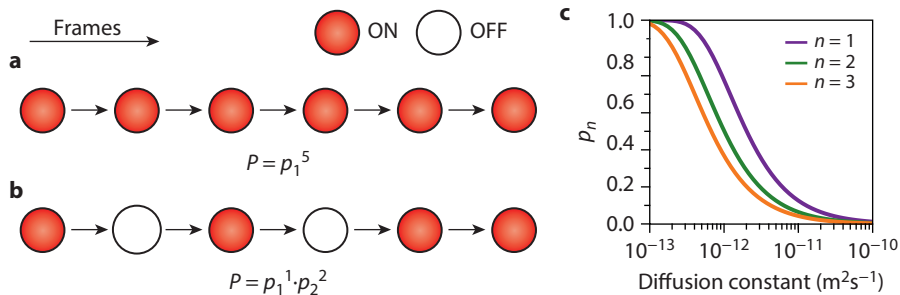
Figure 5.10 • (a,b) Schematic representation of a trajectory with a span of six frames without (panel **a**) and with blinking (panel **b**). The trajectory recognition success probability P is given below each trajectory. (**c**) The recognition success probability of a single displacement p_n given as a function of the diffusion coefficient. The localisation error σ was fixed at 10 nm, pixel jump Δr_{max} at 384 nm (six pixels), and the frame time Δt at 30 ms.

To model the trajectory recognition success probability, we need to compute the probability that the displacements of every single step in the trajectory are recognised by the tracking algorithm. We start by modelling the recognition success probability of a single step in the trajectory, which allows us to compute the recognition success probability of the full trajectory. First, we considered a molecule that is continuously fluorescent and does not blink. This means that each step in the trajectory spans one frame. We assumed 2-dimensional Brownian motion with a displacement probability in x and y given by a normal distribution with a standard deviation of $\sqrt{2Dt}$, with D the diffusion coefficient and t the delay time.[144] We assumed that the error in the localisations is normally distributed with a standard deviation of σ. The recognition success probability of a single step in the trajectory p in the case of no blinking[145] is given by

$$p_1 = 1 - \exp\left(\frac{-\Delta r_{max}^2}{\text{MSD}}\right) \qquad (5.2)$$

where Δr_{max} is the pixel jump and MSD is the mean squared displacement. The subscript for p_1 indicates that the displacement of this step spans one frame, which corresponds to a molecule that does not blink, and the MSD depends on the frame time Δt as

$$\text{MSD} = 4D\Delta t + 4\sigma^2. \qquad (5.3)$$

The probability that a full trajectory is recognised by the tracking algorithm is given by

$$P = p_1^{N-1} \qquad (5.4)$$

with N the span of the trajectory in frames. The span is the number of frames between the first and last localisation of the trajectory. An example is depicted in Figure 5.10a.

Blinking affects the probability that a single-molecule trajectory is properly identified. During periods when the molecule is off, it cannot be localised, and localisations are missing. These so-called *localisation gaps* in the trajectory result in steps that span more than one frame. We can generalise Equation 5.2 and Equation 5.3 for steps that span n frames

$$p_n = 1 - \exp\left(\frac{-\Delta r_{max}^2}{\text{MSD}}\right) \qquad (5.5)$$

with

$$\text{MSD} = 4Dn\Delta t + 4\sigma^2. \qquad (5.6)$$

To compute the trajectory recognition success probability, we multiplied all values of p weighted in the exponent by their occurrence in the trajectory. The probability that a full trajectory is recognised by the tracking algorithm becomes

$$P = p_1^h p_2^k p_3^l \cdots \quad \text{with}$$
$$1h + 2k + 3l + \cdots = N - 1. \qquad (5.7)$$

The indices h, k, l are the number of times a step spanning $n = 1, 2, 3$ frames occurs in a trajectory, respectively. The span of the trajectory N includes frames in which the molecule is not localised. This relation is depicted for a single trajectory in Figure 5.10b. The step recognition success probability p_n as a function of the diffusion coefficient is shown in Figure 5.10c. Depending on the blinking gap, we should include a different number of factors in Equation 5.7. The maximum number of n is always one frame larger than the blinking gap. The average values of h, k, l depend on the blinking statistics of the molecules. We estimated the h, k, l values directly from the statistical distribution of localisation gaps in the experimental data. These values can be fractional as they are computed from the mean over many trajectories.

5.6.1 • Classification and motion analysis results

Table 5.2 • Overview of the MSD analysis results for the population and individual trajectory fit. The diffusion coefficient (*D*), localisation error (*ε*), standard error of the fit (σ), and the number of trajectories is given. The median (med.) of the distribution of *D* and *ε* of the individual trajectories have been rounded to three digits. The movement of individual fluorescent molecules within the sinusoidal and straight zeolite channels were tracked in the b-oriented and a-oriented zeolite films, respectively.

Population	Sample	Tracked in channel type	Population fit		Individual trajectory fit		Trajectories	
			$D \pm \sigma$ (m²/s) ×10⁻¹⁴	$\varepsilon \pm \sigma$ (m) ×10⁻⁸	Med. D (m²/s) ×10⁻¹⁴	Med. ε (m) ×10⁻⁸	Number	Fraction (%)
Mobile	Parent	Sinusoidal	1.38 ± 0.11	4.06 ± 0.11	0.477	4.28	29	11
Mobile	Parent	Straight	2.64 ± 0.24	4.03 ± 0.20	1.73	3.92	476	22
Mobile	Hierarch.	Sinusoidal	2.51 ± 0.13	4.42 ± 0.09	1.50	4.65	1592	20
Mobile	Hierarch.	Straight	2.49 ± 0.29	4.47 ± 0.21	1.44	4.42	337	14
Hybrid	Parent	Sinusoidal	0.007 ± 0.009	2.292 ± 0.017	0.00159	3.38	52	19
Hybrid	Parent	Straight	0.267 ± 0.013	2.454 ± 0.019	0.0643	3.25	541	24
Hybrid	Hierarch.	Sinusoidal	0.31 ± 0.04	2.81 ± 0.05	0.0384	3.19	1761	22
Hybrid	Hierarch.	Straight	0.21 ± 0.04	3.12 ± 0.05	0.0173	3.27	337	14
Immobile	Parent	Sinusoidal	0.026 ± 0.006	2.694 ± 0.010	0.00131	2.56	188	70
Immobile	Parent	Straight	0.045 ± 0.004	2.527 ± 0.006	0.000177	2.65	1193	54
Immobile	Hierarch.	Sinusoidal	0.028 ± 0.011	2.253 ± 0.018	0.00368	2.37	4717	58
Immobile	Hierarch.	Straight	0.012 ± 0.010	2.207 ± 0.018	0.00551	2.22	1760	72

5

Chapter **6**

Molecular accessibility and diffusion in large zeolite crystals visualised with resorufin

Abstract • Confocal laser scanning microscopy is used to visualise molecular accessibility and diffusion in the hierarchical, anisotropic pore structure of large (~10 μm-sized) zeolite-β crystals. Most used fluorescent probes with favourable photophysical properties do not fit in the zeolite's micropores. Therefore, the small resorufin molecule is studied as fluorescent probe. It is widely used in life and materials science but only in its deprotonated form because the protonated molecule is barely fluorescent in aqueous solution. The work in this chapter shows that protonated resorufin is in fact strongly fluorescent when confined within the zeolite micropores, which makes it an interesting, charge-neutral probe for diffusion through microporous materials. We demonstrate its application by direct visualisation of a diffusion barrier between the zeolite subunits and anisotropic diffusion through zeolite-β's straight channels.

6.1 • Introduction

One of the industrially most applied zeolites is zeolite-β. It has numerous applications in the production of fine chemicals as well as in the petrochemical industry, often as catalyst for alkylation and transalkylation reactions.[185,229,230] Zeolite-β has a large pore size that accommodates bulkier guest molecules than zeolite ZSM-5. In Chapter 5, the enormous impact of ZSM-5's pore geometry on the diffusivity and adsorption frequency of the guest molecules was shown. Diffusion limitations of the micropores (< 2 nm diameter) could be alleviated by the introduction of a secondary pore network (≥ 2 nm diameter). This

illustrates that mass transport is often limiting in zeolite application because of the strong interaction between guest molecules and the micropores of the zeolite host material.[15,182] Therefore, rational design of more efficient zeolite materials requires careful characterisation of their pore network and understanding of mass transport therein, including the involved intricate host–guest chemistry.

Zeolite-β has the BEA framework constituting of intersecting 6.6 × 6.7 Å straight channels along the crystallographic a- and b-axis (Figure 6.1a). These channels are built up from rings of twelve tetrahedra, classifying zeolite-β as a large-pore zeolite. The struc-
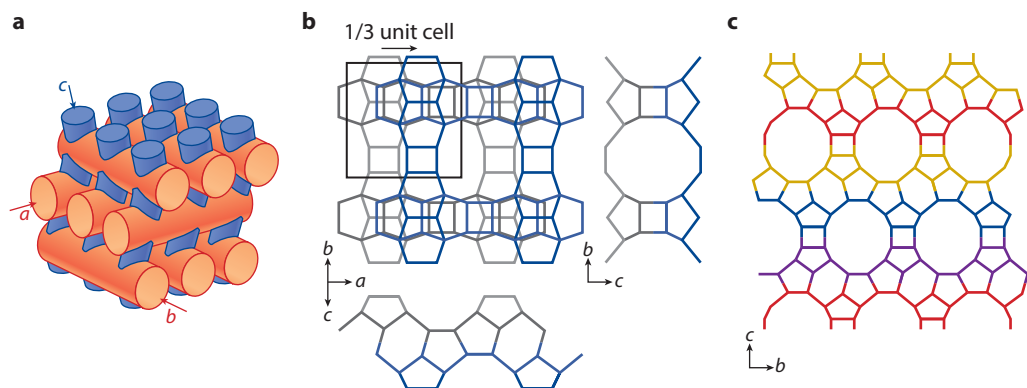
Figure 6.1 • (**a**) Micropore topology of the BEA zeolite framework (polymorph A). Arrows indicate the straight and sinusoidal zeolite channels aligned in the crystallographic a, b-direction and c-direction, respectively. Adapted from Bárcia et al.[235] (**b**) Stacking of the layers in zeolite-β via a mirror operation followed by a translation of 1/3 unit cell. Adapted from the *Database of disordered zeolite structures*.[7] (**c**) Formation of the straight channels in disordered zeolite-β observed along the crystallographic a-axis. The stacked layers are colour coded by their translation, which follow the random translations 1/3***b***, −1/3***a***, 1/3***b***, 1/3***a***, −1/3***b***, and −1/3***a*** with respect to the layer above, given from top to bottom.

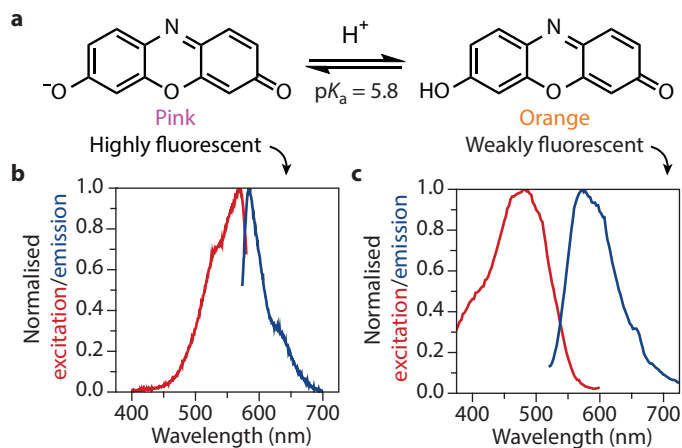**Figure 6.2** • (**a**) Properties of resorufin in basic (left) and acidic (right) aqueous solution. (**b**) Excitation (λ_{ex} = 569 nm) and emission (λ_{em} = 585 nm) spectra of deprotonated resorufin at pH = 9. Deprotonated resorufin has an absorption maximum at 570 nm. (**c**) Excitation (λ_{ex} = 500 nm) and emission (λ_{em} = 620 nm) spectra of protonated resorufin at pH = 2. Protonated resorufin has an absorption maximum at 483 nm.

ture of zeolite-β can be understood from the stacking of layers that are mirrored and translated with ±1/3 unit cell alternating along the *a*- and *b*-axis (Figure 6.1b).[7,8,231,232] Ordered polymorphs are formed when the stacking follows certain patterns, e.g., in polymorph A the translations −1/3*a*, −1/3*b*, 1/3*a*, and 1/3*b* are repeated. However, purely ordered structures have not been observed experimentally as aluminosilicate zeolite-β.[7,233,234] In reality, the zeolite is disordered along the crystallographic *c*-axis. Along this axis, well-defined sinusoidal channels with a size of 5.6 × 5.6 Å and zigzag shape are present in the ordered polymorph A (see Figure 6.1a), whereas these channels are randomly shaped in the disordered zeolite. Regardless of the (dis)order along the crystallographic *c*-axis, uniform straight channels are formed in the zeolite (Figure 6.1c). The channels in the *a*-, *b*-, and *c*-direction are interconnected, creating an anisotropic, three-dimensional pore network.[7,8,231,232] Thus, consideration of the pore anisotropy when investigating molecular diffusion and the zeolite pore structure is essential for the improvement of zeolite-β and other zeolite materials.

The advent of microimaging techniques, notably interference microscopy and infrared microimaging, has enabled direct measurements of mass transport within zeolites at the single-crystal level.[15,30,37,197] These techniques have been essential in the measurement of dif-

fusion barriers in zeolites and other porous materials (see Section 2.1.2). To fit a diffusion model to the microscopy recordings, the relationship between the measured signal and local molecular concentration must be known. Cuboid crystal shapes and symmetries are preferred for these microimaging techniques as the concentration of diffusing molecules is only obtained as a two-dimensional projection.[37] Anisotropic diffusion in more complex zeolite crystal shapes, such as zeolite-β's truncated bipyramid shape, could be straightforwardly interpreted only when the concentration is imaged in three dimensions. Confocal laser scanning microscopy (CLSM) is a promising technique to accomplish this using fluorescent molecules. Even information about the molecule's microenvironment, such as polarity and pH, could be inferred directly from its emission spectrum.[236,237] Nonetheless, reports of CLSM used for the visualisation of diffusion in microporous solids are scarce[238,239] because most fluorescent probe molecules are larger than typical zeolite pores, prohibiting them from entering.

Resorufin is an interesting fluorescent molecule for CLSM microimaging experiments in zeolites because it is sufficiently small to enter the zeolite pores and has favourable photophysical properties. The molecule has a pK_a of 5.8 in water, meaning that above pH = 5.8 a majority exists in free solution in a deprotonat-

6

ed, anionic form (Figure 6.2a). It is this form of resorufin that is used for fluorescence assays in biology and catalysis[240,241] because of its long excitation and emission wavelength, high fluorescence quantum yield, large molar absorptivity, and good stability against light irradiation and pH changes.[242–244] Below pH = 5.8 resorufin exists in aqueous solution predominantly as the neutral, protonated molecule, which is poorly soluble and only weakly fluorescent,[244] and consequently, has not found use as a fluorescent probe (Figure 6.2a). The excitation and emission spectra of protonated and deprotonated resorufin are given in Figure 6.2b,c.[245] In this chapter, we investigate resorufin as a probe for CLSM microimaging experiments and demonstrate its application in large zeolite-β crystals.

6.2 • Results and discussion

6.2.1 • Resorufin for microimaging experiments

Two batches of large zeolite-β with Si/Al = 50 were synthesised. Through X-ray diffraction, we show that the BEA framework was successfully synthesised by comparison with a commercial reference zeolite-β (Figure 6.3a). High-resolution scanning electron microscopy (SEM) revealed that the crystals are typically > 10 μm in diameter and have the characteristic truncated bipyramid shape (Figure 6.3b,c). For performing a typical CLSM microimaging ex-

periment, we introduced an aqueous solution of deprotonated resorufin (Res⁻) to zeolite-β suspended in water. Barely any fluorescence signal from inside the zeolite crystal was observed for excitation wavelengths around its absorption maximum (Figure 6.4a). The weak signal observed under 560 nm excitation is consistent with deprotonated Res⁻ in Figure 6.4c. Surprisingly, we did observe the strongest fluorescence signal inside the zeolite when excited at 493 nm, which corresponds to the absorption maximum of ResH (Figure 6.4b). The emission spectrum matches the ResH reference spectrum in Figure 6.4d and confirms that ResH instead of Res⁻ is the dominant fluorescent species inside the zeolite near neutral pH, despite its weak fluorescence in aqueous solution.

We further investigated the ResH fluorescence inside the zeolite and in homogeneous aqueous solution via the excited-state fluorescence lifetime (Section 2.2.1). A lifetime of 3.0 ns was found for Res⁻ in aqueous solution; however, a completely different picture emerged for ResH. We found two lifetime components ($\tau_1 \ll 0.3$ and $\tau_2 = 0.49$ ns), while one would expect only a single component for a single fluorescent species in solution. Our unexpected result is likely due to molecular aggregation. The occurrence and type of ResH aggregation in aqueous solution are discussed next.
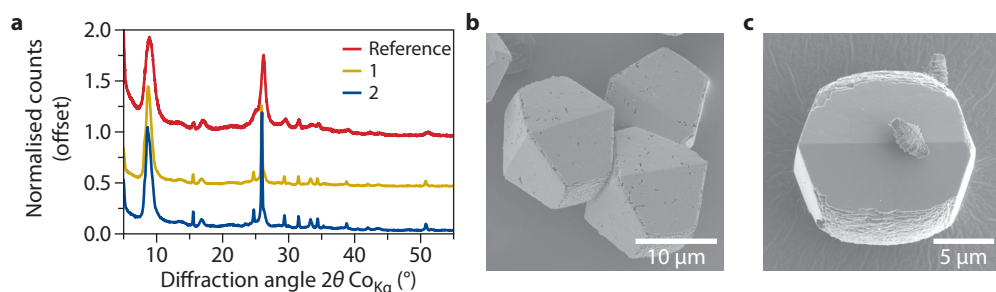
Figure 6.3 • (**a**) X-ray diffractogram of a reference zeolite-β (Zeolyst CP811E-75) and two batches of Si/Al = 50 zeolite-β labelled with their batch number. The synthesised zeolite-β matches the reference, which confirms the successful synthesis of the BEA framework. The peaks in the diffractogram are narrower for the synthesised zeolites than for the commercial reference because the crystals are better defined. (**b,c**) High-resolution scanning electron microscopy micrographs of batch 1 (panel **b**) and 2 (panel **c**).

Figure 6.4 • (**a,b**) Selective excitation of deprotonated resorufin (Res⁻; panel **a**) and protonated resorufin (ResH; panel **b**) in and around a zeolite-β crystal incubated for 3 h in a slightly pH-basic resorufin solution. Res⁻ is highly fluorescent in aqueous solution and can be excited at 560 nm close to its absorption maximum of 570 nm. ResH is weakly fluorescent in aqueous solution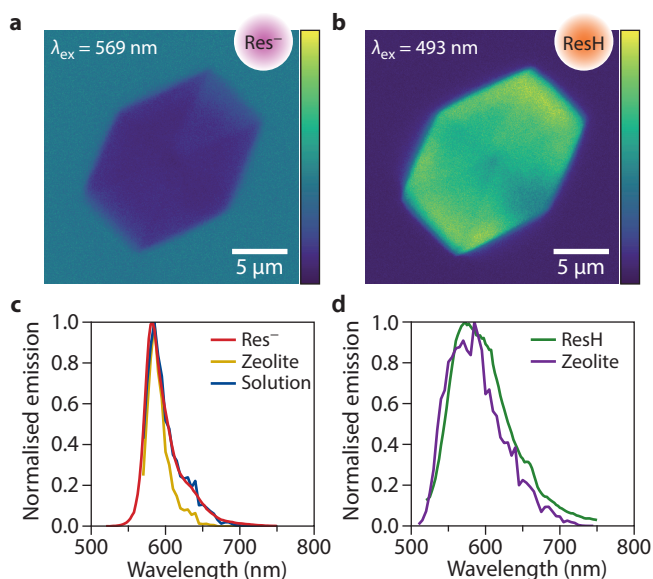 and can be excited at 493 nm close to its absorption maximum of 483 nm. The micrographs were recorded with confocal laser scanning microscopy through the centre plane of the crystal. The images show the same zeolite crystal excited with the same intensity and displayed with the same false colour scale. (**c**) Emission spectra in the zeolite and solution from panel **a** overlaid with a reference spectrum of Res⁻ recorded in aqueous solution. (**d**) Emission spectrum in the zeolite from panel **b** overlaid with a reference spectrum of ResH recorded in aqueous solution.

Aggregation was confirmed via a concentration series of ResH ultraviolet–visible (UV–Vis) absorption spectra, shown in Figure 6.5. The spectra were recorded over a range of 0.5 μM to 0.1 mM at pH = 2. When normalised to the concentration and corrected for Rayleigh
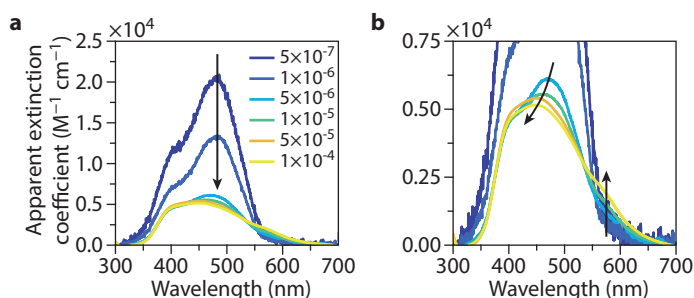
Figure 6.5 • (**a**) Ultraviolet–visible absorption spectra of protonated resorufin in a pH = 2 HCl/KCl solution at concentrations ranging from 5×10^{-7} to 1×10^{-4} M (see legend) normalised by the concentration. Spectra have been corrected for Rayleigh scattering. The arrows depict the trends in peak position as a function of increasing protonated resorufin (ResH) concentration. (**b**) Zoom of panel a showing the peak shifts at 5×10^{-6} to 1×10^{-4} M.

Figure 6.6 • (**a–c**) Optimised geometries of various protonated resorufin dimer aggregates in water computed with density functional theory using an implicit solvent model. Top row contains the dimer with the N–N configuration where the nitrogen atom is on the same side in the dimer, while the bottom row contains the N–O configuration with the nitrogen (blue) and oxygen (red) atoms on the same side of the dimer. Optimised geometries of the H-dimer (panel **a**), J-dimer head-to-tail (panel **b**), and J-dimer zigzag (panel **c**) are shown.

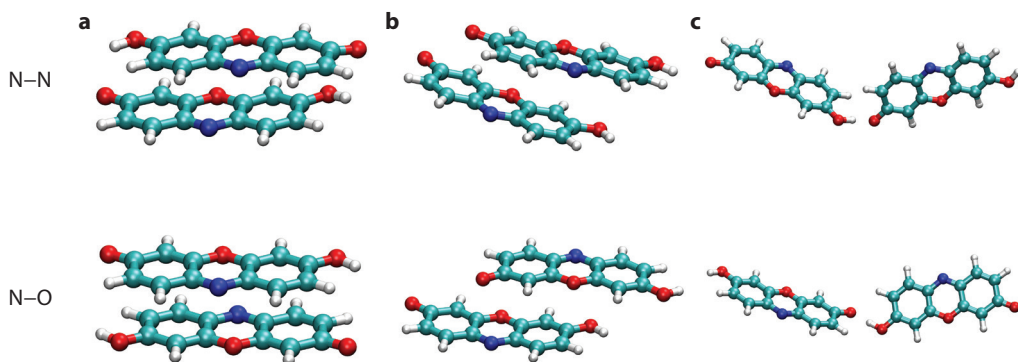scattering (see Methods), the relative absorption decreased and the spectral shape changed with increasing concentration, which is typical for aggregation. At low concentrations (0.5–1 µM), we identified the spectrum of the ResH monomer in line with previous reports.[245] Altogether, the change in the absorbance maxima as a function of the concentration confirms the presence of aggregated ResH in solution.

Density functional theory (DFT) simulations revealed that in aqueous solution both H- and J-aggregation are thermodynamically preferred over the monomer with a reaction enthalpy between −42.1 kJ/mol and −37.9 kJ/mol depending on the resorufin orientation and aggregation type. Here, three types of dimer aggregates were considered, each with a configuration where the nitrogen atoms of the resorufin are on the same (N–N) or the opposite side (N–O), which are shown in Figure 6.6a–c. J-aggregates with head-to-tail orientation were not stable in aqueous solution, because no minima on the potential energy surface were found for this type of dimers, and these aggregates were not considered further.

Time-dependent DFT was used to compute the UV–Vis absorption spectra of the aggregates to relate the thermodynamic data with experimental absorption spectra. The simulated absorption spectra are shown in Figure 6.7a–d. In the experimental spectra, we observed that the main absorption band at 480 nm is blue shifted (Figure 6.5b), which is in line with the simulated spectra of H-dimer aggregates (Figure 6.7a,b). Moreover, the band at 400 nm was increased in absorbance with respect to the band at 480 nm. This indicates the formation H-type aggregates with an N–O orientation, but further research is required to confirm this interpretation. A new red-shifted band at 570 nm appeared at higher concentrations in the experimental UV–Vis absorption spectra (Figure 6.5b). Based on exciton theory one would ascribe this red-shifted band to J-aggregation (see Section 2.2.1). However, the absorption band is at a much longer wavelength than we found for the simulated J-dimer aggregates (Figure 6.7f,g). Therefore, we believe that this band comes from the formation of Res⁻ molecules within the aggregates. Altogether, the absorbance of the blue-shifted peak is much larger than of the red-shifted one, strongly indicating the dominance of H-aggregation. Considering the thermodynamic calculations and comparing the experimental and simulated UV–Vis absorption spectra, we conclude that H-aggregates are preferentially formed in aqueous solution. The formation of zigzag J-aggregates or deprotonation within the H-aggregates is a minor pathway.

We further confirm that the two different excited-state fluorescence lifetimes measured in an aqueous solution of ResH are the result of molecular H-aggregation. We reconstructed the emission spectra of the $\ll$ 0.3-ns and 0.49-ns lifetime components to identify their molecular origin. Because the lifetime components have a similar emission spectrum identical to ResH, we conclude that both originate from ResH, either from monomeric molecules (0.49 ns) or aggregates ($\ll$ 0.3 ns) (Figure 6.8a). The lifetime of H-aggregates is known to be shorter because of efficient non-radiative pathways that are available when the molecules are in close contact, quenching the fluorescence.[67,68,246] Thus, the poor photophysical properties of ResH in aqueous solution appear to be a result of their aggregation behaviour.

The lifetime in an aqueous slurry of resorufin-stained zeolite-β was measured using 510 nm excitation, which allowed for simultaneous excitation of Res$^-$ and ResH. Upon confinement in the zeolite, two different fluorescent species were present resulting in a biexponential decay with lifetime components of τ_1 = 1.1 and τ_2 = 3.2 ns (Figure 6.8b). The reconstructed emission spectrum of the τ_1 = 1.1-ns component matches the emission spectrum of ResH (Figure 6.8c),[243,245] while the spectrum of the 3.2-ns lifetime component is in agreement with the spectrum of aqueous Res$^-$ (Figure 6.8d). No $\tau \ll$ 0.3-ns lifetime component was found for resorufin confined in the zeolite, showing that aggregation-induced quenching is suppressed inside the zeolite micropores at these concentrations, which leads to enhanced ResH fluorescence with respect to aqueous solution.

We compared the fluorescence lifetimes obtained from resorufin confined in the zeolite with references recorded in aqueous solution. The fluorescence lifetime of Res$^-$ increased marginally from 3.0 to 3.2 ns in presence of the zeolite, which indicates only limited interaction with the zeolite. Importantly, the fluorescence lifetime of monomeric ResH in-
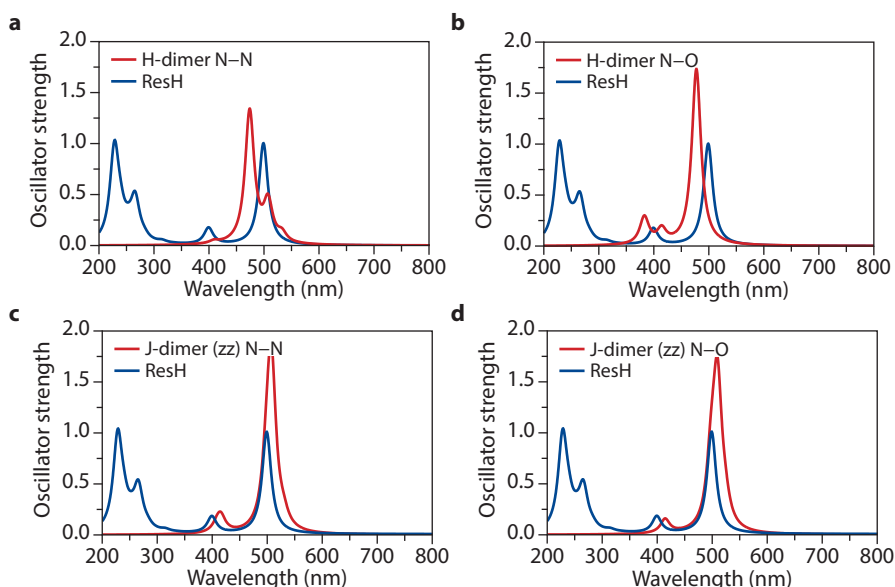
Figure 6.7 • (**a–d**) Simulated ultraviolet–visible absorption spectra of ResH compared with various protonated resorufin ResH dimer aggregates. The absorption spectra were computed with time-dependent density functional theory using an implicit solvent model. The spectra of the H-dimer ResH N–N (panel **a**), H-dimer ResH N–O (panel **b**), J-dimer zigzag (zz) N–N (panel **c**), and J-dimer zz N–O (panel **d**) with respect to ResH are shown.

creased through interaction with the zeolite, from 0.49 to 1.10 ns, resulting in enhanced fluorescence. Similar enhancements have been observed for the fluorophore pyronine Y, when strongly confined within microporous aluminophosphate crystals, as a result of the rigidity imposed on the molecule by the micropores.[68] Based on these observations, we expect that monomeric ResH is stabilised inside the zeolite micropores resulting in brighter ResH fluorescence upon confinement.

6.2.2 • Guest–guest and guest–host interactions

We characterised the interactions that affect ResH fluorescence inside the zeolite. First, the effect of the solution pH on the acid dissociation of resorufin confined inside the pores of
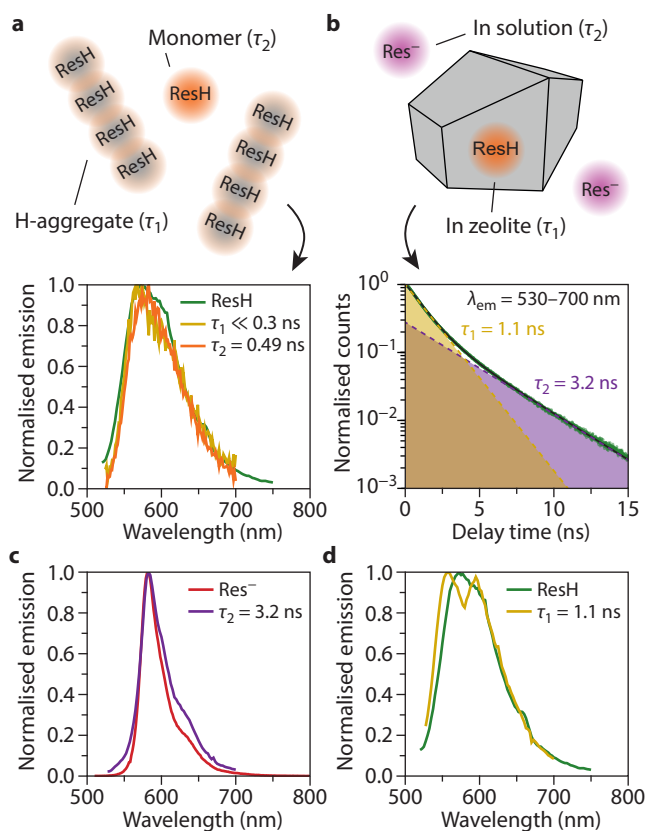
Figure 6.8 • (**a**) Normalised emission spectra of the $\tau_1 \ll 0.3$ ns and $\tau_2 = 0.49$ ns components of protonated resorufin (ResH) overlaid with a reference emission spectrum of ResH recorded in aqueous solution. We assign τ_1 to weakly fluorescent H-aggregates and τ_2 to fluorescent ResH monomers. The spectrum belonging to τ_1 0.3 ns was smoothed with a moving average over 25 nm. (**b**) Decay curve of the fluorescence from an aqueous slurry of resorufin-stained zeolite-β averaged over the detection wavelengths 530–700 nm (green dots) and a bi-exponential fit (black solid line). The decay components $\tau_1 = 1.1$ ns (yellow) and $\tau_2 = 3.2$ ns (purple) of the fit are indicated by the dashed lines. We assign τ_1 to ResH confined in the zeolite and τ_2 to deprotonated resorufin (Res⁻) in solution. (**c,d**) Normalised emission spectrum of the $\tau_2 = 3.2$ ns (panel **c**) and $\tau_1 = 1.1$ ns component (panel **d**) overlaid with the reference emission spectrum of Res⁻ and ResH recorded in aqueous solution, respectively.

zeolite-β was investigated. We measured the fluorescence emission spectrum after 45 min incubation of the zeolite in a pH = 7 aqueous solution of resorufin. Here, we recorded the emission spectrum of ResH excited close to its absorption maximum (λ_{ex} = 493 nm, Figure 6.9a). Addition of extra ammonia base to reach pH = 9 in solution, then followed by 35 min incubation, resulted in the loss of the ResH emission spectrum inside the zeolite. Instead, we recorded the emission spectrum of Res⁻ even when we excited close to ResH's absorption maximum (λ_{ex} = 493 nm, Figure 6.9b). Thus,

the pH in external solution affects the pH inside the zeolite crystal, which can be probed locally with resorufin via measurement of its dissociation state.

We further investigated the effect of the solution pH on the dissociation state of resorufin in two different crystals, incubated in a resorufin solution of pH = 7 or pH = 9 (Figure 6.9c,d). We followed the acid dissociation of resorufin by exciting close to the absorption maximum of ResH (λ_{ex} = 493 nm) or Res⁻ (λ_{ex} = 560 nm) and recording the fluorescence emission. Based
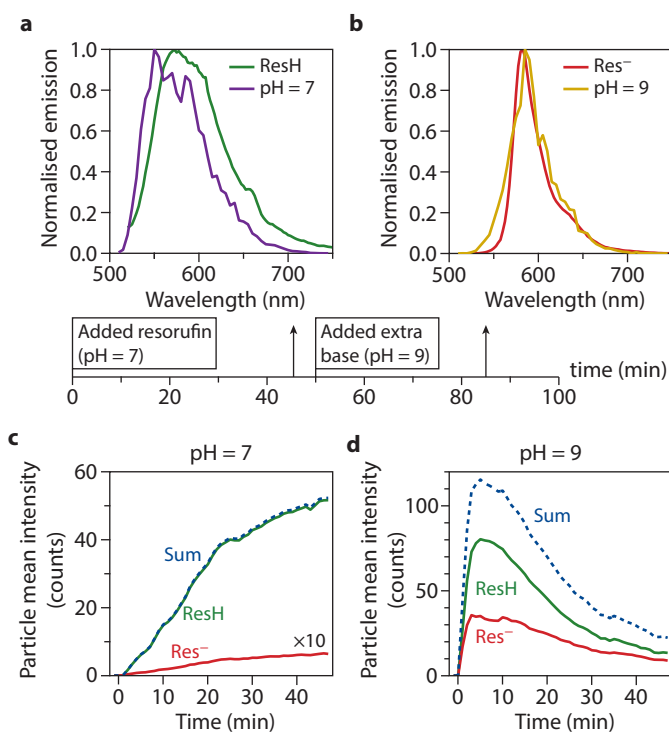
Figure 6.9 • (**a,b**) Fluorescence emission spectra of resorufin inside a zeolite-β crystal (λ_{ex} = 493 nm). The zeolite crystal was soaked in Milli-Q water followed by incubation in ~10 nM ammonia and 50 μM resorufin starting at time = 0 min. Fluorescence emission spectra after 45 min (panel **a**; solution pH = 7) and after addition of additional ammonia base to a total concentration of ~5 μM followed by 35 min incubation (panel **b**; solution pH = 9) are shown. Reference spectra of protonated resorufin (ResH; panel **a**) and deprotonated resorufin (Res⁻; panel **b**) in aqueous solution indicate that ResH is predominantly present at a pH = 7, while the ResH has been deprotonated at pH = 9. (**c,d**) Total intensity as a function of time inside two different H-zeolite-β crystals after incubation in an ammonia pH = 7 (panel **c**) or 9 solution (panel **d**) and 50 μM resorufin. An excitation wavelength of 493 nm and 560 nm was used to selectively excite ResH and Res⁻, respectively. The signal from the 560 nm excitation in panel **d** was multiplied by 10. The emission was recorded in the centre plane of the zeolite with confocal laser scanning microscopy in all panels.

Figure 6.10 • (a–c) Optimised geometries of dimer aggregates of various protonated resorufin aggregates in the straight pores of zeolite-β, computed with density functional theory. The straight pores run horizontally in the image and are not explicitly shown. Only the dim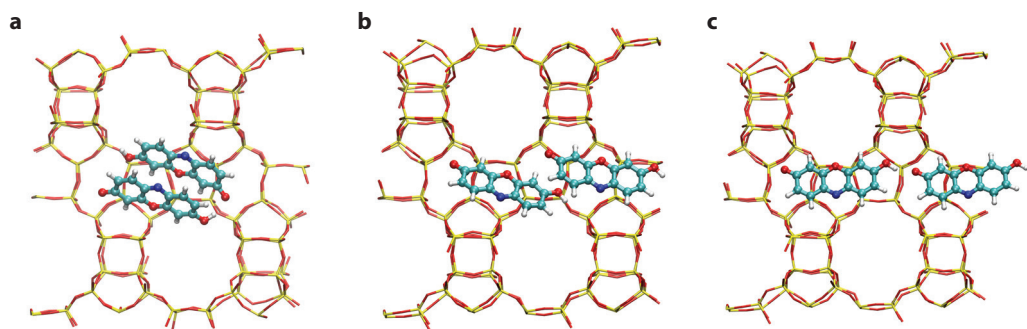er aggregates with N–N configuration with H-dimer (panel **a**), J-dimer head-to tail (panel **b**), and J-dimer zigzag (panel **c**) are shown.

on the UV–Vis absorption spectra of the molecules, cross-excitation of Res⁻ at 493 nm and ResH at 560 nm excitation wavelengths can occur to a slight degree (Figure 6.2b,c). In Figure 6.9c, the temporal evolution of the ResH and Res⁻ fluorescence intensity inside a single zeolite-β crystal is shown at solution pH = 7. The Res⁻ fluorescence intensity was low compared to the ResH intensity at solution pH = 7, and the Res⁻ signal was likely a result of cross-excitation of ResH (note the 10× magnification of the Res⁻ signal). The intensity profile of ResH did not yet reach a maximum or plateau after 45 min. At solution pH = 9, both ResH and Res⁻ were present simultaneously within the zeolite (Figure 6.9d). In contrast to the filling at pH = 7, the intensity profile of ResH did reach a maximum within 10 min at pH = 9. The summed intensity decreased steadily after its peak, and the loss in ResH or Res⁻ was not compensated by gain of the conjugate dissociation state. This indicates that the measured resorufin fluorescence intensity inside the zeolite crystal is sensitive to another process besides the local pH. We examined three processes that could lead to a loss in ResH fluorescence intensity during the filling of the zeolite particle.

The decrease in overall fluorescence in the zeolite could be a result of aggregation-induced quenching at high concentrations. The enthalpy of ResH aggregation inside the straight

pores of zeolite-β was computed with DFT. The same types of dimer aggregates as in aqueous solution were considered, and their structures are shown in Figure 6.10a–c. In contrast to aggregation in aqueous solution, H-stacking is always unfavoured, with an endothermic reaction energy of > 10 kJ/mol, showing that the straight channels are not large enough to accommodate H-dimers. J-type aggregation is very favourable leading to the formation of J-dimers in zigzag orientation with a reaction enthalpy of −49.4 kJ/mol and −71.3 kJ/mol with respect to two different relative orientations (N–N and N–O). These aggregates are known to quench fluorescence in confinement. Martínez-Martínez et al. reported that fluorescent molecules confined in microporous MgAPO had the highest relative quantum yield when pore structure did not allow close-packed J-aggregates, and the fluorescence intensity decreased when J-aggregation was possible.[68]

ResH J-aggregation in the pores of zeolite-β was further investigated with UV–Vis absorption spectroscopy and DFT calculations. We compared the baseline-corrected absorption spectrum of zeolite-β crystals incubated in an aqueous resorufin solution with the absorption spectrum of monomeric ResH (Figure 6.11). We found that the main absorption band was red-shifted by 20–25 nm with respect to the monomer, while the absorption band at 400
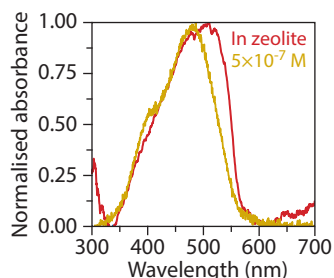
Figure 6.11 • Normalised ultraviolet–visible absorption spectrum in zeolite-β overlaid with the bulk absorption spectra of protonated resorufin in aqueous solution at 5×10^{-7} M. The zeolite-β sample was incubated for 5 minutes in 100 mM resorufin at pH = 9. The absorption spectrum of the zeolite sample was recorded with microspectroscopy and was baseline corrected.

nm remained the same. Moreover, we found a similar red shift and broadening for dried and Milli-Q-water-washed samples both incubated in a resorufin solution with pH = 7 and 9. The red shift is an indication that ResH J-aggregation occurs within the pores of zeolite-β.

The measured red shift in absorbance was compared with time-dependent DFT computations of the J-aggregate UV–Vis absorption spectra shown in Figure 6.12a–d. The measured red shift of 20–25 nm was larger than the computed 6–15 nm shift as a result of confinement by the zeolite; therefore, the red shift is likely the result of J-aggregation. Our computations revealed that a red shift of 11–27 nm is expected for J-aggregates, which is in line with our observations. Nevertheless, we must be careful with these assignments as the shifts in absorption wavelength as result of aggregation are small and the accuracy of the calculations and measurement is limited. Based on the
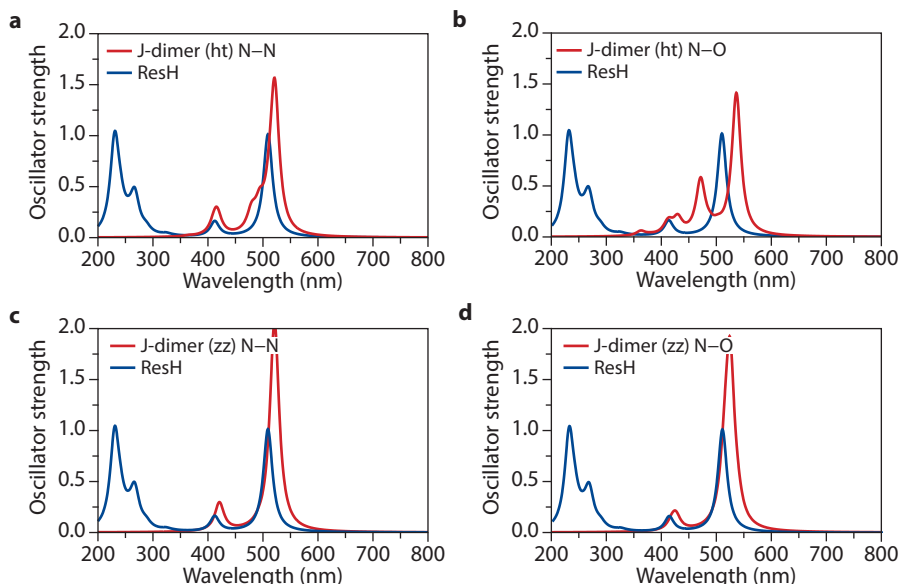
Figure 6.12 • (**a–d**) Simulated ultraviolet–visible absorption spectra of ResH compared with various protonated resorufin ResH dimer aggregates. The absorption spectra were computed with time-dependent density functional theory using the optimised geometries of the molecules embedded in the zeolite. The zeolite framework has not been taken into account during the simulation of the spectra and was only considered during the geometry optimisation. The spectra of J-dimer head-to-tail (ht) N–N (panel **a**), J-dimer ht N–O (panel **b**), J-dimer zigzag (zz) N–N (panel **c**), and J-dimer zz N–O (panel **c**) with respect to ResH are shown.
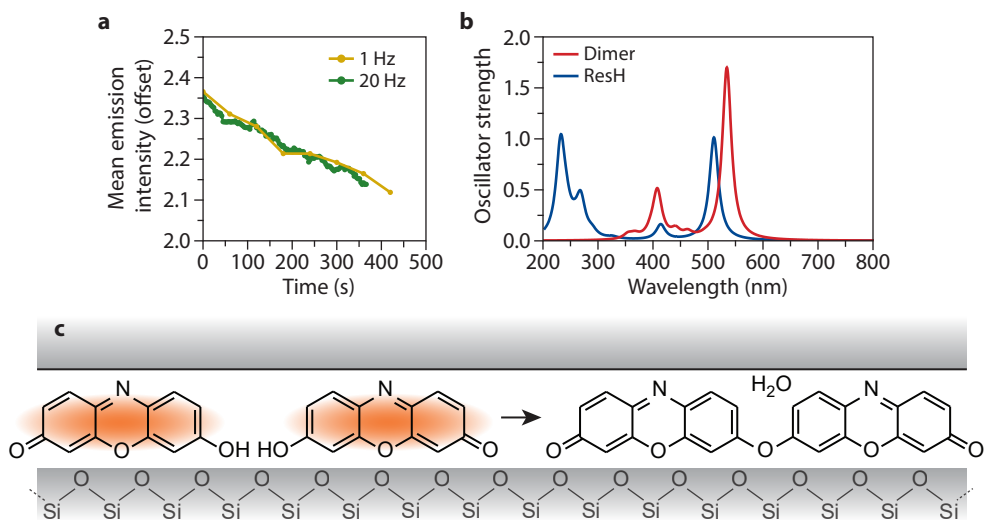
Figure 6.13 • (**a**) Total emission intensity from a H-zeolite-β crystal incubated in Milli-Q water followed by 32 minutes incubation in 12.5 mM HEPES (pH = 7.4) and 50 μM resorufin (λ_{ex} = 493 nm). The emission was recorded with confocal laser scanning microscopy through the centre plane of the same crystal at a rate of 1 and 20 Hz. The 20 Hz series was recorded after the 1 Hz series and therefore had to be offset by 0.35 to overlay the curves. At both imaging rates, the decrease in mean intensity was similar, which indicates that resorufin photobleaching due to laser exposure is not a dominant factor in the observed fluorescence intensity decrease over time. (**b**) Simulated ultraviolet–visible absorption spectra of protonated resorufin compared with a covalent resorufin dimer. The absorption spectra were computed with time-dependent density functional theory using the optimised geometries of the molecules embedded in the zeolite. The zeolite framework was not taken into account during the simulation of the spectra and was only considered during the geometry optimisation. (**c**) Schematic representation of the condensation reaction forming a covalent dimer.

---

thermodynamic calculations, simulation of the absorption spectra, and UV–Vis absorption microspectroscopy, the formation of J-aggregates in a zigzag geometry likely occurs when ResH is embedded in the pores of zeolite-β. These aggregates are known to reduce the fluorescence intensity.

Two alternative explanations for the decrease in intensity are less likely: photobleaching by the laser and the formation of a non-fluorescent covalent dimer. First, we investigated the effect of photobleaching by recording the same field of view at a fast and slow imaging rate, thereby changing the laser exposure (Figure 6.13a). We found that the intensity decrease is independent of the excitation rate, which shows that the loss of fluorescence intensity is not related to photobleaching. Second, we investigated the

condensation reaction of two ResH molecules into a non-fluorescent covalent dimer (Figure 6.13c). Alkylation of the 7-hydroxy group of resorufin, such as in the covalent dimer, is expected to result in the quenching of the resorufin fluorescence.[240,247] Our DFT calculations showed that the condensation reaction is very endothermic and has a reaction enthalpy of +71.2 kJ/mol. Therefore, it seems unlikely that the large intensity decrease can be explained by this pathway. Nevertheless, the simulated UV–Vis absorption spectrum of the dimer in the zeolite contained a main adsorption peak around 534 nm with another band at 400 nm, which is similar to the measured experimental UV–Vis absorption spectrum in zeolite-β (compare simulated red-shift in Figure 6.13b with experimental one in Figure 6.11). Thus, it cannot be excluded that small fractions of a
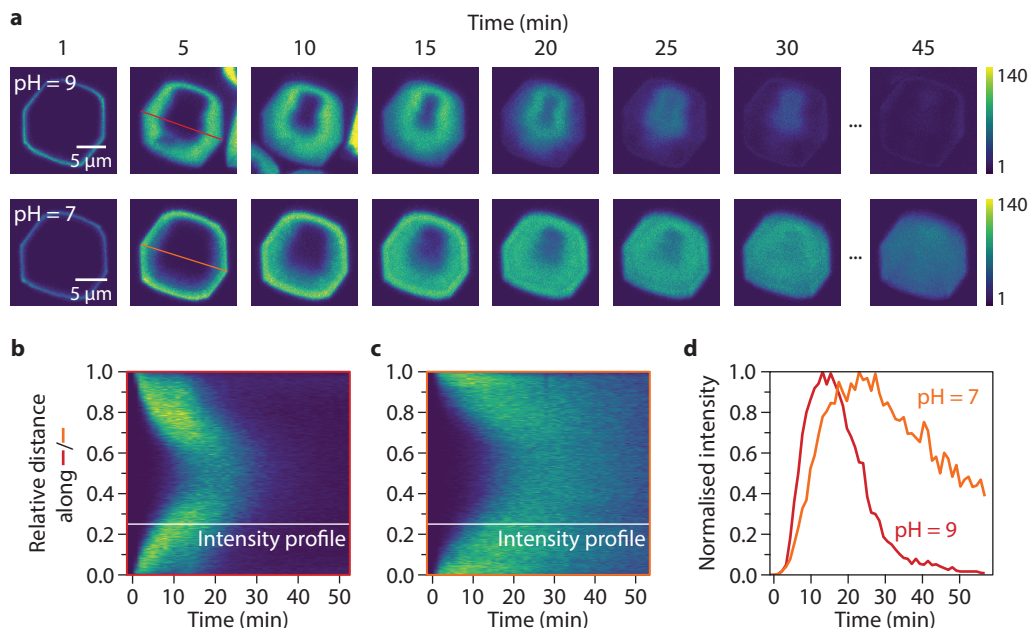
Figure 6.14 • (**a**) Confocal laser scanning microscopy micrographs of H-zeolite-β crystals incubated in Milli-Q water followed by an incubation in 50 μM resorufin at two pH starting at time = 0 min (λ_{ex} = 493 nm). The asymmetry in the filling is due to the tilt of the crystal with respect to the image plane. Because of this, the left bottom part of the zeolite is close to the edge parallel to the image plane and therefore closer to the outer surface of the zeolite. (**b,c**) Kymographs along the red and orange lines in panel **a** are respectively shown in panels **b** (pH = 9) and **c** (pH = 7). (**d**) Intensity profile at 25% of the relative position (white lines in panels **b,c**) in pH = 9 and 7 conditions.

covalent dimer are formed. Considering these factors, a decrease in fluorescent intensity due to J-aggregation inside zeolite-β is the most plausible explanation for the observed ResH fluorescence intensity.

6.2.3 • Interactions studied via the filling profile

The different resorufin filling profiles at solution pH = 7 and pH = 9 (such as shown in Figure 6.9c,d) were further investigated. To understand these kinds of profiles, we have a closer look at the guest–guest and guest–host interactions identified in the previous section and their effect on the filling of the zeolite. The zeolite crystals were first incubated in water, and an aqueous resorufin solution was added at time = 0 min. The resorufin diffusion into two zeolite-β crystals at an external pH = 7 and

9 is shown in Figure 6.14a. We represent the intensity profile through the crystals' centre with a kymograph (Figure 6.14b,c), and the intensity profile at a quarter relative position is plotted in Figure 6.14d. Here, a fast rise followed by a slower decay of the fluorescence intensity describes both profiles. However, the intensity peaks later and the rates of the rise and decay are lower at an external pH = 7.

The filling behaviour provides insight into guest–guest and guest–host interactions. The concentration profile of resorufin and ammonia inside the zeolite was computed over time with a diffusion model. From this, we calculated an intensity profile by either considering aggregation-induced quenching or deprotonation of ResH as a function of the modelled local pH. Here, we assumed that all fluorescence originated from ResH. The models are

described in the methods section of this chapter. Then, we compared the simulated and experimental kymographs to find the dominant guest–guest and guest–host interactions. The intensity profile with a fast rise followed by a slower decay at pH = 7 in Figure 6.14d could be reproduced in both scenarios indicated before involving aggregation-induced quenching or deprotonation of resorufin as a function of the modelled local pH.

First, the model that considered the local pH inside the zeolite pores was evaluated. A rise in the filling profile was a result accumulation of ResH into the zeolite pores in acidic conditions, whereas a decay was due to deprotonation of ResH to Res$^-$ by the ammonia base. Deprotonation only occurred when the total concentration of ammonia in external solution $[A]_{tot}$ was approximately greater than the concentration of zeolite Brønsted-acid sites $[Z]_{tot}$. Based on the Si/Al ratio and the density of Si tetrahedra in the zeolite-β structure, we computed a $[Z]_{tot}$ of 0.5 M.[7,8] This is much larger than $[A]_{tot}$ in experiment, which we approximated to be 1×10^{-8} M and 5×10^{-6} M in a solution of pH = 7 and 9, respectively. Thus, to explain deprotonation of ResH inside the zeolite, we have to consider conditions that deviate strongly from the expected $[A]_{tot}$ and $[Z]_{tot}$ in experiment.

We discuss three different conditions where qualitatively different filling occurs, containing both a rise and decay in the intensity profile. The simulated filling behaviour over time is shown in a kymograph of the ResH intensity in Figure 6.15a–c. The intensity profile at a relative position of 25% (Figure 6.15d–f) can be directly compared with the experimental results shown in Figure 6.14d. First, we consider the scenario that $[Z]_{tot} = 0.5$ M, which matches the expected concentration of zeolite Brønsted-acid sites. For deprotonation to occur, $[A]_{tot}$ should be 5–8 orders of magnitude higher than in experiment, which describes a strong affinity of the zeolite for ammonia. A decay is observed in the filling profile at $[A]_{tot} = 1$ M and $[Z]_{tot} = 0.5$ in Figure 6.15a,d. Second, we consider filling profiles where $[Z]_{tot} \ll 0.5$ M yields both a rise and decay in the filling pro-

file, e.g., $[Z]_{tot} = 10^{-5}–10^{-4}$ M and $[A]_{tot} = 1 \times 10^{-4}$ M in Figure 6.15b,c,e,f. Such a simultaneous increase in $[A]_{tot}$ and decrease in $[Z]_{tot}$ with respect to the experimental conditions might be possible if protons from the zeolite are exchanged for NH_4^+ species, maintaining charge balance.

We gain additional insight in the shape of the intensity profiles via a plot of the pH as a function of the ammonia concentration inside the zeolite $[A]_{zeo}$ in Figure 6.15g–h. This plot can be considered as a titration curve of the zeolite Brønsted-acid sites and resorufin with an ammonia base. In the simulated filling profiles, the ammonia concentration changes over time as a result of diffusion into the zeolite particle, whereas in the titration curve the ammonia concentration is increased linearly. We took a constant resorufin concentration for the titration curve, matching the external resorufin concentration $[R]_{tot}$. This is simplified with respect to the simulated filling profiles, where the resorufin concentration inside the zeolite changes over time due to diffusion. The titration curves are discussed below.

In the first set of $[A]_{tot}$, $[R]_{tot}$, and $[Z]_{tot}$ concentrations, the titration curve revealed that the pH was governed by the protons supplied by the zeolite at low $[A]_{zeo}$ (Figure 6.15g). After the pH-buffering capacity of the acidic zeolite was used by the basic ammonia at increasing $[A]_{zeo}$, the pH rapidly rose, and the ammonia started buffering at pH $\approx$ 9. The steep slope above the $pK_{a,R}$ explains the rapid decay in the intensity profile (Figure 6.15d). Here, a small change in ammonia concentration resulted in almost full deprotonation of the resorufin. In the second condition, the slope of the pH as a function of $[A]_{zeo}$ is less steep and approximately constant around the $pK_{a,R}$ (Figure 6.15h). This resulted in similar rise as decay rates in the intensity profile (Figure 6.15e). A slower decay than rise was observed in a third condition (Figure 6.15f), where the slope in the titration curve around the $pK_{a,R}$ is small. A large extent of deprotonation was only achieved close to equilibrium of $[A]_{zeo}$ with the external solution, i.e., the right side of Figure 6.15i, leading to a slow intensity decay
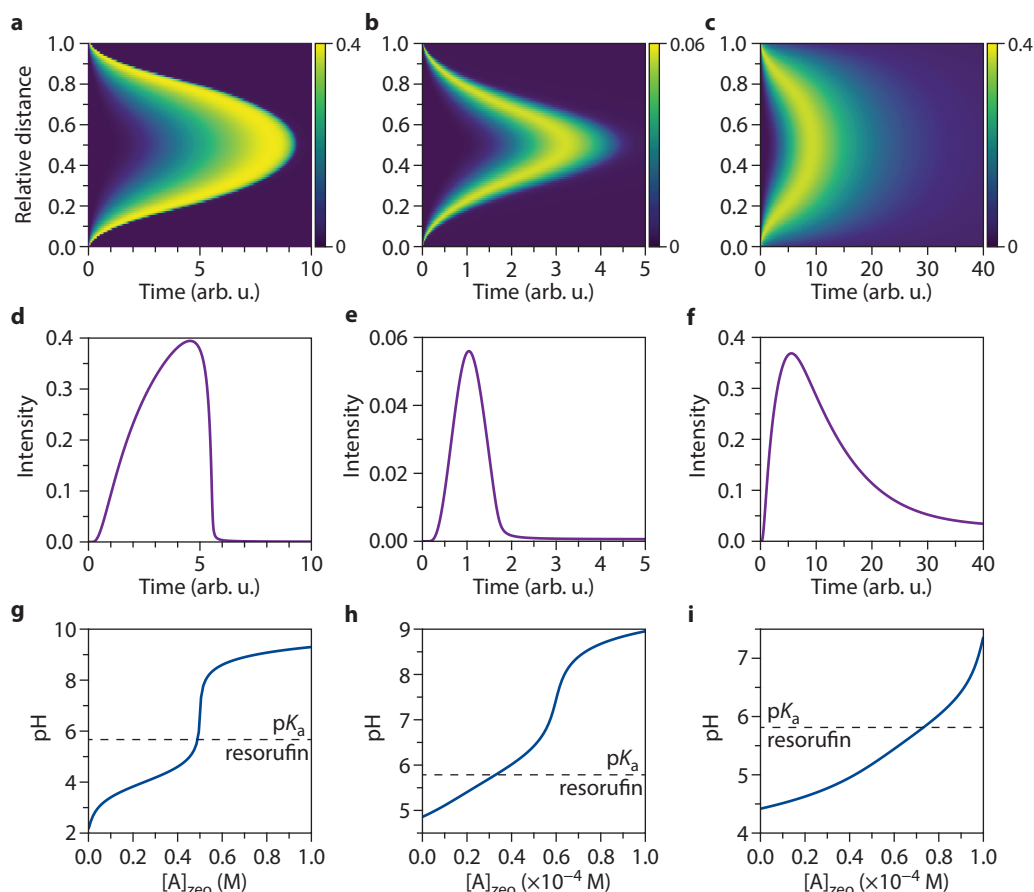
Figure 6.15 • (**a–c**) Kymograph of the intensity of protonated resorufin computed with a one-dimensional diffusion model that accounts for a weak acid–base equilibrium between the ammonia, resorufin, zeolite Brønsted-acid sites, and water. The total concentration of ammonia and resorufin was fixed at a relative position of 0 and 1, while the concentration of zeolite Brønsted-acid sites was kept constant in the domain <0,1>. The ammonia and resorufin were allowed to diffuse in with a diffusion coefficient of 0.01. The concentrations were $[Z]_{tot} = 0.5$ M, $[A]_{tot} = 1$ M, and $[R]_{tot} = 5 \times 10^{-5}$ M (panel **a**); $[Z]_{tot} = 1 \times 10^{-5}$ M, $[A]_{tot} = 1 \times 10^{-4}$ M, and $[R]_{tot} = 5 \times 10^{-5}$ M (panel **b**); and $[Z]_{tot} = 5 \times 10^{-5}$ M, $[A]_{tot} = 1 \times 10^{-4}$ M, and $[R]_{tot} = 5 \times 10^{-5}$ M (panel **c**). (**d–f**) Intensity profile at 25% of the relative position for the conditions in panels **a–c**, respectively. (**g–i**) pH as a function of $[A]_{zeo}$ for a fixed $[Z]_{tot}$ and $[R]_{tot}$, where $[A]_{zeo}$ is varied from zero to $[A]_{tot}$. The concentrations $[Z]_{tot}$, $[A]_{tot}$, and $[R]_{tot}$ are the same as in panels **a–c**, respectively. The pK_a of resorufin is indicated by the horizontal dashed line.

as observed in experiment (Figure 6.14d). The slow decay could not be reproduced when simulating the experimental conditions at pH = 9, using the same parameters as in Figure 6.15c,f but a 250× higher ammonia concentration. In these conditions, our model shows that the resorufin is not slowly deprotonated over time. The ammonia would buffer at pH ≈ 9 close to the

equilibrium of $[A]_{zeo}$ (such as in Figure 6.15h), and the slow decay in the intensity profile is lost—in discrepancy with experiment.

More likely is the second scenario, where the fluorescence intensity is quenched at increasing resorufin concentration due to J-aggregation of the molecules. The fluorescence intensity $I(x, t)$

was modelled as the ResH concentration $C(x,t)$ minus a factor accounting for aggregation-induced quenching, $I(x,t) \propto c(x,t) - Ac(x,t)^2$, with A a proportionality constant. The intensity profile matched the shape of the experimental profile well both at pH = 7 and 9 (Figure 6.16a,c). The stretching of the curve could be explained by an increase in the surface barrier (Figure 6.16b,c). We conjecture that a higher concentration of ResH aggregates in solution at pH = 7 might block surface pore openings, thereby increasing the surface barrier. This leads to the stretching of the intensity profiles as observed in experiment. Variations in the surface barrier of individual zeolites crystals from the same synthesis have been reported.[36,39] This can account for the observed variations in the shape of the profile between crystals from the same synthesis batch. Altogether, we have established above that both the local pH and J-aggregation are factors that affect the observed fluorescence intensity at 493 nm excitation, which can both be probed with resorufin. Based on the modelling results, we conclude that J-aggregation is the dominant interaction explaining the filling profile in the conditions used in this work.

6.2.4 • HEPES buffer for diffusion and accessibility measurements

Interpretation of the zeolite crystal filling for accessibility and diffusion measurements is most straightforward when some guest–host and guest–guest interactions are suppressed. Then, we can approximate that the ResH fluorescence is directly proportional to its local concentration. We used a HEPES buffer to quench guest–host and guest–guest interactions. Its effectiveness is demonstrated by the slower total ResH fluorescence intensity decrease in a HEPES buffer close to pH = 7 (Figure 6.17) than with the ammonia base at pH = 7 (Figure 6.14a). We rationalise that HEPES mitigates changes in local pH as well as J-aggregation. First, HEPES is a pH-buffer molecule and keeps the pH constant around 7, where resorufin deprotonation occurs only slowly. The sodium ions present in solution, which were added to adjust the pH of the buffer, could acts as a counterion for the hydroxyl anions, thereby allowing HEPES to buffer the pH throughout the micropores. Second, the relatively high concentration of HEPES molecules (250× higher than resorufin in solution) could serve as a spacer between resorufin molecules, preventing J-aggregation. In this situation, we could regard the resorufin molecules as a fluorescent tracer for the diffusion of HEPES molecules into the zeolite micropores. Based on the diameter of the HEPES molecule (6.9 Å), we expect that it can enter the zeolite's micropores as it is 0.4 Å smaller than resorufin (7.3 Å) but find it unlikely that the molecule
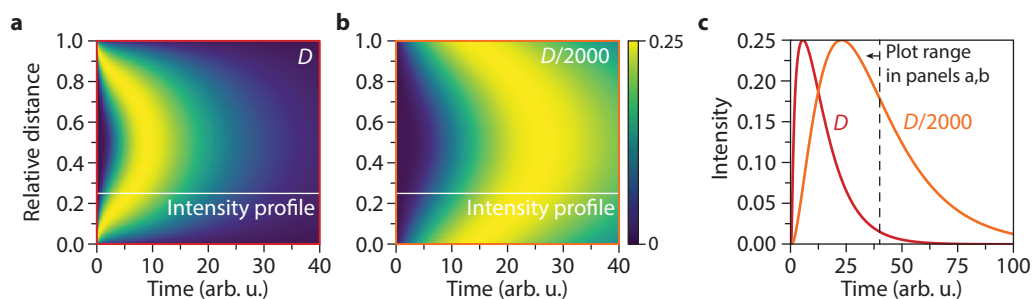
Figure 6.16 • (**a,b**) Kymograph of the intensity of protonated resorufin corrected for J-aggregation. The kymograph was computed with a one-dimensional diffusion model that accounted for no diffusion barrier at the surface of the crystal in panel **a** and a diffusion barrier of $D/2000$ in panel **b**. The diffusion coefficient D of protonated resorufin was 0.01. The concentration of protonated resorufin was fixed to 1 at a relative position of 0 and 1, and diffusion barriers with a width of 0.01 were placed next to the resorufin sources. Simulation details can be found in the methods section. (**c**) Intensity profile at 25% of the relative position for the conditions in panels **a,b**.

Time (min)

1   5   10   15   20   25   30   45

water / HEPES

5 µm

110

1
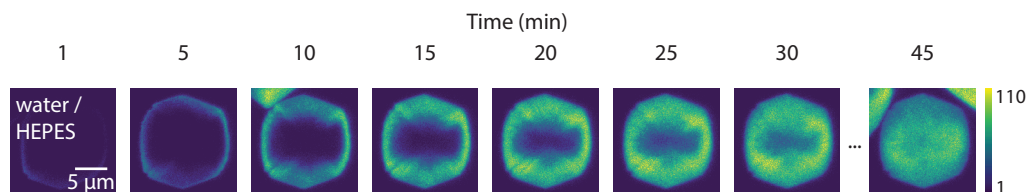
Figure 6.17 • Confocal laser scanning microscopy micrographs of a H-zeolite-β crystal incubated in Milli-Q water followed by an incubation in 50 µM resorufin in 12.5 mM HEPES (pH = 7.4, λ_{ex} = 493 nm). The sample imaged through the centre plane of the crystal over a period of 45 min.

can pass resorufin in the micropores. We used HEPES in the resorufin accessibility and diffusion measurements below.

6.2.5 • Pore space of zeolite-β mapped with resorufin

The accessibility and diffusion were visualised in the hierarchical and anisotropic pore structure of zeolite-β crystals. We observed strong variations in the ResH fluorescence intensity from different zeolite crystals incubated for 5 days (Figure 6.18a), despite the homogeneous appearance of the zeolite crystals in SEM. The filling is in most cases homogenous, and resorufin staining revealed that the micropore structure is accessible throughout the whole crystal (Figure 6.18b). The intensity is lower at the interface between the subunits (Figure 6.18c). This demonstrates that these regions do not contain a microporous structure and allow for ResH H-aggregation or have a lower accessibility.[248] We used rhodamine 110 (Figure 6.18g) complementary to resorufin to visualise non-microporous defect voids because it does not fit inside the zeolite's micropores.[238,249] These defect voids make up a *secondary* pore space, which together with the micropores form a hierarchical pore structure. We found a strong heterogeneity in the accessible secondary pore space, ranging from crystals with a secondary pore structure only at the edges to a fully permeated network (Figure 6.18d). The pyramidal subunits, which are marked yellow in Figure 6.18h, in many cases have an elaborate accessible secondary pore structure (Figure 6.18e). Recent crystal-growth simulations confirmed that the pyramidal subunits are highly defective.[250–252] Most of the secondary

pores fan out from the centre all the way to the outer surface. We conjecture that these pores are formed from defects in an early stage of the crystal growth and propagate in the growth direction.[253] Focused ion beam (FIB)–SEM of a cut through the centre crystal plane revealed that the density of meso- and macropores is significantly higher in the pyramidal subunits than in other regions (Figure 6.18f). This shows that the higher density of these pores resulted in a more interconnected secondary pore network.

6.2.6 • Diffusion of resorufin/HEPES in zeolite-β

We demonstrate that ResH can be used as a probe to visualise mass transport at the single-crystal level without background contributions from the surrounding solution, which provides good contrast in the early stages of diffusion. Snapshots from a time-lapse microscopy video of ResH diffusion into a large zeolite-β crystal are shown in Figure 6.19a. Resorufin preferentially enters the crystal through the side edges via the exposed straight channels as marked by the white arrows in Figure 6.19b (i.e., crystallographic *a*- and *b*-axes in Figure 6.18h). The van der Waals diameter of resorufin (7.3 Å) is slightly larger than the size of the straight pores (6.7 Å), which are known to accommodate molecules with dimensions larger than their pore opening.[7,8,255] The observed diffusion anisotropy is in line with our understanding of the pore structure that the 'sinusoidal' pore openings are exposed at the surface of the pyramidal subunits. Resorufin is 1.7 Å larger than the sinusoidal pore openings (5.6 Å in polymorph A) and is not likely to dif-
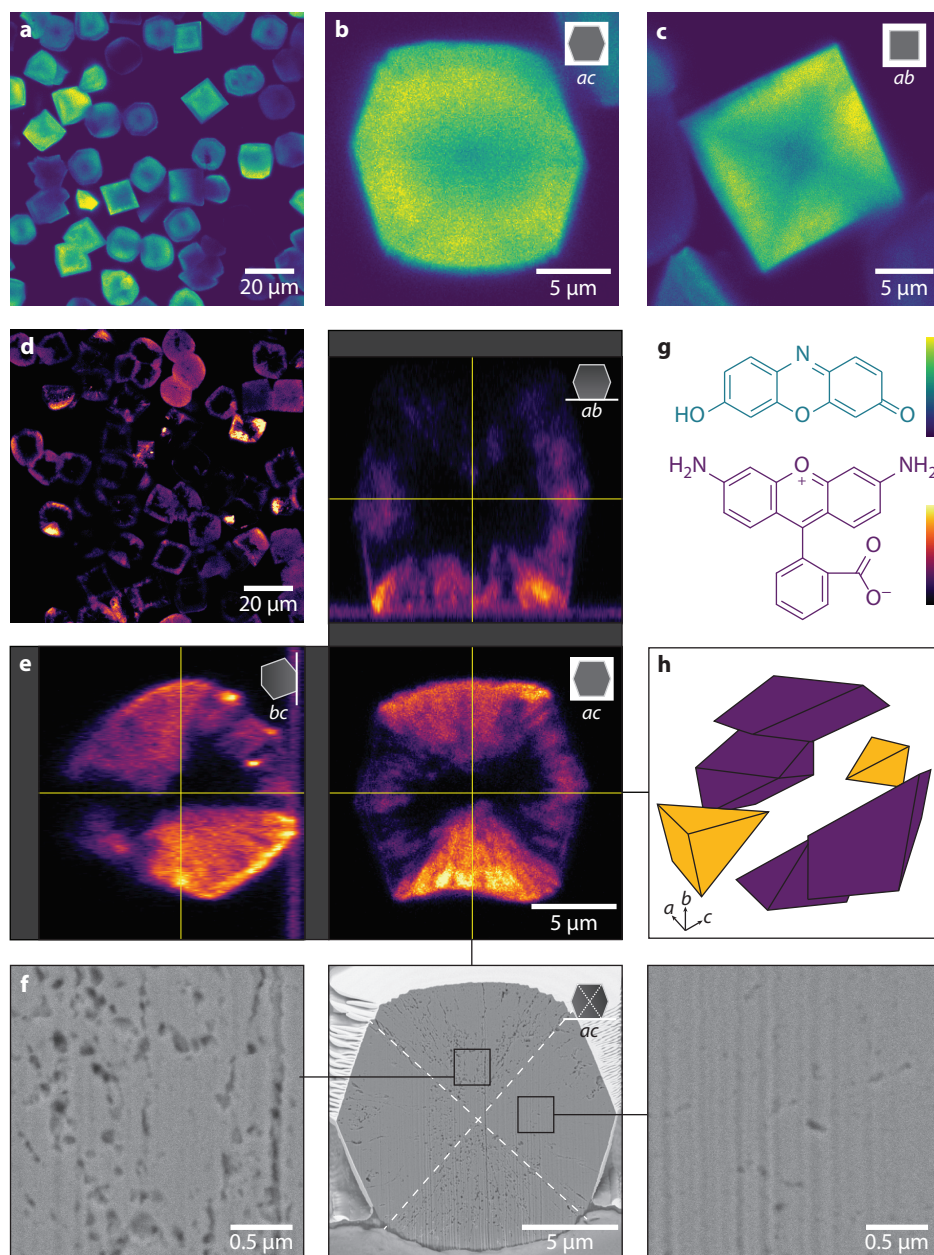
Figure 6.18 • (**a–e**) Confocal laser scanning microscopy micrographs of H-zeolite-β crystals incubated for 5 days in a resorufin in 12.5 mM HEPES (panels **a–c**; pH = 7.4, λ_{ex} = 493 nm) and rhodamine 110 solution (panels **d,e**). A strong inter-crystal heterogeneity is apparent in the zoomed-out micrographs in panels **a,d**. Most crystals are filled homogeneously with resorufin in panel **b**. The boundaries between the crystal subunits can be discerned sometimes in panels **b,c**. Orthogonal cross sections through the centre of the same crystal are shown in panel **e**. The cartoon in the top right corner indicates the crystal orientation. (**f**) Focused ion beam–scanning electron microscopy cross section shows the meso- and macropore structure. The dotted

lines indicate the subunit boundaries, and the black boxes indicate the magnified regions in the pyramidal (left) and side (right) subunits. Rhodamine 110 does not fit into the zeolite's micropores and mostly stains in the pyramidal subunits (panel **e**) because of their higher meso- and macroporosity. (**g**) Chemical structure of protonated resorufin (top) and rhodamine 110 at neutral pH (bottom).[254] (**h**) Exploded view of zeolite-β and its subunits with the pyramidal subunits marked in yellow and side subunits marked in purple. The crystallographic axes are indicated below.[253]

fuse through—even so when considering the random pore geometry in the disordered zeolite-β—which explains the negligible diffusion along the direction of these pores.[7,8]

The subunit boundaries impede diffusion along the direction of the straight pores, as evidenced by the clear diffusion front along this line.[248,251,256] To visualise the diffusion barrier more clearly, Figure 6.19c,d shows the intensity profile along two lines parallel to the straight channels as a function of time.[253] Figure 6.19c

traces the red line of Figure 6.19b, which avoids the subunit boundaries, while Figure 6.19d traces the orange line of Figure 6.19b, which crosses such boundary. Until the ResH molecules reached the boundary, the filling proceeded similarly along both lines. The subunit boundary at 2.5 μm distance from the crystal surface (Figure 6.19d) slows down the filling as a result of the imposed diffusion resistance (Figure 6.19e).[248] Figure 6.19a,b reveals that the diffusion front is ragged with spikes towards the crystal's centre, following the di-
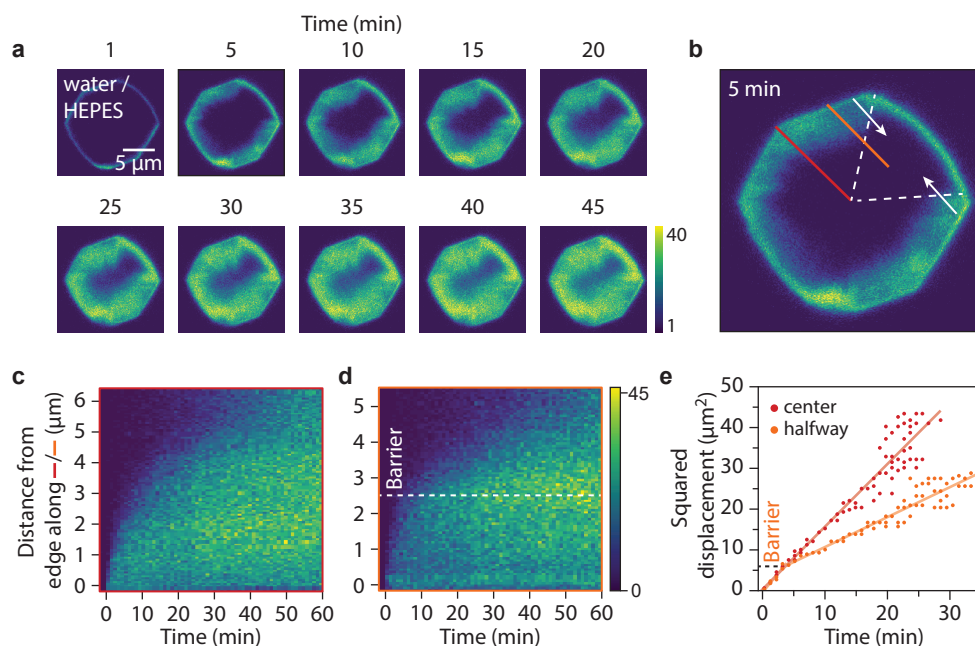
Figure 6.19 • (**a**) Confocal laser scanning microscopy images of a H-zeolite-β crystal in Milli-Q water followed by an incubation in 50 μM resorufin in 12.5 mM HEPES (pH = 7.4, λ_{ex} = 493 nm) starting at time = 0. (**b**) At 5 min incubation time in resorufin solution, it becomes apparent that the diffusion is along the direction of the straight channels (white arrows) and is hindered by the inter-subunit boundaries (white dashed line). (**c,d**) Kymograph along the red *centre* (panel **c**) and orange *halfway* (panel **d**) solid lines marked in panel **b**. (**e**) Squared displacement of the diffusion front along the centre and halfway positions (dots) and fits serve as guide to the eye (solid lines). The subunit boundary is indicated by the dashed horizontal line in both panels **d,e**.

rection of the secondary pore network towards the crystal's centre. However, a large diffusion improvement in the direction of the secondary pore network in the pyramidal subunits is not observed. Large enhancements have been reported in hierarchical zeolites with an elaborate secondary pore network, provided that the network was interconnected along the diffusion direction (see also Chapter 5).[181,208] We suspect that the secondary pore network in our samples is not sufficiently interconnected to facilitate large diffusion enhancements.

We showcase the quantitative analysis of the diffusion along the straight channels via kymograph analysis. The kymograph described in the Figure 6.19c was taken for diffusion coefficient estimation. We fitted the first 15 min of the kymograph to prevent contributions from resorufin diffusing in from out-of-plane directions. Some parts of the zeolite have a higher brightness after filling than others. To reduce this effect, we normalised the intensity to the equilibrium sorption profile at 60 min (Figure 6.20a). We fitted the kymograph to the well-known solution of Fick's second law (Equation 2.2) assuming a constant source of resorufin molecules diffusing in from one end, which models the excess in solution, and a concentration-independent diffusion coefficient D, i.e.,

$$\frac{C(x,t)}{C_0} = 1 - \mathrm{erf}\left(\frac{x}{2\sqrt{Dt}}\right) \qquad (6.1)$$

with c the resorufin concentration, c_0 the resorufin concentration at the source, x the distance from the source, and t the time after exposure to the source. We assume that the measured intensity I is directly proportional to the local resorufin concentration $I_{\mathrm{normal}}(x,t) \propto c(x,t)$. The normal diffusion model and residuals of the fit are shown in Figure 6.20b,c. A diffusion coefficient of 7×10^{-15} m^2 s^{-1} was found for this crystal.

The normal diffusion model is not able to fully
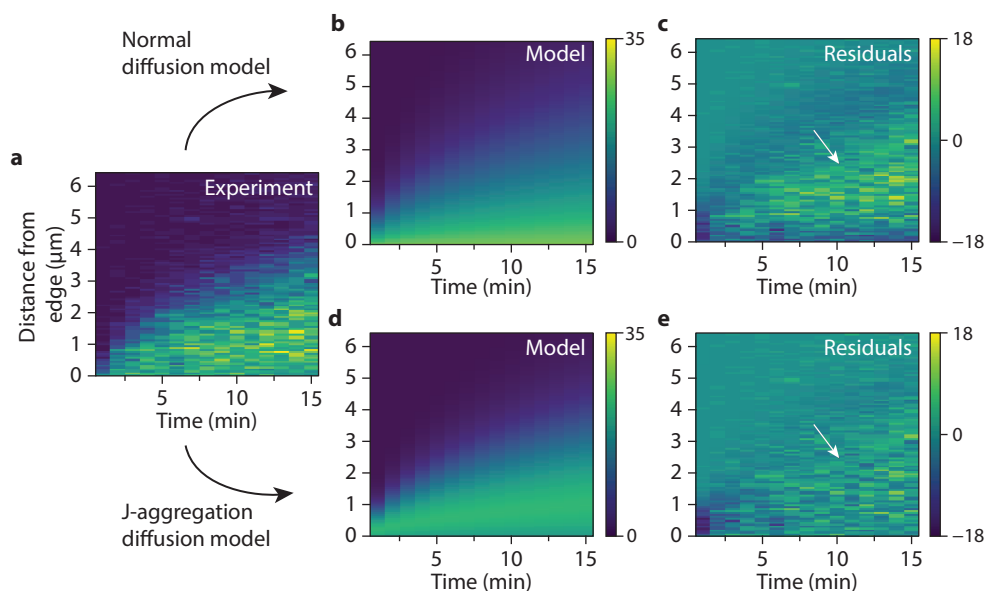
Figure 6.20 • (**a**) Kymograph along red solid line marked in (*centre* position in Figure 6.19b) cropped and normalised to last five frames of the full range (Figure 6.19c). (**b,c**) Normal diffusion model fit to the kymograph in panel **a** plotted in the same false colour scale (panel **b**) and its residuals (panel **c**). (**d,e**) J-aggregation diffusion model fit to the kymograph in panel **a** plotted in the same false colour scale (panel **d**) and its residuals (panel **e**). The aggregation diffusion model has smaller residuals, particularly in the domain marked by the white arrows in panels **c,e**.

describe the kymograph. The model underestimates the measured intensity in the domain indicated by the white arrow in the residuals plot (Figure 6.20c). We investigated whether this could be the result of aggregation-induced fluorescence quenching due to J-aggregation. Following our findings in Section 6.2.2, we included aggregation-induced quenching in the model using Equation 6.12. The J-aggregation model and residuals of the fit are shown in Figure 6.20d,e. The J-aggregation model describes the measured intensity better than the normal diffusion model, as evidenced by the residuals closer to zero (Figure 6.20e). A diffusion coefficient of 3×10^{-15} m^2 s^{-1} was found for this crystal, which is significantly lower than 7×10^{-15} m^2 s^{-1} found with the normal diffusion model. This analysis shows the importance of the understanding of guest–host and guest–guest interactions for diffusion coefficient estimation.

6.3 • Conclusions

It was found that—contrary to current understanding—the protonated form of resorufin is a viable fluorescent probe. Inside the zeolite, H-aggregation-induced fluorescence quenching is largely suppressed and protonated resorufin is stabilised, resulting in a bright fluorescence. The results described in this chapter indicate that resorufin is pH-responsive and that the solution pH affects both the dissociation state of resorufin inside the zeolite pores and the rate of entrance into the zeolite. We directly visualised anisotropic diffusion through the straight pores of zeolite-β and found a diffusion coefficient of 3×10^{-15} m^2 s^{-1}. Moreover, we directly showed the diffusion barrier imposed by the zeolite's subunit boundaries. In contrast to interference microscopy and infrared microimaging, the taken approach allows rapid and direct visualisation of diffusion in microporous crystals with complex shapes. Analysis is straightforward as the diffusion can be readily analysed without the need for simulations to estimate the concentration profile as a two-dimensional projection. The small size of the resorufin probe makes it uniquely placed to investigate accessibility, diffusion (barriers), and possibly even the local pH in zeolites and other microporous materials.

6.4 • Contributions & acknowledgements

6.5 • Methods

6.5.1 • Experimental

Chemicals and materials. Aerosil 130 (SiO$_2$, Evonik), aluminum hydroxide (Al(OH)$_3$, 65%, Acros Organics), ammonium hexafluorosilicate ((NH$_4$)$_2$SiF$_6$, 98%, Sigma-Aldrich), ammonium hydroxide (NH$_3$, 35 w%, Sigma-Aldrich), ammonium nitrate (NH$_4$NO$_3$, ≥ 99 %, Sigma-Aldrich), 4-(2-hydroxyethyl)-1-piperazineethanesulfonic acid (HEPES, ≥ 99.5%, Sigma-Aldrich), resorufin (95%, Sigma-Aldrich), rhodamine 110 (C$_{20}$H$_{14}$N$_2$O$_3$ · HCl, ≥ 99.0%, Sigma-Aldrich), potassium hydroxide (KOH, 85%, Alfa Aesar), and tetraethylammonium hydroxide (TEAOH, 35 w% aqueous solution, Sigma-Aldrich). All chemicals were used as received with no further purification except water, which in all cases was purified through a Milli-Q system to a resistivity of 18.2 MΩ·cm.

Preparation of large zeolite-β crystals. Large zeolite-β crystals were synthesised using a secondary silica source method similar to that of Pham et al.[185] The typical precursor gel composition was as fol-

lows: 4 SiO_2 : x Al_2O_3 : 1.92 TEAOH : 0.36 $(NH_4)_2SiF_6$: 0.4 KOH : 31.20 H_2O, with x varied depending on desired Si/Al. Synthesis was carried out in the following way, using Si/Al = 90 as an example. 12.62 g TEAOH, 0.93 g H_2O and 0.66 g KOH were added to a plastic beaker in that order and stirred until a clear solution had formed. 6.01 g SiO_2 was then slowly added under stirring until a thick yellow gel had formed. This constitutes Solution I. To a separate plastic beaker, 7.57 g TEAOH, 1.64 g $(NH_4)_2SiF_6$ and 0.10 g $Al(OH)_3$ were stirred until a homogeneous gel had formed. This constitutes Solution II. Solution II was then added to Solution I and vigorously stirred for 1 h, after which it was aged without stirring for 24 h. This formed a pale-yellow solid gel that was then crushed using a pestle and mortar and transferred to a Teflon lined autoclave for hydrothermal treatment under autogenous pressure at 150 °C for 7 days. After treatment, samples were washed three times with water and dried at 120 °C overnight. The zeolites were then calcined with a temperature ramp of 1 °C/min to 550 °C where they were kept for 6 h. This calcination procedure was repeated prior to characterisation, spectroscopy, and microscopy measurements, ideally not longer than three weeks before the measurement. All zeolite-β used in this work have a Si/Al of 50 unless otherwise stated.

Ion exchange. In 50 mL polypropylene centrifugal tubes, 2 M ammonium nitrate solution was added to zeolite sample (~1 mL NH_4NO_3(aq) per 0.1 g zeolite). The tubes were placed in an oil bath at 50 °C that was magnetically stirred at 250 rpm. After 40 minutes the tube caps were momentarily loosened to prevent pressure build-up. The exchange was continued for 24 h at 50 °C. The zeolite slurries were vacuum filtrated over a Büchner funnel and washed three times with 30 mL water. The NH_4^+-exchanged zeolite was heated overnight in a Nabertherm Muffle furnace at 450 °C to decompose the ammonium and obtain acidic zeolite with a proton cation.

Characterisation of the zeolite-β crystals. High-resolution scanning electron microscopy (SEM) and focused ion beam (FIB)–SEM was performed on a FEI Helios NanoLab G3 UC instrument. Prior to the measurement, the zeolite crystals were loaded on Al stubs with carbon tape and sputter-coated with 10–20 nm of Pt. The exterior of the particles was imaged by collecting secondary electrons with an Everhart–Thornley detector or through-the-lens detector. For cross sections, an extra layer of Pt was deposited via FIB-assisted deposition, before removing half of the particle with a Ga FIB and cleaning of the exposed cross section with precision milling. The cross section was imaged by collecting backscattered electrons with a through-the-lens detector.

X-ray diffraction patterns were collected on a Bruker D2 Phaser operated at 30 kV and 10 mA with a cobalt radiation source, Co Kα = 1.789 Å.

Resorufin solutions. To make a 1 M resorufin stock solution in water, ammonium hydroxide was added to a 25 mL volumetric flask to dissolve the resorufin. The ammonium hydroxide content was varied to obtain the desired pH, and citrazinic acid buffer or HCl/KCl was added to obtain aqueous protonated resorufin in acidic conditions at pH = 2.

Ultraviolet–visible (UV–Vis) absorption spectroscopy. UV–Vis absorption spectroscopy of the aqueous resorufin solutions was done on a UV-Cary 200 spectrophotometer. The UV–Vis microspectroscopy measurements were performed with a CRAIC 20/30 PV UV–Vis–NIR microspectrophotometer using a 35× objective. A 75 W xenon lamp was used for illumination. A blank of zeolite-β incubated in water was recorded, which was set as reference, before measuring zeolite-β samples containing resorufin.

Excitation, emission, and fluorescence lifetime measurements. The room temperature UV–Vis excitation and emission spectra were recorded on an Edinburgh Instruments FLS920 fluorescence spectrometer equipped with a 450 W xenon arc lamp, mirror optics for powder samples, and photo-multiplier tube (R928, Hamamatsu). For the excitation and emission beams, a double monochromator according to Czerny–Turner design (TMS300, Bentham) was used. The spectra were corrected for the instrumental response and wavelength-dependent lamp output. Fluorescence lifetime measurements were performed with the same set-up using a 510 nm (EPL-515, Edinburgh Instruments) picosecond pulsed diode laser operating at 20 MHz. Time-resolved emission spectroscopy was performed to record the decay curves as a function of emission wavelength in the range of 530–700 nm. The instrument response function was obtained from a

suspension of scattering silica spheres in water. The zeolite-β was incubated in a 100 μM resorufin solution for a couple of hours and dried overnight in air at room temperature. Prior to the measurement, a droplet of water was added to the stained sample, yielding a zeolite slurry.

Confocal laser scanning microscopy. Time-lapse movies and emission spectra were recorded using a Leica TCS SP8 confocal microscope equipped with a super continuum white light laser (SuperK, NKT Photonics), HyD detector and a 93×/1.30 glycerol/water immersion objective (Leica). The laser light was circularly polarised using a quarter waveplate. The laser excitation wavelength was 493 nm for protonated resorufin (ResH) and 560 nm for deprotonated resorufin (Res⁻), while the detection range was 510–700 nm and 570–700 nm, respectively. The photoluminescence was time gated from 0.3–12 ns. The coverslips were rinsed with isopropanol and dried to a 0.45 μm filtered nitrogen gas stream followed by oxygen-plasma cleaning for 5 min. The coverslip was placed in a Attofluor™ Cell Chamber (Thermo Fisher) and zeolite-β sample was sprinkled onto the coverslip. Excess zeolite was removed by tapping the cell while upside down. Water was first added to the in-situ cell until saturation of the zeolite crystals to ensure no influence from capillary forces. Once a suitable crystal was located, imaging was started and a solution of Res⁻ was gently introduced. In a typical time-lapse experiment, 500 μL Milli-Q water was added to the liquid cell and the confocal laser scanning microscopy time-lapse recording was started. After two minutes 500 μL of 100 μM resorufin solution was added to the liquid cell, which was defined as the start of the experiment.

To investigate the intensity distribution of zeolite-β at equilibrium conditions, the zeolite-β sample was incubated ex-situ. Confocal laser scanning microscopy micrographs were recorded with a 100×/1.4 oil-immersion confocal objective (Leica) on the same set-up as earlier described. ResH was imaged with the settings described above and rhodamine 110 was excited at 500 nm and its fluorescence emission was recorded from 510–600 nm. To incubate the samples ex-situ, a couple mg of sample was put in a 4 mL glass vial and 2 mL Milli-Q water was added. After approximately one minute, 2 mL 100 μM resorufin or rhodamine 110 solution was added, and the vial was shaken briefly. The sample was ho-

mogeneously dispersed over the bottom of the vial and stored in the dark for 5 days. In all cases, the solution was still coloured indicating that an excess of fluorescent molecules was present. The liquid was removed, and the sample was washed with Milli-Q water twice to remove surface-bound fluorophores. After washing, the water was removed with a pipette and the sample was put on a cleaned coverslip. A droplet of type F immersion oil (Leica) was deposited over the sample to roughly index match the crystals with their surroundings. The hydrophobic character of the oil prevented dissolution of the fluorophores into the liquid medium. The sample was imaged directly.

6.5.2 • Data processing, analysis, and modelling

Excited-state lifetime and time-resolved emission spectroscopy. The lifetime decay curves were fitted with a custom-written iterative reconvolution routine in MATLAB 2019b (The MathWorks), which has conceptually been described in Section 2.2.1. The tails and background of the instrument response function (IRF) were removed with a threshold of 100 counts. The maximum of the decay curve was set as zero delay time, and the IRF was convolved with the decay models. In some cases, an additional $\ll 0.3$ ns lifetime component had to be modelled in the decay curve. This was not modelled as an exponential decay but was approximated by a set amplitude in the bin at 0 ns delay time. The exponential decay(s) and 0 ns contribution were summed to model the full decay curve before convolution with the IRF. We coin their combination a *zero delay–exponential hybrid* model.

The decay curve of aqueous Res⁻ was fitted with a mono-exponential decay model, whereas aqueous ResH was properly described by a zero delay–exponential hybrid model including a bi-exponential decay with a fixed component of 3.01 ns to account for Res⁻ signal. The area below the $\tau \ll 0.3$-ns lifetime component did not converge properly when the initial guess was far off. Because the short component is dominant in the decay curve, we used a fit of the decay curve with only the contribution at 0 ns delay time as an initial guess for the fit of the zero delay–exponential hybrid model. If a lower and probably incorrect initial guess was picked, the ResH lifetime became shorter, so the value presented in this

chapter is an upper limit of the ResH lifetime in solution.

Fluorescent species were identified via their emission spectrum by recording the arrival times of the emitted photons per range of emission wavelength and reconstructed the emission spectra of individual lifetime components. The emission spectra of the lifetime components were recovered from the lifetime decay curves as follows. A decay curve intensity $I(t)$ with delay time t was fitted with bi-exponential decay for two fluorescence components

$$I(t) = A_1 e^{-t/\tau_1} + A_2 e^{-t/\tau_2} \qquad (6.2)$$

with the fluorescence lifetime τ_i and amplitude A_i of the i-th fluorescent species. The lifetimes τ_1 and τ_2 were obtained from the average decay curve over the full emission wavelength range. As the detection wavelength was altered, the relative contribution from each fluorescent species also changed. In a second step, the amplitudes A_1 and A_2 were fitted at each detection wavelength with a fixed τ_1 and τ_2 to quantify the relative contribution. The contribution of the i-th fluorescent species to the detected signal at some wavelength λ is

$$\int_0^\infty A_i e^{-t/\tau_i} \mathrm{d}t = A_i \tau_i. \qquad (6.3)$$

Therefore, by integrating the contribution of each of these species in the decay curve at different wavelengths, the emission spectrum of the two species with distinct fluorescence lifetimes was reconstructed. The reconstructed emission spectrum of $A_i \tau_i$ belonged to the species with excited-state lifetime τ_i and was used directly to identify the fluorescent molecule. For spectrum reconstruction of aqueous ResH, we fixed τ_1 and τ_2 to 0.03 and 0.48 ns. Here, the bi-exponential model converged better than the zero delay–exponential hybrid model, yielding qualitatively similar spectra with less noise.

UV–Vis absorption background correction. Aggregation and/or agglomeration of ResH results in the formation of molecular aggregates that are large enough to scatter visible light. The aggregates are usually much smaller than the wavelength of visible light; hence, their scattering behaviour can be described by Rayleigh scattering. The scattering mag-

nitude has a strong dependency on the wavelength. The scattered light will not reach the detector in a UV–Vis absorption spectroscopy experiment and will be incorrectly interpreted as absorbed light. We corrected the UV–Vis absorption spectra for Rayleigh scattering as follows. Raleigh scattering scales with wavelength λ as $I/I_0 \propto 1/\lambda^4$, with I the intensity of scattered light and I_0 the incident light intensity. The absorbance A of a purely Rayleigh scattering solution with constant background A_0 can be derived[257,258]

$$
\begin{aligned}
A &= \log_{10}\left(\frac{I_0}{I}\right) + A_0 \\
&= \log_{10}\left(\frac{I_0}{I_0 - I_{\text{scatter}}}\right) + A_0 \qquad (6.4) \\
&= \log_{10}\frac{1}{1 - \alpha\lambda^{-4}} + A_0
\end{aligned}
$$

with α a proportionality constant. Equation 6.4 was fitted to the UV–Vis spectra in the domains 300–325 nm and 675–700 nm using a least-squares fit algorithm. The spectra were corrected by subtraction of the Rayleigh scattering component.

A linear baseline was subtracted for spectra recorded inside the zeolite with microspectroscopy. The baseline was estimated from the absorbance at wavelengths of 330 and 620 nm.

Density functional theory computations. First-principles static calculations were performed using the CP2K[259] and Amsterdam Density Functional (ADF)[217] software packages. The equilibrium geometries of the ground states of the gas-phase compounds were determined at the B3LYP-D3[227,228,260] and TZ2P[221] level of theory using the ADF software. In order to mimic the presence of aqueous solution implicit water solvent represented by conductor-like screening model (COSMO) was used.[261] The zeolite environment was modelled by using a periodic models of siliceous zeolite-β within the CP2K software. Geometries were optimised using the BLYP-D3 functional,[228] TZVP-MOLOPT[262] basis set and GTH[263] pseudopotentials. The reaction enthalpy ΔE for the formation of an aggregate (agglomerate) from two separate molecules was computed as

$$\Delta E_{\text{complex}}^{\text{gas-phase}} = E_{\text{complex}}^{\text{gas-phase}} - 2E_{\text{ResH}}^{\text{gas-phase}}, \qquad (6.5)$$

where $E_{\text{complex}}^{\text{gas-phase}}$ is the ground-state energy of the selected aggregate (H-type or J-type) or ResH covalent dimer and $E_{\text{ResH}}^{\text{gas-phase}}$ is the energy of a single ResH molecule in the gas phase. Similarly, the reaction enthalpy $E_{\text{complex}}^{\text{zeo}}$ for the formulation of an aggregate inside zeolite-β was computed as

$$\Delta E_{\text{complex}}^{\text{zeo}} = E_{\text{complex}}^{\text{zeo}} - 2E_{\text{ResH}}^{\text{zeo}} + E_{\text{zeo}}, \qquad (6.6)$$

where $E_{\text{complex}}^{\text{zeo}}$ and $E_{\text{ResH}}^{\text{zeo}}$ are the ground-state energy of the selected aggregate (H-type or J-type) or dimer and monomer, respectively, loaded in the straight channels of the zeolite-β. is the internal energy of the empty zeolite, without ResH.

Vertical electronic excitation energies of selected molecules were determined by using time-dependent density functional theory at the B3LYP/TZ2P level of theory as implemented within the ADF software using the COSMO solvent model for water. The absorption spectra were computed on both gas-phase and zeolite-embedded models. In the case of zeolite-embedded model, only geometries of the resorufin and its derivatives were considered, not the framework itself.

Modelling of the intensity profile along the straight channels. To model one-dimensional diffusion in the direction of the straight pores, we numerically solved Fick's second law (Equation 2.2) in discretised space via a forward Euler scheme, where c is the concentration of a species, D its diffusion coefficient, and x the position.[264] The total concentration of resorufin and ammonia was kept constant at the edges of the simulation box ($x = 0$ and 1) and their concentration profile inside the box was computed using Equation 2.2. The concentration of the zeolite Brønsted-acid sites was kept constant in the box.

Next, the local pH was computed from the time- and space-dependent concentration of ammonia and resorufin, which followed from the diffusion model, and the constant concentration of zeolite Brønsted-acid sites and water. Then, we computed the dissociation of resorufin from the local pH to obtain a concentration of ResH in each discretised point in space. We modelled the pH as an equilibrium of the weak acid resorufin[257]

$$K_{\text{a,R}} = \frac{[\text{H}^+][\text{R}^-]}{[\text{HR}]}, \qquad (6.7)$$

the zeolite weak Brønsted-acid sites

$$K_{\text{a,Z}} = \frac{[\text{H}^+][\text{Z}^-]}{[\text{HZ}]}, \qquad (6.8)$$

the weak base ammonia

$$K_{\text{b,A}} = \frac{[\text{A}^+][\text{OH}^-]}{[\text{A}]}, \qquad (6.9)$$

and water

$$K_{\text{w}} = [\text{H}^+][\text{OH}^-] \qquad (6.10)$$

with [X] the concentration of species X (R = resorufin, Z = zeolite Brønsted-acid sites, and A = ammonia), $K_{\text{a,X}}$ the acid dissociation constant of species X, and $K_{\text{b,X}}$ the base dissociation constant of species X. Charge balance in the system can be written as

$$[\text{A}^+] + [\text{H}^+] = [\text{R}^-] + [\text{Z}^-] + [\text{OH}^-]. \qquad (6.11)$$

Then, we can write Equation 6.11 in terms of $[\text{A}]_{\text{tot}}$, $[\text{R}]_{\text{tot}}$, $[\text{Z}]_{\text{tot}}$, $[\text{H}^+]$, and the dissociation constants using the relations that described the acid/base dissociation equilibria in Equation 6.7–Equation 6.10, $K_{\text{w}} = K_{\text{a,X}}K_{\text{b,X}}$, $[\text{A}]_{\text{tot}} = [\text{A}^+] + [\text{HA}]$, $[\text{R}]_{\text{tot}} = [\text{R}^-] + [\text{HR}]$, and $[\text{Z}]_{\text{tot}} = [\text{Z}^-] + [\text{Z}]$. Here, $[\text{X}]_{\text{tot}}$ is the total concentration of the species X, i.e., the sum of dissociated and non-dissociated molecules. The resulting equation was written in the form of a fifth order polynomial for $[\text{H}^+]$. The dissociation constants used, $K_{\text{a,R}} = 10^{-5.8}$, $K_{\text{a,Z}} = 10^{-4}$, $K_{\text{a,A}} = 10^{-9.3}$, and $K_{\text{w}} = 10^{-14}$, were based on reported values[244,257,265] and on computed K_{a} values for acidic silanols on a quartz surface.[266] The fifth order polynomial could be rapidly solved for values of $[\text{H}^+]$ with a polynomial roots solver. Only real and positive solutions were accepted, which resulted in one solution of $[\text{H}^+]$ per set of $[\text{A}]_{\text{tot}}$, $[\text{R}]_{\text{tot}}$, and $[\text{Z}]_{\text{tot}}$. The ResH concentration $[\text{HR}]$ was computed from $[\text{H}^+]$. Its concentration inside the zeolite, $c(x, t)$, is directly proportional to the measured fluorescence intensity $I(x, t) \propto c(x, t)$ in our model.

We modelled aggregation-induced fluorescence quenching and assumed that quenching is instantaneous. The ResH concentration inside the zeolite, $c(x, t)$, was simulated with the diffusion model described before. The measured intensity is

$$I_{\text{J-aggregation}}(x, t) \propto c(x, t) - Ac(x, t)^2 \qquad (6.12)$$

with a proportionally constant A. We picked A as such that $I_{\text{J-aggregation}}(x, t) = 0$ at equilibrium. To model a surface diffusion barrier, we reduced the diffusion through a thin slice (1% relative width) at the edges of the simulation box.

Molecular size calculation. The molecular size of resorufin and HEPES was estimated using the atomic coordinates after energy minimisation with the MM2 force field. This method is native to the Perkin Elmer Chem3D software. The diameter of the smallest cylinder that fully enclosed the atom coordinates of the molecule was computed with the RADI software.[267,268] The van der Waals radii of the atoms in contact with the cylinder were added to the computed diameter to account for the electron–electron repulsion between the molecule and pore wall, yielding the molecular diameter.

Chapter 7

Summary and outlook

7.1 • Summary

Catalysis is a pillar of modern society as it is essential in the production of everyday products, such as fuels, pharmaceutical intermediates, and plastics. The transition from fossil-feedstock-based production to more sustainable, circular production processes has to be established in the near future. Innovations including the development of new catalysts and the optimisation of existing ones will be of paramount importance to make this transition happen. These catalysts are often solid materials, which we call heterogeneous catalysts. We focussed in this PhD thesis on industrially relevant zeolite materials, which have an anisotropic, ordered network of pores with a diameter < 2 nm (micropores). Zeolite particles are often embedded in a support material with a pore diameter of ≥ 2 nm (meso- and macropores) together making up a heterogeneous catalyst particle. For the development of new catalyst materials or optimisation of existing ones, characterisation of their pore space and a detailed understanding of mass transport through the pores are required.

In this PhD thesis, we investigated and applied fluorescent molecules or nanoparticles (guests) to probe the pore space of heterogeneous catalysts (hosts) and mass transport therein. The fluorescent emitters report on properties of the catalyst via guest–host interactions. Therefore, we referred to the emitters as *fluorescent reporters* or *probes* in this PhD thesis. Guest–host interaction can be a resistance on the movement of the reporters by the pore space, reversible and irreversible adsorption of probes on the pore wall, or a chemical reaction between the guest and host (Figure 7.1). It is advantageous to follow reporters via their fluorescence because it can be detected with high sensitivity, e.g., to determine the location of the reporter, which makes it possible to probe individual molecules or nanoparticles. A second advantage is that the fluorescence emission spectrum is often dependent on the chemical identity of the fluorescent reporter. Thus, chemical reactions of the guest with the host can be followed directly via the guest's emission spectrum.

Analysis of the trajectories obtained with single-molecule tracking in inorganic porous hosts is often challenging because trajectories are short and/or motion is heterogeneous. In **Chapter 3**, we presented the software package *DiffusionLab* for motion analysis of such challenging datasets. This approach relies on the pooling of trajectories with a similar motion behaviour into a *population*. The average motion characteristics of a population can be computed and compared without losing information at the single-molecule level about, e.g., the spatial distribution of adsorption. We demonstrated the software via the analysis of simulated trajectories resembling the motion of molecules with reversible adsorption in a three-dimensional space. Movement of the simulated molecules in and out of focus—in combination with the reversible adsorption—resulted in short trajectories with heterogeneous motion behaviour. We found, in agreement with an earlier study,[61] three different types of trajectories. Mobile trajectories resembled molecules that were constantly moving, whereas immobile trajectories resembled stationary molecules that were adsorbed. We observed a third type of trajectories that contained both mobile and immobile segments. The individual trajectories were first classified based on properties that described aspects of the trajectory, such as its *length* and *tortuosity*. We showed that classification models constructed with machine learning performed excellently for the classification of our simulated datasets. The classification model could be adapted manually for the classification of datasets with similar motion behaviour, and we used this insight to create the classification model in **Chapter 5**. Next, the diffusion coefficient of the population was computed with MSD analysis. We demonstrated the classification and motion analysis by correctly recovering the (simulated) diffusion coefficient of the molecules in between adsorption events.

In **Chapter 4**, we introduced a microfluidic device designed for the characterisation of fluorescent reporters in confinement. The device consists of a two-dimensional *model pore* with a height of 50 nm. This design allowed for the measurement of long trajectories, which fa-
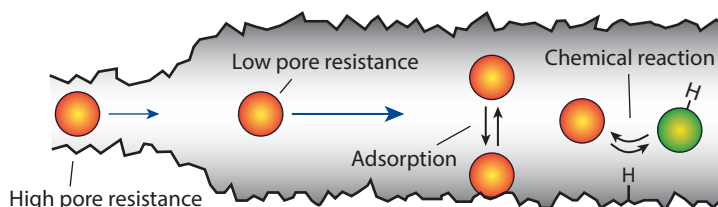
Figure 7.1 • Interactions between the fluorescent reporter (guest) and catalyst's pore (host): 1) resistance of the host pore on the mobility of the guest, e.g., the reporter 'feels' a higher resistance in a narrow pore than in a wider one resulting in a lower probe mobility; 2) adsorption to the pore wall causes the reporter to become (temporarily) immobile or diffuse over the pore wall; and 3) a chemical reaction of the fluorescent reporter with the pore can lead to a change in the emission colour of the reporter.

cilitated detailed probe characterisation. We investigated guest–host adsorption of single quantum-dot emitters to the pore wall and guest diffusion through the model pore. In our experiment, transient adsorption could not be distinguished from a dramatically increased diffusion resistance (hydrodynamic drag) near the pore wall, and we referred collectively to these events as *trapping*. Transient traps as short as a 175 ms were measured using the model pore. We found that the quantum-dot trapping could be tuned via the solution pH, likely because of a change in the electrostatic repulsion between the probe and pore wall. As a result, trapping was almost completely suppressed in specific pH conditions. The quantum dots exhibited normal diffusion in the artificial pore, and this conclusion was supported by the absence of time- and spatially-dependent diffusion. We found—in the reported conditions—a small variation in the diffusion coefficient, which we ascribed to a change in size of the quantum-dot nanoparticles. Building on this knowledge, we defined conditions that allowed for mapping of the accessible pore space of a model-pore array and a real-life catalyst particle. In a well-defined one-dimensional pore array, we quantified flow of the solvent through the pores and retrieved the pore size directly from the single-particle trajectories. Furthermore, we mapped the accessible pore space of a polymerisation catalyst-support particle with tens of nanometre precision.

We studied the diffusion of furfuryl alcohol oligomer molecules in the straight and the si-

nusoidal pores of ZSM-5 zeolites in **Chapter 5**. The pore types have a similar effective pore size but a different pore shape. The single-molecule trajectories revealed that the molecules travelled in a stop-and-go fashion because of frequent reversible adsorption events. Both the mobility, when the molecules were not adsorbed over hundreds of milliseconds, and the frequency of adsorption was different in the straight and sinusoidal pores. These factors together determined the average, effective diffusion coefficient through the zeolite, and an order of magnitude difference in this value was found between the two pore types. As expected, the more tortuous shape of the sinusoidal pores resulted in a slower average diffusion of the molecules in these pores than in the straight pores. Additional meso- and macropores with a diameter ≥ 2 nm were etched into the zeolite material to promote diffusion. We quantified that the adsorption was increased in the straight pores after etching. This was likely because of residual extra-framework silicon and aluminium left in these pores, which created adsorption sites. Contrarily, the molecular mobility increased, and the adsorption frequency of the molecules decreased in the sinusoidal pores, which indicated the formation of an interconnected secondary pore network. The effectiveness of the etching procedure to reduce mass transport limitations in ZSM-5 zeolites relies mainly on the formation of this secondary pore network.

In **Chapter 6**, we studied the guest–host interactions of the fluorescent resorufin molecule

inside the micropores of large (~10 mm-sized) zeolite-β crystals. We showed that resorufin molecules were protonated after entering the zeolite, which provided contrast between the resorufin species inside the zeolite micropores and in aqueous solution. Our results demonstrated the fluorescence of the protonated resorufin was boosted inside the zeolite's micropores, while it was quenched in solution, further enhancing the contrast between resorufin in solution and in zeolite. Resorufin exhibited sensitivity to the pH inside the zeolite and has potential to be used as pH sensor within the zeolite pores. The filling behaviour of the zeolite changed as a function of the solution pH, which we ascribed to variations in the diffusion barrier at the outer surface of the zeolite crystals. The zeolite's pore network was visualised, and the homogeneous distribution of resorufin molecules through zeolite-β showed that the micropores in the crystals were fully accessible. A secondary pore network of meso- and macropores with pore diameter of ≥ 2 nm was imaged using a fluorescent molecule, unlike resorufin, that did not fit in the micropores. We found that these pores were oriented in the growth direction of the zeolite crystal, which indicated that they were formed from defects in an early stage of the crystal growth and propagated in the growth direction. Finally, we visualised that diffusion through the straight pores of zeolite-β was impeded when diffusing through the boundaries between the zeolite subunits. Using a normal diffusion model and considering aggregation-induced quenching, we quantified the diffusion coefficient in the straight pores of zeolite-β and found a value of 3×10^{-15} m^2 s^{-1}.

7.2 • Outlook

While the use of fluorescent reporters is a common tool to map functional domains and mass transport in biological systems, it is still rather a niche application in materials science. For cells, probes have been developed that bind specifically to certain cell organelles. Future research efforts should aim at building a similar toolbox of fluorescent molecules to stain inorganic materials. The probes reported in **Chapters 6** are valuable additions to such a toolbox. The application of resorufin to image microporosity in other pore systems, such as metal–organic frameworks (i.e., MOFs), with similar pore sizes is an equally promising future research direction. The potential of using fluorescent reporters for catalyst characterisation is enormous despite the many more experimental challenges that need to be overcome when studying solid materials in comparison to the cellular systems studied in biology. Many porous catalyst materials have an inhomogeneous refractive index and strong absorption of visible light; however, both advanced model system and experiment design can tackle these challenges: 1) development and application of fluorophores operating in the infrared allows deeper imaging into the sample due to reduced light scattering. This comes at the expense of a lower resolution, because of the longer wavelength of infrared than visible light, and larger fluorescent molecules. 2) One could design optically transparent model systems with pore spaces representative for real pore systems, which increases the signal-to-noise and allows imaging deep into the sample. The mass transport behaviours could then be directly translated to the porous solid of interest. We have taken a first step in this direction in **Chapter 4**. 3) For materials with a heterogeneous matrix, the signal-to-noise ratio can be drastically improved by slicing the porous solid into slabs. Reconstruction of mass transport through the pore space will still be a complex task if the accessibility of the full pore space must be considered.

Correlation of single-molecule localisation microscopy with other microscopy techniques that can capture the pore space has great value with high potential for the future. By overlay of single-molecule trajectories with transmission electron micrographs, Zürner et al. have provided the first direct evidence that single-molecule trajectories follow the pore-connectivity and accessibility in mesoporous silica.[106] In more complex, heterogeneous pore spaces such as fluid catalytic cracking particles, mass transport was dominated by transient adsorption of the molecules.[61] In **Chapters 3, 4 & 5**, we refer to these traps (among others) as adsorption, but in fact, the microscopic origin

of the traps remains an open question. Our results in **Chapter 5** have indicated that extra-framework atoms could create adsorption sites, while attractive (van der Waals) interactions appeared to play a role for the nanoparticles studied in **Chapter 4**. Correlation of the single-molecule trajectories with the pore space and composition imaged with, e.g., X-ray tomography techniques or focused ion beam–scanning electron microscopy could identify the adsorption sites—if present. The combination of pore-space mapping using fluorescent reporters correlated with single molecule or nanoparticle tracking, such as in **Chapter 4**, is a promising approach to obtain fast and reliable information about the accessible pore space and would allow correlation in a single experiment.

References

1. Allan, R. P. *et al.* Summary for policymakers. in *Climate Change 2021: The Physical Science Basis. Contribution of Working Group I to the Sixth Assessment Report of the Intergovernmental Panel on Climate Change* (eds. Masson-Delmotte, V. *et al.*) (Cambridge University Press, Cambridge, 2021).

2. Ritchie, H. & Roser, M. CO_2 and greenhouse gas emissions. *Our World in Data* https://ourworldindata.org/emissions-by-sector (2020).

3. Chorkendorff, I. & Niemantsverdriet, J. W. *Concepts of Modern Catalysis and Kinetics.* (Wiley-VCH, Weinheim, 2007).

4. Ed. Gold, V., *The IUPAC Compendium of Chemical Terminology: The Gold Book.* (International Union of Pure and Applied Chemistry (IUPAC), 2019).

5. Van Santen, R. A. Complementary structure sensitive and insensitive catalytic relationships. *Acc. Chem. Res.* **42**, 57–66 (2009).

6. Wright, P. A. & Pearce, G. M. Structural chemistry of zeolites. in *Zeolites and Catalysis: Synthesis, Reactions and Applications* (eds. Čejka, J., Corma, A. & Zones, S.) 171–207 (Wiley-VCH, Weinheim, 2010).

7. International Zeolite Association. Database of zeolite structures. *IZA Structure Commission* http://www.iza-structure.org/databases/.

8. Baerlocher, C., McCusker, L. B., Olson, D. & Meier, W. M. *Atlas of Zeolite Framework Types.* (Published on behalf of the Structure Commission of the International Zeolite Association by Elsevier, 2007).

9. Collins, F., Rozhkovskaya, A., Outram, J. G. & Millar, G. J. A critical review of waste resources, synthesis, and applications for zeolite LTA. *Microporous Mesoporous Mater.* **291**, 251–258 (2020).

10. Bellussi, G., Carati, A. & Millini, R. Industrial potential of zeolites. in *Zeolites and Catalysis: Synthesis, Reactions and Applications* (eds. Čejka, J., Corma, A. & Zones, S.) 449–491 (Wiley-VCH, Weinheim, 2010).

11. Vogt, E. T. C. & Weckhuysen, B. M. Fluid catalytic cracking: Recent developments on the grand old lady of zeolite catalysis. *Chem. Soc. Rev.* **44**, 7342–7370 (2015).

12. Vollmer, I., Jenks, M. J. F., Mayorga González, R., Meirer, F. & Weckhuysen, B. M. Plastic waste conversion over a refinery waste catalyst. *Angew. Chem.* **133**, 16237–16244 (2021).

13. Mitchell, S., Michels, N.-L., Kunze, K. & Pérez-Ramírez, J. Visualization of hierarchically structured zeolite bodies from macro to nano length scales. *Nat. Chem.* **4**, 825–831 (2012).

14. Whiting, G. T. *et al.* Multiscale mechanistic insights of shaped catalyst body formulations and their impact on catalytic properties. *ACS Catal.* **9**, 4792–4803 (2019).

15. Kärger, J., Ruthven, D. M. & Theodorou, D. N. *Diffusion in Nanoporous Materials.* (Wiley-VCH, Weinheim, 2012).

16. Kärger, J. & Ruthven, D. M. Diffusion in nanoporous materials: Fundamental principles, insights and challenges. *New J. Chem.* **40**, 4027–4048 (2016).

17. Peng, P., Gao, X.-H., Yan, Z.-F. & Mintova, S. Diffusion and catalyst efficiency in hierarchical zeolite catalysts. *Natl. Sci. Rev.* **7**, 1726–1742 (2020).

18. Buurmans, I. L. C. & Weckhuysen, B. M. Heterogeneities of individual catalyst particles in space and time as monitored by spectroscopy. *Nat. Chem.* **4**, 873–886 (2012).

19. Hendriks, F. C. *et al.* Integrated transmission electron and single-molecule fluorescence microscopy correlates reactivity with ultrastructure in a single catalyst particle. *Angew. Chem. Int. Ed.* **57**, 257–261 (2018).

20. Mehrer, H. & Stolwijk, N. A. Heroes and highlights in the history of diffusion. *Diffus. Fundam.* **11**, 1 (2009).

21. Philibert, J. One and a half century of diffusion: Fick, Einstein, before and beyond. *Diffus. Fundam.* **4**, 6 (2006).

22. Graham, T. On the law of the diffusion of gases. *Lond. Edinb. Dublin Philos. Mag. J. Sci.* **2**, 269–276 (1833).

23. Graham, T. The bakerian lecture. On the diffusion of liquids. *Philos. Trans. R. Soc. Lond.* **140**, 1–46 (1850).

24. Fick, A. On liquid diffusion. *Lond. Edinb. Dublin Philos. Mag. J. Sci.* **10**, 30–39 (1855).

25. Brown, R. A brief account of microscopical observations made in the months of June, July and August 1827, on the particles contained in the pollen of plants; and on the general existence of active molecules in organic and inorganic bodies. *Philos. Mag.* **4**, 161–173 (1828).

26. Einstein, A. Über die von der molekularkinetischen Theorie der Wärme geforderte Bewegung von in ruhenden Flüssigkeiten sus-

pendierten Teilchen. *Ann. Phys.* **322**, 549–560 (1905).

27. Perrin, J. *Atoms.* (Constable & Company Ltd., London, 1915).

28. Patterson, G. Jean Perrin and the triumph of the atomic doctrine. *Endeavour* **31**, 50–53 (2007).

29. Kärger, J., Ruthven, D. M. & Valiullin, R. Diffusion in nanopores: Inspecting the grounds. *Adsorption* **27**, 267–281 (2021).

30. Kärger, J. *et al.* Microimaging of transient guest profiles to monitor mass transfer in nanoporous materials. *Nat. Mater.* **13**, 333–343 (2014).

31. Geet, A. L. V. & Adamson, A. W. Diffusion in liquid hydrocarbon mixtures. *J. Phys. Chem.* **68**, 238–246 (1964).

32. Chmelik, C. *et al.* Mass transfer in a nanoscale material enhanced by an opposing flux. *Phys. Rev. Lett.* **104**, 085902 (2010).

33. Kärger, J. & Caro, J. Interpretation and correlation of zeolitic diffusivities obtained from nuclear magnetic resonance and sorption experiments. *J. Chem. Soc. Faraday Trans. 1* **73**, 1363–1376 (1977).

34. Kärger, J. & Ruthven, D. M. On the comparison between macroscopic and n.m.r. measurements of intracrystalline diffusion in zeolites. *Zeolites* **9**, 267–281 (1989).

35. Vasenkov, S. *et al.* PFG NMR study of diffusion in MFI-type zeolites: Evidence of the existence of intracrystalline transport barriers. *J. Phys. Chem. B* **105**, 5922–5927 (2001).

36. Kärger, J. *et al.* NMR study of mass transfer in granulated molecular sieves. *AIChE J.* **34**, 1185–1189 (1988).

37. Chmelik, C., Gläser, R., Haase, J., Hwang, S. & Kärger, J. Application of microimaging to diffusion studies in nanoporous materials. *Adsorption* **27**, 819–840 (2021).

38. Hibbe, F. *et al.* Monitoring molecular mass transfer in cation-free nanoporous host crystals of type AlPO-LTA. *J. Am. Chem. Soc.* **134**, 7725–7732 (2012).

39. Remi, J. C. S. *et al.* The role of crystal diversity in understanding mass transfer in nanoporous materials. *Nat. Mater.* **15**, 401–406 (2016).

40. Chmelik, C., Heinke, L., Valiullin, R. & Kärger, J. A new view of diffusion in nanoporous materials. *Chem. Ing. Tech.* **82**, 779–804 (2010).

41. Chmelik, C. & Kärger, J. In situ study on molecular diffusion phenomena in nanoporous catalytic solids. *Chem. Soc. Rev.* **39**, 4864–4884 (2010).

42. De Cremer, G., Sels, B. F., Vos, D. E. D., Hofkens, J. & Roeffaers, M. B. J. Fluorescence micro(spectro)scopy as a tool to study catalytic materials in action. *Chem. Soc. Rev.* **39**, 4703–4717 (2010).

43. Janssen, K. P. F. *et al.* Single molecule methods for the study of catalysis: From enzymes to heterogeneous catalysts. *Chem Soc Rev* **43**, 990–1006 (2014).

44. Michaelis, J. & Bräuchle, C. Reporters in the nanoworld: Diffusion of single molecules in mesoporous materials. *Chem. Soc. Rev.* **39**, 4731–4740 (2010).

45. Tachikawa, T. & Majima, T. Single-molecule, single-particle fluorescence imaging of TiO2-based photocatalytic reactions. *Chem. Soc. Rev.* **39**, 4802–4819 (2010).

46. Weckhuysen, B. M. Chemical imaging of spatial heterogeneities in catalytic solids at different length and time scales. *Angew. Chem. Int. Ed.* **48**, 4910–4943 (2009).

47. Higgins, D. A., Park, S. C., Tran-Ba, K.-H. & Ito, T. Single-molecule investigations of morphology and mass transport dynamics in nanostructured materials. *Annu. Rev. Anal. Chem.* **8**, 193–216 (2015).

48. Manzo, C. & Garcia-Parajo, M. F. A review of progress in single particle tracking: from methods to biophysical insights. *Rep. Prog. Phys.* **78**, 124601 (2015).

49. Vangindertael, J. *et al.* An introduction to optical super-resolution microscopy for the adventurous biologist. *Methods Appl. Fluoresc.* **6**, 022003 (2018).

50. Birkhoff, G. D. Proof of a recurrence theorem for strongly transitive systems. *Proc. Natl. Acad. Sci. U. S. A.* **17**, 650–655 (1931).

51. Feil, F. *et al.* Single-particle and ensemble diffusivities—test of ergodicity. *Angew. Chem. Int. Ed.* **51**, 1152–1155 (2012).

52. Ristanović, Z. *et al.* Quantitative 3D fluorescence imaging of single catalytic turnovers reveals spatiotemporal gradients in reactivity of zeolite H-ZSM-5 crystals upon steaming. *J. Am. Chem. Soc.* **137**, 6559–6568 (2015).

53. Van Loon, J. *et al.* Rationalizing acid zeolite performance on the nanoscale by correlative fluorescence and electron microscopy. *ACS*

Catal. **7**, 5234–5242 (2017).

54. Layek, A., Loon, J. V., Roeffaers, M. B. J. & Kubarev, A. V. Correlated super-resolution fluorescence and electron microscopy reveals the catalytically active nanorods within individual H-ZSM-22 zeolite particles. *Catal. Sci. Technol.* **9**, 4645–4650 (2019).

55. Hellriegel, C., Kirstein, J. & Bräuchle, C. Tracking of single molecules as a powerful method to characterize diffusivity of organic species in mesoporous materials. *New J. Phys.* **7**, 23 (2005).

56. Hellriegel, C. *et al.* Diffusion of single streptocyanine molecules in the nanoporous network of sol–gel glasses. *J. Phys. Chem. B* **108**, 14699–14709 (2004).

57. McCain, K. S., Hanley, D. C. & Harris, J. M. Single-molecule fluorescence trajectories for investigating molecular transport in thin silica sol–gel films. *Anal. Chem.* **75**, 4351–4359 (2003).

58. Seebacher, C. *et al.* Observation of translational diffusion of single terrylenediimide molecules in a mesostructured molecular sieve. *J. Phys. Chem. B* **106**, 5591–5595 (2002).

59. Kirstein, J. *et al.* Exploration of nanostructured channel systems with single-molecule probes. *Nat. Mater.* **6**, 303–310 (2007).

60. Maris, J. J. E., Fu, D., Meirer, F. & Weckhuysen, B. M. Single-molecule observation of diffusion and catalysis in nanoporous solids. *Adsorption* **27**, 423–452 (2021).

61. Hendriks, F. C. *et al.* Single-molecule fluorescence microscopy reveals local diffusion coefficients in the pore network of an individual catalyst particle. *J. Am. Chem. Soc.* **139**, 13632–13635 (2017).

62. Valeur, B. & Berberan-Santos, M. N. *Molecular Fluorescence.* (Wiley-VCH, Weinheim, 2012).

63. Dobrucki, J. W. & Kubitscheck, U. Fluorescence microscopy. in *Fluorescence Microscopy* (ed. Kubitscheck, U.) 85–132 (Wiley-VCH, Weinheim, 2017).

64. Wahl, M. Time-correlated single photon counting. *PicoQuant Technical Notes* 1–14 (2014).

65. McRae, E. G. & Kasha, M. The molecular excitation model. in Physical Processes in *Radiation Biology* (eds. Augenstein, L., Mason, R. & Rosenberg, B.) 23–42 (Academic Press, Cambridge, 1964).

66. Kasha, M., Rawls, H. R. & El-Bayoumi, M. A. The exciton model in molecular spectroscopy. *Pure Appl. Chem.* **11**, 371–392 (1965).

67. Alarcos, N., Cohen, B., Ziółek, M. & Douhal, A. Photochemistry and photophysics in silica-based materials: Ultrafast and single molecule spectroscopy observation. *Chem. Rev.* **117**, 13639–13720 (2017).

68. Martínez-Martínez, V., García, R., Gómez-Hortigüela, L., Pérez-Pariente, J. & López-Arbeloa, I. Modulating dye aggregation by incorporation into 1D-MgAPO nanochannels. *Chem. Eur. J.* **19**, 9859–9865 (2013).

69. Guralchuk, G. Ya. *et al.* Anomalous surfactant-induced enhancement of luminescence quantum yield of cyanine dye J-aggregates. *J. Phys. Chem. C* **112**, 14762–14768 (2008).

70. Anantharaman, S. B. *et al.* Enhanced room-temperature photoluminescence quantum yield in morphology controlled J-aggregates. *Adv. Sci.* **8**, 1903080 (2021).

71. Wang, M., Silva, G. L. & Armitage, B. A. DNA-templated formation of a helical cyanine dye J-aggregate. *J. Am. Chem. Soc.* **122**, 9977–9986 (2000).

72. Kubitscheck, U. Principles of light microscopy. in *Fluorescence Microscopy* 23–83 (Wiley-VCH, Weinheim, 2017).

73. Naredi-Rainer, N., Prescher, J., Hartschuh, A. & Lamb, D. C. Confocal microscopy. in *Fluorescence Microscopy* (ed. Kubitscheck, U.) 165–202 (Wiley-VCH, Weinheim, 2017).

74. Betzig, E. Proposed method for molecular optical imaging. *Opt. Lett.* **20**, 237–239 (1995).

75. Dickson, R. M., Cubitt, A. B., Tsien, R. Y. & Moerner, W. E. On/off blinking and switching behaviour of single molecules of green fluorescent protein. *Nature* **388**, 355–358 (1997).

76. Betzig, E. *et al.* Imaging intracellular fluorescent proteins at nanometer resolution. *Science* **313**, 1642–1645 (2006).

77. Dedecker, P., Duwé, S., Neely, R. K. & Zhang, J. Localizer: fast, accurate, open-source, and modular software package for superresolution microscopy. *J. Biomed. Opt.* **17**, 126008 (2012).

78. Katrukha, E. A., Cloin, B., Teeuw, J. & Kapitein, L. C. Detection of Molecules plugin for ImageJ. *Utrecht University* https://github.com/ekatrukha/DoM_Utrecht (2017).

79. Babcock, H. P. & Zhuang, X. Analyzing single molecule localization microscopy data using cubic splines. *Sci. Rep.* **7**, 552 (2017).

80. Crocker, J. C. & Grier, D. G. Methods of Digital Video Microscopy for Colloidal Studies. *J. Colloid Interface Sci.* **179**, 298–310 (1996).

81. Wöll, D., Kölbl, C., Stempfle, B. & Karrenbauer, A. A novel method for automatic single molecule tracking of blinking molecules at low intensities. *Phys. Chem. Chem. Phys.* **15**, 6196–6205 (2013).

82. Vogelsang, J. *et al.* A reducing and oxidizing system minimizes photobleaching and blinking of fluorescent dyes. *Angew. Chem. Int. Ed.* **47**, 5465–5469 (2008).

83. Berglund, A. J. Statistics of camera-based single-particle tracking. *Phys. Rev. E* **82**, 011917 (2010).

84. Michalet, X. & Berglund, A. J. Optimal diffusion coefficient estimation in single-particle tracking. *Phys. Rev. E* **85**, 061916 (2012).

85. Metzler, R., Jeon, J.-H., Cherstvy, A. G. & Barkai, E. Anomalous diffusion models and their properties: non-stationarity, non-ergodicity, and ageing at the centenary of single particle tracking. *Phys. Chem. Chem. Phys.* **16**, 24128–24164 (2014).

86. Vestergaard, C. L., Blainey, P. C. & Flyvbjerg, H. Optimal estimation of diffusion coefficients from single-particle trajectories. *Phys. Rev. E* **89**, 022726 (2014).

87. Qian, H., Sheetz, M. P. & Elson, E. L. Single particle tracking. Analysis of diffusion and flow in two-dimensional systems. *Biophys. J.* **60**, 910–921 (1991).

88. Michalet, X. Mean square displacement analysis of single-particle trajectories with localization error: Brownian motion in an isotropic medium. *Phys. Rev. E* **82**, 041914 (2010).

89. Kepten, E., Weron, A., Sikora, G., Burnecki, K. & Garini, Y. Guidelines for the fitting of anomalous diffusion mean square displacement graphs from single particle tracking experiments. *PLoS ONE* **10**, e0117722 (2015).

90. Shuang, B. *et al.* Improved analysis for determining diffusion coefficients from short, single-molecule trajectories with photoblinking. *Langmuir* **29**, 228–234 (2013).

91. Relich, P. K., Olah, M. J., Cutler, P. J. & Lidke, K. A. Estimation of the diffusion constant from intermittent trajectories with variable position uncertainties. *Phys. Rev. E* **93**, 042401 (2016).

92. Vestergaard, C. L., Pedersen, J. N., Mortensen, K. I. & Flyvbjerg, H. Estimation of motility parameters from trajectory data. *Eur. Phys. J. Spec. Top.* **224**, 1151–1168 (2015).

93. Lindén, M., Ćurić, V., Amselem, E. & Elf, J. Pointwise error estimates in localization microscopy. *Nat. Commun.* **8**, 15115 (2017).

94. Karslake, J. D. *et al.* SMAUG: Analyzing single-molecule tracks with nonparametric Bayesian statistics. *Methods* **193**, 16–26 (2020).

95. Lindén, M. & Elf, J. Variational algorithms for analyzing noisy multistate diffusion trajectories. *Biophys. J.* **115**, 276–282 (2018).

96. Persson, F., Lindén, M., Unoson, C. & Elf, J. Extracting intracellular diffusive states and transition rates from single-molecule tracking data. *Nat. Methods* **10**, 265–269 (2013).

97. Rowland, D. J. & Biteen, J. S. Measuring molecular motions inside single cells with improved analysis of single-particle trajectories. *Chem. Phys. Lett.* **674**, 173–178 (2017).

98. Wöll, D. & Flors, C. Super-resolution fluorescence imaging for materials science. *Small Methods* **1**, 1700191 (2017).

99. Cordes, T. & Blum, S. A. Opportunities and challenges in single-molecule and single-particle fluorescence microscopy for mechanistic studies of chemical reactions. *Nat. Chem.* **5**, 993–999 (2013).

100. Vestergaard, C. L. Optimizing experimental parameters for tracking of diffusing particles. *Phys. Rev. E* **94**, 022401 (2016).

101. Aitken, C. E., Marshall, R. A. & Puglisi, J. D. An oxygen scavenging system for improvement of dye stability in single-molecule fluorescence experiments. *Biophys. J.* **94**, 1826–1835 (2008).

102. Werley, C. A. & Moerner, W. E. Single-molecule nanoprobes explore defects in spin-grown crystals. *J. Phys. Chem. B* **110**, 18939–18944 (2006).

103. Feil, F., Cauda, V., Bein, T. & Bräuchle, C. Direct visualization of dye and oligonucleotide diffusion in silica filaments with collinear mesopores. *Nano Lett.* **12**, 1354–1361 (2012).

104. Jung, C. *et al.* Diffusion of oriented single molecules with switchable mobility in networks of long unidimensional nanochannels. *J. Am. Chem. Soc.* **130**, 1638–1648 (2008).

105. Lebold, T. *et al.* Tuning single-molecule dynamics in functionalized mesoporous silica. *Chem. Eur. J.* **15**, 1661–1672 (2009).

106. Zürner, A., Kirstein, J., Döblinger, M., Bräuchle, C. & Bein, T. Visualizing single-molecule

diffusion in mesoporous materials. *Nature* **450**, 705–708 (2007).

107. Avlasevich, Y., Li, C. & Müllen, K. Synthesis and applications of core-enlarged perylene dyes. *J. Mater. Chem.* **20**, 3814–3826 (2010).

108. Weil, T., Vosch, T., Hofkens, J., Peneva, K. & Müllen, K. The rylene colorant family—tailored nanoemitters for photonics research and applications. *Angew. Chem. Int. Ed.* **49**, 9068–9093 (2010).

109. Hoang, H. T. *et al.* Analysis of single quantum-dot mobility inside 1D nanochannel devices. *Nanotechnology* **22**, 275201 (2011).

110. Lee, C. H., Crosby, A. J., Emrick, T. & Hayward, R. C. Characterization of heterogeneous polyacrylamide hydrogels by tracking of single quantum dots. *Macromolecules* **47**, 741–749 (2014).

111. Liu, X. *et al.* Nanographenes: Ultrastable, switchable, and bright probes for super-resolution microscopy. *Angew. Chem. Int. Ed.* **59**, 496–502 (2020).

112. Ristanović, Z., Kubarev, A. V., Hofkens, J., Roeffaers, M. B. J. & Weckhuysen, B. M. Single Molecule Nanospectroscopy Visualizes Proton-Transfer Processes within a Zeolite Crystal. *J. Am. Chem. Soc.* **138**, 13586–13596 (2016).

113. Roeffaers, M. B. J. *et al.* Super-Resolution Reactivity Mapping of Nanostructured Catalyst Particles. *Angew. Chem. Int. Ed.* **48**, 9285–9289 (2009).

114. Kox, M. H. F., Mijovilovich, A., Sättler, J. J. H. B., Stavitski, E. & Weckhuysen, B. M. The catalytic conversion of thiophenes over large H-ZSM-5 crystals: an X-ray, UV/Vis, and fluorescence microspectroscopic study. *ChemCatChem* **2**, 564–571 (2010).

115. Kox, M. H. F., Stavitski, E. & Weckhuysen, B. M. Nonuniform catalytic behavior of zeolite crystals as revealed by in situ optical microspectroscopy. *Angew. Chem. Int. Ed.* **46**, 3652–3655 (2007).

116. Ristanović, Z. *et al.* Reversible and site-dependent proton-transfer in zeolites uncovered at the single-molecule level. *J. Am. Chem. Soc.* **140**, 14195–14205 (2018).

117. Stavitski, E., Kox, M. H. F. & Weckhuysen, B. M. Revealing shape selectivity and catalytic activity trends within the pores of H-ZSM-5 crystals by time- and space-resolved optical and fluorescence microspectroscopy. *Chem. Eur. J.* **13**, 7057–7065 (2007).

118. Geerts, H. *et al.* Nanovid tracking: A new automatic method for the study of mobility in living cells based on colloidal gold and video microscopy. *Biophys. J.* **52**, 775–782 (1987).

119. Shen, H. *et al.* Single particle tracking: From theory to biophysical applications. *Chem. Rev.* **117**, 7331–7376 (2017).

120. Liao, Y., Yang, S. K., Koh, K., Matzger, A. J. & Biteen, J. S. Heterogeneous single-molecule diffusion in one-, two-, and three-dimensional microporous coordination polymers: Directional, trapped, and immobile guests. *Nano Lett.* **12**, 3080–3085 (2012).

121. Dong, B. *et al.* In situ quantitative single-molecule study of dynamic catalytic processes in nanoconfinement. *Nat. Catal.* **1**, 135–140 (2018).

122. Matysik, A. & Kraut, R. S. TrackArt: The user friendly interface for single molecule tracking data analysis and simulation applied to complex diffusion in mica supported lipid bilayers. *BMC Res. Notes* **7**, 274 (2014).

123. Tinevez, J.-Y. *et al.* TrackMate: An open and extensible platform for single-particle tracking. *Methods* **115**, 80–90 (2017).

124. Rösch, T. C., Oviedo-Bocanegra, L. M., Fritz, G. & Graumann, P. L. SMTracker: a tool for quantitative analysis, exploration and visualization of single-molecule tracking data reveals highly dynamic binding of B. subtilis global repressor AbrB throughout the genome. *Sci. Rep.* **8**, 15747 (2018).

125. Hansen, A. S. *et al.* Robust model-based analysis of single-particle tracking experiments with Spot-On. *eLife* **7**, e33125 (2018).

126. Lee, B. H. & Park, H. Y. HybTrack: A hybrid single particle tracking software using manual and automatic detection of dim signals. *Sci. Rep.* **8**, 212 (2018).

127. Kuhn, T., Hettich, J., Davtyan, R. & Gebhardt, J. C. M. Single molecule tracking and analysis framework including theory-predicted parameter settings. *Sci. Rep.* **11**, 9465 (2021).

128. Lerner, J. *et al.* Two-parameter single-molecule analysis for measurement of chromatin mobility. *STAR Protoc.* **1**, 100223 (2020).

129. Tarantino, N. *et al.* TNF and IL-1 exhibit distinct ubiquitin requirements for inducing NEMO–IKK supramolecular structures. *J. Cell*

Biol. **204**, 231–245 (2014).

130. Liu, Y. *et al.* TXM-Wizard: A program for advanced data collection and evaluation in full-field transmission X-ray microscopy. *J. Synchrotron Radiat.* **19**, 281–287 (2012).

131. Dosset, P. *et al.* Automatic detection of diffusion modes within biological membranes using back-propagation neural network. *BMC Bioinformatics* **17**, 197 (2016).

132. Granik, N. *et al.* Single-particle diffusion characterization by deep learning. *Biophys. J.* **117**, 185–192 (2019).

133. Kowalek, P., Loch-Olszewska, H. & Szwabiński, J. Classification of diffusion modes in single-particle tracking data: Feature-based versus deep-learning approach. *Phys. Rev. E* **100**, 032410 (2019).

134. Muñoz-Gil, G., Garcia-March, M. A., Manzo, C., Martín-Guerrero, J. D. & Lewenstein, M. Single trajectory characterization via machine learning. *New J. Phys.* **22**, 013010 (2020).

135. Verdier, H. *et al.* Learning physical properties of anomalous random walks using graph neural networks. *J. Phys. Math. Theor.* **54**, 234001 (2021).

136. Li, D., Yao, Q. & Huang, Z. WaveNet-based deep neural networks for the characterization of anomalous diffusion (WADNet). *J. Phys. Math. Theor.* **54**, 404003 (2021).

137. Manzo, C. Extreme learning machine for the characterization of anomalous diffusion from single trajectories (AnDi-ELM). *J. Phys. Math. Theor.* **54**, 334002 (2021).

138. Muñoz-Gil, G. *et al.* Objective comparison of methods to decode anomalous diffusion. *Nat. Commun.* **12**, 6253 (2021).

139. Katrukha, E. A. *et al.* Probing cytoskeletal modulation of passive and active intracellular dynamics using nanobody-functionalized quantum dots. *Nat. Commun.* **8**, 14772 (2017).

140. COMSOL Multiphysics®.

141. James, G., Witten, D., Hastie, T. & Tibshirani, R. *An Introduction to Statistical Learning.* (Springer, New York, 2013).

142. Mortensen, K. I., Churchman, L. S., Spudich, J. A. & Flyvbjerg, H. Optimized localization analysis for single-molecule tracking and super-resolution microscopy. *Nat. Methods* **7**, 377–381 (2010).

143. Deschout, H., Neyts, K. & Braeckmans, K. The influence of movement on the localization precision of sub-resolution particles in fluorescence microscopy. *J. Biophotonics* **5**, 97–109 (2012).

144. Saxton, M. J. Modeling 2D and 3D diffusion. in *Methods in Membrane Lipids* (ed. Dopico, A. M.) 295–321 (Humana Press, Totowa, 2007).

145. Schütz, G. J., Schindler, H. & Schmidt, T. Single-molecule microscopy on model membranes reveals anomalous diffusion. *Biophys. J.* **73**, 1073–1080 (1997).

146. Volpe, G., Gigan, S. & Volpe, G. Simulation of the active Brownian motion of a microswimmer. *Am. J. Phys.* **82**, 659–664 (2014).

147. Mortensen, K. I., Flyvbjerg, H. & Pedersen, J. N. Confined brownian motion tracked with motion blur: Estimating diffusion coefficient and size of confining space. *Front. Phys.* **8**, 583202 (2021).

148. Sage, D. *et al.* Super-resolution fight club: Assessment of 2D and 3D single-molecule localization microscopy software. *Nat. Methods* **16**, 387–395 (2019).

149. Backer, A. S. & Moerner, W. E. Extending single-molecule microscopy using optical fourier processing. *J. Phys. Chem. B* **118**, 8313–8329 (2014).

150. Thompson, R. E., Larson, D. R. & Webb, W. W. Precise nanometer localization analysis for individual fluorescent probes. *Biophys. J.* **82**, 2775–2783 (2002).

151. Liu, Y., Meirer, F., Krest, C. M., Webb, S. & Weckhuysen, B. M. Relating structure and composition with accessibility of a single catalyst particle using correlative 3-dimensional micro-spectroscopy. *Nat. Commun.* **7**, 12634 (2016).

152. Everett, D. H. Manual of Symbols and Terminology for Physicochemical Quantities and Units, Appendix II: Definitions, Terminology and Symbols in Colloid and Surface Chemistry. *Pure Appl. Chem.* **31**, 577–638 (1972).

153. Whiting, G. T., Nikolopoulos, N., Nikolopoulos, I., Chowdhury, A. D. & Weckhuysen, B. M. Visualizing pore architecture and molecular transport boundaries in catalyst bodies with fluorescent nanoprobes. *Nat. Chem.* **11**, 23–31 (2019).

154. Da Silva, J. C. *et al.* Assessment of the 3D pore structure and individual components of preshaped catalyst bodies by X-ray imaging. *ChemCatChem* **7**, 413–416 (2015).

155. De Winter, D. A. M., Meirer, F. & Weckhuysen, B. M. FIB-SEM tomography probes the mesoscale pore space of an individual catalytic cracking particle. *ACS Catal.* **6**, 3158–3167 (2016).

156. Chen, P. *et al.* Spatiotemporal catalytic dynamics within single nanocatalysts revealed by single-molecule microscopy. *Chem. Soc. Rev.* **43**, 1107–1117 (2014).

157. Keh, H. J. & Chen, P. Y. Slow motion of a droplet between two parallel plane walls. *Chem. Eng. Sci.* **56**, 6863–6871 (2001).

158. Douglas, J. F., Johnson, H. E. & Granick, S. A simple kinetic model of polymer adsorption and desorption. *Science* **262**, 2010–2012 (1993).

159. Frantz, P. & Granick, S. Kinetics of polymer adsorption and desorption. *Phys. Rev. Lett.* **66**, 899–902 (1991).

160. Lebold, T., Michaelis, J. & Bräuchle, C. The complexity of mesoporous silica nanomaterials unravelled by single molecule microscopy. *Phys. Chem. Chem. Phys.* **13**, 5017–5033 (2011).

161. Israelachvili, J. N. *Intermolecular and Surface Forces.* (Academic Press, Cambridge, 2011).

162. Eichmann, S. L., Anekal, S. G. & Bevan, M. A. Electrostatically confined nanoparticle interactions and dynamics. *Langmuir* **24**, 714–721 (2008).

163. Lin, B., Yu, J. & Rice, S. A. Direct measurements of constrained Brownian motion of an isolated sphere between two walls. *Phys. Rev. E* **62**, 3909–3919 (2000).

164. Volk, A. & Kähler, C. J. Density model for aqueous glycerol solutions. *Exp. Fluids* **59**, 75 (2018).

165. Janzen, J., Song, X. & Brooks, D. E. Interfacial thickness of liposomes containing poly(ethylene glycol)-cholesterol from electrophoresis. *Biophys. J.* **70**, 313–320 (1996).

166. Bergman, M. J., Pedersen, J. S., Schurtenberger, P. & Boon, N. Controlling the morphology of microgels by ionic stimuli. *Soft Matter* **16**, 2786–2794 (2020).

167. Sahai, N. & Sverjensky, D. A. Evaluation of internally consistent parameters for the triple-layer model by the systematic analysis of oxide surface titration data. *Geochim. Cosmochim. Acta* **61**, 2801–2826 (1997).

168. Saxton, M. J. Lateral diffusion in an archipel-ago. Single-particle diffusion. *Biophys. J.* **64**, 1766–1780 (1993).

169. Simson, R., Sheets, E. D. & Jacobson, K. Detection of temporary lateral confinement of membrane proteins using single-particle tracking analysis. *Biophys. J.* **69**, 989–993 (1995).

170. Vrljic, M., Nishimura, S. Y. & Moerner, W. E. Single-molecule tracking. in *Lipid Rafts* (ed. McIntosh, T. J.) 193–220 (Humana press, Totawa, 2007).

171. Jin, D. *et al.* Nanoparticles for super-resolution microscopy and single-molecule tracking. *Nat. Methods* **15**, 415–423 (2018).

172. Argauer, R. J. & Landolt, G. R. Crystalline zeolite ZSM-5 and method of preparing the same. *US Pat.* US3702886A (1972).

173. Chang, C. D. & Lang, W. H. Process for manufacturing olefins. *US Pat.* US4025576A (1977).

174. Yarulina, I., Chowdhury, A. D., Meirer, F., Weckhuysen, B. M. & Gascon, J. Recent trends and fundamental insights in the methanol-to-hydrocarbons process. *Nat. Catal.* **1**, 398–411 (2018).

175. Stöcker, M. Methanol to olefins (MTO) and methanol to gasoline (MTG). in *Zeolites and Catalysis: Synthesis, Reactions and Applications* (eds. Čejka, J., Corma, A. & Zones, S.) 687–711 (Wiley-VCH, Weinheim, 2010).

176. Dai, H. *et al.* Finned zeolite catalysts. *Nat. Mater.* **19**, 1074–1080 (2020).

177. Chen, L.-H. *et al.* Hierarchically structured zeolites: from design to application. *Chem. Rev.* **120**, 11194–11294 (2020).

178. Gao, S. *et al.* Cavity-controlled diffusion in 8-membered ring molecular sieve catalysts for shape selective strategy. *J. Catal.* **377**, 51–62 (2019).

179. Li, K., Valla, J. & Garcia-Martinez, J. Realizing the commercial potential of hierarchical zeolites: new opportunities in catalytic cracking. *ChemCatChem* **6**, 46–66 (2014).

180. Mitchell, S. *et al.* Structural analysis of hierarchically organized zeolites. *Nat. Commun.* **6**, 8633 (2015).

181. Sun, M.-H. *et al.* Hierarchical zeolite single-crystal reactor for excellent catalytic efficiency. *Matter* **3**, 1226–1245 (2020).

182. Van den Bergh, J., Gascon, J. & Kapteijn, F. Diffusion in zeolites – impact on catalysis. in *Zeolites and Catalysis: Synthesis, Reactions and Applications* (eds. Čejka, J., Corma, A. & Zones,

S.) 361–387 (Wiley-VCH, Weinheim, 2010).

183. Van Vu, D., Miyamoto, M., Nishiyama, N., Egashira, Y. & Ueyama, K. Selective formation of para-xylene over H-ZSM-5 coated with polycrystalline silicalite crystals. *J. Catal.* **243**, 389–394 (2006).

184. Wang, C. *et al.* Maximizing sinusoidal channels of HZSM-5 for high shape-selectivity to p-xylene. *Nat. Commun.* **10**, 4348 (2019).

185. Pham, T. C. T., Kim, H. S. & Yoon, K. B. Growth of uniformly oriented silica MFI and BEA zeolite films on substrates. *Science* **334**, 1533–1538 (2011).

186. Jeon, M. Y. *et al.* Ultra-selective high-flux membranes from directly synthesized zeolite nanosheets. *Nature* **543**, 690–694 (2017).

187. Fu, D., Van der Heijden, O., Stanciakova, K., Schmidt, J. E. & Weckhuysen, B. M. Disentangling reaction processes of zeolites within single-oriented channels. *Angew. Chem. Int. Ed.* **59**, 15502–15506 (2020).

188. Kärger, J. Measurement of diffusion in zeolites—a never ending challenge? *Adsorption* **9**, 29–35 (2003).

189. Caro, J. *et al.* Selective sorption uptake kinetics of n-hexane on ZSM 5 - a new method for measuring anisotropic diffusivities. *J.Phys. Chem.* **97**, 13685–13690 (1993).

190. Hong, U. *et al.* PFG NMR study of diffusion anisotropy in oriented ZSM-5 type zeolite crystallites. *Zeolites* **11**, 816–821 (1991).

191. Zeng, S. *et al.* Differentiating diffusivity in different channels of ZSM-5 zeolite by pulsed field gradient (PFG) NMR. *ChemCatChem* **12**, 403–408 (2019).

192. Hong, U., Kärger, J., Pfeifer, H., Müller, U. & Unger, K. K. Observing diffusion anisotropy in zeolites by pulsed field gradient NMR. *Z. Für Phys. Chem.* **173**, 225–234 (1991).

193. Bär, N.-K., Kärger, J., Pfeifer, H., Schäfer, H. & Schmitz, W. Diffusion anisotropy in natural chabazite. *Microporous Mesoporous Mater.* **22**, 289–295 (1998).

194. Jobic, H. Diffusion of linear and branched alkanes in ZSM-5. A quasi-elastic neutron scattering study. *J. Mol. Catal. Chem.* **158**, 135–142 (2000).

195. Jobic, H. & Farago, B. Unidimensional diffusion of long n-alkanes in nanoporous channels. *J. Chem. Phys.* **129**, 171102 (2008).

196. O'Malley, A. J., Parker, S. F. & Catlow, C. R. A. Neutron spectroscopy as a tool in catalytic science. *Chem. Commun.* **53**, 12164–12176 (2017).

197. Gueudré, L. *et al.* Micro-imaging by interference microscopy: A case study of orientation-dependent guest diffusion in MFI-type zeolite host crystals. *Materials* **5**, 721–740 (2012).

198. Kärger, J. Random walk through two-channel networks: A simple means to correlate the coefficients of anisotropic diffusion in ZSM-5 type zeolites. *J. Phys. Chem.* **95**, 5558–5560 (1991).

199. Kärger, J., Demontis, P., Suffritti, G. B. & Tilocca, A. "Two-step" model of molecular diffusion in silicalite. *J. Chem. Phys.* **110**, 1163–1172 (1999).

200. Smit, B. & Maesen, T. L. M. Molecular simulations of zeolites: Adsorption, diffusion, and shape selectivity. *Chem. Rev.* **108**, 4125–4184 (2008).

201. Qin, Z. *et al.* The mosaic structure of zeolite crystals. *Angew. Chem. Int. Ed.* **55**, 15049–15052 (2016).

202. Knott, B. C. *et al.* Consideration of the aluminum distribution in zeolites in theoretical and experimental catalysis research. *ACS Catal.* **8**, 770–784 (2018).

203. Fu, D. *et al.* Highly Oriented Growth of Catalytically Active Zeolite ZSM-5 Films with a Broad Range of Si/Al Ratios. *Angew. Chem. Int. Ed.* **56**, 11217–11221 (2017).

204. Roeffaers, M. B. J. *et al.* Space- and time-resolved visualization of acid catalysis in ZSM-5 crystals by fluorescence microscopy. *Angew. Chem. Int. Ed.* **46**, 1706–1709 (2007).

205. Roeffaers, M. B. J. *et al.* Relating pore structure to activity at the subcrystal level for ZSM-5: An electron backscattering diffraction and fluorescence microscopy study. *J. Am. Chem. Soc.* **130**, 13516–13517 (2008).

206. Choura, M., Belgacem, N. M. & Gandini, A. Acid-Catalyzed Polycondensation of Furfuryl Alcohol: Mechanisms of Chromophore Formation and Cross-Linking. *Macromolecules* **29**, 3839–3850 (1996).

207. Sastre, G., Raj, N., Catlow, C. R. A., Roque-Malherbe, R. & Corma, A. Selective diffusion of C8 aromatics in a 10 and 12 MR zeolite. A molecular dynamics study. *J. Phys. Chem. B* **102**, 3198–3209 (1998).

208. Kortunov, P. *et al.* The role of mesopores in

intracrystalline transport in USY zeolite: PFG NMR diffusion study on various length scales. *J. Am. Chem. Soc.* **127**, 13055–13059 (2005).

209. Silaghi, M.-C., Chizallet, C., Sauer, J. & Raybaud, P. Dealumination mechanisms of zeolites and extra-framework aluminum confinement. *J. Catal.* **339**, 242–255 (2016).

210. Liu, L. *et al.* Regioselective generation and reactivity control of subnanometric platinum clusters in zeolites for high-temperature catalysis. *Nat. Mater.* **18**, 866–873 (2019).

211. Schneider, D., Kondrashova, D., Valiullin, R., Bunde, A. & Kärger, J. Mesopore-promoted transport in microporous materials. *Chem. Ing. Tech.* **87**, 1794–1809 (2015).

212. Taylor, J. R. *An Introduction to Error Analysis: The Study of Uncertainties in Physical Measurements.* (University Science Books, Sausalito, 1996).

213. Kühne, T. D. *et al.* CP2K: An electronic structure and molecular dynamics software package - Quickstep: Efficient and accurate electronic structure calculations. *J. Chem. Phys.* **152**, 194103 (2020).

214. Lippert, G., Hutter, J. & Parrinello, M. The Gaussian and augmented-plane-wave density functional method for ab initio molecular dynamics simulations. *Theor. Chem. Acc.* **103**, 124–140 (1999).

215. Yanai, T., Tew, D. P. & Handy, N. C. A new hybrid exchange–correlation functional using the Coulomb-attenuating method (CAM-B3LYP). *Chem. Phys. Lett.* **393**, 51–57 (2004).

216. Lehtola, S., Steigemann, C., Oliveira, M. J. T. & Marques, M. A. L. Recent developments in libxc — A comprehensive library of functionals for density functional theory. *SoftwareX* **7**, 1–5 (2018).

217. Te Velde, G. *et al.* Chemistry with ADF. *J. Comput. Chem.* **22**, 931–967 (2001).

218. Software for chemistry & materials. *Software for Chemistry & Materials* https://www.scm.com/.

219. Van Gisbergen, S. J. A. *et al.* Density-functional-theory response-property calculations with accurate exchange-correlation potentials. *Phys. Rev. A* **57**, 2556–2571 (1998).

220. Van Gisbergen, S. J. A., Snijders, J. G. & Baerends, E. J. Implementation of time-dependent density functional response equations. *Comput. Phys. Commun.* **118**, 119–138 (1999).

221. Van Lenthe, E. & Baerends, E. J. Optimized Slater-type basis sets for the elements 1–118. *J. Comput. Chem.* **24**, 1142–1156 (2003).

222. Valencia, D., Whiting, G. T., Bulo, R. E. & Weckhuysen, B. M. Protonated thiophene-based oligomers as formed within zeolites: understanding their electron delocalization and aromaticity. *Phys. Chem. Chem. Phys.* **18**, 2080–2086 (2016).

223. Hazardous substances data bank (HSDB): 711. *National Library of Medicine* https://pubchem.ncbi.nlm.nih.gov/source/hsdb/711 (2022).

224. Hemelsoet, K. *et al.* Identification of intermediates in zeolite-catalyzed reactions by in situ UV/Vis microspectroscopy and a complementary set of molecular simulations. *Chem. – Eur. J.* **19**, 16595–16606 (2013).

225. VandeVondele, J. *et al.* Quickstep: Fast and accurate density functional calculations using a mixed Gaussian and plane waves approach. *Comput. Phys. Commun.* **167**, 103–128 (2005).

226. Becke, A. D. Density-functional exchange-energy approximation with correct asymptotic behavior. *Phys. Rev. A* **38**, 3098–3100 (1988).

227. Lee, C., Yang, W. & Parr, R. G. Development of the Colle-Salvetti correlation-energy formula into a functional of the electron density. *Phys. Rev. B* **37**, 785–789 (1988).

228. Grimme, S., Antony, J., Ehrlich, S. & Krieg, H. A consistent and accurate ab initio parametrization of density functional dispersion correction (DFT-D) for the 94 elements H-Pu. *J. Chem. Phys.* **132**, 154104 (2010).

229. De Baerdemaeker, T. *et al.* Catalytic applications of OSDA-free Beta zeolite. *J. Catal.* **308**, 73–81 (2013).

230. Van Minnebruggen, S. *et al.* Alkylation of isobutane with butenes using OSDA-free zeolite Beta. *J. Catal.* **406**, 206–212 (2022).

231. Newsam, J. M., Treacy, M. M. J., Koetsier, W. T. & De Gruyter, C. B. Structural characterization of zeolite Beta. *Proc. R. Soc. Lond. Ser. Math. Phys. Sci.* **420**, 375–405 (1988).

232. Higgins, J. B. *et al.* The framework topology of zeolite Beta. *Zeolites* **8**, 446–452 (1988).

233. Corma, A., Navarro, M. T., Rey, F., Rius, J. & Valencia, S. Pure polymorph C of zeolite Beta synthesized by using framework isomorphous substitution as a structure-directing mechanism. *Angew. Chem. Int. Ed.* **40**, 2277–2280 (2001).

234. Corma, A., Navarro, M. T., Rey, F. & Valencia, S. Synthesis of pure polymorph C of Beta zeolite in a fluoride-free system. *Chem. Commun.* 1486–1487 (2001).

235. Bárcia, P. S., Silva, J. A. C. & Rodrigues, A. E. Adsorption equilibrium and kinetics of branched hexane isomers in pellets of BETA zeolite. *Microporous Mesoporous Mater.* **79**, 145–163 (2005).

236. Kumarasinghe, R., Higgins, E. D., Ito, T. & Higgins, D. A. Spectroscopic and polarization-dependent single-molecule tracking reveal the one-dimensional diffusion pathways in surfactant-templated mesoporous silica. *J. Phys. Chem. C* **120**, 715–723 (2016).

237. Zhujun, Z. & Seitz, W. R. A fluorescence sensor for quantifying pH in the range from 6.5 to 8.5. *Anal. Chim. Acta* **160**, 47–55 (1984).

238. Seebacher, C. *et al.* Visualization of mesostructures and organic guest inclusion in molecular sieves with confocal microscopy. *Adv. Mater.* **13**, 1374–1377 (2001).

239. Han, S., Hermans, T. M., Fuller, P. E., Wei, Y. & Grzybowski, B. A. Transport into metal–organic frameworks from solution is not purely diffusive. *Angew. Chem. Int. Ed.* **51**, 2662–2666 (2012).

240. Tian, L., Feng, H., Dai, Z. & Zhang, R. Resorufin-based responsive probes for fluorescence and colorimetric analysis. *J. Mater. Chem. B* **9**, 53–79 (2021).

241. Chen, P. *et al.* Single-molecule fluorescence imaging of nanocatalytic processes. *Chem. Soc. Rev.* **39**, 4560–4570 (2010).

242. Bueno, C. *et al.* The excited-state interaction of resazurin and resorufin with aminesin aqueous solutions. Photophysics and photochemical reaction. *Photochem. Photobiol.* **76**, 385–390 (2002).

243. Ryder, A. G., Power, S. & Glynn, T. J. Fluorescence-lifetime-based pH sensing using resorufin. in *Opto-Ireland 2002: Optics and Photonics Technologies and Applications* vol. 4876 827–835 (International Society for Optics and Photonics, Bellingham, 2003).

244. Coleman, D. J. *et al.* A long-wavelength fluorescent substrate for continuous fluorometric determination of α-mannosidase activity: Resorufin α-d-mannopyranoside. *Anal. Biochem.* **399**, 7–12 (2010).

245. Brühwiler, D., Gfeller, N. & Calzaferri, G. Resorufin in the channels of zeolite L. *J. Phys. Chem. B* **102**, 2923–2929 (1998).

246. Flamigni, L., Venuti, E., Camaioni, N. & Barigelletti, F. A spectroscopic investigation of the temperature and solvent sensitivities of resorufin. *J. Chem. Soc. Faraday Trans. 2* **85**, 1935–1943 (1989).

247. Jiao, Y., Zhu, B., Chen, J. & Duan, X. Fluorescent sensing of fluoride in cellular system. *Theranostics* **5**, 173–187 (2015).

248. Karwacki, L. *et al.* Morphology-dependent zeolite intergrowth structures leading to distinct internal and outer-surface molecular diffusion barriers. *Nat. Mater.* **8**, 959–965 (2009).

249. Roeffaers, M. B. J. *et al.* Morphology of large ZSM-5 crystals unraveled by fluorescence microscopy. *J. Am. Chem. Soc.* **130**, 5763–5772 (2008).

250. Trueman, M., Akporiaye, D. & W. Anderson, M. Simulating intergrowth formation in zeolite crystals: Impact on habit and functionality. *Faraday Discuss.* **235**, 343–361 (2022).

251. Hendriks, F. C. *et al.* Probing zeolite crystal architecture and structural imperfections using differently sized fluorescent organic probe molecules. *Chem. Eur. J.* **23**, 6305–6314 (2017).

252. Parvulescu, A. N. *et al.* Chemical imaging of catalyst deactivation during the conversion of renewables at the single particle level: Etherification of biomass-based polyols with alkenes over H-Beta zeolites. *J. Am. Chem. Soc.* **132**, 10429–10439 (2010).

253. Sun, J. *et al.* Synthesis, surface and crystal structure investigation of the large zeolite beta crystal. *Microporous Mesoporous Mater.* **102**, 242–248 (2007).

254. Jeannot, V., Salmon, J.-M., Deumié, M. & Viallet, P. Intracellular accumulation of rhodamine 110 in single living cells. *J. Histochem. Cytochem.* **45**, 403–412 (1997).

255. Hendriks, F. C., Valencia, D., Bruijnincx, P. C. A. & Weckhuysen, B. M. Zeolite molecular accessibility and host–guest interactions studied by adsorption of organic probes of tunable size. *Phys. Chem. Chem. Phys.* **19**, 1857–1867 (2017).

256. Geier, O. *et al.* Interference microscopy investigation of the influence of regular intergrowth effects in MFI-type zeolites on molecular uptake. *J. Phys. Chem. B* **105**, 10217–10222 (2001).

257. Harris, D. C. & Lucy, C. A. *Quantitative Chemical Analysis*. (MacMillan Learning, New York, 2020).

258. Moosmüller, H. & Arnott, W. P. Particle optics in the Rayleigh regime. *J. Air Waste Manag. Assoc.* **59**, 1028–1031 (2009).

259. Hutter, J., Iannuzzi, M., Schiffmann, F. & VandeVondele, J. C2PK: Atomistic simulations of condensed matter systems. *WIREs Comput. Mol. Sci.* **4**, 15–25 (2014).

260. Becke, A. D. Density-functional thermochemistry. III. The role of exact exchange. *J. Chem. Phys.* **98**, 5648–5652 (1993).

261. Pye, C. C. & Ziegler, T. An implementation of the conductor-like screening model of solvation within the Amsterdam density functional package. *Theor. Chem. Acc.* **101**, 396–408 (1999).

262. VandeVondele, J. & Hutter, J. Gaussian basis sets for accurate calculations on molecular systems in gas and condensed phases. *J. Chem. Phys.* **127**, 114105 (2007).

263. Krack, M. Pseudopotentials for H to Kr optimized for gradient-corrected exchange-correlation functionals. *Theor. Chem. Acc.* **114**, 145–152 (2005).

264. Langtangen, H. P. & Linge, S. *Finite Difference Methods for Diffusion Processes*. (University of Oslo, Oslo, 2016).

265. Ed. Rumble, J. *CRC Handbook of Chemistry and Physics*. (CRC Press, Boca Raton, 2022).

266. Liu, X., Cheng, J., Lu, X. & Wang, R. Surface acidity of quartz: Understanding the crystallographic control. *Phys. Chem. Chem. Phys.* **16**, 26909–26916 (2014).

267. Petitjean, M. Applications of the radius-diameter diagram to the classification of topological and geometrical shapes of chemical compounds. *J. Chem. Inf. Comput. Sci.* **32**, 331–337 (1992).

268. Petitjean, M. About the algebraic solutions of smallest enclosing cylinders problems. *Appl. Algebra Eng. Commun. Comput.* **23**, 151–164 (2012).

Samenvatting voor iedereen

Het verminderen van het gebruik van fossiele grondstoffen, zoals steenkool, olie en aardgas, is één van de grootste uitdagingen van deze tijd. Alleen op deze manier kunnen we verdere klimaatverandering tegengaan en de samenleving verduurzamen. Om minder fossiele grondstoffen te gebruiken, zullen we alternatieve manieren moeten vinden om alledaagse producten te maken uit meer duurzame bronnen. Daarnaast zullen we beter moeten worden in het hergebruiken van producten. Katalyse speelt een grote rol in deze verduurzaming, omdat ze nodig is voor de vervaardiging van enorm veel producten. Denk aan de brandstof in de auto, plastic van verpakkingen en voedingsmiddelen zoals margarine en chocola. Ter illustratie, bij 85–90% van de producten uit de chemische industrie is een katalysator betrokken. De alternatieve chemische processen die nodig zijn voor de verduurzaming vragen om de ontwikkeling van nieuwe katalysatoren of de optimalisatie van bestaande katalysatoren en bijhorende chemische processen. De ontwikkelde methoden en bevindingen die in dit proefschrift gepresenteerd worden, dragen hieraan bij door een beter begrip van de werking van katalysatoren. Hierdoor kan men sneller en gerichter verbeteringen in het 'ontwerp' van een katalysator aanbrengen en dus doelgerichter chemische processen verduurzamen.

9.1 • Wat is een katalysator?

Katalyse is overal om ons heen. Als je aan iemand op straat vraagt wat een katalysator is, dan is het antwoord vaak "zit dat niet in de uitlaat van een auto?". Deze autokatalysator versnelt de chemische reacties die zorgen voor de afbraak van schadelijke stoffen in uitlaatgassen. Katalyse is echter op veel meer plekken om ons heen. Net zoals de autokatalysator de afbraakreacties van uitlaatgassen versnelt, zijn er talloze chemische reacties die gigantisch versneld worden door specifieke katalysatoren. Zo'n katalysator zorgt ervoor dat de chemische reactie bij lagere temperaturen kan plaatsvinden terwijl er minder afval wordt geproduceerd. In veel gevallen is het zelfs onhaalbaar om de chemische reactie uit te voeren zonder katalysator. Een belangrijke groep van katalysatoren zijn heterogene katalysatoren. Hierbij

is de katalysator (vaak een vaste stof) in een andere fase dan de moleculen die betrokken zijn bij de chemische reactie (vaak een gas en/of vloeistof). De heterogene katalysator is een complex mengsel van verschillende componenten met ieder hun eigen taak. Verspreid in het katalysatormateriaal zitten plekken waar de chemische omzetting daadwerkelijk plaatsvindt. Dit noemen we de reactiecentra van de katalysator. De reactiecentra kunnen zich bijvoorbeeld op het oppervlak van metalen nanodeeltjes of in de poriën van een katalysatordeeltje bevinden. De lengteschalen die van belang zijn voor heterogene katalyse zijn samenvat in Figuur I.

In dit proefschrift bestuderen we heterogene katalysatoren die zeolieten bevatten, omdat ze het reactiecentrum herbergen voor veel type reacties die nodig zijn voor de verduurzaming van chemische productieprocessen. Zeolieten zijn gemaakt van silicium- en zuurstofatomen en hebben een goed gedefinieerde kristalstructuur. Door een klein beetje silicium (Si^{4+}) atomen in het kristal te vervangen door aluminium (Al^{3+}) atomen ontstaat er een overmaat aan negatieve lading, die gecompenseerd moet worden door toevoeging van een positief geladen ion om het zeolietmateriaal ladingsneutraal te houden. Als dit ion een proton (H^+) is, dan gedraagt het materiaal zich als een zuur. De protonen geven het zeoliet katalytische eigenschappen en zijn de reactiecentra van het zeoliet. Deze reactiecentra bevinden zich niet op het oppervlak van een nanodeeltje, zoals in het voorbeeld in Figuur I, maar binnen in het zeolietmateriaal. Doordat het zeoliet een geordende kristallijne structuur heeft, bevat het zeoliet een repeterend netwerk van poriën met een diameter van enkele atomen groot. Dit is erg klein en veel soorten moleculen passen hierdoor niet in de poriën, waardoor ze niet bij de reactiecentra kunnen komen. Hierdoor stuurt het zeoliet welke beginstoffen (we noemen dit vaak reactanten) er kunnen reageren over de reactiecentra en welke producten er gevormd kunnen worden. Deze eigenschap maakt zeolieten erg interessant voor katalyse, omdat ze de chemische omzetting relatief gecontroleerd kunnen laten verlopen.
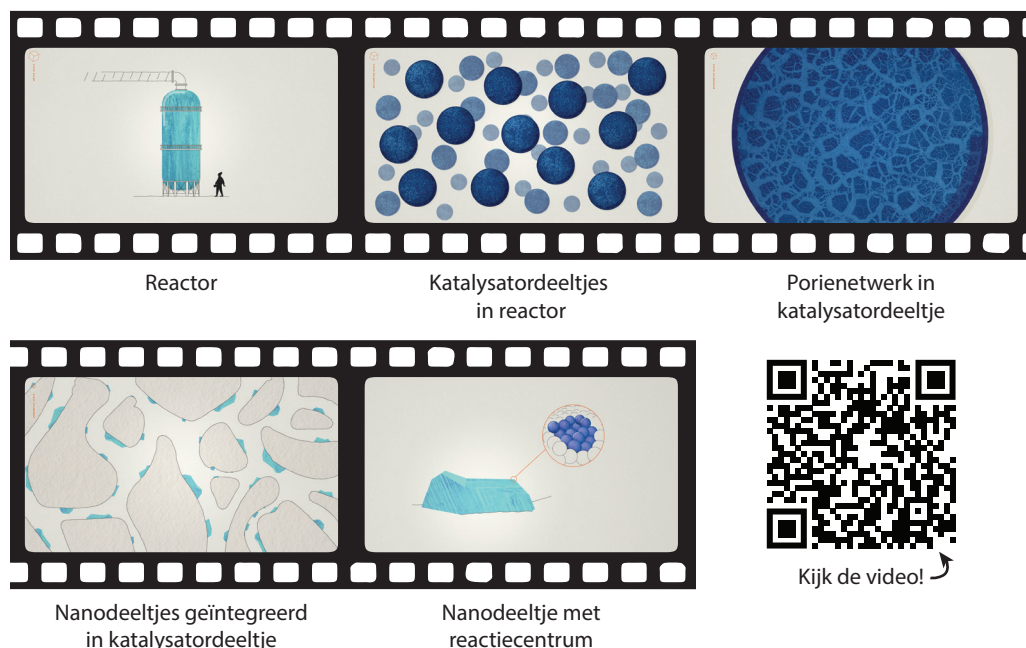
Figuur I • De lengteschalen die belangrijk zijn in heterogene katalyse van groot naar klein. De verkleining van de reactor (10 meter) naar het reactiecentrum op een metalen nanodeeltje (1 nanometer) is 10.000.000.000×. Scan de QR-code voor de introductievideo over de lengteschalen in heterogene katalyse. De beelden in de filmrol zijn momentopnames uit deze video. De animatie is gemaakt door Studio Synopsis in samenwerking met Edo A. G. de Kruijff, Noah Romijn, dr. Ivo A. W. Filot en de auteur van dit proefschrift in opdracht van het Gravitatie Programma *Netherlands Center for Multiscale Catalytic Energy Conversion* (MCEC), financieel ondersteund door de *Nederlandse Organisatie voor Wetenschappelijk Onderzoek* (NWO).

Om een chemische reactie over de reactiecentra te laten verlopen, is het belangrijk dat de reactanten hier efficiënt naartoe kunnen verplaatsen en de producten er makkelijk vandaan kunnen bewegen. Dit bewegingsproces heet diffusie en gebeurt spontaan door de botsingen met andere moleculen en de poriën van de katalysator. Een nadeel van de kleine poriën in het zeoliet is dat de reactanten en producten er langzaam doorheen bewegen. Daarom worden de stukjes zeoliet klein gehouden, zodat de moleculen zo min mogelijk afstand door het materiaal hoeven af te leggen. De zeolieten worden gemengd met (poreuze) dragermaterialen, zoals silica (SiO_2), alumina (Al_2O_3) en/of kleimineralen, die zorgen voor stabiliteit van de zeolietdeeltjes terwijl de zeolieten goed bereikbaar blijven voor de reactanten. Samen vormen deze componenten een katalysatordeeltje.

9.2 • Wat is het doel van dit proefschrift?

Het doel van dit proefschrift is een beter begrip van katalysatoren op basis van zeolietmateriaal. We focussen specifiek op het begrijpen van de diffusie van moleculen door het katalysatordeeltje. Om dit uit te leggen, kunnen we het katalysatordeeltje voorstellen als een stad waar mensen voor hun werk met de auto naartoe reizen. De poriën in de katalysator zijn de wegen en de reactanten en producten zijn forenzen in de auto. Er zijn snelwegen en provinciale wegen die mensen in de buurt van hun bestemming brengen (dit is analoog aan het dragermateriaal), terwijl kleinere straten het transport naar de werkplek in de wijk verzorgen (analoog aan het zeoliet). Een goe-
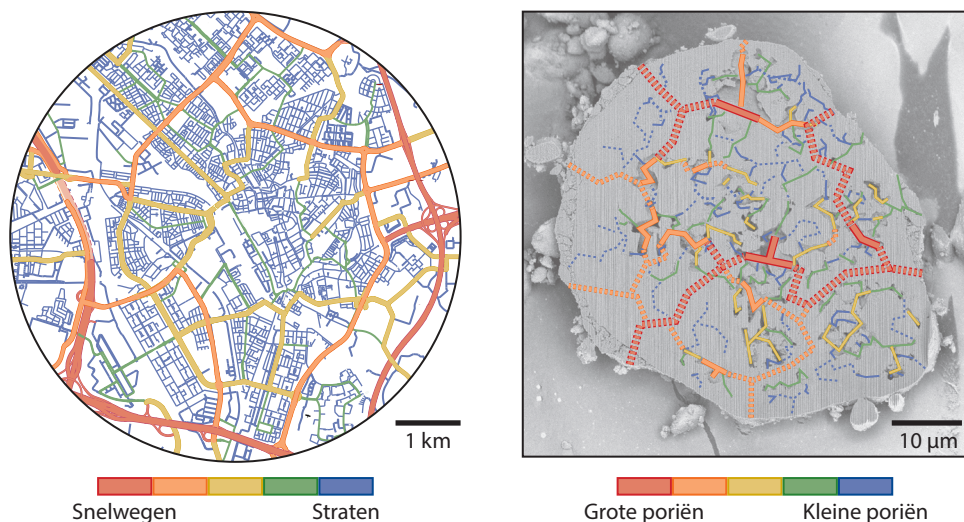
Figuur II • Het porienetwerk van een katalysatordeeltje (rechts) kan worden vergeleken met de wegen in een stad (links). Het netwerk van snelwegen en straten zorgt ervoor dat de hele stad goed bereikbaar is, net zoals een poriestructuur met grote en kleine poriën ervoor zorgt dat moleculen zich efficiënt door het katalysatordeeltje kunnen voortbewegen. De poriën van het katalysatordeeltje (rechts) zijn ingetekend over een dwarsdoorsnede van een katalysator uit Hoofdstuk 4. De gestippelde lijnen geven (fictieve) poriën aan op andere dieptes in de driedimensionale structuur. De wegen (links) zijn getekend op basis van data verkregen van openstreetmap.org van de stad Utrecht.

de balans van snelwegen en kleine straatjes is van belang om files te voorkomen en te zorgen dat mensen snel van en naar hun werk kunnen reizen. Deze balans zien we in echte steden zoals Utrecht en in echte katalysatordeeltjes, die beide zijn afgebeeld in Figuur II. In dit proefschrift willen we beter begrijpen wat het wegennetwerk van een katalysatordeeltje efficiënt maakt—en wat niet. We proberen de relatie te vinden tussen de eigenschappen van het porienetwerk (wegen) en reisgedrag van de moleculen (forenzen). Dit doen we door individuele of groepen moleculen te volgen als ze door de katalysator heen bewegen. Vaak weten we niet hoe de poriën in het katalysatordeeltje eruitzien en bestuderen we eerst het reisgedrag van de moleculen om het poriënnetwerk in kaart te brengen, bijvoorbeeld door te kijken waar files ontstaan. Daarna kunnen we de relatie tussen het porienetwerk en de diffusie van moleculen onderzoeken.

We volgen fluorescente moleculen en nanodeeltjes in een katalysatordeeltje. Als een molecuul of deeltje fluorescent is, betekent dat dat het licht van een rodere kleur uitstraalt wanneer het wordt beschenen. Dit is bekend van de *glow-in-the-dark* sterren die vroeger in menig kinderkamer hingen (en in mijn eigen studentenhuis). In de meeste materialen wordt het licht echter vrijwel direct weer uitgezonden en blijft het materiaal niet de hele nacht 'gloeien'. Voorbeelden van fluorescentie zijn te vinden in Figuur III. Het voordeel van fluorescentie is dat we het met hoge gevoeligheid kunnen waarnemen met een fluorescentiemicroscoop. Zelfs individuele moleculen en nanodeeltjes kunnen op deze manier over tijd gevolgd worden. Dit doen we in **Hoofdstukken 3, 4 & 5**. Ook de concentratie van fluorescente stoffen kan zo goed (over tijd) gemeten worden, wat we doen in **Hoofdstuk 6**. Het tweede voordeel is dat de kleur van het geabsorbeerde en uitgezonde licht verandert als de chemische eigenschappen van het molecuul of nanodeeltje veranderen, bijvoorbeeld door een reactie met het zeoliet. Hierdoor kunnen we het waarnemen als de reactie heeft plaatsge-
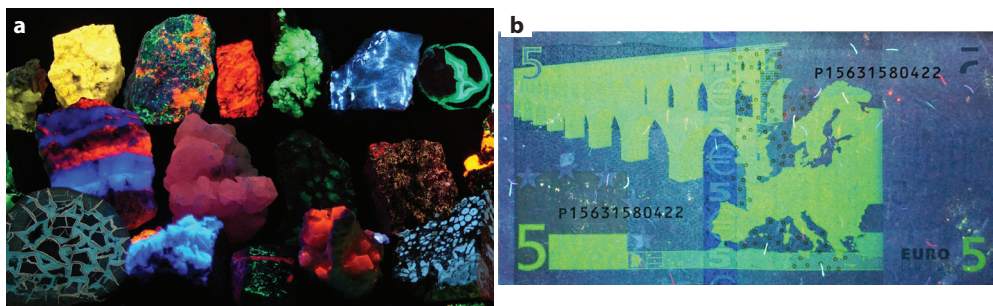
Figuur III • Voorbeelden van fluorescentie en fosforescentie onder belichting van ultraviolet licht (**a**) in natuurlijk voorkomende mineralen en (**b**) als beveiliging op een vijf eurobiljet. Bron foto in paneel **a**: Hannes Grobe/AWI op Wikipedia. Foto in paneel **b** met dank aan prof. dr. Andries Meijerink.

vonden en werkt het fluorescente molecuul of nanodeeltje als een sensor voor de chemische eigenschappen van de katalysator. Dit fenomeen komt terug in **Hoofdstuk 6**.

9.3 • Wat staat er in dit proefschrift?

We beginnen in **Hoofdstuk 2** met een uitleg van de theoretische achtergrond die nodig is om de basisprincipes van dit proefschrift te begrijpen. We focussen hier op de oorsprong en de natuurkundige beschrijving van het begrip diffusie. Daarnaast wordt uitgelegd hoe fluorescente moleculen en nanodeeltjes worden gemeten met behulp van verschillende soorten fluorescentiemicroscopie. We leggen uit hoe we nauwkeurig de *afgelegde paden* van de moleculen en nanodeeltjes uit een microscopiefilmpje kunnen halen. Uit deze paden kunnen we vervolgens met behulp van de natuurkundige beschrijving van diffusie de *diffusieconstante* bepalen, wat een maat is voor de verplaatsing van de moleculen en nanodeeltjes door het poreuze katalysatormateriaal. Om dit goed te kunnen bepalen, moeten we begrijpen wat voor soort diffusie er in de katalysator plaatsvindt. Tot slot wordt er een overzicht gegeven van eerder behaalde inzichten in diffusie in zeolieten en in het bijzonder experimenten waarin individuele moleculen werden gevolgd in katalysatordeeltjes.

Het bepalen en vergelijken van diffusie op basis van het afgelegde pad van individuele moleculen en nanodeeltjes is niet eenvoudig.

Het diffusiegedrag in katalysatoren is vaak grillig en gevarieerd. Daarnaast zijn de gemeten afgelegde paden vaak kort waardoor ze individueel niet genoeg informatie bevatten over het diffusiegedrag om een nauwkeurig beeld te geven. **Hoofdstuk 3** bespreekt de *DiffusionLab* software en de methode die we hebben ontwikkeld voor het analyseren deze afgelegde paden. De paden worden eerst in categorieën opgedeeld met een vergelijkbare diffusiesoort, waarna de diffusie wordt geanalyseerd en de diffusieconstante wordt bepaald. Het voordeel van deze aanpak is dat de gemiddelde diffusie kan worden berekend van een groep van paden zonder informatie te verliezen over de ruimtelijke spreiding van de diffusiesoort. De afgelegde paden worden op basis van hun eigenschappen ingedeeld in verschillende groepen. Voorbeelden van een eigenschap zijn de lengte of vorm van de afgelegde paden. Omdat er vaak (tien)duizenden paden in een enkele meting gevonden worden, gebruiken we een statistische analyse (die ook bekend staat als kunstmatige intelligentie, tegenwoordig afgekort als AI van *artificial intelligence*) om de paden automatisch in te delen. Vervolgens kan de methode handmatig worden aangepast voor metingen op andere katalysatoren of in andere meetcondities. We laten in dit hoofdstuk, met behulp van gesimuleerde paden, zien dat deze aanpak erg effectief is en de diffusie-eigenschappen correct weet te verkrijgen. We hebben deze methode gebruikt in **Hoofdstuk 5**.

In **Hoofdstuk 4** onderzoeken we hoe de afgelegde paden van fluorescente nanodeeltjes gebruikt kunnen worden om de poriën van een katalysator in kaart te brengen. Door bij te houden waar de nanodeeltjes komen, kan er een kaart worden gemaakt van de toegankelijke poriën en hun onderlinge verbindingen. Om dit goed te kunnen doen, is het belangrijk om te weten hoe een nanodeeltje zich gedraagt als het door de poriën heen beweegt: wanneer adsorbeert het nanodeeltje aan de poriewand en hoe beweegt het deeltje door de poriën? Dit soort vragen zijn lastig te beantwoorden door direct naar industriële katalysatoren te kijken, omdat ze vaak een onregelmatige poriestructuur hebben. Daarom hebben we een kunstmatige porie ontwikkeld waarin de moleculen en nanodeeltjes eenvoudig kunnen worden gevolgd met behulp van fluorescentiemicroscopie. Van de kunstmatige porie weten we heel precies hoe deze eruitziet en hoe groot het is. Het is belangrijk dat het nanodeeltje tijdens de meting niet adsorbeert aan de poriewand, en dus tijdelijk vastgeplakt zit, omdat dit zorgt voor fouten bij het bepalen van het afgelegde pad. Door metingen in de kunstmatige porie hebben we geleerd dat adsorptie van de nanodeeltjes kan worden onderdrukt door de zuurtegraad van het oplosmiddel te variëren. Hierdoor hebben we bijvoorbeeld stroming in de poriën kunnen meten. In een industrieel-relevant katalysatordeeltje hebben we verder gevonden dat maar 9% van het katalysatorvolume toegankelijk is voor het nanodeeltje. Dit is slechts 65% van de het totale porievolume in de katalysator. We zien hiernaast veel mogelijkheden voor het inzetten van de kunstmatige porie kunnen om fundamentele vraagstukken over diffusie in katalysatoren te onderzoeken.

Hoofdstuk 5 bespreekt de resultaten van een studie waarbij we de diffusie van individuele fluorescerende moleculen volgen in zeolieten. Deze zeolieten hebben twee verschillende soorten poriën, namelijk sinusoïde en rechte poriën, die beiden een vergelijkbaar formaat maar een verschillende vorm hebben. We zien dat de moleculen regelmatig adsorberen in de zeolietporiën, waardoor de moleculen langzamer door het zeoliet heen bewegen. Met behulp van de *DiffusionLab* software en me-

thode beschreven in **Hoofdstuk 3** hebben we de mobiliteit van de moleculen (wanneer deze niet geadsorbeerd zijn) gekwantificeerd, net als het plaatsvinden van adsorptie. De vorm van de zeolietporiën speelt een grote rol en de gemiddelde diffusieconstante in de rechte poriën was 10× hoger dan in de sinusoïde poriën. Zowel de mobiliteit van de moleculen neemt toe wanneer deze niet geadsorbeerd zijn en de moleculen zijn in totaal minder vaak geadsorbeerd. In de industrie is het gebruikelijk om grote poriën in zeolieten te etsen, naast de kleine poriën die van nature in zeolieten zitten, om diffusie door de zeolietdeeltjes te stimuleren. Onze resultaten laten zien dat de toevoeging van deze grotere poriën de diffusie door sinusoïde zeolietporiën verbetert. Hier tegenover staat dat diffusie in de rechte poriën wordt gereduceerd door een toename van adsorptie, waarschijnlijk veroorzaakt door achtergebleven materiaal na het etsen. Het etsen van grotere poriën in het zeoliet helpt met het versnellen van diffusie in het zeolietmateriaal, maar hierbij is het van belang dat restproducten van het etsen goed worden opgeruimd. Als zeolieten in een katalysatordeeltje worden gebracht, moet ervoor gezorgd worden dat de zeolietporiën waar de moleculen het snelste doorheen bewegen in contact staan met de poriën in het dragermateriaal.

In **Hoofdstuk 6** kijken we naar het de concentratie van fluorescente moleculen wanneer deze door de poriën van een zeolietdeeltje diffunderen. De meeste fluorescente moleculen die worden gebruikt met fluorescentiemicroscopie zijn zo groot dat ze niet in de poriën van een zeoliet passen. Daarom onderzoeken we een molecuul met de naam *resorufin* dat wel in de poriën past. We hebben ontdekt dat dit molecuul in de poriën van een zeoliet fluorescent is, terwijl het molecuul niet fluorescent is wanneer het in water is opgelost. Het resorufinmolecuul ondergaat een chemische reactie, waardoor de fluorescentie-eigenschappen veranderen in de zeolietporiën en we specifiek de fluorescentie van dit molecuul kunnen meten. In waterige oplossing ondergaat een klein deel van de resorufinmoleculen dezelfde reactie. We zien deze moleculen niet, omdat ze in waterige oplossing samenklonteren waardoor ze

hun fluorescente eigenschappen verliezen. In de zeolietporiën is er geen ruimte om samen te klonteren en blijft het molecuul fluorescent. Deze eigenschappen gebruiken we om te kijken welk deel van de zeolietdeeltjes toegankelijk is via de poriën en zo een kaart van het zeoliet-deeltje te maken. Daarnaast onderzoeken we diffusie van de resorufinmoleculen vanuit een waterige oplossing in de zeolietporiën. Door het concentratieprofiel van resorufin in het zeoliet te meten en deze te vergelijken met een natuurkundige beschrijving kunnen we de diffusieconstante van deze moleculen in de zeoliet bepalen. Onze metingen laten zien dat diffusie door een zeolietdeeltje erg vertraagd kan worden als de geordende structuur van de zeoliet tijdelijk onderbroken wordt, dus ideali-ter bestaat het zeoliet in een katalysatordeeltje uit één ononderbroken stuk.

In **Hoofdstuk 7** vatten we bevindingen uit dit proefschrift samen en leggen we verbanden tussen de verschillende hoofdstukken. We slui-ten af met een vooruitblik en aanbevelingen voor toekomstig onderzoek.

Acknowledgements

Promoveren kan erg individualistisch zijn, maar zo heeft het voor mij nooit gevoeld. Met drie (co)promotoren en meerdere projecten op basis van nauwe samenwerking heb ik veel in teamverband gewerkt. Ik wil graag de mensen bedanken die mij hebben geholpen tijdens mijn promotieonderzoek en deze tijd zo leuk hebben gemaakt.

Bert, bedankt voor de vrijheid die je me hebt gegeven tijdens mijn promotie. Jouw kritische blik en oog voor het grotere geheel zijn erg waardevol geweest in het doen en opschrijven van mijn promotieonderzoek. Jij waakte voor het chemische verhaal als ik te veel oog had voor de methode en analyse. Daarnaast heb ik heb veel van je geleerd over de wetenschappelijke wereld en wat er komt kijken bij het draaiende houden van zo'n grote onderzoeksgroep.

Freddy, bedankt voor je uitgebreide commentaar op mijn manuscripten en tijdens de vele *Bravelingenbijeenkomsten*. Ik heb me vaak verwonderd over jouw snelle begrip en haast feilloze wetenschappelijke intuïtie. Daarnaast kan ik jouw focus op taal en interpunctie enorm waarderen. Hier heb ik veel van opgestoken en het correct gebruik van een -, –, – en — vind ik nu een vereiste voor een leesbaar stuk tekst. Iets anders waarin we elkaar konden vinden is het feit dat zo'n klein, rond, speculaasachtig stuk strooigoed een kruidnoot heet, ondanks dat veel mensen om ons heen het een pepernoot blijven noemen. Erg *bonding* vond ik dat. Jouw deur stond altijd open voor vragen of je liep langs voor een praatje. Dit heeft er mede voor gezorgd dat de Bravelingen zo'n hechte groep zijn geworden, waar ik met veel plezier onderdeel van was.

Florian, thank you for the countless discussions and brainstorm sessions about science and other topics. The *Pore-Space Exploration* meetings were always a pleasure to attend, particularly when we went deep into a coding, physics or statistics topic. Your energy and enthusiasm were very motivating. I appreciate that you always took the time if there was something to discuss. Even when you were busy, you gave me the feeling that we had all the time in world.

The PhD research was done in collaboration with many people. **Donglong**, you have been a great help when I just started my PhD and you were finishing yours. I have learned a lot from you when we were writing the review and experimental paper together. Your zeolite ZSM-5 films are truly a piece of art. **Luke**, I have always enjoyed your humour and banter. It was a pleasure to spend time with you in the lab and after work. The *Swamp Water* beer we brewed together is still one of my favourites. **Rafael**, our collaboration was not an easy project, and I am grateful we could do it together. After measuring noisy images day after day, the feeling of victory was amazing when we finally saw the quantum dots diffusing in your nanofluidic device. **Yadi**, you have contributed much to the research in this thesis, and it was great when you could join in the lab. I appreciated your help and advice—in the lab and outside work. You are one of the kindest persons I know. **Katarina**, thank you for performing the density functional theory calculations, which have been important in supporting our scientific conclusions. **Nikos**, your excellent focused ion beam–scanning electron microscopy images have gotten a prominent place in the thesis. Thank you. **Alfons**, bedankt voor je input tijdens werkbesprekingen en uitgebreide commentaar op het manuscript dat uiteindelijk Hoofdstuk 6 is geworden. Jouw encyclopedische kennis en creativiteit zijn indrukwekkend. Het was erg fijn om daaruit te kunnen putten.

During my PhD research, I had the pleasure of supervising a number of students. **Marita**, you were a great student with excellent lab skills and a high level of independence. Thanks to the groundwork you have laid, we later successfully measured diffusion of single quantum dots in a silica catalyst particle. **Kevin**, jouw project was niet eenvoudig en ik vind het knap hoe je je snel wegwijs hebt gemaakt in het onderwerp. Het was erg gezellig om met je te praten over wetenschap en zaken daarbuiten. Ik hoop dat we jouw mooie resultaten snel kunnen publiceren. **Jesse** en **Winston**, het was leuk en leerzaam om jullie te begeleiden tijdens jullie (literatuur)onderzoek. Bedankt voor jullie inzet. **Bill** en **Koen**, bedankt voor jullie bijdrage aan

je me tijdens mijn bedrijfsstage met Florian en Bert in contact hebt gebracht. Terugkijkend is dat een bepalend moment geweest. **Kordula**, I enjoyed our random chats about crabs and other nonsense that sometimes took an unexpected turn. **Adrian**, **Huygen**, **Jelle** (Bos), **Jelle** (Kranenborg), **Jim**, **Joëlle**, **Kris**, **Laura** (Zoutendijk), **Matteo**, **Mariangela, Robin**, **Thimo**, and **Ward** thanks for the chats and fun during *borrels* and house parties. **Jim**, we wisten elkaar te vinden tijdens MCEC events en daarbuiten. Jouw bijdrage aan de Afwasdeuntjes heeft de lijst naar een hoger niveau gebracht. Bij het stofzuigen geniet ik daar nog elke week van.

Conferences are the cherry on the cake of the PhD experience. I would like to highlight the NAM conference, where I spent a great time with **Francesco**, **Laura** (Barberis), **Luc**, **Nienke**, **Romy**, and **Suzan**. Some of us even went to the MoMA, a show at Broadway, and a rooftop bar overlooking Manhattan—all in one day. **Sebastian** (Rejman), your platinum membership at a hotel chain got us to the best view of the hotel over New York City. Thank you, that was absolutely amazing. **Romy** en **Tom**, bedankt voor jullie zorgen en geduld tijdens ons verblijf in Japan voor de TOCAT conferentie. Een ontstoken voet brengt je helaas niet ver.

At the Ornstein laboratory, I had the joy to share an office with **Anna**, **Jessi**, **Pepijn**, and later with **Alptug**, **Vincent**, and **Zahra**. **Jessi**, bedankt dat je me in OL0.12 hebt geïntroduceerd. Het was erg interessant om van dichtbij te zien hoe jij je thesis aan het afronden was—zo wist ik een beetje wat er komen ging. We hebben het ook veel gehad over jouw ervaringen in de Verenigde Staten en het doen van een postdoc in het buitenland. Ik heb je advies onder het genot van een kopje koffie erg op prijs gesteld. **Anna**, thank you for being an amazing office mate and keeping the plant(s) alive. **Vincent**, terwijl ik druk bezig was met afronden kwam jij nieuw in OL0.12. Door mijn contractverlengingen hebben we gelukkig nog veel tijd gehad om elkaar af te leiden.

Stijn, als maker van de Bravescoop heb je indirect een grote bijdrage geleverd aan deze thesis. Ik heb enorm veel van je geleerd over het bou-

wen en uitlijnen van onze microscoop. Je bent goed in het helder en gestructureerd uitleggen, waar ik veel profijt van heb gehad. Het is leuk dat we elkaar buiten werk ook hebben leren kennen, vaak in combinatie met een spelletje. **Mark**, ik moet altijd erg lachen om je humor en scherpe observaties. We wisten elkaar vaak te vinden op de *MCEC Annual Meeting, DO days* en verschillende *Schools*. Op een uitje van SCM naar de Biesbosch hebben we zelfs als enige een bever gezien. Ik hoop dat we binnenkort in Zwitserland ook een *Murmeltier* kunnen spotten—maar dan écht. **Sander**, bedankt voor je behulpzaamheid in het optisch lab en met theoretische zaken. Het gemak waarmee jij fysische modellen in elkaar zet, vond ik fascinerend om te zien. Ik ben er zeker van dat je mooi onderzoek zult doen tijdens je promotietraject; en daarna. **Harith**, it was a pleasure to organise the group outing together and getting to know you better. **Maarten**, wie had in jaar één van de scheikundestudie gedacht dat we elkaar zo vaak tegen het lijf zouden lopen? Bedankt voor alle leuke gesprekjes als we elkaar tijdens de pauze of op een ander moment tegenkwamen. **Roy**, ik vond het leuk om je te zien hoe je van eerstejaars student bij het practicum tot gewaardeerd onderzoeker bij SCM bent uitgegroeid.

Bedankt **Sebi** voor de leuke herinneringen van ons samen. Bier brouwen, sport kijken, of een hapje eten. Je bracht veel mensen bij elkaar, zoals bij de *Der Herr der Ringe* bordspelavonden. Het verdriet dat jij er niet meer bij kan zijn, is nog steeds niet te omschrijven. **Angela**, **Joyce** en **Mirjam**, heel erg bedankt voor de steun in de periode die volgde.

Work hard, play hard. **Jasper**, **Marieke** en **Maxime**, wat een heerlijk stel pannenkoeken zijn we toch. Laten we vooral zo blijven. Een vriendschap die begon in Zweden heeft ondertussen vele verhuizingen binnen Europa overleefd. Ik kan niet wachten tot we weer *drinksies* kunnen gaan doen (wellicht met kaasfondue?). Joe joe. **Pim** en **Stan**, bedankt voor onze vriendschap, die al zo lang bestaat als ik herinneringen heb. **Jim**, bedankt voor je onophoudelijke interesse in mijn onderzoek, goede vragen en commentaar. Ik had je graag als vakgenoot gezien, maar

waar we een slimme scheikundige zijn verloren, hebben we er een excellente jurist voor teruggekregen.

Verder wil ik graag mijn **moeder**, **vader**, **Aad**, **Astrid** en **Frederieke** bedanken voor al jullie interesse en steun. **Papa**, het was leuk om met jou mijn nieuwste experimenten te bespreken. We konden hier altijd op hoog niveau over praten. Ook heb ik veel van je geleerd over het opmaken van tekst; veel van jouw tips heb ik kunnen toepassen in het proefschrift. **Mama**, bedankt voor al je hulp en steun als de promotie wat minder soepel liep. Gelukkig kon ik bij jou thuis makkelijk ontspanning vinden, vaak

met een kopje rooibos- of jasmijnthee. **Frede-rieke**, je hebt heel wat gesprekken tijdens het avondeten moeten doorstaan waarin ik aan het ratelen was over mijn studie en/of onderzoek. Ik ben er trots op dat het nu aan jou is. Ik hoop dat je net zoveel lol gaat beleven aan jouw studie (en misschien wel promotie?!) als ik heb gehad.

Tot slot, **Saskia**, bedankt voor al je liefde en steun tijdens de afgelopen jaren. Het was een hele leuke tijd en ik hoop dat we nog heel lang zo door mogen gaan. Ons volgende avontuur in Zwitserland is net begonnen; ik heb er enorm veel zin in!

List of publications

The articles below are organized in reverse order of their publication and/or submission date.
* The scientific results described in this PhD thesis are based on these articles.
+ Both authors contributed equally.

11.* **Fluorescent-probe characterisation for pore-space mapping with single-particle tracking**
Mayorga González, R.,+ Maris, J. J. E.,+ Wagner, M., Ganjkhanlou, Y., Bomer, J. G., Werny, M. J., Odijk, M., Rabouw, F. T., Weckhuysen, B. M. & Meirer, F.
Manuscript in preparation

10.* **Molecular accessibility and diffusion in large zeolite crystals visualised with resorufin**
Maris, J. J. E.,+ Parker, L. A.,+ Stanciakova, K., Nikolopoulos, N., Berendsen, K. M. H., Van Blaaderen, A., Meirer, F., Rabouw, F. T., & Weckhuysen, B. M.
Submitted

9.* **Classification-based motion analysis of single-molecule trajectories using DiffusionLab**
Maris, J. J. E., Rabouw, F. T., Weckhuysen, B. M. & Meirer, F.
Sci. Rep. **12**, 9595 (2022)

8.* **Unravelling channel structure–diffusivity relationships in zeolite ZSM-5 at the single-molecule level**
Fu, D.,+ Maris, J. J. E.,+ Stanciakova, K., Nikolopoulos, N., Van der Heijden, O., Mandemaker, L. D. B., Siemons, M. E., Salas Pastene, D., Kapitein, L. C., Rabouw, F. T., Meirer, F. & Weckhuysen, B. M.
Angew. Chem. Int. Ed. **64**, e202114388 (2022)

7. **Dual fluorescence in glutathione-derived carbon dots revisited**
Ganjkhanlou, Y.,+ Maris, J. J. E.,+ Koek, J., Riemersma, R., Weckhuysen, B. M. & Meirer, F.
J. Phys. Chem. C **126**, 2720–2727 (2022)

6.* **Single-molecule observation of diffusion and catalysis in nanoporous solids**
Maris, J. J. E., Fu, D., Meirer, F. & Weckhuysen, B. M.
Adsorption **27**, 423–452 (2021)

5. **ArGSLab: a tool for analyzing experimental or simulated particle networks**
Immink, J. N., Maris, J. J. E., Capellmann, R. F., Egelhaaf, S. U., Schurtenberger, P. & Stenhammar, J.
Soft Matter **17**, 8354–8362 (2021)

4. **On the role of softness in ionic microgel interactions**
    Bergman, M. J., Nöjd, S., Mohanty, P. S., Boon, N., Immink, J. N., Maris, J. J. E.,
    Stenhammar, J. & Schurtenberger, P.
    Soft Matter **17**, 10063–10072 (2021)

3. **Crystal-to-crystal transitions in binary mixtures of soft colloids**
    Immink, J. N., Bergman, M. J., Maris, J. J. E., Stenhammar, J. & Schurtenberger, P.
    ACS Nano **14**, 14861–14868 (2020)

2. **Using patchy particles to prevent local rearrangements in models of
    non-equilibrium colloidal gels**
    Immink, J. N., Maris, J. J. E., Schurtenberger, P. & Stenhammar, J.
    Langmuir **36**, 419–425 (2019)

1. **Reversible formation of thermoresponsive binary particle gels with tunable
    structural and mechanical properties**
    Immink, J. N., Maris, J. J. E., Crassous, J. J., Stenhammar, J. & Schurtenberger, P.
    ACS Nano 13, 3292–3300 (2019)

List of presentations

October 2022
Mass transport in porous solids probed with fluorescent reporters (oral presentation)
in the group of Prof. David Norris at ETH Zürich, Switzerland

July 2022
Towards more efficient zeolites: Visualizing motion on the single-molecule level (oral presentation)
at the 9th Tokyo Conference on Advanced Catalytic Science and Technology (TOCAT-9), Fukuoka, Japan

July 2022
Towards more efficient zeolites: Visualizing motion on the single-molecule level (oral presentation)
at the 20th International Zeolite Conference (IZC), Valencia, Spain

July 2022
Photophysics and applications of resorufin in zeolite micropores (poster presentation)
at the 20th International Zeolite Conference (IZC), Valencia, Spain

May 2022
Towards more efficient zeolites: Visualizing motion on the single-molecule level (oral presentation)
at the 27th North American Catalysis Society Meeting (NAM-27), New York City, New York, United States of America

May 2022
Direct visualization of resorufin accessibility and diffusion in zeolite-β (oral presentation)
at the 23rd Netherlands' Catalysis and Chemistry Conference (NCCC), Noordwijkerhout, The Netherlands

December 2021
Photophysics and applications of resorufin in zeolite micropores (poster presentation)
at the Netherlands Research Council CHemistry As Innovating Science Conference (NWO CHAINS), online

May 2021
Making more efficient zeolites: Visualizing motion on the single-molecule level (poster presentation)
at the Spring Meeting of the European Materials Research Society (E-MRS), online

March 2021
Making more efficient zeolites: Visualizing motion on the single-molecule level (poster presentation)
at the 22nd Netherlands' Catalysis and Chemistry Conference (NCCC), online
Prize for best poster, awarded by VIRAN (€500)

March 2020
DiffusionLab: Analysis of single-fluorophore trajectories in porous catalysts (poster presentation)
at the 21st Netherlands' Catalysis and Chemistry Conference (NCCC), Noordwijkerhout, The Netherlands

March 2019
Quantitative fluorescence imaging of proton transfer between furfuryl alcohol oligomers and acid sites in zeolite ZSM-5 (poster presentation)
at the Probing Chemical Reactions by Single-Molecule Spectroscopy Conference, Kloster Höchst, Germany

March 2019
Quantitative fluorescence imaging of proton transfer between furfuryl alcohol oligomers and acid sites in zeolite ZSM-5 (poster presentation)
at the 20th Netherlands' Catalysis and Chemistry Conference (NCCC), Noordwijkerhout, The Netherlands

About the author

Erik Maris was born in Gouda, the Netherlands, on May 10, 1994. In 2012, he graduated from the Grotius College in Delft, after which he studied chemistry at Utrecht University. He was awarded with the *VNCI TopSector Chemistry Scholarship*, which he received during his bachelor's studies. In 2015, he obtained his bachelor's degree *cum laude* with a research project on multi-modal spectroscopy for the methanol-to-olefins reaction, in the group of prof. Bert Weckhuysen. Erik continued his studies in Utrecht and followed the master's programme *Nanomaterials: Chemistry and Physics*. He was awarded the *VNCI TopSector Chemistry Scholarship* and received the scholarship for two years during the master's programme. For his master's thesis research, he moved to Sweden for a year to join the group of prof. Peter Schurtenberger at Lund University, investigating binary thermo-responsive-particle gels. During his 5-month internship, he worked with nickel-based catalysts in the company BASF. He received his master's degree *cum laude* in 2018.

In May 2018, Erik started as a PhD researcher under the supervision of prof. Bert Weckhuysen, dr. Florian Meirer, and dr. Freddy Rabouw in the *Inorganic Chemistry and Catalysis* group of the Department of Chemistry at Utrecht University. His research project was funded by the Gravitation Program *Netherlands Center for Multiscale Catalytic Energy Conversion* (MCEC). The main results of the research project are described in this PhD thesis, which have been published in peer-reviewed academic journals and presented at (inter)national conferences. As part of his project, Erik supervised several BSc and MSc students as well as lab and theoretical courses. He was an active member of the MCEC community and helped organise a number of social and outreach activities. Among others, he chaired a team that realised an educational video called *Visualizing Multiscale Catalysis*, in collaboration with a professional animation studio.

Chapter pages:
1. Gouda, Zuid Holland, the Netherlands
2. Delft, Zuid Holland, the Netherlands
3. Utrecht Science Park, Utrecht, the Netherlands
4. Afsluitdijk, Noord Holland & Friesland, the Netherlands
5. Almere Oostvaarders, Flevoland, the Netherlands
6. Noordoostpolder, Flevoland, the Netherlands
7. Zürich, Zürich, Switzerland